The large scale structures. A window on the dark components of the Universe

Stéphane Ilic Ilić

Université Paris-Sud

Ecole Doctorale Particules, Noyaux, Cosmos (ED 517)
Institut d'Astrophysique Spatiale (IAS)

Discipline : Cosmologie

Thèse de doctorat

Soutenue le 23 octobre 2013 par

Stéphane Ilić

The large scale structures : a window on the Dark components of the Universe

Directeur de thèse :	Mathieu Langer	Maître de Conférences (IAS, Orsay)
Co-directeur de thèse :	Marian Douspis	Astronome Adjoint (IAS, Orsay)

Composition du jury :

Président du jury :	Alain Abergel	Professeur (IAS, Orsay)
Rapporteurs :	François-Xavier Désert	Astronome (IPAG, Grenoble)
	Martin Kunz	Professeur (ITP, Genève)
Examinateurs :	Jean-Christophe Hamilton	Directeur de recherche (APC, Paris)
	Patricio Vielva	Professeur (IFCA, Santander)

"When I reach for the edge of the universe, I do so knowing that along some paths of cosmic discovery, there are times when, at least for now, one must be content to love the questions themselves."

Neil deGrasse Tyson

UNIVERSITÉ PARIS-SUD

Abstract

Institut d'Astrophysique Spatiale

Doctor of Science

The large scale structures : a window on the Dark components of the Universe

by Stéphane Ilić

The dark energy is one of the great mysteries of modern cosmology : it is an unknown component supposed to fill the whole universe and be responsible for the current acceleration of the expansion of our Universe. Its study is a major focus of my thesis : the way I choose to study and characterize this Dark Energy is based on the large-scale structure of the Universe through a probe called the integrated Sachs-Wolfe effect (iSW). This effect is theoretically detectable in the cosmic microwave background (CMB) : this light, which originated in the early Universe (380,000 years after the Big Bang), travelled through large structures in the Universe (galaxies and clusters) before reaching us, all of them underlain by gravitational potentials. The acceleration of the expansion (and dark energy) has the effect of stretching and "flattening" these potentials during the crossing of photons, which has the effect of providing some extra energy of these FDC photons, which will depend on the properties of the dark energy. The iSW effect has a direct but weak effect on the power spectrum of the temperature fluctuations of the FDC effect : it therefore requires the use of external data to be detectable. A conventional approach to this problem is to correlate the FDC with a tracer of the distribution of matter in the Universe (usually galaxy surveys), and therefore the underlying gravitational potential. This has been attempted numerous times with surveys covering a large range of wavelengths, the measured correlation has yet to give a definitive and unambiguous result on the detection of the iSW effect. This is mainly due to the shortcomings of current surveys that are not deep enough and/or have a too low sky coverage. A part of my thesis is devoted to the correlation of FDC with another diffuse background, namely the cosmological infrared background (CIB), which is composed of the integrated emission of the non-resolved distant galaxies. I was able to show that it is an excellent tracer of the gravitational potentials, being free from many of the shortcomings of current surveys. The results of this study shows that the levels of significance for the expected correlation CIB-CMB exceed those of current surveys, and compete with those predicted for the

future generation of very large surveys to come (Pan-STARRS, LSST, Euclid). In the following, my thesis was then focused on the individual imprint of the largest structures in the Universe in the CMB by iSW effect. According to an article by Granett et al. (2008), the iSW effect was directly detected by a stacking approach of patches of the CMB at the positions of superstructures. However, the high measured amplitude of the effect seems to be at odds with predictions from the standard model of cosmology. My work on the subject was first involved revisiting this study with my own protocol, completed and associated with a variety of statistical tests to check the significance of these results. This point proved to be particularly difficult to assess and subject to possible selection bias. I extended the use of this detection method to other available catalogues of structures, more consequent and supposedly more sophisticated in their detection algorithms. The results from one of these new catalogues (Sutter et al., 2012) suggests the presence of a signal at scales and amplitude more consistent with the theory, but at more moderate levels of significance than the catalogue and Granett al. At the same time, being a member of the HFI Core Team of the Planck Collaboration, I also performed the same detection using data from the new satellite. The results of the stacking approach introduced a number of questions concerning the nature of the expected signal : this led me to actively work on a theoretical prediction of the iSW effect produced by the superstructures previously mentioned, through simulations based on general relativity and the Lematre-Tolman-Bondi metric. This allowed me to reproduce the structures of Granett et al. and predict the exact full theoretical iSW effect of these structures. This work showed that the central amplitude of the measured signal is consistent with the LCDM theory, but the measured signal shows non-reproducible features that are not compatible with my predictions. An extension of my framework to the additional catalogues that I considered will verify the significance of their associated signals and their compatibility with the theory . Another part of my thesis focuses on a distant time in the history of the Universe, called reionisation : the transition from a neutral universe to a fully ionised one under the action of the first stars and other ionising sources. This period has a significant influence on the CMB and its statistical properties, in particular the power spectrum of its polarisation fluctuations. In my case, I focused on the use of temperature measurements of the intergalactic medium during the reionisation in order to investigate the possible contribution of the disintegration and annihilation of the hypothetical dark matter. Starting from a theoretical work based on several models of dark matter, I computed and compared predictions to actual measures of the IGM temperature, which allowed me to extract new and interesting constraints on the critical parameters of the dark matter and crucial features of the reionisation itself.

Acknowledgements/Remerciements

Je tiens à remercier toutes les personnes que j'ai rencontrées dans ma vie, pour avoir joué un rôle (aussi ténu soit-il) pour faire de moi ce que je suis aujourd'hui.

...

...

...

Voilà pour la version ultra-courte de mes remerciements (avec une petite rime en prime) s'il m'était demandé de les résumer en une phrase ! Mais comme un bon nombre de personnes incluses dans l'ensemble sus-nommé mérite bien plus que deux simples lignes, il est impératif que je les remercie plus en détail :

- En tout premier lieu, je tiens à remercier une nouvelle fois les membres du jury d'avoir accepté mon invitation à évaluer ma thèse et ma soutenance, et également pour leurs questions très pertinentes qui me seront utiles pour la suite et la conclusion de certains de mes travaux présentés ! Je tiens en particulier à remercier mes rapporteurs, F.-X. Désert et M. Kunz (une connaissance de longue date !) pour leur relecture attentive de mon manuscrit et leurs commentaires pertinents, malgré les contraintes de temps importantes que je leur ai imposés !

- La seconde catgorie de personnes qui je souhaite adresser mes remerciements, c'est l'ensemble du personnel de l'IAS avec qui j'ai pu interagir au cours de ces 6 (!) dernières années, et qui ont toujours été d'une gentillesse et d'une aide exceptionnelles ! Un grand merci donc Vronique, Patricia, Nicole, Delphine, Chlo, Hlne, et tous les autres que j'oublie certainement !

- Merci galement aux nombreux permanents du laboratoire avec qui j'ai pu avoir des échanges toujours agréables et enrichissants ! Hervé, Guilaine, Jonathan, Laurent,...et tous les autres, une fois de plus !

- Parmi le groupe cité ci-dessus, je suis particulièrement reconnaissants envers Nabila, Alexandre, et mes trés chers directeurs Mathieu et Marian, qui ont façonné le scientifique que je suis aujourd'hui, et que je suis heureux de compter parmi mes amis !

- S'il y a bien un groupe de personnes qui ont rendu le quotidien de ma thèse particulièrement agréable, il s'agit du groupe des thésards et post-docs de l'IAS, dont la camaraderie, la bonne humeur et la festivité font du laboratoire un endroit si agréable vivre (et travailler !) pour moi !

- Un chaleureux merci mes “vieux” amis, qui m’ont connu bien avant la thèse, pendant, et après, et qui ont toujours répondus présents pour des moments de détente complètement déconnectés du boulot, des étoiles et de l’Univers ! Merci les gars !

- Qui serais-je galement sans mes proches, commencer par mes parents et grands-parents qui, au deà du fait d’avoir permis mon existence (!), ont toujours su me supporter (dans les deux sens du terme !) tout au long de mes tudes et de ma vie.

- Je réserve une catégorie à part entière à la femme de mon coeur (qui se reconnaîtra) : pour elle, un simple poutou suffira, car les mots ne suffiraient pas à lui exprimer-mer ma gratitude pour son support, sa gentillesse et son amour pendant cette aventure éprouvante qu’est la thèse !

- Last, but not least : qui serais-je enfin sans mes très chers frères, à qui je voue un respect et une admiration sans égales ? Merci du fond du coeur de m’avoir accompagné littéralement depuis mes premiers pas, et d’être toujours là quand il le faut : vous êtes vraiment les meilleurs du monde, et je pense vraiment pas que je serai là où j’en suis sans vous ! Ready to die forever !

Contents

List of Figures

List of Tables

Abbreviations

CMB	**C**osmic **M**icrowave **B**ackground
DE	**D**ark **E**nergy
DM	**D**ark **M**atter
EoR	**E**poch **o**f **R**eionisation
FIR	**F**ar **I**nfra**R**ed
HEALPix	**H**ierarchical **E**qual **A**rea iso**L**atitude **Pix**elization
IGM	**I**nter**G**alactic **M**edium
ΛCDM	**L**ambda **C**old **D**ark **M**atter
LRG	**L**uminous **R**ed **G**alaxies
LSS	**L**arge **S**cale **S**tructures
LTB	**L**emaître-**T**olman-**B**ondi (metric)
QSO	**Q**uasi-**S**tellar **O**bjects
RMS	**R**oot **M**ean **S**quare
SDSS	**S**loan **D**igital **S**ky **S**urvey
SLS	**S**urface of **L**ast **S**cattering
S/N	**S**ignal to **N**oise ratio

Dedicated to the ones no longer with us
to gaze upon this beautiful Universe

Chapter 1

Introduction: the ingredients to a good cosmological probe

The state of our current understanding of our Universe may seem quite frustrating, to say the least. On the one hand, cosmologists have accumulated in the last decades a tremendous amount of data coming from a large number of ground- and space-based instruments, scrutinising the whole range of the electromagnetic spectrum. The results derived from theses experiments allowed to expand and refine our knowledge in many fields of astrophysics and helped strengthen what is currently regarded as the standard model of cosmology: the ΛCDM paradigm. However, despite this ever-growing wealth of data and the tighter and tighter agreement between theory and observations, the intrinsic nature of 95% of the energy content of the Universe still eludes us!

Even more ironic is the fact this "known unknown" consists of the two very elements that gave their names to the standard model of cosmology: first, the Cold Dark Matter (CDM), whose existence was first postulated to account for the evidence of "missing mass" from measurements of galaxy rotation curves. This hypothetical type of matter is referred to as "Dark" to indicate one of the few certainties that we have: its absence of emission/absorbtion of light at any significant level. The nature of the DM is still uncertain, with models ranging from axions, to supersymmetric particles, and even black holes. And secondly, the so-called cosmological constant symbolised by the Greek letter Λ, as it was fist introduced by Albert Einstein himself – but for a wholly different purpose. It is nowadays the preferred theory to explain the elusive "Dark Energy", responsible for the accelerated expansion of the Universe, and it accounts for 68.3% (Planck Collaboration, 2013e) of the Universe's energy budget.

Despite the mystery surrounding these elements (often called the "Dark components" or "Dark sector" of the Universes) and this rather hazy situation, progress in the field of

cosmology is far from being hampered by this apparent "obscurity", quite the contrary: cosmologists are all the more hard at work to unravel these fundamental components and the very nature of our Universe. However, rather than focusing only on a never-ending race to improve the precision of our instruments, a substantial effort in now also spent on the search for new and ingenious ways to exploit and combine existing tools and datasets, find new and clever observables, and turn them all into powerful probes of our Universe.

The majority of the work presented in this thesis revolves around one of such probes, which calls for a unique combination of cosmological observables and is aimed at the study of the Dark Energy: the so-called integrated Sachs-Wolfe effect. In this introductory chapter, I will briefly present the origin and physical processes involved in this particular effect, as well its related observables and possible probes.

1.1 The Cosmic Microwave Background

The existence of a background of photons roaming the Universe was speculated upon as far back as the middle of the 20th century (Alpher et al., 1948): this relic of decoupled radiation arises in the Big Bang scenario as a natural consequence of the expansion of the Universe and its hot and dense past. It was almost two decades later that the Cosmic Microwave Background (CMB) was finally discovered (Penzias and Wilson, 1965, an achievement awarded by nothing less than the Nobel Prize) and immediately interpreted (Dicke et al., 1965) as this formidable source of cosmological information that it would soon become.

We now know that the CMB is an almost isotropic radiation, matching a perfect blackbody spectrum at a temperature of $T = 2.7260 \pm 0.0013$K (Mather et al., 1994, Fixsen, 2009). Its emission dates back to the epoch of recombination of the hydrogen and helium atoms when the Universe was about 300,000 years old. Before this epoch, the Universe was opaque to light due to the presence of a high density of free electrons which prevented the photons from freely propagating by Compton scattering. Then, the fluctuations of the physical fields at recombination (such as temperature, density and velocity) left their imprints in the CMB in the form of anisotropies both in temperature and polarisation. A crucial consequence is that the CMB radiation and its fluctuations represent therefore an image, a snapshot of the Universe at that particular time. These fluctuations are often called primordial (or primary) anisotropies, since they originate from physical processes that occurred at recombination and even before – indirectly giving us a glimpse of the otherwise inaccessible early Universe (numerous reviews of these processes can be found in the literature, e.g. Hu, 1995, Hu et al., 1997).

Establishing the tremendous potential of these anisotropies, cosmologists undertook the task of measuring them with an ever-increasing precision. A myriad of instruments were developed in the last three decades, from ground-based missions (DACI, CBI, SPT, ACT,...) to balloons (BOOMERanG, MAXIMA, Archeops,...) and finally three successive generations of satellites: in 1989, the COBE satellite was the first to be launched to observe the CMB and succeeded in providing the first angular power spectrum of CMB anisotropies. Then, the WMAP (2003-2011) and *Planck* (2009-2012) satellites were launched and observed those small fluctuations with unprecedented sensitivities and accuracy (cf. Fig. 1.1). The latest data from *Planck* allows us to put the tightest constraints to date on many aspects of the standard model of cosmology. Among these we find: the measurement of a highly significant deviation from scale invariance of the primordial power spectrum, a revision of the density parameters of the Universe (with some significantly different from previous measurements), the confirmation of several large scale anomalies in the CMB temperature distribution, new limits on the number and mass of neutrinos, the measure of the gravitational lensing of CMB anisotropies at $25\,\sigma$, and no evidence for non-Gaussian statistics of the CMB anisotropies.

Although the CMB signal has been almost unchanged since recombination, some small alterations still arise due to several effects occurring on the paths of these photons. Such late-time modifications of the CMB are called secondary anisotropies and represent too, a mine of cosmological information, since their features depends heavily on the assumed cosmological model. Among others, different types of secondary anisotropy may be generated when the photons go through high density areas such as clusters of galaxies. In this case the high temperatures and velocities of high energy electrons in the interstellar gas can be transferred to the photons via inverse Compton scattering, producing characteristic, frequency dependent anisotropies on small scales called thermal and kinetic Sunayev-Zel'dovich effect respectively. Another example, as a fraction of the hydrogen in the Universe becomes ionised again at late times, the CMB photons will undergo Compton scattering again, smearing out a part of the primary anisotropies; reionisation may happen globally or locally around some sources, and will actually be the focus of a chapter of the present thesis (cf. Chap. 5). A description of these (and other) secondary anisotropies can be found in reviews such as Aghanim et al. (2008).

The central topic of my thesis concerns yet another type of secondary anisotropies, due to the influence of the gravitational potentials on the streaming CMB photons. More precisely, it concerns one of the effects that variations in these potentials may have along the path of the photons, and is commonly called the integrated Sachs-Wolfe effect (iSW). The detailed principle of this process will be discussed first in Sec. 1.4 and extensively throughout the whole manuscript; as we will see, the large scale structures of the Universe play a crucial rôle in this effect.

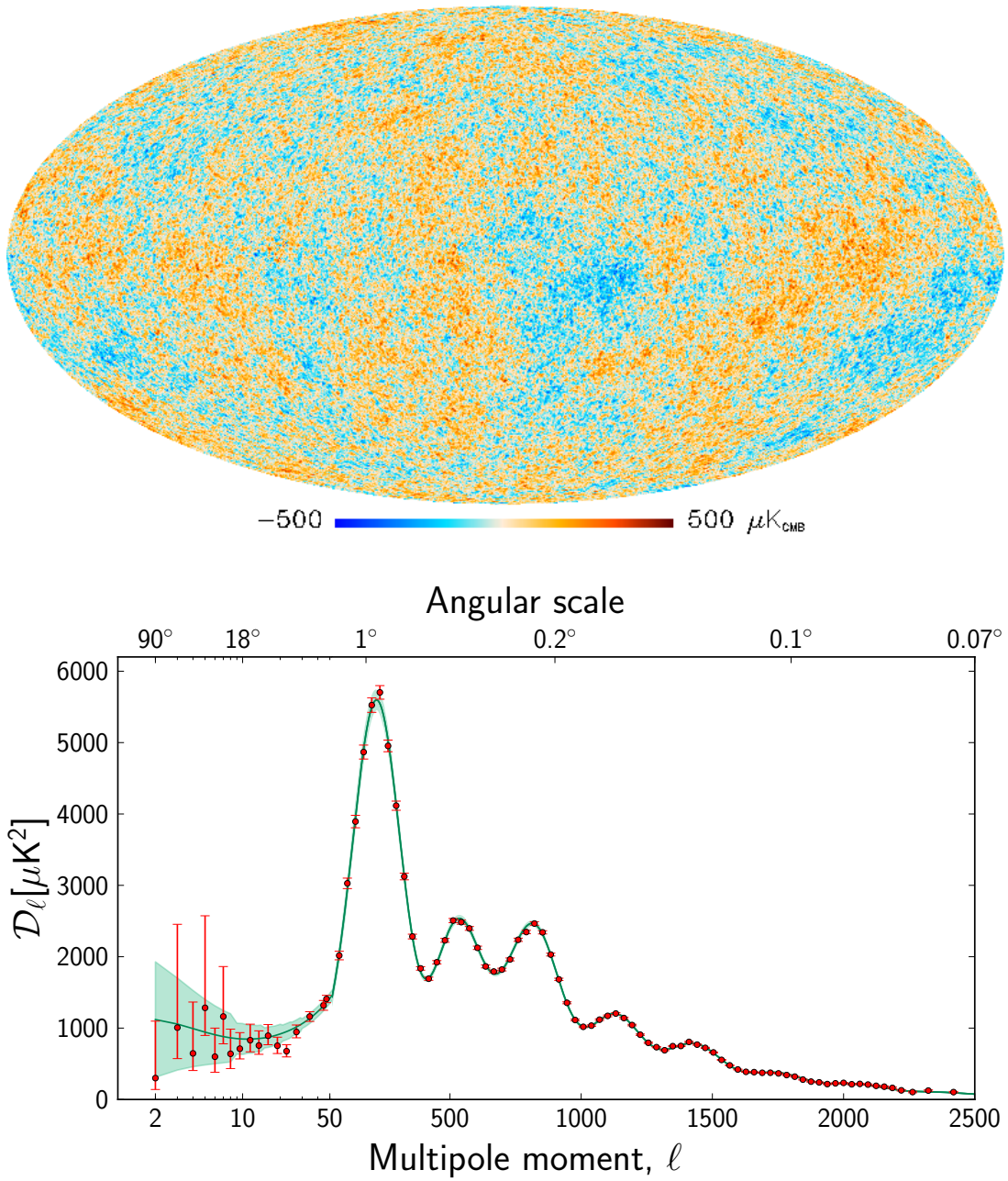

FIGURE 1.1: *Top:* The SMICA map of the CMB temperature anisotropies (with 3% of the sky replaced by a constrained Gaussian realization) as constructed by Planck Collaboration (2013a). *Bottom:* The angular power spectrum of the CMB temperature anisotropies from *Planck*, well fit by a simple six-parameter ΛCDM. The shaded area around the best-fit curve represents cosmic variance, including the sky cut used. The error bars on individual points also include cosmic variance. Both figures borrowed from Planck Collaboration (2013d).

1.2 Large scale structures and perturbation theory

In the context of secondary anisotropies, the CMB I just briefly described can be seen as some sort of cosmic "embroidery" of a myriad of physical processes, all along the way from its emission until it finally reaches us more than 13 billions years later.

As mentioned before, the presence of all kinds of structures (galaxies, clusters, voids,...) on the line of sight is partly responsible for these secondary anisotropies. Indeed, although the working assumption of a homogeneous and isotropic Universe (the so-called cosmological principle) is successful in describing the overall behaviour of the expansion and its relation to the energy content (through the use of the well-known FriedmannLematreRobertsonWalker, or FLRW metric) if we look at our Universe closer, we see that isotropy and homogeneity are broken on small scales. Therefore, one needs to form a more complex model in order to have the tools to describe more of the details we observe, such as the structure of the matter distribution and, consequently, the anisotropies in the CMB. This can be achieved by what is called a first-order perturbative theory built on top of the zero-order homogeneous theory of the FLRW model. This theory was first introduced by Lifshitz (1946); for more detailed reviews, the interested reader can refer to Bertschinger (1995) and Weinberg (2008). The general idea is to start from the classical, unperturbated FLRW metric $g_{\mu\nu}$:

$$g_{00} = -1 \tag{1.1}$$

$$g_{0i} = g_{i0} = 0 \tag{1.2}$$

$$g_{ij} = a^2 \delta_{ij} \tag{1.3}$$

with $a(t)$ being the well-known scale factor of the Universe. From there, we introduce the fact that the observed Universe is not perfectly homogeneous and isotropic: we assume, however, at the simplest order that these inhomogeneities lead only to small variations of the geometry. To do so, we define the perturbed geometry by:

$$g'_{\mu\nu} = g_{\mu\nu} + a^2 \epsilon_{\mu\nu} \tag{1.4}$$

with $g_{\mu\nu}$ being the same FLRW metric as before and with $|\epsilon_{\mu\nu}| \ll 1$. Similarly, a small perturbation is also added to the energy momentum tensor T^{μ}_{ν}. The Einstein equations of general relativity put constraints on these additional terms, but a gauge degree of freedom remains. One of the most commonly used gauge, called longitudinal (or conformal), allows to rewrite the perturbed metric with only two additional functions

(other than $a(t)$), Φ and Ψ, both of which depends on both space and time:

$$g'_{00}(\vec{x},t) = -1 - 2\Psi(\vec{x},t) \tag{1.5}$$

$$g'_{0i}(\vec{x},t) = g_{i0}(\vec{x},t) = 0 \tag{1.6}$$

$$g'_{ij}(\vec{x},t) = a^2\delta_{ij}(1 + 2\Phi(\vec{x},t)) \tag{1.7}$$

The perturbations Φ corresponds to the Newtonian potential, and Ψ the perturbation to the spatial curvature. Since the perturbations in the universe are small at the times and scales of interest, we treat Φ and Ψ as small quantities, dropping all terms quadratic in them. These functions (called "Bardeen potentials") will be of particular importance in the Sec. 1.4 in order to introduce and define the iSW effect (see also Durrer, 2004, for additional reference).

The perturbative theory, and the standard model in general, have to be capable of predicting the behaviour of many observables, and in particular the distribution of large scale structures in the Universe. In order to confront it to the data, a number of large galaxy surveys have been performed since the middle of the 70s, starting with astronomers of the Centre for Astrophysics (CfA) in Cambridge, who were the first to conduct the first 3D survey with a statistically significant number of galaxies with redshifts (Huchra et al., 1983) with a mean redshift of 0.025, and a coverage of 0.2 square degree. This particular survey revealed for the first time the aforementioned breakdown of homogeneity and isotropy in the local Universe, showing a "foamy" distribution of matter composed of large voids and filaments of galaxies. Since then, tremendous progresses have been accomplished on the coverage and depth of these surveys: one of the most recent (and still active), the Sloan Digital Sky Survey (SDSS Adelman-McCarthy et al., 2008) contains now more than 200 millions objects, and more than 1 million galaxies with their spectra resolved, both in the North and South hemispheres and with a mean redshift of 0.3.

The study of these surveys in themselves and their statistical properties is an invaluable source of cosmological information (for an overview, see e.g. Sodré, 2012, and the references therein). But for the purpose of my work, I was more interested in their link to other cosmological observables, in particular to the CMB itself, and how does the underlying cosmological model influence their relation and interaction.

1.3 The (current) ruler of our Universe: the Dark Energy

The first conclusive proof of the existence of the most prominent member of the "Dark sector" came in 1998, when Perlmutter, Schmidt et Riess (Riess et al., 1998, Perlmutter

et al., 1999) evidenced the acceleration of the expansion of our Universe through measurements of type Ia supernovae luminosity distances (cf. example in Fig. 1.2). Since the previous consensus at that time was in favour of a decelerated or linear expansion, these observations prompted cosmologists to hypothesise the existence of a new form of unknown energy responsible for this acceleration, which was henceforth referred to as the "Dark Energy".

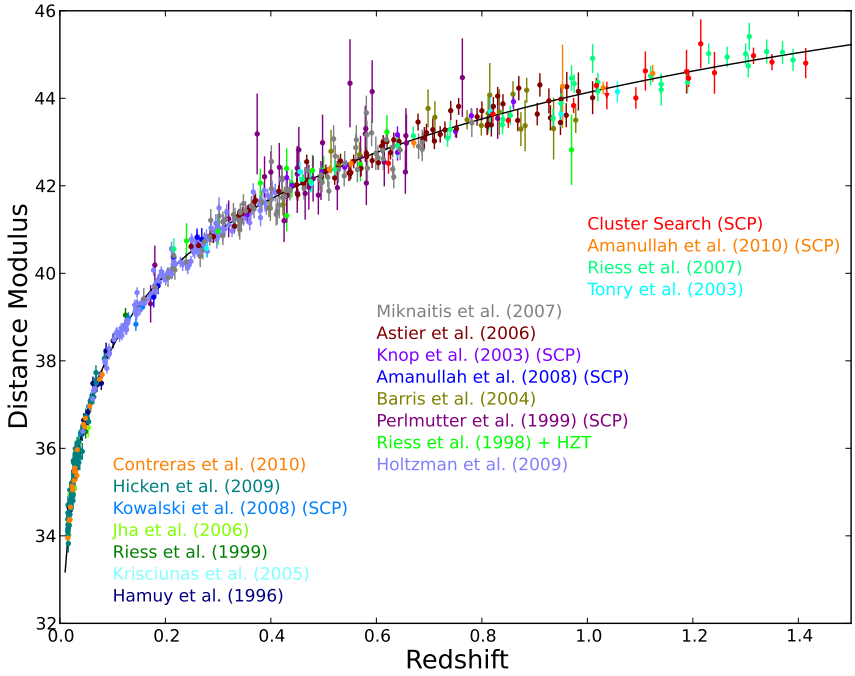

FIGURE 1.2: Status of the measurements of the Hubble diagram of type Ia supernovae as reported in Suzuki et al. (2012). The plot shows the distance modulus (related to the observed magnitude of the supernova) as a function of the redshift. The solid line represents the best-fit cosmology for a flat ΛCDM universe for supernovae alone ($\Omega_\Lambda = 1 - \Omega_m = 0.729 \pm 0.014$).

1.3.1 Models of Dark Energy

From then on, a multitude of theoretical models have been proposed to find a physical explanation for this peculiar component of our Universe, whose nature is still considered as one of the most important open questions in modern cosmology. The simplest model which can explain most of the current observations is obtained by adding a so-called cosmological constant Λ to the Einstein equations: this constant had been first incorrectly introduced by Einstein in order to obtain a static Universe, which proved later incompatible with the discovery of the Hubble expansion. In its modern form, we can think of an interpretation of the cosmological constant as the energy of vacuum, with an energy density constant in time and space and a negative equation of state, which started dominating the evolution of the Universe only at relatively recent times

($z \sim 0.4$) when the matter density was diluted enough. Despite its success in reproducing the majority of equations and its status in the "standard model" of cosmology, the cosmological constant is problematic, especially when we try to estimate the vacuum energy quantitatively: its estimated value from the standard model of particle physics is 10^{120} higher than its observed cosmological value! This discrepancy of 120 orders of magnitude is possibly the worst prediction of todays physics, and is known as the cosmological constant problem (Weinberg, 1989).

Since the identification of Dark Energy with the vacuum presents the aforementioned difficulties, a range of possible alternatives is currently being explored (although at the moment, every observation remains perfectly consistent with the simplest model of the cosmological constant). The confrontation with these problems has led theorists to speculate that vacuum energy may not be a constant, but a dynamical quantity, which happens to be small today because of the advanced age of the Universe. These "dynamical vacuum energy" models are usually called quintessence. The most natural and popular way to realise a dynamical model is to introduce one or more scalar fields which contributed to the total energy density of the Universe. This class of models was introduced by Wetterich (1988), Ratra and Peebles (1988); for a review, see e.g. Linder (2008).

All the theories mentioned so far are based on the introduction of some additional component to the stress-energy tensor with certain properties which will induce the desired accelerated behaviour of the expansion at late times. An interesting alternative is to modify the geometrical part of the Einstein equation instead. These are the so-called modified gravity theories, such as the $f(R)$ models – perhaps one of the simplest and most popular extensions of general relativity (for an introduction see e.g. Amendola and Tsujikawa, 2010). A more drastic approach is to assume that the 4D Universe we observe is in reality embedded in a higher dimensionality bulk, whose extra dimensions are unobservable thanks to some mechanism. The latter models are called braneworld, such as the Dvali-Gabadadze-Porrati (DGP) model (Dvali et al., 2000).

Finally, while a great effort is being made to find a solution to the Dark Energy problem with the introduction of interesting new physics, it is still possible for current observations to be explained by well known gravitational effects. This can happen if at large scales we drop the homogeneity assumption on which the FLRW metric is based: by doing so, non-linear gravitational effects arise which might be similar to the effects of a homogeneous accelerating Universe (Kolb et al., 2006). This approach is often called "backreaction" as the presence of the inhomogeneities acts on the background evolution and changes it. On the other hand, several attempts exist to build models which could satisfy all pieces of observational evidence generally based on the idea that if we

happen to be in an underdense region, gravity will appear locally weaker as matter is attracted to denser regions elsewhere. This concept can be realised by models such as the Lemaître-Tolman-Bondi (LTB, see Enqvist, 2008), although it was shown that these models have some trouble reproducing simultaneously all the current cosmological observables (see e.g Bull et al., 2012).

1.3.2 Probes of the Dark Energy

It is important to underline that the supernovae measurements mentioned earlier are not able to prove the existence of the Dark Energy by themselves: they have to be combined with other cosmological observations, most notably about the geometry of our Universe. More generally, many other probes of the Dark Energy were devised since its first discovery, allowing us to accumulate enough evidence to make it one of the pillar of the current standard model of cosmology.

Among those probes, we find first the constraint on flatness we see in the cosmic microwave background. As we know, the CMB radiation is not perfectly isotropic and has small angular fluctuations. The angular power spectrum of these presents detailed, observable features that depend on the cosmological parameters. In particular, the total energy density of the Universe is measured by the position of the first peak (cf. Fig. 1.1): this is because this scale corresponds to the angular dimension of the cosmological horizon at the epoch of last scattering. Accurate measurements available today conclude that the Universe is Euclidean, with a total energy density close to critical ($\Omega_{\text{total}} \simeq 1$). However, at first glance, this is in clear contrast with the sum of the "observed" components of the Universe (i.e. mainly matter in all its forms, which amounts to $\Omega_{\text{m}} \simeq 0.3$): the simplest solution is then to introduce heuristically a new component with an energy density ~ 0.7, i.e. the Dark Energy.

Additional evidence for Dark Energy comes from the observation of the large scale structure in the Universe. The baryon acoustic oscillations (BAO), besides leaving a large oscillatory pattern in the CMB angular power spectrum, also produce much smaller oscillations in the matter power spectrum, corresponding to a single bump in the matter angular correlation function at a scale of $\sim$ 150 Mpc. A measurement of this bump in a catalogue of sources (e.g. luminous red galaxies) is an accurate estimation of the angular distance to that characteristic scale, whose value again indicates the presence of Dark Energy (Eisenstein et al., 2005, Percival et al., 2007a). More generally, statistics associated to the distribution of galaxies (number counts, mass function,...) also allows to put constraints on the features of the Dark Energy. Weak gravitational lensing (e.g. Schneider, 2005) is a powerful technique to map the distribution of Dark Matter in

the Universe by observing the distortion of background galaxies by the foreground Dark Matter distribution. This distortion has been detected since 2000, its observation putting constraints on the matter energy density – again pointing indirectly at a Dark Energy dominated Universe. The deployment of a new generation of almost full-sky lensing surveys such as Pan-STARRS, LSST or Euclid has the potential to make weak lensing one of the most powerful methods to constrain Dark Energy in the near future. Further evidence of Dark Energy comes from another gravitational effect on the CMB of the distribution of matter on the CMB, whose evolution is tightly influence by Dark Energy itself: the measurement of the integrated Sachs-Wolfe effect, which we will be the central point of my thesis and described in the following section.

1.4 Shedding light on the Dark Energy: the integrated Sachs-Wolfe effect

As mentioned earlier, a particular type of temperature anisotropies is found in the CMB due to the effect of the gravitational potentials on the streaming CMB photons. The earliest effect to occur is called the "ordinary" Sachs-Wolfe effect: it is caused by the gravitational redshift occurring at the surface of last scattering. The effect is not constant across the sky due to differences in the matter/energy density at the time of last scattering (Sachs and Wolfe, 1967). In the framework of the linear, pertubative theory the effective temperature change of the photons can be directly expressed as a function of the Bardeen potentials Φ and Ψ at recombination.

However, the effect I am interested in alters the CMB power spectrum at a much more recent epoch. When streaming through space from the last scattering surface, the CMB photons undergo the effect of the local gravitational field at late times, which can also be described using the Bardeen potentials. This effect can be integrated along the line of sight and is expressed by the so-called Sachs-Wolfe equation:

$$\delta_T^{\mathrm{ISW}} = \int_{\eta_{\mathrm{SLS}}}^{\eta_0} e^{-\tau(\eta)} (\dot{\Phi} - \dot{\Psi})[(\eta_0 - \eta)\hat{\mathbf{n}}, \eta] \, \mathrm{d}\eta \tag{1.8}$$

where Φ and Ψ are the Bardeen gravitational potentials in the conformal gauge described earlier, η is the conformal time (with η_{SLS} at the surface of last scattering and η_0 today), dots represent conformal-time derivatives, τ is the optical depth, and $e^{-\tau(\eta)}$ is the CMB photon visibility function (accounting for the damping by Thomson scattering of CMB photons off free electrons). Note that in the ΛCDM paradigm, we consider that the Universe is composed of perfect fluids (whatever they are) so that there is no anisotropic stress (non-zero off-diagonal terms of the energy momentum tensor): after

some calculations in perturbation theory (see e.g. Durrer, 2004), it can be shown that it leads to the following relation between Bardeen potentials:

$$\Phi = -\Psi \tag{1.9}$$

leading to an alternative formulation of the iSW effect very often found in the literature:

$$\delta_T^{\mathrm{ISW}} = 2 \int_{\eta_{\mathrm{SLS}}}^{\eta_0} e^{-\tau(\eta)} \dot{\Phi}[(\eta_0 - \eta)\hat{\mathbf{n}}, \eta] \, \mathrm{d}\eta \tag{1.10}$$

We understand here that the iSW effect can happen only if the gravitational potential vary with time. The evolution of the potential is tightly linked to the evolution of the density through the Poisson equation. In the framework of perturbation theory, we can show that the evolution of density perturbations is controlled by a function called the "growth function" $D(a)$, and that in turn the potential is proportional to $D(a)/a$. In a matter-dominated Universe, the linear evolution of density inhomogeneities is proportional to $a(t)$ (i.e. $D(a) \propto a$, see e.g. Chapter 7 of Dodelson, 2003, for reference), so that the linear evolution of the potentials is null: the iSW effect cannot occur if the dominant fluid is composed of matter. However, in our best-fit cosmological model, the presence of Dark Energy causes a decay of these potentials due to the accelerated expansion of our Universe (Kofman and Starobinskii, 1985): this is usually referred to as the "late" integrated Sachs-Wolfe effect (iSW). Since the transition from a matter- to a DE-dominated occurred recently (in redshift) according to the standard model, new anisotropies were formed in the CMB at recent times, when the horizon size was comparable with its current value. Therefore the affected scales are generally the largest, at multipoles $\ell < 100$ (cf. Fig. 1.1). The physical picture is very straightforward; as a CMB photon falls into a gravitational potential well, it gains energy; as the photon climbs out of a potential well, it loses energy. These effects exactly cancel if the potential is time independent, but can result in a net kick if the potential evolves as the photon passes through it. The exact opposite phenomenon, i.e. a loss of energy, happens if the photon crosses a cosmic void. It should be noted that the iSW effect is not exclusively a signature of the standard model and its associated Λ: it is interesting to remark that in most modified gravity scenarii the gravitational potentials have a different time evolution even during the matter era, thus making this effect a potential discriminant between different theories (as shown by Lue et al., 2004). This also applies to other Dark Energy models, which all have their unique "version" of the iSW effect.

In contrast to this "late" iSW effect, it is interesting to note that some "early" iSW effect may have occurred some time after recombination due to a non-negligible radiation contribution in the energy balance, thus the gravitational potentials are decaying for

some time after the creation of the CMB. As the horizon size was much smaller then than today, the small additional anisotropies will be produced on higher multipoles, at scales comparable with the first acoustic peak ($\ell \simeq 200$). However, the relative signal is embedded in the primary CMB anisotropies, which are much larger and make a direct measurement challenging. Of interesting note is also that at smaller angular scales, the photons from the CMB may undergo some energy shift when they cross a high density region, like a galaxy cluster. In this case linear theory breaks down, and again the gravitational potentials are not constant even in a matter-dominated era. This effect represents the non-linear part of the iSW, and is known as Rees-Sciama (Rees and Sciama, 1968). Since it is sourced by non-linear regions, its contribution to the CMB power spectrum typically peaks around $\ell \simeq 100$, and is always much smaller than the primary CMB. However, possible approach to the practical measurement of this phenomenon has been proposed in the literature (cf. Schäfer, 2008).

Probing the iSW effect As a consequence of what I mentioned above, a direct measurement of the iSW contribution to the CMB power spectrum is made virtually impossible by the embedding of the small iSW signal in the much larger primary CMB anisotropies at the relevant multipoles (10 times at the very least for the lowest, and increasingly more for higher ℓs). Furthermore, the total iSW signal is due to all the density fluctuations, both positive and negative, along the line of sight: on small scales, the individual temperature differences are small and they tend to cancel out. The most significant iSW effect results from the coherent large scale potentials, but unfortunately these scales are precisely where the CMB signal is mostly dominated by cosmic variance.

However, this situation changed when Crittenden and Turok (1996) presented a new technique, which made it possible to extract this effect by cross-correlating the observed CMB map with some tracer of the matter density field. The method is based on the fact that the primary CMB anisotropies have been generated at the surface of last scattering, and therefore are completely uncorrelated from the large scale structure present in recent times; on the other hand, the iSW temperature correlates with the density of galaxies, which should trace the potential wells and hills which bring about the anisotropies. We can then extract the late iSW signal by measuring the cross-correlation of some tracer of the large scale structure – typically a galaxy survey – with the CMB.

Unfortunately the ability to detect the cross-correlation is limited because the signal falls off on small scales. Not only is cosmic variance an important factor, but there is also the fortuitous correlations that can happen between the galaxy surveys and the CMB anisotropies produced at last scattering. Many groups have tried to detect the late iSW effect in the past decade using this cross-correlation technique, using successively the

COBE, WMAP, and *Planck* data for the CMB, and a large variety of galaxy catalogues observed in different regions of the electromagnetic spectrum. However, as described in details in Sec. 2.1.4 of this manuscript, some inconsistencies between studies appear, and a clear and definitive signal has yet to be found.

During my Ph.D. thesis, I focused on a new and innovative tracer of the matter density to be used in such cross-correlation methods, namely the Cosmic Infrared Background. As I show in Chap. 2 this particular background presents all the required characteristics of a good tracer for such studies, while having none of the shortcomings of the current surveys. Another probe of the iSW effect was recently introduced by Granett et al. (2008), and is based on detecting the correlation in a localised way: these authors considered the luminous red galaxies from the SDSS, and studied regions in the sky surrounding superclusters and supervoids of scale $\sim$ 140 Mpc, and then stacked the CMB signal in the surrounding area. The result shows that the CMB appears in average hotter around the clusters and colder around the voids, at a large significance, but with peculiar features that I point out in Chap. 3. This is an interesting result because it represents the first localisation of the iSW signal, but it has the drawback of being dependent on the particular choice of superclusters and on the particular filter scale adopted for the signal detection – caveats that I alleviated in my work, by performing a more thorough analysis and considering more recent (and much more consequent) alternative catalogues of structures, all described in Chap. 3. These new results of mine prompted even more questions regarding the nature of the iSW effect and its signature in such a context, which lead me to devise a new approach to predicting the expected iSW effect from structures in the Universe, detailed in Chap. 4. Interestingly enough, it makes use of the LTB metric (mentioned earlier in the context of DE models) but in a totally different context.

1.5 A glimpse at the Dark components through the reionisation

For the sake of completeness, I would like to mention also a work that I carried out in parallel to all the primary work related to the iSW effect, and reported in Chap. 5. Indeed, I also took a particular interest during my thesis to the rôle that played another actor of the Dark Sector in the framework of cosmic reionisation (briefly mentioned in this introduction), namely: the Dark Matter, whose possible influence has the potential of being traceable, and used to constrain DM models.

Chapter 2

Unravelling the iSW effect through the matter distribution

2.1 CMB Cross-correlation with tracers of matter

The end of the last chapter painted the iSW effect of CMB photons as a clever probe that has the potential to independently prove the existence of Dark Energy in our Universe. However, the faintness of this signal makes it almost impossible to detect, at least using only the CMB as such. The story does not end here though, thanks to the resourcefulness of cosmologists at finding ways to detect and exploit the iSW effect more efficiently. Among the methods devised, one of them stands as the leading technique in the literature: the cross-correlation of the CMB with the distribution of matter in the Universe.

2.1.1 The principle

Before going into the details of this approach, let us recall the main ideas it is based on. As discussed in Chapter 1, the iSW effect felt by the CMB photons in a ΛCDM universe is a result of the stretching of the large scale potentials in the Universe, caused by the acceleration of the expansion which is itself due to the presence of Dark Energy. Of course, one has to remember that these gravitational potentials originate from the presence of matter in the form of large Dark Matter halos in which sit clusters of galaxies (in the ΛCDM cosmology). Following this, it is reasonable to believe that there exists a certain degree of correlation between the distribution of matter and the resulting pattern of the iSW effect that it generates in the CMB across the sky. The link between these two elements is of course not trivial since, as its name suggests, the iSW effect is an

integrated effect: CMB photons that come from a particular direction in sky have been affected by the matter distribution along the whole line of sight. This is then further complicated by two competing phenomena: on the one hand the iSW effect is expected in the ΛCDM paradigm to be redshift-dependent with the most recent structures in the Universe yielding a more pronounced effect as they are locally more DE-dominated. However, these very structures are also closer and closer to us so that their number becomes limited by the available volume around us. At some point, the stronger iSW effect of the closest large structures becomes balanced by their increasing scarcity and therefore gets progressively harder to detect. We therefore intuit already that there will be an optimal redshift for the detection of the iSW effect, at some point between $z = 0$ and the start of the era in which Dark Energy became cosmologically important.

Now that we have a grasp of the motivations behind the use of cross-correlation and its associated features, we will have in the next subsection a closer look at the theoretical tools used to describe this correlation.

2.1.2 Theoretical framework

As seen in Sec. 1.2 and Sec. 1.4, the anisotropies that are generated by the iSW effect are directly correlated to the distribution of matter through the evolution of the gravitational potential $\dot{\Phi}$. Exploiting this correlation and detecting the iSW effect can be done via several approaches; I will focus here on the most widely used method which is based in spherical harmonic space.

All cross-correlations methods suppose that we have first a map of the temperature of the CMB at hand $T(\hat{\mathbf{n}})$, or rather, a map of the *relative* fluctuations of this background:

$$\delta_T(\hat{\mathbf{n}}) = \frac{T(\hat{\mathbf{n}}) - \bar{T}}{\bar{T}} \tag{2.1}$$

with $\bar{T}$ the mean temperature of the CMB (with the latest measurements indicating $\bar{T} = 2.7260 \pm 0.0013$, cf. Fixsen, 2009). On the other hand, we need a survey that traces the distribution of galaxies, from which we derive a map of the projected galaxy overdensity field:

$$\delta_g(\hat{\mathbf{n}}) = \frac{N(\hat{\mathbf{n}}) - \bar{N}}{\bar{N}} \tag{2.2}$$

where $N(\hat{\mathbf{n}})$ is the number of galaxies in the pixel corresponding to the direction $\hat{\mathbf{n}}$ and $\bar{N}$ is the mean number of galaxies per pixel. Both maps are therefore in dimensionless units – which is always welcomed to simplify calculations. Then, for the approach that I consider here, we use the fact that any field can be decomposed into a series of functions which form an orthonormal set, as do the spherical harmonic functions $Y_{\ell m}(\theta, \phi)$. It

follows both the CMB temperature map (δ_T) and the overdensity map (δ_g) can be decomposed into:

$$\delta_X(\theta,\phi) = \sum_{\ell,m} a^X_{\ell m} Y_{\ell m}(\theta,\phi), \tag{2.3}$$

where $a^X_{\ell m}$ ($X = g, T$) are the spherical harmonic coefficients of the field resulting from its decomposition. The main quantity of interest for us is the 2-point galaxy-temperature cross-correlation as a function of the multipole ℓ, whose estimator is:

$$\hat{C}_{Tg}(\ell) = \frac{1}{(2\ell+1)} \sum_m \mathcal{R}e\left[a^g_{\ell m}(a^T_{\ell m})^*\right] = \frac{1}{(2\ell+1)} \sum_m \mathcal{R}e\left[a^T_{\ell m}(a^g_{\ell m})^*\right], \tag{2.4}$$

It traces the degree of correlation between the two maps in harmonic space. We can intuit that in the absence of Dark Energy and hence of the iSW effect, the correlation between these two will be reduced to only fortuitous coincidences. But now that we have defined its computation, let us take a more precise look at the expected cross-correlation signal $C_{Tg}(\ell)$.

Firstly, the fluctuations of the CMB temperature $\delta_T(\hat{\mathbf{n}})$ are known to be composed of several contributions, often categorised into primordial and secondary anisotropies. However, for the large scales that we consider the only ones that are correlated to the distribution of matter in the Universe are the secondary anisotropies generated through the late iSW effect. In the remainder of this section, I will associate the notation $\delta_T(\hat{\mathbf{n}})$ to these iSW fluctuations only. One way of expressing these temperature fluctuations on a particular line of sight is written as the following redshift-integral from the surface of last scattering (SLS) to us:

$$\delta_T(\hat{\mathbf{n}}) = \int_{z_{\rm SLS}}^{0} e^{-\tau(z)}(\dot{\Phi} - \dot{\Psi})[\hat{\mathbf{n}}, z]\, \mathrm{d}z. \tag{2.5}$$

where the dot denotes here differentiation with respect to z (details about the equation and its terms can be found in Sec. 1.4). Since the matter density is related to the gravitational potential Φ and Ψ by the Poisson equation, these iSW temperature fluctuations will be related to the observed galaxy density contrast, given by:

$$\delta_g(\hat{\mathbf{n}}) = \int_{z_{\rm SLS}}^{0} b_g(z) \frac{\mathrm{d}N}{\mathrm{d}z}(z) \delta_m(\hat{\mathbf{n}}, z)\, \mathrm{d}z. \tag{2.6}$$

In this expression, $\mathrm{d}N/\mathrm{d}z$ is called the selection function of the survey (from which the density map is derived) and represents simply the redshift distribution of galaxies in the survey. More accurately, this function gives the number of galaxies contained in a shell of width $\mathrm{d}z$ at redshift z; it is often normalised and then describes the fraction of objects per redshift (an example of such selection function is shown in Fig. 2.1). The

term δ_m corresponds to the matter density perturbations, which are related to the galaxy overdensities by a factor b_g: indeed, although we correlate in practice the CMB map with a galaxy map, we aim at probing in reality the correlation with the underlying distribution of Dark Matter. This "galaxy bias" can theoretically evolve in time and be a function of scale. However, it is generally assumed to be time and scale independent for simplicity. For our purposes, a time dependent bias would be equivalent to changing the selection function of the survey. A possible scale dependence of the bias is more problematic, but on the very large scales (> 10 Mpc) we are considering, the scale dependence is expected to be weak (see e.g. Blanton et al., 1999, Percival et al., 2007b).

We are here interested in the correlation between δ_T and δ_g: their angular cross-correlation function in real space is defined as:

$$C^{Tg}(\vartheta) \equiv \langle \delta_T(\hat{\mathbf{n}}_1)\delta_g(\hat{\mathbf{n}}_2)\rangle \tag{2.7}$$

with the average carried over all the pairs at the same angular distance $\vartheta = |\hat{\mathbf{n}}_1 - \hat{\mathbf{n}}_2|$. As mentioned before, it is often preferred to work in the harmonic space and study the cross-correlation spectrum $C_{Tg}(\ell)$ instead of the function $C^{Tg}(\vartheta)$. Those two quantities are related through Legendre polynomials P_ℓ:

$$C^{Tg}(\vartheta) = \sum_{l=2}^{\infty} \frac{2\ell+1}{4\pi} C_\ell^{Tg} P_\ell[\cos(\vartheta)]. \tag{2.8}$$

After some calculations (for detailed steps, see e.g. Garriga et al., 2004), it follows that the cross-correlation power spectrum is given by:

$$C_\ell^{Tg} = 4\pi \int \frac{dk}{k} \Delta^2(k) I_\ell^{\mathrm{iSW}}(k) I_\ell^g(k), \tag{2.9}$$

where $\Delta(k)$ is the scale invariant matter power spectrum $\Delta^2(k) \equiv 4\pi k^3 P(k)/(2\pi)^3$ and the two integrands are respectively:

$$I_\ell^{\mathrm{iSW}}(k) = -2 \int e^{-\tau(z)} (\dot{\Phi}_k - \dot{\Psi}_k) j_\ell[k\chi(z)] dz \tag{2.10}$$

$$I_\ell^g(k) = \int b_g(z) \frac{dN}{dz}(z) \delta_m(k,z) j_\ell[k\chi(z)] dz, \tag{2.11}$$

where Φ_k, Ψ_k and $\delta_m(k,z)$ are the Fourier components of the gravitational potentials and matter perturbations for the wavenumber k, $j_\ell(x)$ are the spherical Bessel functions and χ is the comoving distance. The two integrands I_ℓ^{iSW} and I_ℓ^g can then be calculated for a given cosmological model using numerical codes that compute all the relevant quantities needed (the details of the corresponding equations can be found in Garriga et al., 2004).

Of interesting note is that in the linear theory of perturbations (an approximation which

should be more than valid here considering the large scales involved) the growth of the gravitational potentials is directly proportional to the ratio $D(a)/a$ (cf. Sec. 1.4) where a is the scale factor and $D(a)$ is called the (linear) growth function. Under the same framework it can be shown that in a flat, matter-dominated universe, this function is proportional to a so that the gravitational potentials are constant in time. As a result, the terms $\dot{\Phi}_k$ and $\dot{\Psi}_k$ in Eq. 2.10 would be equal to 0 and so would the integral – and the cross-correlation spectrum C_ℓ^{Tg} itself. Therefore, we confirm here that in the absence of Dark Energy (or more accurately, if the dominant component of the Universe were pressureless matter) there would be no iSW effect and no correlation between the CMB temperature and the distribution of matter.

2.1.3 Application to detectability & test case

We reviewed in the previous section the analytic expression of the correlation between the CMB anisotropies and the distribution of matter through their cross-correlation power spectrum. The question now arises about the use of these theoretical predictions for the study of the Dark Energy.

The first application of these theoretical tools is to give the possibility to predict the detectability of the aforementioned correlation. Assuming a given cosmological model and that both the CMB temperature and the galaxy maps behave as Gaussian random fields, the covariance on the iSW cross-correlation signal (in the absence of noise) can be calculated by:

$$\sigma^2[C_\ell^{Tg}] = \frac{(C_\ell^{Tg})^2 + C_\ell^{gg} C_\ell^{TT}}{2\ell + 1}, \tag{2.12}$$

where C_ℓ^{TT} is the full CMB temperature-temperature power spectrum (and not only the secondary anisotropies generated by the iSW effect) and C_ℓ^{gg} is the galaxy auto-correlation function that can be calculated theoretically:

$$C_\ell^{gg} = 4\pi \int \frac{dk}{k} \Delta^2(k) I_\ell^g(k) I_\ell^g(k) \tag{2.13}$$

(see Eq. (2.9) for a description of the terms). We can identify two sources of variance in Eq. 2.12: the cosmic variance of the correlation itself (the $(C_\ell^{Tg})^2$ term), and the fortuitous coincidences that arise between the CMB temperature and the galaxy distribution (the $C_\ell^{gg} C_\ell^{TT}$ term).

It follows then that the theoretical signal-to-nose ratio (S/N) of this iSW detection for a given multipole range $[\ell_{\rm min}, \ell_{\rm max}]$ is:

$$\left(\frac{S}{N}\right)^2 = \sum_{\ell=\ell_{\rm min}}^{\ell_{\rm max}} \frac{(C_\ell^{Tg})^2}{\sigma^2[C_\ell^{Tg}]} = \sum_{\ell=\ell_{\rm min}}^{\ell_{\rm max}} (2\ell+1) \frac{(C_\ell^{Tg})^2}{(C_\ell^{Tg})^2 + C_\ell^{gg} C_\ell^{TT}}. \tag{2.14}$$

The cumulative character of the S/N is due to the fact that, in the ideal case we consider here (Gaussian fields, full-sky maps), the power spectrum estimates at different multipoles are independent from one another (no off-diagonal terms in the covariance matrix).[1] For illustration purposes, I will consider two fictitious full-sky surveys, one with a selection function (see Eq. 2.6) similar to the eighth data relase (DR8) of the Sloan Digital Sky Survey (SDSS, Aihara et al., 2011) and one with a higher median redshift (both are shown in Fig. 2.1). Assuming the best-fit ΛCDM cosmology from *Planck* (Planck Collaboration, 2013e), I calculate the theoretical auto-correlation (C_ℓ^{gg}) and cross-correlation (C_ℓ^{Tg}) spectra for such surveys. To do so, I use a modified version of the cosmological code `CMBFAST` (Seljak and Zaldarriaga, 1996) named `CROSS_CMBFAST` (Corasaniti et al., 2005) which computes both these spectra, as well as the usual `CMBFAST` outputs, i.e. the CMB temperature and polarisation spectra. I illustrate in Fig. 2.2 the resulting cross-correlation spectra and the ideal S/N estimation defined in Eq. 2.14: as we can see, the signal peaks in the $\ell = 10-20$ multipole range and quickly falls at smaller scales. Similarly, the largest contributions to the signal-to-noise ratio come mainly from the lowest multipoles, with the total S/N quickly reaching a plateau: this shows that most of the significant signal is below $\ell = 100$, at that is it pointless to consider higher multipoles in cross-correlation studies. It is important to notice here the crucial influence of the redshift range (through the selection function) covered by the surveys considered, as already intuited at the end of Sec. 2.1.1. Here, we can witness that the S/N is substantially higher for the survey with the higher median redshift compared to the SDSS-like one (4.5 versus 3.3 for the cumulative S/N).

The above test cases give us an idea about the expected characteristics of the cross-correlation in terms of the signal itself and its detectability; however, the predictive tools used here can be extended to any given survey (through the selection function) and to a large variety of cosmologies (included in the `CROSS_CMBFAST` code). We can now wonder: how can we use these tools to constrain cosmological models and learn more about the Dark Energy? There are several tests that we can think of and that are used in the literature; I will briefly present the most widely used without diving too deep into calculations (a review of these methods can be found in Dupé et al., 2011).

[1] This is often not exactly true when working when real datasets (due to partial sky coverage, non-Gaussian contamination, etc.) and has to be accounted for properly, e.g. using Monte-Carlo simulations (see later in this Chapter).

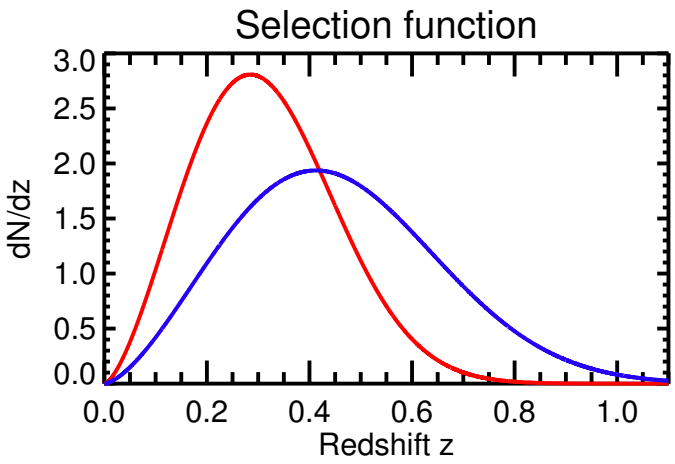

FIGURE 2.1: Redshift distributions of the two fictitious surveys considered (see text for details). These selection functions follow a widely-used analytical expression that describes well such quantities: $dN/dz(z) = Az^m \exp -(z/z_0)^\beta$, where A is chosen so that the function is normalized to unity. The parameters m and β control the slope of the rise and fall respectively, while z_0 fixes the median redshift of the distribution $z_{\rm med}$ ($= z_0\sqrt{2}$). Here I chose $z_0 = 0.48287$, $m = 1.51964$ and $\beta = 2.34207$ for the SDSS-like distribution (red curve), and increased z_0 to 0.7 for the second one (blue curve).

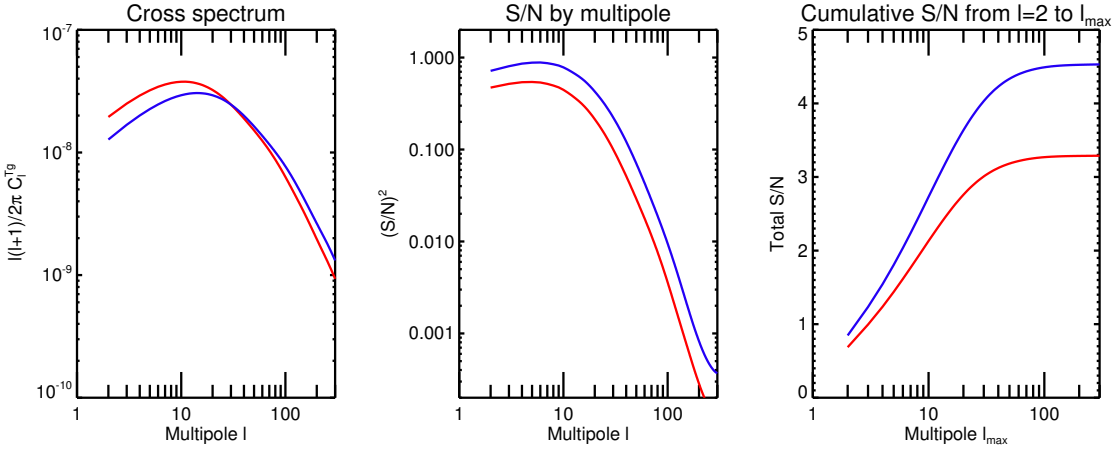

FIGURE 2.2: Theoretical cross-correlation results for the SDSS-like survey (red curves) and a second one with higher median redshift (blue curves). *Left panel:* Theoretical angular cross power spectra of the CMB-galaxy correlation. *Middle panel:* Contribution to the total squared S/N of the signal as a function of the multipole ℓ. *Right panel:* Total cumulative S/N of the cross-correlation signal for the multipole range $\ell = [2, \ell_{max}]$ as a function of ℓ_{max}.

The first one is actually independent of the cosmology and does not assume any kind of DE model (besides its existence itself): it consists in measuring the cross-correlation on the data and checking how much it departs from a scenario with no correlations at all, i.e. without Dark Energy. This is the so-called "null hypothesis", and basically consists in performing a χ^2 test on the measured correlation with respect to a "null model", i.e. a model with zero correlation. If the test shows a significant deviation from the null model, then it constitutes a proof of the existence of the Dark Energy (assuming a flat Universe) but does not give any additional information beyond that.

In a second time, we can go further and try to check how the data fares against the prediction from a given cosmological model: using a similar χ^2 test, we can compare the measured correlation with the theoretical (non-zero) one predicted beforehand using the framework that I described above. Although this test cannot give a definitive answer on whether a given model is "the right one", inversely it can invalidate the model if the computed χ^2 is too high. A third and last approach, called "amplitude fitting" (or "template matching"), combines both of the previous ideas: considering a cosmological model (often the fiducial one that we try to (in)validate), we construct a "template" by multiplying its associated theoretical correlation by an "amplitude factor". The method consists then in computing the amplitude (and associated error) that fits the best the measured correlation: a value close to 1 then indicates an agreement with the underlying model. If this amplitude simultaneously shows a sufficiently large S/N (i.e. a small associated error), it intrinsically disproves the null hypothesis and strongly hints at the presence of Dark Energy.

We can already intuit here that the presence of sources of noise and partial sky coverage will complicate the extraction of the iSW signal. The next paragraph will be an overview of the current state of the detection of the iSW effect through cross-correlation techniques.

2.1.4 State-of-the-art of the iSW detection

In the literature, many attempts have been made to detect an iSW signal through the cross-correlation of the CMB with galaxy surveys, with varying degrees of success. I do not intend to summarize here all of the results so far, since such type of compilation has already been made in the past: for reference, in Table 1 of Dupé et al. (2011) the authors present a "meta-analysis" of iSW detections (up to the publication of their work) and their reported statistical significance. Over the last decade a large variety of surveys has been explored, exploiting the whole spectrum of light: X-ray (Boldt, 1987, XRB survey); optical (Adelman-McCarthy et al., 2008, Agüeros et al., 2006, SDSS), near infrared (Jarrett et al., 2000, 2MASS); radio (Condon et al., 1998, NVSS). The cross-correlation studies also followed the evolution of CMB observations, from the first detected anisotropies of the Cosmic Microwave Background Explorer (Bennett et al., 1990, COBE) to the succession of releases by the Wilkinson Microwave Anisotropy Probe (Spergel et al., 2003, WMAP) and the latest publication of the *Planck* satellite (Planck Collaboration, 2013d).

What strikes the most when reviewing the current results of the literature are their wide diversity, as the reported significances range from negligible (Sawangwit et al., 2010) to

$4.4\,\sigma$ (Giannantonio et al., 2012). Although these differences can be partly attributed to the specific features[2] of each survey (and CMB maps) and to the methods[3] used by the authors of each work, some puzzling discrepancies are still present. Indeed, a couple of analyses based of very similar (if not identical) datasets have yielded contradictory conclusions on the level of detection of an iSW signal (see Dupé et al., 2011, again for reference), while other works reported a signal at odds with ΛCDM expectations ($1\,\sigma$ excess in Giannantonio et al. 2012, $2\,\sigma$ in Ho et al. 2008).

This intriguing situation may find its source in the characteristics of the current (and past) generation of surveys, or rather, their shortcomings. Indeed, for each of them, a trade-off has often been made between the deepness of the survey and its coverage, resulting in the end in the observation of a small total volume of the Universe. Unfortunately, this is a crucial point for the iSW studies and has a dramatic impact on the potential S/N of the detection: considering a smaller volume results simultaneously in a decrease of the theoretical signal and an increase of its variance. Coupled to this is the intrinsic weakness of the signal, and the presence of galactic foregrounds in both the CMB and the LSS maps that also mask crucial large scale data and can introduce spurious correlations. Therefore, any method claiming to detect the iSW effect may not be as thorough as required in accounting for missing data. Ideally, any reported detection level should be independent of any assumption or particular cosmology. Very recent works aimed at a better control of systematics (see e.g. Hernández-Monteagudo et al., 2013a, for a thorough review of potential contaminants in SDSS), while others made use of the latest releases of both CMB and LSS data (Planck Collaboration, 2013c). In both cases, the correlations were found to have much less discrepancies with ΛCDM and a good agreement with their expected amplitude (cf. "amplitude fitting" tests in Sec. 2.1.3), but with relatively low significances ($1.5 - 3\,\sigma$ range).

It is quite established that current surveys are far from ideal: to further the point, Afshordi (2004) showed that obtaining a near optimal iSW detection (at a $\sim 5\,\sigma$ level) would require an all-sky survey with about 10 million galaxies almost uniformly distributed within $0 < z < 1$, with systematics below $\sim 0.1\%$ and systematic errors in redshift estimates < 0.05 – again, far from the characteristics of currently available datasets. However, the next generation of probes will address many of the current shortcomings: surveys such as Euclid, Pan-STARRS or LSST will get much closer to the ideal requirements for the detection of the iSW effect (see Douspis et al., 2008, Dupé et al., 2011, for forecasts) and will also – needless to say – improve our knowledge of a vast range

[2] In terms of the redshift range of the surveyed objects and the fraction of the sky covered by the survey

[3] Not all of the cross-correlation works base their analysis in harmonic space, as some prefer working in real space or using wavelets; although the tools and estimators are different, the different tests (χ^2, null hypothesis,...) remain however the same and similar to those described in Sec. 2.1.3.

of cosmological topics. For the time being, considering the landscape depicted above, there are a few possible orientations that can be taken regarding iSW studies: the first is to make the most of the current available data and has already been explored quite extensively, notably through the combination of surveys in the context of LSS/CMB cross-correlation (see e.g. Giannantonio et al., 2012, Ho et al., 2008). However, some innovative ways of using the LSS and CMB are also explored, such as the study of the impact of individual structures in the CMB that I will develop in Chapter 3. A second possible line of research would be to anticipate the future release of data from the next generation of surveys and develop optimised tools in advance, in order to make the most of the improved accuracy and avoid potential biases and caveats: this will be the topic of the next section of this chapter (Sec. 2.2). Finally, considering the great time scales involved in the schedule of the aforementioned surveys, an interesting approach would also be to look for alternative, promising, and already available tracers of matter (and gravitational potentials) to cross-correlate to the CMB: this will be the central point of the Sec. 2.3, through the use of the Cosmic Infrared Background.

2.2 Optimising the cross-correlation for iSW detection

The work that I will present in this section originates from a pre-thesis internship: it aims at exploring, optimising and proof-testing a protocol that I devised for the exploitation of the iSW effect, through CMB/LSS cross-correlation and in the context of next-generation surveys. With this prospective work I have no pretension of giving here a complete and exhaustive method for the analysis of these datasets, but I will focus on a few crucial points that allowed me to point out some interesting features and potential problems of this kind of analysis.

2.2.1 Context and tools

Being entirely theoretical in nature, this study required me to simulate realistic datasets and analyse them thoroughly – a task that required the use of accurate numerical code and tools. The first requirement was to be able to predict, for a given "next-gen-like" survey and a cosmology, the theoretical cross-correlation between the CMB and these LSS, as well as their auto-correlation. If we assume that these two fields are Gaussian in nature (which I will do), the only quantities that we need to compute are their angular cross- and (respective) auto-correlation power spectra in harmonic space. To do so I used the numerical code `CROSS_CMBFAST` that I already mentioned in Sec. 2.1.3.

To develop a little further on this particular code, its specificities, and qualities, it has the particular feature of adopting a top-down approach, starting from the primordial spectrum of fluctuations. This differs from other similar studies where the starting point is the present matter power spectrum (which is evolved backward in order to find its correlation with the CMB). The approach of `CROSS_CMBFAST` unifies the treatment of CMB and matter power spectra, and is more convenient for taking full account of possible fluctuations in the Dark Energy. Moreover, since all perturbations are evolved numerically with the `CMBFAST` code, it does not resort to the frequently used approximate analytical expressions for the growth function (mentioned at the end of 2.1.2), or the also commonly used "Limber approximation" for small angles (Limber, 1954).

In order to thoroughly test my protocol (described in the next section) against "real-life" situations, I also needed to work with realistic simulations of CMB and LSS maps. For the creation and efficient exploitation of such maps I used the HEALPix (Hierarchical Equal Area isoLatitude Pixelization) package (Górski et al., 2005): this suite of codes is based on a specific pixelization scheme of a spherical surface that is particularly suited to fast and accurate statistical and astrophysical analysis of massive full-sky data sets. It contains all the required tools to produce maps based on Gaussian realisations of a given power spectrum, as well as perform a decomposition of a map into its spherical harmonic coefficients (and consequently its power spectrum).

2.2.2 Simulations, covariance estimation and parameter recovery

The main idea that motivated my work presented here was to investigate a way to recover as much information as possible on the Dark Energy from a single survey with ideal characteristics (full-sky coverage, large redshift range, noiseless) and its cross-correlation with the CMB. I started by fixing a reference cosmological model, that I chose to be at that time the best-fit ΛCDM model derived from the WMAP 7-year data (Larson et al., 2011). In the meantime, I also fixed the characteristics of the mock survey that I considered, through the choice of its selection function – the only quantity needed to model a survey (in the linear regime) beside the cosmology; I illustrate this survey in Fig. 2.3.

In this particular context, the information that we are trying to obtain from CMB/LSS correlation becomes simply the density parameter Ω_Λ of the Dark Energy. From there, the protocol that I devised for the Ω_Λ reconstruction is the following:

- I consider a CMB map and a galaxy overdensity map;

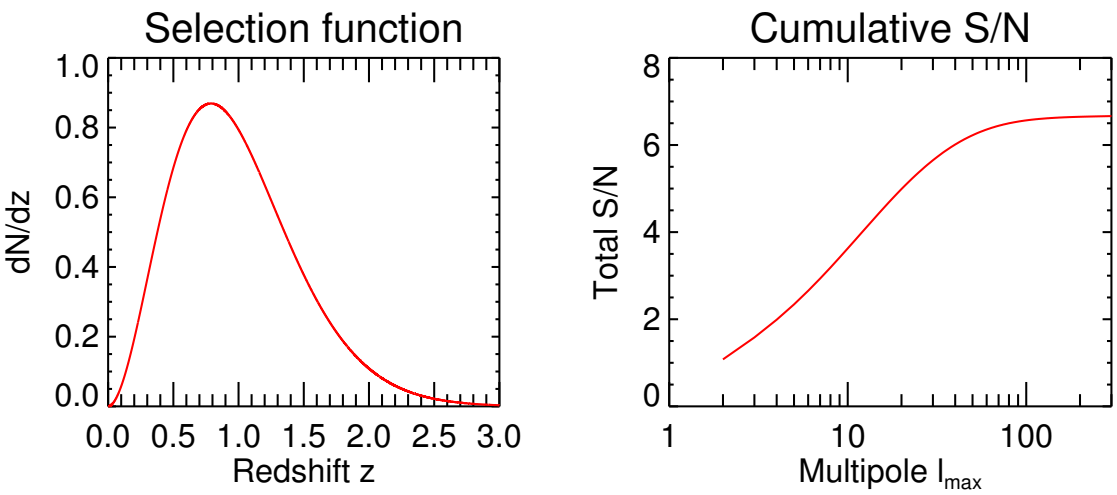

FIGURE 2.3: *Left panel:* Normalised redshift distribution of my fiducial survey, following a similar analytical form as the one mentioned in Fig. 2.1. The parameters chosen here are $z_0 = 0.95$, $m = 1.9$ and $\beta = 1.5$. *Right panel:* Total cumulative S/N of the theoretical cross-correlation signal for this survey as a function of ℓ_{max}.

- I assume that the selection function of the galaxy survey has already been estimated beforehand by other means;
- I use the tools of the HEALPix package to extract the cross-correlation power spectrum C_ℓ^{Tg}(data) from the two "data" maps;
- I use the `CROSS_CMBFAST` code to compute the expected theoretical cross power spectra $C_\ell^{Tg}(\Omega_\Lambda)$ for a large range of Ω_Λ values (between 0.3 and 0.9);
- Using a χ^2 test, I look for the model that fits best the measured spectrum and keep the corresponding Ω_Λ as the reconstructed DE density parameter.

Although this protocol is fairly straightforward, there is a specific point that requires a particular attention: the computation of the χ^2, or more specifically the computation of the covariance matrix involved in the calculation. Indeed, for a given measured spectrum $C_\ell^{\rm data}$, the χ^2 of a given model $C_\ell^{\rm theo}$ is given by:

$$\chi^2 = {}^{\rm T}\left(C_\ell^{\rm data} - C_\ell^{\rm theo}\right) \mathcal{M}^{-1} \left(C_\ell^{\rm data} - C_\ell^{\rm theo}\right), \tag{2.15}$$

$\mathcal{M}$ being the covariance matrix, each of its elements containing the covariance of the cross-correlation power spectrum $C_\ell^{\rm data}$ between two multipoles, i.e.:

$$\mathcal{M}_{ij} = \text{Covar}\left(C_{\ell_i}^{\rm data}, C_{\ell_j}^{\rm data}\right). \tag{2.16}$$

The tricky part here is that there are several methods for computing this matrix, that differ quite substantially from each other. For the simplest approach, we suppose that the survey considered is quite ideal and that there is no correlation between multipoles,

which is generally true only for full-sky surveys. It follows that the covariance matrix is diagonal and that an analytical approach is sufficient to compute its elements using the theoretical covariance already shown in Eq. (2.12) of Sec. 2.1.3. However, this approach is inadequate for more realistic scenarii, since galaxy surveys are often plagued with partial sky coverage, and contaminants that may further complicate the analysis. Although I do consider an ideal survey here, it is still necessary to go beyond this simple case, especially from the perspective of the potential application of the protocol to real datasets.

For these reasons, two alternative methods have been devised, often called "MC1" and "MC2" in the literature (see e.g. Giannantonio et al., 2008, for an application of these approaches). They are both based on Monte-Carlo techniques (hence the "MC") and consist in generating a very large number of as-accurate-as-possible maps (CMB and/or LSS) of which we derive the covariance matrix of the cross-correlation. To be more precise, let us start with the MC2 method: assuming a fiducial model, the principle of the method is to generate N pairs[4] of galaxy & CMB maps with the same characteristics as the original ones and their expected cross-correlation. In practice, these maps are obtained by generating Gaussian realisations of the theoretical power spectra derived from the fiducial cosmology and the knowledge of the considered survey (for the details of the calculations, see e.g. Giannantonio et al., 2008). We then reproduce in these maps the known features of the original maps, whether it is a partial sky coverage (with a mask) or a known contaminant. From there, we compute the cross power spectrum for each of these N pairs of maps, and then derive each element of the covariance matrix according to:

$$\mathcal{M}_{ij} = \mathrm{Covar}\left(C_{\ell_i}, C_{\ell_j}\right) = \frac{1}{N}\sum_{k=1}^{N}[C_{\ell_i}^k - \overline{C}_{\ell_i}][C_{\ell_j}^k - \overline{C}_{\ell_j}] \tag{2.17}$$

where the C_ℓ^k (with k from 1 to N) are the cross power spectra of each simulated pair, and $\overline{C}_\ell$ is the average of these power spectra over the N pairs. Now the only difference between the two Monte-Carlo approaches is that in the MC1 method, only maps of the CMB are generated. They are then correlated to the true galaxy map, and from these correlations are computed the elements of the covariance matrix.

The MC1 is the most widely used estimator in the literature: reasonably fast to implement, it accounts for the cosmic variance and the accidental CMB/LSS correlations, supposedly the primary source of error. However it does not account for the variance in the density maps since only CMB maps are randomly generated. The MC2 method alleviates these problems by also generating random density maps (based on a fiducial cosmology and the selection function). However, the method is more time demanding

[4] With N being typically of the order of ten thousands

(more maps to generate) and requires a robust knowledge of the features of the considered survey (including its selection function and systematics) to accurately simulate realisations of it. Finally, a shortcoming common to both approaches is that they are model dependent and could fail if the data model is poorly understood (e.g. non-Gaussianity of the maps).

In the remainder of this section, I will focus on how these two MC methods fare in the context of the objective of my protocol, i.e. the reconstruction of the Ω_Λ parameter. After fixing the input cosmology, I thoroughly tested each method by repeating the following steps thousands of times:

- Simulation of pair of CMB/density maps with the correlation expected from the chosen cosmology;
- Application of my protocol described earlier to search for the best-fitting Ω_Λ;
- Storage of the reconstructed Ω_Λ value in a histogram.

A comparison of the recovered Ω_Λ values for the two MC methods, along with the input value (here $\Omega_\Lambda^{\text{input}} = 0.734$, WMAP7 best-fit), is shown in Fig. 2.4. The most striking feature here is the bias of the MC1 method towards smaller Ω_Λ values: although the width of both distributions is quite large (with a noticeably larger trend for MC1), the peak for the MC1 method is still clearly shifted (to $\Omega_\Lambda \sim 0.69$), while the MC2 method shows a much better agreement (peak at $\Omega_\Lambda \sim 0.74$) with the input value.

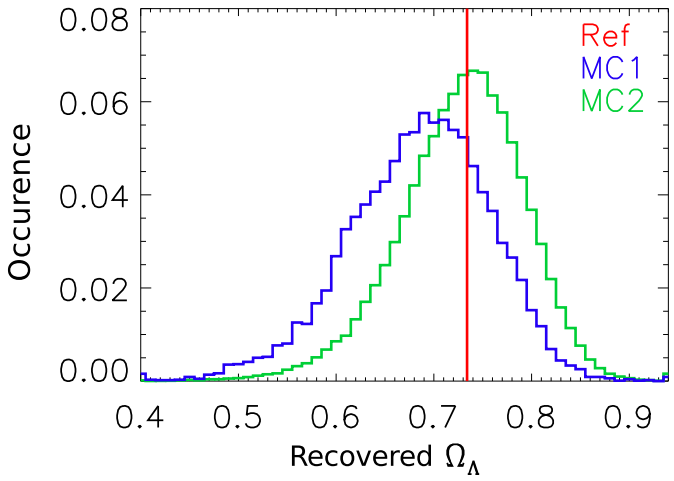

FIGURE 2.4: Normalised histograms of the reconstructed values of Ω_Λ by the protocol described in the text, using either the MC1 (blue) or the MC2 (green) method for the computation of the covariance matrix involved in the χ^2 test. The true input value of Ω_Λ is indicated by the red vertical line and is equal to the best-fit value of the parameter from WMAP7, $\Omega_\Lambda = 0.734$.

We can intuit an explanation for the observed difference between the two methods, which revolves around the asymmetrical nature of the MC1 approach. In the ideal case considered here (no noise, full-sky maps), there are but very little correlations between multipoles: the covariance matrix is nearly diagonal, and the values of its elements tend to the analytical expressions given by Eq. (2.12). Due to the intrinsic weakness of the iSW signal (i.e. C_ℓ^{Tg} is relatively small), we can simplify this equation even further and write:

$$\sigma^2[C_\ell^{Tg}] \sim \frac{C_\ell^{gg} C_\ell^{TT}}{2\ell+1}. \tag{2.18}$$

In the MC2 method, the matrix is computed once and for all using thousands of simulated maps, and is completely independent of the data considered. However, in the MC1 approach, only one density map (the data) is used in the computation of the covariance matrix. As a consequence, the resulting variance will be directly proportional to the spectrum of this particular map, according to Eq. (2.18). Over the thousands of repeated tests that we performed, the Gaussian realisations of this spectrum will be sometimes lower, sometimes higher than the fiducial model, in equal proportions. Then, as said above the "low" realisations will give a smaller covariance matrix (i.e. smaller errors bars), pulling down the Ω_Λ value preferred by the χ^2 test. On the other hand, the "high" realisations will have larger error bars, and therefore will not have the same "pull" towards high Ω_Λ values. This "asymmetry" in the MC1 method is the most likely explanation for the over-abundance of smaller recovered Ω_Λ values when we repeat the test many times.

It stems from the previous analysis that the MC2 method should be the most preferable choice in order to avoid a possible bias on the covariance matrix. However the MC1 approach remains more time-efficient and does not require a deep knowledge of the considered survey and its systematics, a point which is often not properly controlled. In any case, whether we want to generate CMB or density maps, some form of model dependence is always present and has to be accounted for in the interpretation of any result. In the rest of Sec. 2.2, I will use the MC2 method for the covariance matrix, bearing in mind its advantages (no bias in the recovered parameters) and limitations (additional computation time and good knowledge of the considered survey required).

2.2.3 Tomography for iSW studies

By design, the classic approach to the cross-correlation intrinsically misses part of the information about the iSW effect itself, as it looks for an integrated signal along the whole line of sight with no regard for its redshift dependence. Such loss of information could prove to be critical, especially in the context of time-varying models of Dark Energy

(e.g. quintessence). But even for a cosmological constant, the iSW signal recovered by CMB/LSS cross-correlation will have a redshift dependence due to sheer volume effects (already discussed at the end of Sec. 2.1.1). In the case of the mock survey that I used in the previous section, the large redshift coverage and potential iSW S/N (illustrated in Fig. 2.3) might also be squandered by the classic approach described previously. Now the question that I will develop in the present section is the following: Could it be possible to modify my protocol of cross-correlation analysis in order to exploit as much as possible the full potential of such surveys?

The main idea here is to take advantage of the deepness in redshift of the survey: one of the ways that we can think of in order to do so is to "slice" the considered survey. More precisely, instead of integrating the whole distribution of matter contained within it to get one density map, I divided the survey into redshift bins and constructed a density map for each. We intuit here already that some care has to be taken when choosing the shape and the number of bins. The simplest way to slice a survey would be to simply divide its selection function into redshift intervals ("top-hat" cuts), as shown in Fig. 2.5. However, one has to remember that the redshift of surveys objects often have errors in their determination. Hu and Scranton (2004) supposed that photometric redshift estimates are Gaussian distributed with an RMS fluctuation $\sigma(z)$ that increases with redshift as $\sigma(z) = \sigma_{\max}(1+z)/(1+z_{\max})$, i.e. the bins sizes are chosen to increase proportionally to the error. The two free parameters $z_{\max}$ and $\sigma_{\max}$ roughly correspond to the end of the redshift range of the survey and the redshift estimate errors around $z_{\max}$, respectively. Then, a top-hat cut in the $[z_1, z_2]$ interval in estimated redshift becomes a smooth overlapping distribution in actual redshift:

$$n_{z_1 \to z_2}(z) = \frac{1}{2}\frac{dN}{dz}(z)\left[\operatorname{erfc}\left(\frac{z_1 - z}{\sigma(z)\sqrt{2}}\right) - \operatorname{erfc}\left(\frac{z_2 - z}{\sigma(z)\sqrt{2}}\right)\right], \tag{2.19}$$

where dN/dz is the original, full selection function of the survey. An illustration of this redshift slicing is shown in Fig. 2.6, which used the same redshift intervals as the slicing shown in Fig. 2.5. Given this formalism, one could a priori divide a given survey in as many slices as wanted.

Let us now refocus on our objective: the exploitation of a survey for CMB/LSS correlations. We have now a different starting point than in the previous section, as we have now as many density maps as there are redshift slices. From there, the general progression of the protocol remains the same: if we suppose that we divided the considered survey in N redshift bins, we first extract the N angular cross-correlation power spectra of each density map with the CMB. In parallel to this, we compute the expected theoretical cross-correlation of each slice using the knowledge on the survey selection function coupled to the expression in Eq. (2.19). And finally, we perform a χ^2 test on

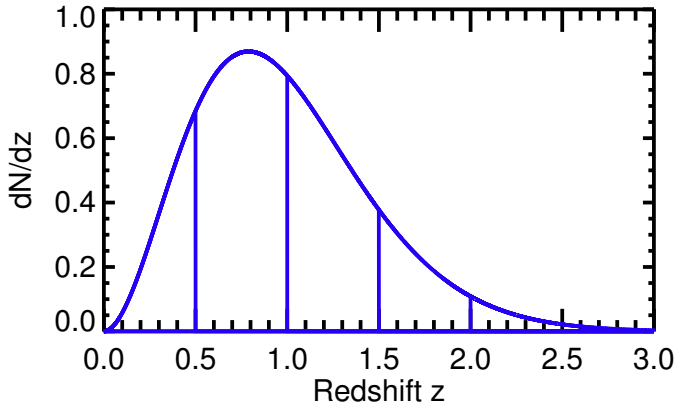

FIGURE 2.5: Illustration of the redshift slicing of the ideal survey considered in Fig. 2.3. The selection function is divided using "top-hat" functions, into five redshift intervals: $z \in [0, 0.5]$, $[0.5, 1]$, $[1, 1.5]$, $[1.5, 2]$ and $[2, \infty]$.

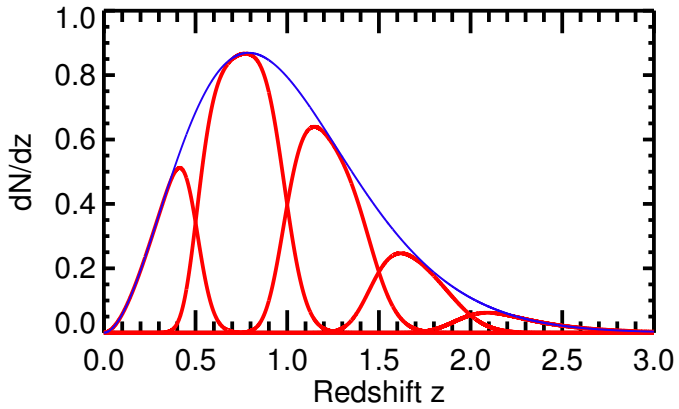

FIGURE 2.6: Redshift slicing of the same survey of Fig. 2.3, using the expression in Eq. (2.19) for the redshift bins. The five divisions have the same bounds (the z_1 and z_2 in Eq. (2.19) expression) as the slices in Fig. 2.5.

all the spectra simultaneously to determine the Ω_Λ that best fits all the data. However, one has to be careful once again in the calculation of the covariance matrix: indeed, as it can be seen clearly in Fig. 2.6, there exists a non-negligible overlap between the different redshift slices. This overlap is practically unavoidable as it originates from the (always present) errors in redshift estimations. It creates therefore correlations between the resulting slices of density maps, which in turns induces a form of redundancy when cross-correlating all these partial maps with CMB. One can then end up with unrealistic results with underestimated errors bars on the recovered parameters. To account for this "leakage" of the redshift bins into one another, I proceeded with some additional steps in the computation of the covariance matrix: when applying the MC2 method, after generating the N partial density maps (and the CMB map), not only did I correlate each map with the CMB, but I also correlated each possible pair of density maps. The end result of this is a non-trivial covariance matrix, that is no longer diagonal even in the case of a ideal survey, as the non-diagonal terms contain the correlations between the overlapping redshift slices of the matter distribution.

Now in order to assess the impact of the redshift slicing on the efficiency of the Ω_Λ reconstruction, I subjected my revised protocol to the same repeated test that I performed in the previous section. A particular point that I did not mention in the previous paragraph is that the simulation of accurate data maps for this test also has to include all the correlations between redshift slices: I therefore had to extensively modify the `CROSS_CMBFAST` code so that it would compute not only the theoretical cross-correlation between CMB and density slices, but also the one between each pair of slices. After that was taken care of, I tested my protocol and explored several slicing strategies, focusing especially on the choice of the number of slices: I compared five numbers of slices ranging from 0 to 10, and present the results of the Ω_Λ reconstruction in Fig. 2.7.

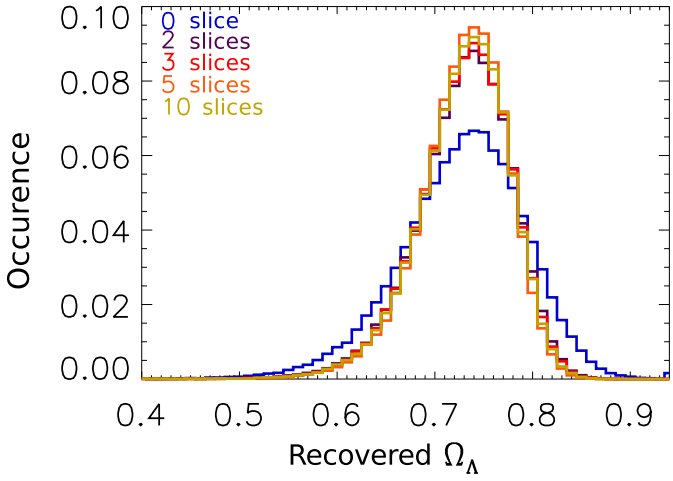

FIGURE 2.7: Normalised histograms of the reconstructed values of Ω_Λ by the protocol described in the text, in the context of several slicing choices of the original survey. The number of slices are 0 (meaning the whole redshift range, blue histogram), 2 (purple), 3 (red), 5 (orange) and 10 (yellow). The true input value of Ω_Λ is again the WMAP7 best-fit value $\Omega_\Lambda = 0.734$.

As we can see there, even a simple division of the survey into two redshift slices yields an appreciable improvement of the Ω_Λ reconstruction, with a significant tightening of the distribution: the standard deviation decreases from $\Delta\Omega_\Lambda \sim 0.120$ to $\Delta\Omega_\Lambda \sim 0.093$ (drop of $\sim 25\%$). The width of the distribution gets even smaller when I further increase the number of slices, although the improvement becomes less and less noticeable, reaching a plateau at some point (particularly visible also in Fig. 2.8). This shows that there is no need to divide the original survey into too many redshift bins, as the information that we can recover on the Ω_Λ parameter seems to reach a limit.

One could possibly ignore this fact (as it has no harmful effect on the reconstruction) and still carelessly consider as many slices as possible, but another important parameter has to be taken into account. As the number of redshift bins increases, so does the number of "density" maps that we have to consider, especially when computing the covariance matrix. In more practical terms, the more maps we have, the more auto-

and cross-correlations we have to perform: one CMB maps and N redshift bins yield N (auto) and $N(N+1)/2$ (cross) spectra. This has two different effects, one of them being the increase in computation time for the matrix, roughly proportional to N^2 (times the number of simulations). The less obvious effect is that each underlying auto- and cross-spectrum gets weaker as we further divide the survey: this has the impeding consequence of requiring a higher number of simulated maps in order for the computed covariance matrix to converge. This particular effect is illustrated in Fig. 2.8, where I show how the width of the distribution of reconstructed Ω_Λ evolves with the number of simulated maps used for the covariance matrix computation. We witness there that the number of simulations required for reaching a plateau does indeed increase for larger numbers of slices, from only 2000 for the original survey to 2-3 times as much for five redshift slices. Combined to the observed convergence of the recovered Ω_Λ distribution, we understand

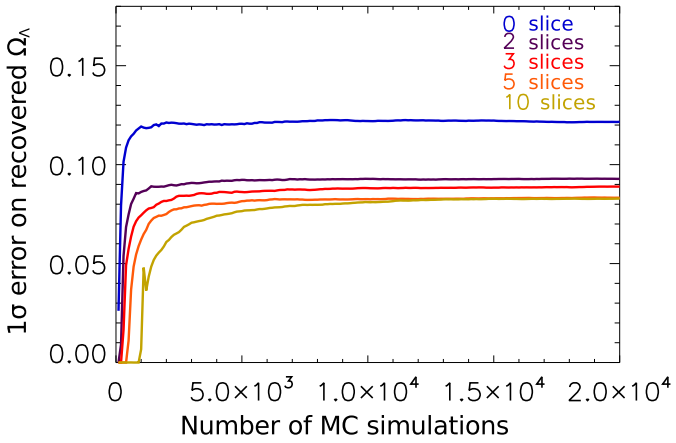

FIGURE 2.8: Standard deviation of the distribution of reconstructed Ω_Λ as a function of the number of sets of simulated maps used in the computation of the covariance matrix. The same slicing choices as in Fig. 2.7 (with their corresponding colours) are explored.

that some form of balance has to be found between the choice of the number of slices (i.e. the precision of the constraints on Ω_Λ) and the number of required simulations (i.e. the computation time needed).

In the end, in this section I only scratched the surface of the topic, as there are many improvements to my protocol that I could consider for a future work. First, in the context of real maps and real surveys, a lot of importance has to be given to the often partial coverage of the sky that has some drastic and intricate effects that affect the cross-correlation, as well as the presence of foregrounds and contaminants that further complicates the interpretation of the signal. On the other hand one could be interested in assessing the full constraining power of the iSW effect on cosmology, without using any underlying model, using the potential of the future generation of surveys. Also in the context of an optimal exploitation of future datasets, the exact choice of redshift slices (shapes) would need a particular tailoring to be as adapted as possible to each

surveys (this kind of work has been explored recently by Jürgens and Schäfer 2012). As a final note, although single surveys are not appropriate for it as of now, the slicing study that I performed may already be applicable to current data in the context of the combination of surveys for iSW detection: indeed, considering several surveys together with their own selection functions is quite similar to considering several slices in redshift (sometimes overlapping) of the same underlying distribution of matter, although some additional care is required to account for the calibration and systematics of each survey.

2.3 The Cosmic Infrared Background and the iSW effect

In Section 2.2, I briefly explored some methods of exploiting the potential of the next generation of surveys, optimising the amount of information extracted while taking care of the possible complications that may appear along the way.

However, no matter how promising these future missions may look, the time scales involved in their schedules does not allow much work other than in the realm of simulations and predictions. As an example, one of the most exciting future satellite, *Euclid*, has its most optimistic launch date scheduled for 2020 ! The ground-based LSST also has a similar schedule. Other experiments may have a closer "due date" (e.g. in the course of 2015 for DES) but still measured in terms of years. On the other end of the spectrum, recent works have been aimed at exploiting as much as possible the current generation of surveys, including attempts at combining several datasets and revising their work at each new data release. In this context, I myself chose to sit in the middle ground: I searched for an alternative tracer of matter that could be correlated to the CMB and that would be both already available in some form, but also with a better potential that the currently used datasets. Such alternatives have already been explored in the literature, for example through the correlation between the iSW effect and the thermal Sunyaev-Zeldovich effect (Taburet et al., 2010), the latter being the result of a boost received by CMB photons from high energy cluster electrons by the inverse Compton scattering: a non-zero correlation is indeed expected between the two effects as these electrons sit in the same gravitational potentials that produce the iSW effect. An interesting aspect of this approach is that it constitutes a "CMB-only" detection of the iSW effect (although with some underlying assumptions). In a similar fashion, the Planck Collaboration (2013c) explored for the first time the correlation of the CMB with the reconstructed gravitational lensing potential extracted from the CMB data itself.

As for myself, using some of the assets and expertise available at the IAS, I set my eyes on an original tracer of matter, which is one of the other few backgrounds of our

Universe: the Cosmic Infrared Background (CIB hereafter), whose characteristics and exploitation for iSW studies I will describe in the next sections.

2.3.1 The blurry red light

First discovered by Puget et al. (1996), the Cosmic Infrared Background (CIB hereafter) is visible roughly from 10 to 1000 μm in wavelength and is one of the backgrounds present in our Universe (see Fig. 2.9). This particular background, present in every survey that covers infrared wavelengths, arises from the accumulated electromagnetic emissions from star-forming galaxies distributed across a large redshift range. It finds its origin in the smallest and farthest galaxies (which cannot be resolved by telescopes and their finite resolution) and in the densest population of galaxies (whose observation is confusion-limited), which thus appear as a blurry background. The earliest epoch for the production of the CIB is thought to be when star formation first began at the end of the Dark Ages (and the onset of the reionisation epoch); contributions continued through the present epoch, including our current Dark Energy dominated era. Similarly to the CMB, the CIB also features anisotropies (first detected and discussed in Lagache and Puget, 2000, Matsuhara et al., 2000) that are shaped by the distribution and clustering of these infrared galaxies in the Universe.

Ever since its discovery, many efforts have been deployed to detect the CIB and its anisotropies with increasing precision, as they contain a lot of information about the star and galaxy formation histories, including their clustering processes. The most recent papers on the CIB anisotropies use sophisticated models which compute the halo occupation distribution (HOD, see e.g. Cooray and Sheth, 2002, Peacock and Smith, 2000) and the Dark Matter halos properties, in order to predict the power spectrum of these anisotropies (see e.g. Pénin et al., 2012).

2.3.2 The CIB as an alternative tracer of matter

We can easily understand that the anisotropies of the CIB are underlined by the galaxy density field and thus the matter density fluctuations: it is therefore reasonable to expect that the CIB has a positive correlation with the CMB through the iSW effect. We should also bear in mind that it contains contributions from galaxies over a very large range of redshift (up to $z \sim 7$, with a peak of emission around $z \sim 2$), and that it is contained in many past and current surveys (such as IRAS or the newly released *Planck*, both covering IR frequencies) that have often a large coverage of the sky. These two points are the reasons that motivated my choice of the CIB as a tracer of matter, as they make

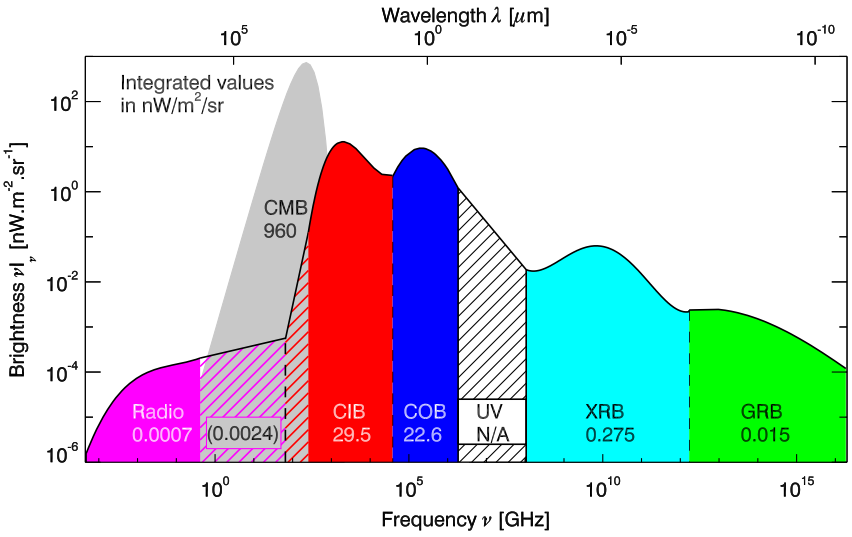

FIGURE 2.9: Schematic Spectral Energy Distributions (SED) of the most important (by intensity) backgrounds in the Universe, and their approximate brightness in $\mathrm{nW.m^{-2}.sr^{-1}}$ written in their respective zones. From right to left: the radio background, the CMB, the CIB, the Cosmic Optical Background (COB), the UV background, the X-Ray Background (XRB) and the Gamma-Ray Background (GRB). Image courtesy of H. Dole.

the CIB a particularly suitable and promising candidate for the iSW detection by cross-correlation with the CMB. However, the extraction of the CIB from a survey remains a challenging and delicate task that is still ongoing to this day: this led me to focus first on a theoretical study of the CIB-CMB cross-correlation through the iSW effect, and an assessment of its detectability.

As mentioned before, the most recent works focused on the studies of CIB anisotropies used sophisticated HOD to predict and describe them. Such models are particularly useful when describing the small, non-linear scales of the CIB. In the context of the iSW effect, we focus on much larger scales which is why I used a simpler model for the CIB, similar to the description made by Knox et al. (2001). The general definition of the CIB anisotropies at a given frequency ν and in a given direction $\hat{\mathbf{n}}$ can be then written as the following line-of-sight integral:

$$\delta T_{\mathrm{CIB}}(\hat{\mathbf{n}}, \nu) = \int_{z_{\mathrm{far}}}^{0} dz\, a(z)\, \delta j(\hat{\mathbf{n}}, \nu, z) \tag{2.20}$$

with δj being the emissivity anisotropies of the CIB. The integration is made from some initial time z_{far} before star formation began to our location at the $z = 0$. In their work, Knox et al. hypothesized that the CIB anisotropies are direct tracers of the matter density fluctuations $\delta = \delta\rho_m/\bar{\rho}_m$, up to a bias factor. Therefore, the previous expression becomes an integral of the product between a mean far infrared (FIR) emissivity and

the matter density fluctuation field:

$$\delta T_{\rm CIB}(\hat{\mathbf{n}}, \nu) = \int_{z_{\rm far}}^{0} dz\, a(z)\, b_j(\nu, z)\, \bar{j}(\nu, z)\, \delta(\hat{\mathbf{n}}, z) \tag{2.21}$$

Here the quantity $b_j(\nu, z)$ is some form of bias that links the matter distribution and the emissivity. It is frequency- and redshift-dependent and is here defined by:

$$\frac{\delta j(\hat{\mathbf{n}}, \nu, z)}{\bar{j}(\nu, z)} = b_j(\nu, z)\ \delta(\hat{\mathbf{n}}, z) \tag{2.22}$$

with $\bar{j}(\nu, z)$ being the mean emissivity per comoving unit volume at frequency ν as a function of redshift z. We can observe here some similarities between Eq. (2.21) and the expression in Eq. (2.6) of the galaxy density contrast for the usual surveys. However the selection function has been replaced by the emissivity function, with an additional scale factor as we no longer consider individual objects that we count on the sky, but rather the light that the objects emit (which of course gets redshifted in the time it takes to reach us). There is also here an added dependence on the frequency through the emissivity: although overlapping, it is different populations of objects that we observe when surveying different wavelengths. This emissivity function is derived using an empirical, parametric model based on number counts of galaxies: at the time of this study I used the work of Béthermin et al. (2011), although a more recent update has been published since (see Béthermin et al., 2012).

Examples of such emissivities are shown in Fig. 2.10 (left panel): it should be noted that they not only depend on the frequency but also on the experiment considered, because each instrument possesses a unique bandpass for each frequency and has its own resolution. This results in the observation of a "unique" CIB map by every pair of frequency and instrument, corresponding to a population of objects just as unique. The depth in redshift of the CIB is also illustrated in this figure, with emissivity functions that theoretically reach much higher redshifts that any current (and even some future) surveys. We should however keep in mind that, according to Eq. (2.21), these functions have to be multiplied by the scale factor (right panel of Fig. 2.10) in order to be compared to the selection function of classic galaxy surveys. This causes a decrease at high z but even then, they still cover a larger range of redshift than typical galaxy surveys (see e.g. Fig. 2.1 and 2.3 for comparison). We also note that Fig. 2.10 shows significant overlaps in redshift between the emissivity functions at different frequencies which will consequently induce correlations between CIB observations, similarly to those between redshift slices of a same survey (discussed in Sec. 2.2.3). At this point, this overlap already indicates that a combined used of CIB observations at several frequencies may not yield improvements in the detection of the iSW effect.

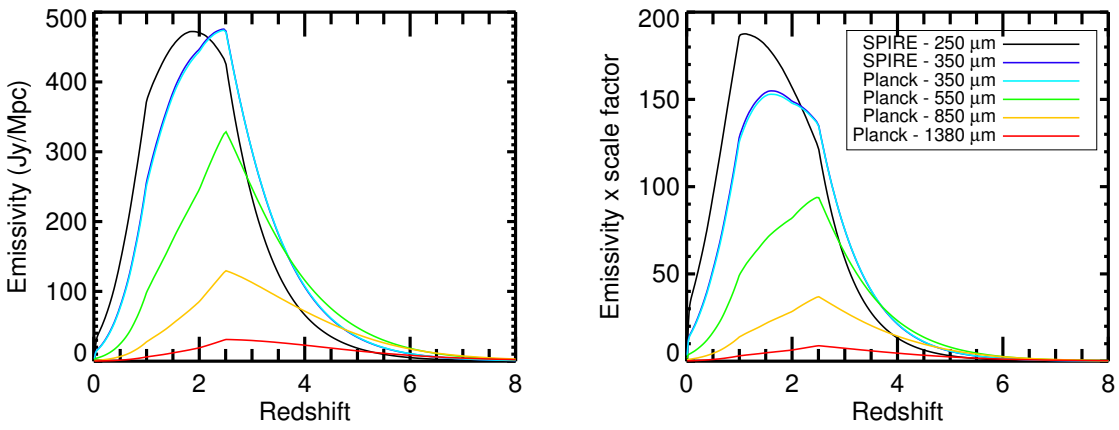

FIGURE 2.10: *Left panel:* Emissivities as functions of redshift for six experiment/frequency pairs, computed using the model of Béthermin et al. (2012). Notice the very slight difference between instruments at 350 μm due to a difference in bandpass. *Right panel:* Same functions multiplied by the scale factor $a(z)$, or equivalently $1/(1+z)$, for comparison purposes with selection functions of galaxy surveys.

A last element that needs to be pointed out is the previously mentioned linear bias[5] $b_j(\nu, z)$ present in Eq. (2.21) that I chose constant in redshift here: $b_j(\nu, z) = b_{\rm lin}(\nu)$. To obtain it for each frequency that I considered, I computed the value of $b_{\rm lin}$ that gives the best agreement between my calculation of the linear CIB power spectrum and those obtained from the *Planck* data (Planck Collaboration, 2011a). This point will be discussed in more detail in the next subsection.

Now, starting from Eq. (2.21) we can use the same formalism as for the CMB-galaxy correlation in order to derive the theoretical CMB-CIB cross-correlation at any given frequency. Following the same steps from Eq. (2.7) to (2.11) (from Sec. 2.1.2), we end up with similar expressions for both the cross- and auto-correlation spectrum of the CIB, except that the galaxy bias is replaced by the emissivity one, and the mean emissivity (times the scale factor) plays the rôle of the selection function. The next section will be dedicated to the computation of the expected value of these modified equations in several contexts

2.3.3 Predictions on the CIB-CMB cross-correlation

2.3.3.1 Computing the expected correlations

To compute the expressions mentioned at the end of the previous section, I once again adapted the `CROSS_CMBFAST` code to use it for this CIB study, performing a number

[5]This bias here represents our matter-emissivity bias in Eq. (2.21) and (2.22) and should not be confused with the widely used galaxy-Dark Matter bias, though ours *does* contain information about how the emitting objects populate Dark Matter halos.

of modifications to suit this new context. In my customised version, for a given cosmology and emissivity function $\bar{j}(\nu, z)$ my code calculates the CIB-CMB angular cross-correlation power spectrum, as well as the predicted auto-correlation power spectrum of the CIB fluctuations.

In Fig. 2.11, I present predictions for the CIB-CMB cross-correlation, at several FIR wavelengths and for different instruments, namely: IRAS at 100 μm, *Herschel* SPIRE at 250, 350 and 500 μm and *Planck* HFI at 350, 550, 850, 1380, and 2097 μm. We note that at 350 μm the SPIRE- and *Planck*-predicted spectra differ slightly from each other, once again due to slight differences in wavelength bandwidth of the two instruments (hence a difference in the emissivities used, see Fig. 2.10).

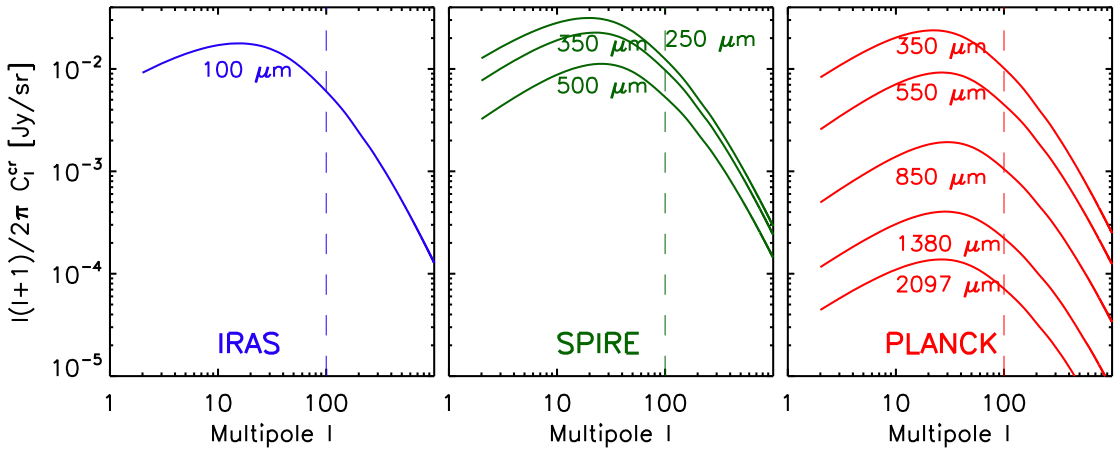

FIGURE 2.11: Theoretical angular cross power spectrum of the CIB-CMB correlation calculated for IRAS at 100 μm (left-hand panel), for *Herschel* SPIRE between 250-500 μm (central panel) and *Planck* HFI between 350-2097 μm (right panel). The linear bias, $b_{\rm lin}$, is fixed here to 1 at all frequencies in order to compare the non-biased CIB power spectra. The vertical dashed line on each panel marks the upper limit of the multipoles used in our analysis: this choice comes from the vanishing of the iSW signal (see Fig. 2.13) and the rise of non-linearities at higher ℓ.

In a fashion similar to previous galaxy-iSW cross-correlations (see e.g. Fig. 2.2), we note that the cross-correlation peaks around $\ell \simeq 10$–30, and quickly vanishes at higher multipoles. Comparing the signal at the different wavelengths shows that the amplitude of the cross-correlation signal is maximum at a wavelength $\simeq 250$ μm. This is not entirely surprising, since this wavelength roughly corresponds to the maximum of the observed CIB spectral energy distribution (cf. Fig. 2.9).

To get some form of validation for my computed spectra, I compared my predictions for CIB autocorrelation to the measurements of Planck Collaboration (2011a), taking the opportunity to address a concern mentioned in the previous section – namely, the determination of the linear emissivity bias. To obtain it at each frequency, we compute the value of this bias that gives the best agreement between my linear CIB power spectrum and the corresponding one obtained from the *Planck* data. I chose to fit the two spectra

in the range of multipoles $\ell \in [10, 50]$, where most of the iSW signal resides. This is illustrated in Fig. 2.12 where I plotted the biased and non-biased CIB linear spectra and compared them to the ones from Planck Collaboration (2011a) at their four frequencies. Overall, the two sets of spectra show good agreement over the multipoles of interest; the spectra deviate at higher ℓs (starting from $\simeq 100$) due to the rise of non-linearities that I did not account for in my linear model – namely the small-scale correlations between galaxies inside the same halos. The linear bias we obtain this way increases with the wavelength: this is coherent with the fact that as we go further deep into the infrared, the galaxies probed are more luminous at higher z. They reside in more massive and rarer halos, and are therefore more biased.

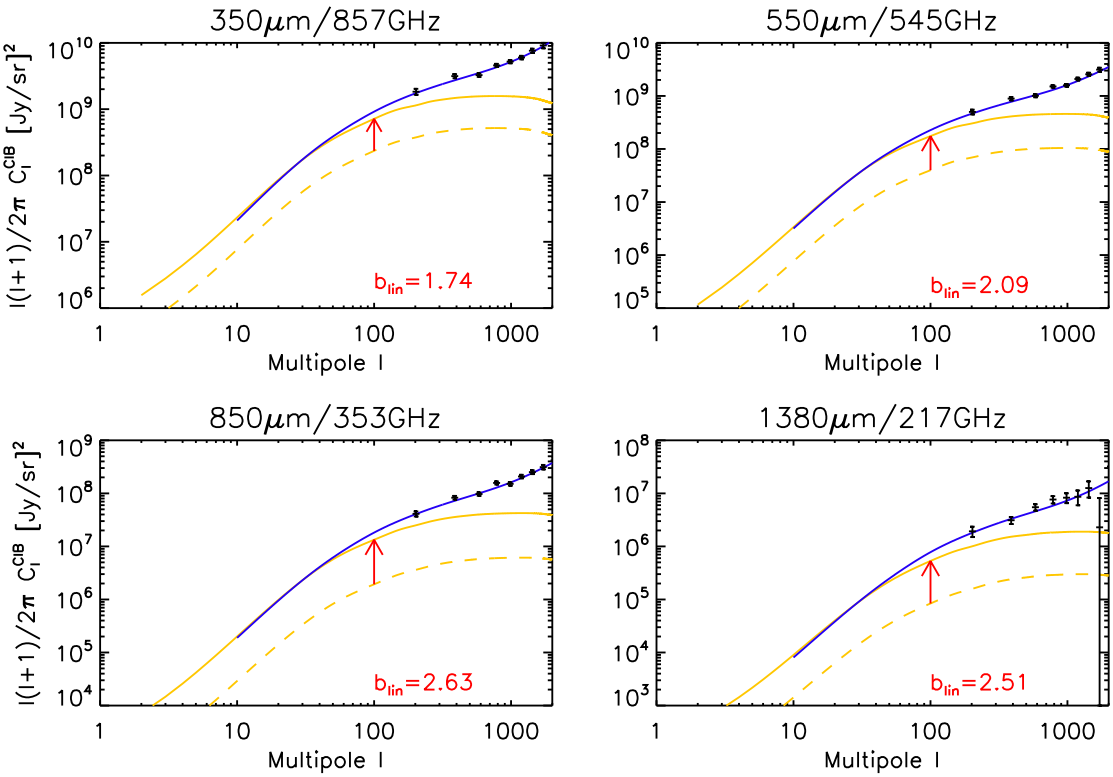

FIGURE 2.12: Angular power spectra of the CIB fluctuations at four frequencies of the *Planck*-HFI instrument, as fitted by the *Planck* Team (blue continuous line) and by our non-biased models (dashed yellow line). For each frequency, we provide in red the linear bias which gives the best agreement between the two models, and plot our models taking into account this bias (solid yellow line). The data points correspond to measurements obtained by the *Planck* Team (Planck Collaboration, 2011a).

It should be also noted that the results on the cross-correlation are also not exact at the highest ℓs, as hinted at by the deviation observed in the auto-correlation spectrum. Indeed, the non-linear counterpart to the iSW effect, called the Rees-Sciama effect, contributes at those scales (see Schäfer et al., 2011, for a discussion). However, in our case the linear part of the iSW largely dominates at the peak observed in Fig. 2.11.

2.3.3.2 Detectability assessment

Following the same progression as for the CMB-galaxy case, I then investigated the detection level of the iSW effect using CMB-CIB cross-correlation by performing a signal-to-noise ratio analysis. Using the power spectra that I computed in the previous section, I can express for each given frequency ν the total signal-to-noise ratio of the iSW detection as follows:

$$\left[\frac{S}{N}\right]^2(\nu) = \sum_{\ell=2}^{\ell_{\max}} (2\ell+1) \frac{[C_\ell^{\rm cr}(\nu)]^2}{[C_\ell^{\rm cr}(\nu)]^2 + C_\ell^{\rm CIB}(\nu) \times C_\ell^{\rm CMB}} \tag{2.23}$$

where $C_\ell^{\rm cr}(\nu)$ is the CMB-CIB cross-correlation spectrum, and $C_\ell^{\rm CIB}(\nu)$ the CIB auto-correlation spectra, both at a given frequency ν, while $C_\ell^{\rm CMB}$ is the CMB auto-correlation spectrum. The total (cumulative) signal-to-noise is summed over multipoles between $\ell = 2$ and $\ell_{\max} \leqslant 100$ where the signal has its major contribution (see Fig. 2.11).

In my analysis I considered first the ideal situation where the CIB and CMB maps used for cross-correlation are noiseless and cover the whole sky. With these assumptions we obtain the highest possible signal-to-noise ratio, the only limitation being the cosmic variance. In Fig. 2.13 I present the predictions for the CIB-CMB cross-correlation in the case of a full-sky CIB map, provided by the previously mentioned instruments and frequencies.

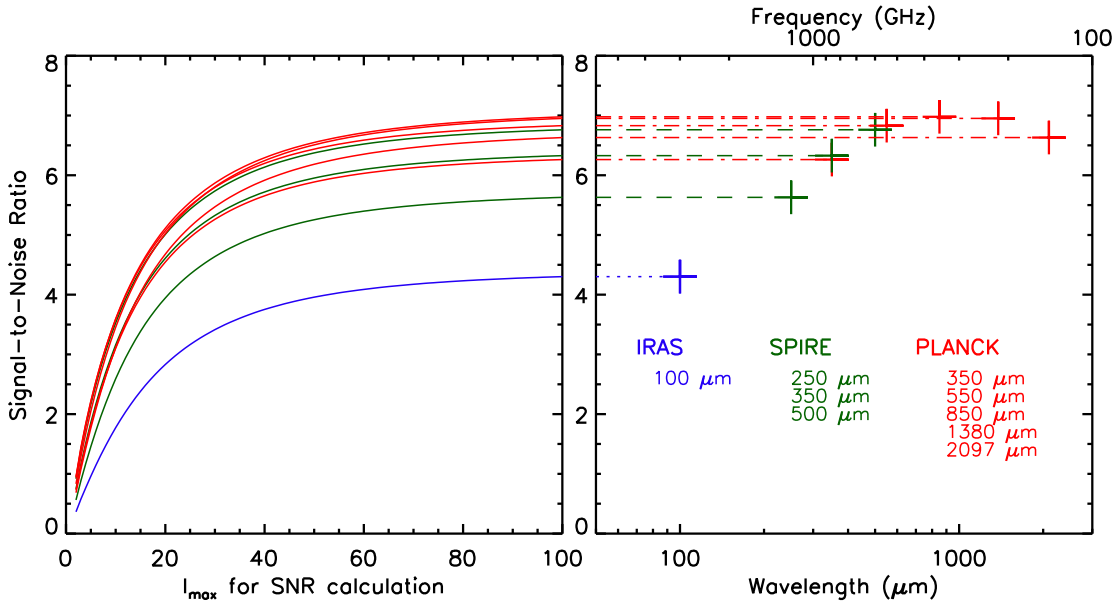

FIGURE 2.13: *Left-hand panel:* Cumulated S/N as a function of ℓ_{max} (defined in Eq. 2.23) for the CMB-CIB cross-correlation, at our chosen frequencies and instruments. *Right-hand panel:* Total S/N with $\ell_{max} = 100$ as a function of frequency/wavelength.

With these optimistic assumptions, I obtained high levels of detection for the CIB-CMB correlation which reach $\simeq 7\sigma$, on par (if not better) with the most promising surveys of the next generation to come (for detailed S/N results, see Table 2.1 in Sec. 2.3.4).

Interestingly, it should be mentioned that these results in the ideal case are independent of the previously discussed linear bias, even if it boosts the correlation signal. This can be understood from Eq. (2.23) where the linear bias can be factorized from each term (one for $C_\ell^{\rm cr}$ and a squared one for $C_\ell^{\rm CIB}$) and therefore cancels out.

As evoked before, we see that the largest contribution to the S/N comes from multipoles smaller than $\simeq 50$. On the other hand, the most interesting feature of these results is that contrary to what could be intuited from Fig. 2.11, the total S/N peaks around $850\,\mu$m instead of $250\,\mu$m for the cross-correlation signal itself. The reason for this is actually quite subtle: it comes from the shape of the "noise" term in the S/N expression in Eq. (2.23), as a function of ℓ, namely:

$$[N_\ell]^2(\nu) \equiv ([C_\ell^{\rm cr}(\nu)]^2 + C_\ell^{\rm CIB}(\nu) C_\ell^{\rm CMB})/(2\ell+1) \tag{2.24}$$

For all the frequencies studied here, this "noise" has roughly the same amplitude *relatively* to its corresponding "signal":

$$[S_\ell]^2(\nu) \equiv [C_\ell^{\rm cr}(\nu)]^2 \tag{2.25}$$

This is illustrated in Fig. 2.14, where I plotted in the left panel all the $[S_\ell(\nu)]^2$ terms with their respective maximum rescaled to unity. In the middle panel, I applied the same rescaling factor of each $[S_\ell(\nu)]^2$ term to the corresponding $[N_\ell(\nu)]^2$ term. By doing this, it is possible to compare the results from all frequencies without changing their associated signal-to-noise ratios. On the resulting graph, we see that at $\ell = 100$ the rescaled noise amplitude is roughly the same, while the signal has the same shape at all frequencies, except for a small shift in ℓ. However there is a major difference in the shape of the noise power spectrum from one frequency to another: its slope changes depending on the frequency, with the steepest one for *Planck* $850\,\mu$m. Therefore its amplitude goes down more quickly than the others as ℓ approaches zero where coincidently the signal is strong, which then boosts the S/N at the low multipoles, and the total S/N.

In light of these results, the optimal frequency for iSW detection appears to be around 353 GHz/850 μm with a maximum S/N reaching 7σ. However in practice, the CIB extraction at this frequency might prove challenging since the CMB becomes dominant here, and increasingly so as we go down in frequency. Therefore the possible residuals in our extracted CIB map have to be accounted for, and other sources of noise as well, which is the purpose of the next subsection.

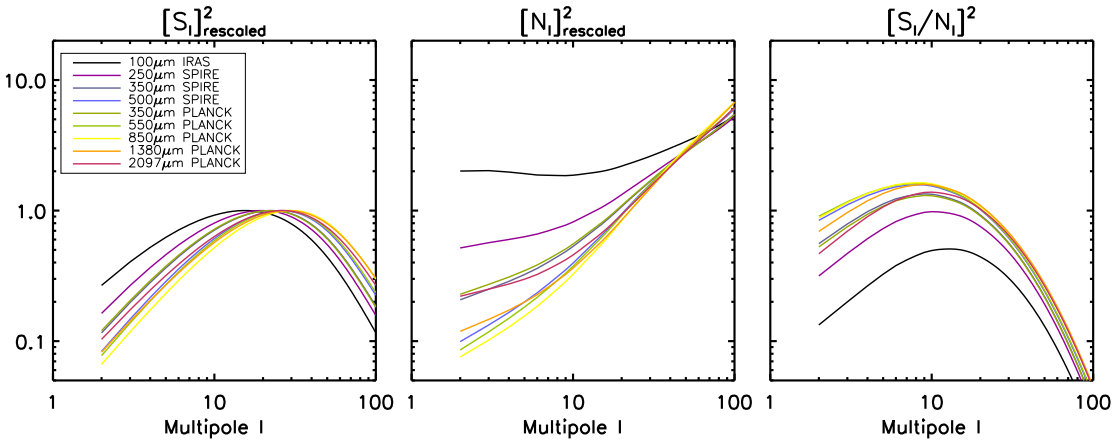

FIGURE 2.14: "Signal" terms (left-hand panel, rescaled to unity) and "noise" terms (middle panel, same rescaling factor as the "signal") of the S/N as functions of ℓ (see text for details) for our chosen frequencies and instruments. The quotient of the two terms, used in the calculation of the S/N itself, is shown in the right-hand panel: the main difference throughout the frequencies comes from the shape of the "noise" term.

2.3.4 Accounting for realistic conditions

The contaminants of the CIB and obstacles to its extraction are many: first the signal is completely dominated on a large part of the sky by emissions from our own galaxy. The contamination from this foreground in the galactic plane is several orders of magnitude above the CIB level and prevents us from extracting the CIB, therefore reducing the "usable" fraction of the sky by at least $\sim 25\%$. Furthermore, the rest of the sky is also quite polluted – from a CIB point-of-view – by these foregrounds full of galactic dust. These will have to be removed from our maps although some residuals might remain in the final CIB map used for the cross-correlation. There may even be a significant CMB residual (especially at *Planck* frequencies) in this map due to an imperfect separation of components, which could have a dramatic impact on the cross-correlation and easily induce false detections.

In the light of these elements, it appeared clearly to me that I needed to carry a more realistic study by including these possible sources of contamination and assess their impact on the iSW detection. To account for these effects on the detectability of the CIB-CMB cross-correlation, I used a more complete formulation of the signal-to-noise ratio, by adding new elements in the noise term. The expression of the S/N therefore becomes at a given frequency ν:

$$\left[\frac{S}{N}\right]^2(\nu) = f_{\rm sky}\sum_{\ell=2}^{\ell_{\rm max}}(2\ell+1)\times \frac{[C_\ell^{\rm cr}(\nu)]^2}{[C_\ell^{\rm cr}(\nu)+N_\ell^{\rm cr}(\nu)]^2+[C_\ell^{\rm CIB}(\nu)+N_\ell^{\rm CIB}(\nu)][C_\ell^{\rm CMB}+N_\ell^{\rm CMB}]} \quad (2.26)$$

where $f_{\rm sky}$ is the fraction of the sky common to the CMB and the CIB maps, and $N_\ell^{\rm cr}$, $N_\ell^{\rm CIB}$ and $N_\ell^{\rm CMB}$ are the noise contributions respectively in the cross, CIB and CMB signal. Since the CMB is expected to be only variance-limited at the multipoles of interest, I fixed here $N_\ell^{\rm CMB} = 0$. However we still have to take into account the CIB contamination.

To do so, I first break the CIB noise power spectrum into several independent parts:

$$N_\ell^{\rm CIB}(\nu) = R_\ell^{\rm CMB}(\nu) + R_\ell^{\rm fore.}(\nu) + N_\ell^{\rm instr.}(\nu) + N_\ell^{\rm correl.}(\nu) \tag{2.27}$$

where these four different terms represent, from left to right, the power spectra of the CMB residual, the galactic foreground residuals, the instrumental noise and finally the noise due to correlation between residuals and the CIB (which appears when autocorrelating the final CIB map).

I quantify the CMB residual in the CIB map as a fraction $f_{\rm CMB}$ of the total CMB map, which affects both the cross-correlation and CIB noise; this approach assumes a "global" CMB contamination (on the whole sky) without any spatial dependence. This consequently defines the noise in the cross signal:

$$N_\ell^{\rm cr}(\nu) = f_{\rm CMB}(\nu) \times C_\ell^{\rm CMB} \tag{2.28}$$

and the following two contributions:

$$R_\ell^{\rm CMB}(\nu) = f_{\rm CMB}^2(\nu) \times C_\ell^{\rm CMB} \tag{2.29}$$

$$N_\ell^{\rm correl.}(\nu) = 2 f_{\rm CMB}(\nu) \times C_\ell^{\rm cr}(\nu) \tag{2.30}$$

In the literature, the power spectrum of foregrounds such as dust emissions are often modelled as (and often found to be close to) power laws: here in my analysis I define the spectrum of the foreground residuals with the following expression:

$$R_\ell^{\rm fore.}(\nu) = \mathcal{A}_{\rm fore.}(\nu) \times C_{\ell=10}^{\rm CIB}(\nu) \left(\frac{\ell}{10}\right)^\alpha , \tag{2.31}$$

This power law has an amplitude defined relatively to the real CIB signal through a chosen constant $\mathcal{A}_{\rm fore.}$, which defines the quantity:

$$\mathcal{A}_{\rm fore.}(\nu) = R_{\ell=10}^{\rm fore.}(\nu) / C_{\ell=10}^{\rm CIB}(\nu) \ , \tag{2.32}$$

i.e. the ratio between the foreground residuals and the CIB spectrum at the multipole $\ell = 10$, approximatively where the cross-signal is at its maximum. The slope of the

spectrum α is fixed here for all frequencies; previous analysis of infrared maps (Miville-Deschênes et al., 2002, Wright, 1998) found it to be $\simeq -3$ for foregrounds at high galactic latitudes. Finally, the instrumental noise power spectra $N_\ell^{\text{instr.}}$ at each frequency are taken from the first ten months of *Planck* data in Planck Collaboration (2011b), and extrapolated to the thirty months, i.e. the end of the fourth *Planck* full-sky survey.

In this section I focused on four of the five previously described *Planck* HFI frequencies, from 217 to 857 GHz. I chose to discard the fifth 143 GHz as the CMB completely dominates the CIB signal there. I also put aside the IRAS frequency here because of its weaker significance (even in the ideal case), and the SPIRE frequencies since the instrument was not scheduled to ever cover very large regions of the sky (i.e. $f_{\text{sky}} \ll 1$), dramatically decreasing its associated S/N – as it is proportional to the square root of f_{sky} in Eq. (2.26).

At this point, the framework that I devised for the S/N calculation has three input parameters at each of the four frequencies: f_{sky}, f_{CMB} and $\mathcal{A}_{\text{fore.}}$, whose values can be chosen freely. The next step would have been to explore this 3D parameter space at each frequency and compute the corresponding S/N at each point. Considering the very large number of possible combinations of parameters, it would not have been practical to perform and display the complete results of such exploration. Therefore I made the decision of fixing f_{sky} to two values of interest:

- $f_{\text{sky}} = 0.75$, which corresponds to an optimistic case where the only part of the sky discarded is the galactic plane; this is an optimistic scenario in the sense that there are other highly contaminated regions where from the component separation techniques might not be able to extract the CIB.
- $f_{\text{sky}} = 0.15$, which is a low estimate of the area of the sky where the current data allow for an efficient CIB extraction. The methods currently employed are based on the use of HI maps as a tracer of the galactic dust, though it only remains valid for an HI column density lower than a specific threshold (see Planck Collaboration, 2011a, for details on these methods).

As far as the two other input parameters are concerned, I limited their ranges to reasonable values, with $f_{\text{CMB}} \in [0, 0.1]$ and $\mathcal{A}_{\text{fore.}} \in [0, 10]$.

Among the four *Planck* frequencies that I kept here, I started by studying the effects of the noise for the frequency that gave the best S/N results in the ideal case (850 μm/353 GHz) – having in mind that a significant drop in S/N at this wavelength would not bode well for the rest of them. The corresponding results are presented in Fig. 2.15 which shows the contour levels of the S/N in the $(f_{\text{CMB}}, \mathcal{A}_{\text{fore.}})$ parameter space.

The influence of the CMB is clearly visible at this frequency, quickly reducing the S/N as its residual level increases. This effect is even more pronounced at 1380 μm/217 GHz, where the S/N is typically twice as low as in the ideal case (see Table 2.1), due to the fact that we get closer to the maximum of the SED of the CMB. It makes this frequency far less significant for the iSW detection than in the ideal case. The presence of instrumental noise – whose effect cannot be appreciated with Fig. 2.15 alone – becomes significant at the two lowest frequencies (217 and 353 GHz), again reducing their value in the cross-correlation. As expected the galactic foreground residuals also decrease the S/N, though their influence is roughly the same at all frequencies as they are defined relatively to the CIB spectrum in this analysis. Lastly, the biggest influence comes from the fraction of the sky through the $f_{\rm sky}$ parameter, as the total S/N scales as $\sqrt{f_{\rm sky}}$. This makes it a crucial requirement for future applications to have the largest possible coverage to minimize this effect – very similarly to the requirement of galaxy surveys.

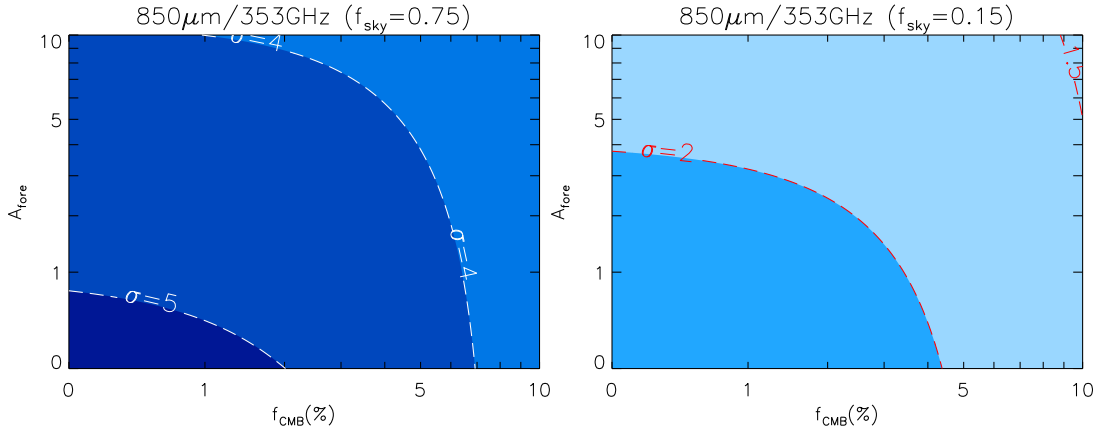

FIGURE 2.15: Total signal-to-noise ratio of the CIB-CMB cross-correlation at 353 GHz, as a function of the CMB residuals (in percentage of the total CMB signal) and the foregrounds residuals (through the parameter $\mathcal{A}_{\rm fore.}$). *Left panel:* $f_{\rm sky} = 0.75$, the results go from less than 4 to more than 5, from the brightest colored area to the darkest. *Right panel:* $f_{\rm sky} = 0.15$, the S/N goes from slightly less than 1.5 to more than 2, again from the brightest to the darkest area.

Taking all these remarks into account and after some exploration of the parameter space, the optimal frequency that stands out in these more realistic scenarii is 545 GHz/550 μm. Indeed, it is weakly influenced by instrumental noise and CMB residuals and also has a higher "original" S/N (in the ideal case) than the other remaining frequency 857 GHz/350 μm. The S/N analysis at 545 GHz is presented in Fig. 2.16: for the case of a large but realistic coverage, the S/N still reaches high and promising values around 4.5 σ. Even in a more pessimistic scenario, the significance of the detection stays around a 2.5 σ level, comparable with the constraints from current galaxy surveys.

However, one may wonder here if it is really necessary to argue and determine which is the

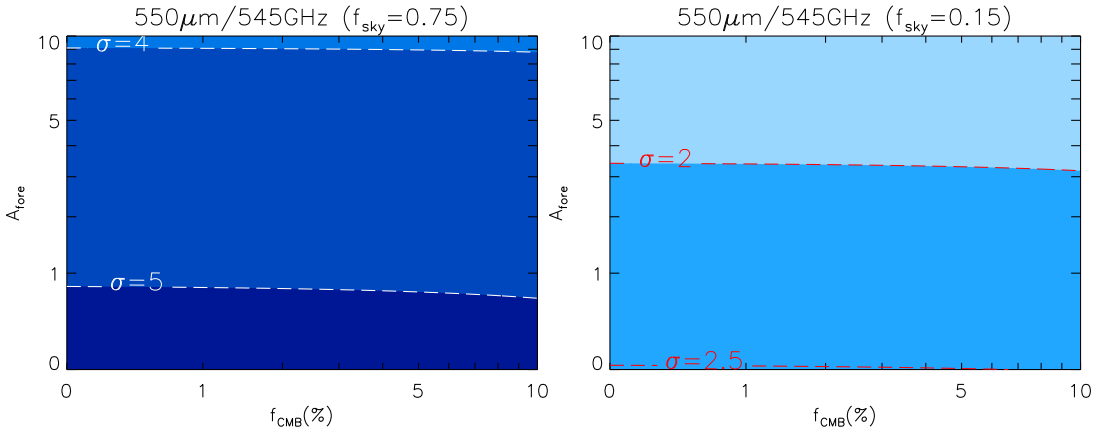

FIGURE 2.16: Total signal-to-noise ratio of the CIB-CMB cross-correlation at 545 GHz as a function of the CMB residuals and the foregrounds residuals. *Left panel:* $f_{\rm sky} = 0.75$, the results go from slightly less than 4 to more than 5, from the brightest to the darkest area. *Right panel:* $f_{\rm sky} = 0.15$, the S/N goes from less than 2 to slightly more than 2.5.

most suited frequency for giving the best results for the CMB-CIB cross-correlation. Indeed, in the same manner as I combined the constraints from redshift slices in Sec. 2.2.3, it is reasonable to consider the possibility of combining the cross-correlation signals from the CIB at several frequencies to improve the S/N – a approach that I will explore in the next (last?) section of this chapter.

2.3.5 Multi-frequency joint analysis

Until now I have only considered a detection at a single CIB frequency and its associated significance. In practice, when handling real data, we will most likely have several maps of the CIB at different frequencies, hence as many cross spectra. For example, in the case of *Planck* we should eventually be able to extract the CIB at four different frequencies on a large fraction of the sky. This could potentially allow to increase the total signal-to-noise ratio of the iSW detection by combining the constraints from all available frequencies. However, the improvement brought by this approach will be limited by the possible intrinsic correlations (and redundant information) between the CIB maps at different frequencies – once again in the same manner as the correlations between redshift slices of a galaxy survey limited the amount of information available.

I expanded my previous S/N formalism to express the theoretical joint significance of a set of n cross-correlations (i.e. CIB at n frequencies, each correlated to the same CMB):

$$\left(\frac{S}{N}\right)^2_{\rm Total} = X^T \mathcal{M}^{-1} X \tag{2.33}$$

with X (X^T) being the column (row) vector of all the cross-correlations:

$$X^T = \begin{pmatrix} X^T(\nu_1) & \cdots & X^T(\nu_n) \end{pmatrix}$$

where $X^T(\nu_i)$ contains the cross-spectrum at the frequency ν_i, from $\ell = 2$ to 100:

$$X^T(\nu_i) = (C^{\rm cr}_{\ell=2}(\nu_i) \ \cdots \ C^{\rm cr}_{\ell=100}(\nu_i))$$

The block matrix $\mathcal{M}$ is the covariance matrix, containing $n \times n$ blocks. Each one of them represents the covariance of two cross-spectra at different CIB frequencies, depending on the position of the block. At the ith line and jth column, the block $\mathcal{M}^{ij}$ is written as:

$$\mathcal{M}^{ij} = \begin{pmatrix} \mathcal{M}^{ij}_{\ell=2} & & 0 \\ & \ddots & \\ 0 & & \mathcal{M}^{ij}_{\ell=100} \end{pmatrix}$$

The diagonality of $\mathcal{M}^{ij}$ comes from the assumption that the different multipoles are uncorrelated; This could prove to be no longer true for small fraction of the sky but gives an upper bound on the S/N. In the noiseless case discussed in Section 2.3.3, the elements of each block can be expressed as follows:

$$\begin{aligned} \mathcal{M}^{ij}_\ell &= \mathrm{Covar}(\mathrm{C}^{\rm cr}_\ell(\nu_{\rm i}), \mathrm{C}^{\rm cr}_\ell(\nu_{\rm j})) \\ &= \frac{C^{\rm cr}_\ell(\nu_i) C^{\rm cr}_\ell(\nu_j) + C^{\rm CMB}_\ell C^{\rm crCIB}_\ell(\nu_i, \nu_j)}{2\ell + 1} \end{aligned}$$

We can see here the dependence on the aforementioned possible correlation between the CIB at frequency ν_i and the CIB at frequency ν_j, through the cross-spectrum $C^{\rm crCIB}_\ell(\nu_i, \nu_j)$. To perform a more advanced analysis, it is easy to modify this expression to account for the possible sources of noise discussed in the previous section.

Once again, the large number of possible combinations of noise parameters makes it unpractical to present a complete study of the joint correlation. Instead I focused on a few particular cases, motivated by my previous findings. A summary of my results on single and joint correlations is presented in Table 2.1. Going back first to the ideal case, I quantified the impact of the joint detection. I found a relatively small gain, as it increases the total S/N by a mere $\simeq 0.15$ compared to the maximum significance of a single detection. This can be attributed to the high correlations between the CIB at its different observed frequencies, which limits the usefulness of the joint cross-correlation.

Considering now more realistic situations, with the presence of instrumental noise, I choose to fix some of the free parameters, with $f_{\rm sky} = 0.75$ and $f_{\rm sky} = 0.15$. A reasonable confidence in component separation techniques allows us to hope for small enough residuals, so that we choose $f_{\rm CMB} = 0.01$ and $\mathcal{A}_{\rm fore.} = 0.01$. In these cases, the joint correlation has a limited interest (respectively a $\simeq 0.15$ and $\simeq 0.07$ gain for $f_{\rm sky} = 0.75$ and 0.15) due to the correlations in both the CIB signals but also in the astrophysical noise contributions – CMB and dust – between frequencies.

CIB Frequency (GHz)	**857**	**545**	**353**	**217**
CIB Wavelength (μm)	**350**	**550**	**850**	**1380**
Ideal case, single correlation S/N	6.26	6.83	6.98	6.95
Joint S/N	7.12			
Realistic case n°1, single correlation S/N ($f_{\rm sky} = 0.75$, $f_{\rm CMB} = 0.01$, $\mathcal{A}_{\rm fore.} = 0.01$)	5.36	5.73	5.39	3.56
Joint S/N	5.88			
Realistic case n°2, single correlation S/N ($f_{\rm sky} = 0.15$, $f_{\rm CMB} = 0.01$, $\mathcal{A}_{\rm fore.} = 0.01$)	2.40	2.56	2.41	1.59
Joint S/N	2.63			

TABLE 2.1: Total signal-to-noise ratio of the CIB-CMB cross-correlation for four of the CIB frequencies of *Planck*-HFI. The results are given for each frequency and for the joint cross-correlation, first for the ideal case discussed in Section 2.3.3.2 and then for two more realistic cases.

In the end, in the context of my model, the joint analysis of several CIB frequencies does not yield a significant improvement over the use of the best single frequency. This answers our interrogation from the end of the previous section: looking for the optimal frequency for the iSW detection is enough and justified here in order to focus the effort in the right direction (especially for the tricky part of the process: the CIB extraction). Nonetheless, the use of additional frequencies – if available – could have a non-negligible impact in the presence of a source of uncorrelated noise (between frequencies), as it would allow to get rid of most of it.

As a conclusion of this first ever investigation of the CIB-CMB cross-correlation, I found very promising results on the iSW effect and its detectability under various observational situations. Expected realistic significances range from ~ 2.5 to 5.5 depending on the frequency, the levels of noise and the fraction of the sky available for analysis: these show a great potential compared to even the most promising galaxy surveys (cf. Afshordi, 2004, Douspis et al., 2008). The results of this work will be valuable in the forthcoming years of analysis and exploitation of the *Planck* data. The formalism I developed provides an accurate and flexible forecast of the expected results of the CIB-CMB cross-correlation and allows to constrain the requirements for a significant iSW detection.

2.4 Related personal publications

• Ilić et al. (2011), "Cross-correlation between the cosmic microwave and infrared backgrounds for integrated Sachs-Wolfe detection", MNRAS, 416, 2688I (reproduced in the following pages)

• Ilic (2012), "Cosmic Microwave and Infrared Backgrounds cross-correlation for ISW detection", contribution to the proceedings of the International Conference on Gravitation and Cosmology, Goa, India, December, 2011

Monthly Notices of the ROYAL ASTRONOMICAL SOCIETY

Mon. Not. R. Astron. Soc. **416,** 2688–2696 (2011) doi:10.1111/j.1365-2966.2011.19221.x

Cross-correlation between the cosmic microwave and infrared backgrounds for integrated Sachs–Wolfe detection

Stéphane Ilić,⋆ Marian Douspis, Mathieu Langer, Aurélie Pénin and Guilaine Lagache

Institut d'Astrophysique Spatiale, UMR8617, Université Paris-Sud & CNRS, Bât. 121, Orsay F-91405, France

Accepted 2011 June 10. Received 2011 June 10; in original form 2011 May 6

ABSTRACT

We investigate the cross-correlation between the cosmic infrared background (CIB) and cosmic microwave background (CMB) anisotropies due to the integrated Sachs–Wolfe (ISW) effect. We first describe the CIB anisotropies using a linearly biased power spectrum, valid on the angular scales of interest. From this, we derive the theoretical angular power spectrum of the CMB–CIB cross-correlation for different instruments and frequencies. Our cross-spectra show similarities in shape with usual CMB–galaxies cross-correlations. We discuss the detectability of the ISW signal by performing a signal-to-noise ratio (S/N) analysis with our predicted spectra. Our results show that (i) in the ideal case of noiseless, full-sky maps, the significances obtained range from 6σ to 7σ depending on the frequency, with a maximum at 353 GHz, and (ii) in realistic cases which account for the presence of noise including astrophysical contaminants, the results depend strongly on the major contribution to the noise term. They span from 2σ to 5σ, the most favourable frequency for detection being 545 GHz. We also find that the joint use of all available frequencies in the cross-correlation does not improve significantly the total S/N, due to the high level of correlation of the CIB maps at different frequencies.

Key words: cosmic background radiation – cosmology: theory – dark energy – large-scale structure of Universe – infrared: diffuse background.

1 INTRODUCTION

The discovery of the acceleration of the expansion of the Universe, made through supernova observations (Riess et al. 1998; Perlmutter et al. 1999) at the end of the last century, has since led to many theories aimed at explaining its origin. These theories have been regrouped under the term 'dark energy' (DE), designating a new and unknown component of our Universe which theoretically amounts to 70 per cent of its total energy budget. Among the many solutions proposed to account for this intriguing phenomenon, one of the leading contenders is the so-called 'cosmological constant', an idea first introduced by Einstein in his original theory of general relativity to achieve a stationary universe, but which he discarded after the discovery of the Hubble redshift. This cosmological constant is assimilated to an intrinsic energy density of the vacuum, and therefore is constant in time and space; it also has an equation of state $w = p/\rho$ equal to -1, both on theoretical grounds and because no confirmed deviations from $w = -1$ have been detected so far. Despite its simplicity, it does reproduce most of the current observations while being (one of) the most 'economical' solution, but it is nevertheless plagued by a few serious theoretical problems (e.g. Padmanabhan 2003; Bass 2011).

⋆E-mail: stephane.ilic@ias.u-psud.fr

Apart from these theoretical issues, the accelerated expansion of the Universe still needs to be tested further in the framework of the Λ cold dark matter model by independent measurements from cosmological observations. Over the last decade, other possible probes have been proposed, such as the study of baryon acoustic oscillations (Eisenstein, Hu & Tegmark 1998; Eisenstein et al. 2005; Bassett & Hlozek 2010, and references therein), which provide a 'standard ruler' in cosmology and are heavily influenced by the energy content of the Universe and so by the DE.

In this article, we focus on an alternative probe of the DE, namely the study of the integrated Sachs–Wolfe (ISW) effect; the 'original' SW effect first introduced at the end of the 1960s (Sachs & Wolfe 1967) describes the imprint on the cosmic microwave background (CMB) of anisotropies caused by gravitational redshift occurring at the surface of last scattering. Its 'integrated' counterpart is similar in that it also has a gravitational origin and contributes to the CMB secondary anisotropies, but it only occurs in a Universe not dominated by matter. Indeed, the ISW effect is caused by the large-scale structures of the Universe, whose gravitational potentials are slowly decaying – instead of being constant in a matter-dominated regime – and therefore giving a net gain (in the case of a potential well) or loss (hill) of energy to the CMB photons that travel across them.

This effect shows in the power spectrum of the CMB temperature anisotropies at large angular scales (low ℓ), but the cosmic variance

at those very multipoles, together with the relatively small amplitude of the ISW effect, makes its direct detection very challenging, if not impossible, when using only the CMB itself. To circumvent this limitation, cosmologists have devised a way to exploit the link between this imprint on the CMB and the large-scale structures causing it, by simply cross-correlating the CMB with matter density maps (actually galaxy maps in practice) and then comparing the results to a null hypothesis and to what is expected from theory.

During the last decade or so, a growing interest has arisen in this field thanks to the development of large galaxy surveys: the Sloan Digital Sky Survey (SDSS; Abazajian et al. 2009, for the latest release), the NRAO VLA Sky Survey (NVSS; Condon et al. 1998), the Two Micron All Sky Survey (2MASS; Jarrett et al. 2000), etc. They allow cosmologists to cross-correlate the CMB as seen by the *Wilkinson Microwave Anisotropy Probe* (*WMAP*) to proxies of the matter density field as seen at many wavelengths: X-rays (Boughn & Crittenden 2004), optical (Granett, Neyrinck & Szapudi 2009), near-infrared (Rassat et al. 2007) or radio (Pietrobon, Balbi & Marinucci 2006). However, this method has yet to produce a definitive and conclusive detection of the ISW effect, with significances so far ranging from negligible (Sawangwit et al. 2010) to 4.5σ (Giannantonio et al. 2008) throughout the literature. The potential of future surveys such as the Large Synoptic Survey Telescope (LSST), the Panoramic Survey Telescope and Rapid Response System (Pan-STARRS) or *Euclid* have also been explored in terms of signal-to-noise ratio (S/N) of the ISW detection (Douspis et al. 2008). Another noteworthy approach by Taburet et al. (2011) considered the cross-correlation of the ISW effect with the thermal Sunyaev–Zel'dovich effect as both effects take place in the same potential wells; this could provide an independent probe for the existence of DE out of pure CMB data.

The originality of our work is to consider here the cosmic infrared background (CIB), first discovered by Puget et al. (1996). This background, visible roughly from 10 to 1000 μm in wavelength, arises from accumulated emissions from star-forming galaxies spanning a large range of redshifts. The earliest epoch for the production of this background is thought to be when star formation first began, and contributions to the CIB continued through the present epoch, including our current DE-dominated era. The CIB also features anisotropies (first detected and discussed by Lagache & Puget 2000 and Matsuhara et al. 2000) that are underlined by the galaxy density field and thus the matter density fluctuations. It is therefore reasonable to expect that it has a positive correlation with the CMB through the aforementioned ISW effect.

In this paper, we first present an analytical calculation of the CMB–CIB cross-correlation signal through the ISW effect. We then use it to compute the expected power spectrum of this correlation in different cases, namely with a CIB observed at several frequencies and with various instruments (*IRAS*, *Herschel*-SPIRE and *Planck*-HFI). With these results we perform a S/N analysis in order to quantify the detectability of the cross-correlation, focusing first on the 'perfect case' scenario, i.e. a situation where both the CMB and CIB are full-sky maps, without noise, so that the detection is only limited by the cosmic variance. We then discuss the effect of noise (including contaminating astrophysical components and instrumental noise) in the maps and its consequences on the S/N. Finally, we end with a few conclusions and discussions about the perspective of application of our predictions.

Throughout all our calculations, we assume a Euclidean universe corresponding to the *WMAP*7 best-fitting cosmology, with adiabatic scalar perturbations and a nearly scale invariant initial power spectrum.

2 MODELLING THE EXPECTED SIGNAL

2.1 CIB anisotropies

Ever since its discovery, many efforts have been deployed to detect the CIB with increasing precision, especially in order to study its anisotropies which contain a lot of information about the star and galaxy formation histories, including their clustering processes. The most recent papers on the CIB anisotropies use sophisticated models which compute the halo occupation distribution (HOD; see e.g. Peacock & Smith 2000; Cooray & Sheth 2002) and the dark matter halo properties, in order to predict the power spectrum of these anisotropies. Recently applied to the new *Planck* data (see *Planck* Collaboration 2011b), this framework allowed us to confirm that the bias between infrared galaxies and the linear theory matter power spectrum is not independent of scale and that the HOD is evolving with redshift.

Such models are particularly useful when describing the small, non-linear scales of the CIB. Since we focus here on the ISW effect which only concerns much larger scales, we can use a simpler model for the CIB, similar to the description made by Knox et al. (2001). The general definition of the CIB anisotropies at a given frequency ν and in a given direction $\hat{\boldsymbol{n}}$ can be then written as the following line-of-sight integral:

$$\delta T_{\rm CIB}(\hat{\boldsymbol{n}}, \nu) = \int_{\eta_{\rm far}}^{\eta_0} {\rm d}z \frac{{\rm d}\eta}{{\rm d}z} a(z) \delta j((\eta_0 - \eta)\hat{\boldsymbol{n}}, \nu, z), \tag{1}$$

with δj being the emissivity fluctuations of the CIB. The integration is made over η, the conformal time, from some initial time $\eta_{\rm far}$ before star formation began to our location at the coordinate origin η_0. In their work, Knox et al. hypothesized that the CIB anisotropies are direct tracers of the matter density fluctuations $\delta = \delta\rho_{\rm m}/\bar{\rho}_{\rm m}$, up to a bias factor. Therefore, the previous expression becomes an integral of the product between a mean far-infrared (FIR) emissivity and the matter density fluctuation field:

$$\delta T_{\rm CIB}(\hat{\boldsymbol{n}}, \nu) = \int_{\eta_{\rm far}}^{\eta_0} {\rm d}z \frac{{\rm d}\eta}{{\rm d}z} a(z) b_j(\nu, z) \bar{j}(\nu, z) \delta((\eta_0 - \eta)\hat{\boldsymbol{n}}, z). \tag{2}$$

The quantity $b_j(\nu, z)$ is a frequency- and redshift-dependent matter-emissivity bias defined by

$$\frac{\delta j((\eta_0 - \eta)\hat{\boldsymbol{n}}, \nu, z)}{\bar{j}(\nu, z)} = b_j(\nu, z)\, \delta((\eta_0 - \eta)\hat{\boldsymbol{n}}, z), \tag{3}$$

and $\bar{j}(\nu, z)$ is the mean emissivity per comoving unit volume at frequency ν as a function of redshift z, which is derived here using the empirical, parametric model of Béthermin et al. (2011). The matter density field δ is described in our analysis by a linear power spectrum. While this approximation is not accurate at small scales where non-linearities arise, it is perfectly valid for the scales of interest in our work since the first hundred multipoles ($\ell < 100$) comprise most of the ISW signal. Following a calculation similar to the one described in the next section, we can express the angular power spectrum of the CIB fluctuations as follows:

$$C_\ell^{\rm CIB}(\nu) = 4\pi \frac{9}{25} \int \frac{{\rm d}k}{k} \Delta^2_{\mathcal{R}} M_\ell^2(k, \nu), \tag{4}$$

where $M_\ell(k, \nu)$ is given in equation (10) and $\Delta^2_{\mathcal{R}}$ is defined below in equation (8).

Lastly, we choose the previously mentioned linear bias[1] $b_j(\nu, z)$ to be constant in redshift: $b_j(\nu, z) = b_{\rm lin}(\nu)$. To obtain

[1] This bias here represents our matter-emissivity bias in equation (3) and should not be confused with the widely used galaxy-dark matter bias, though

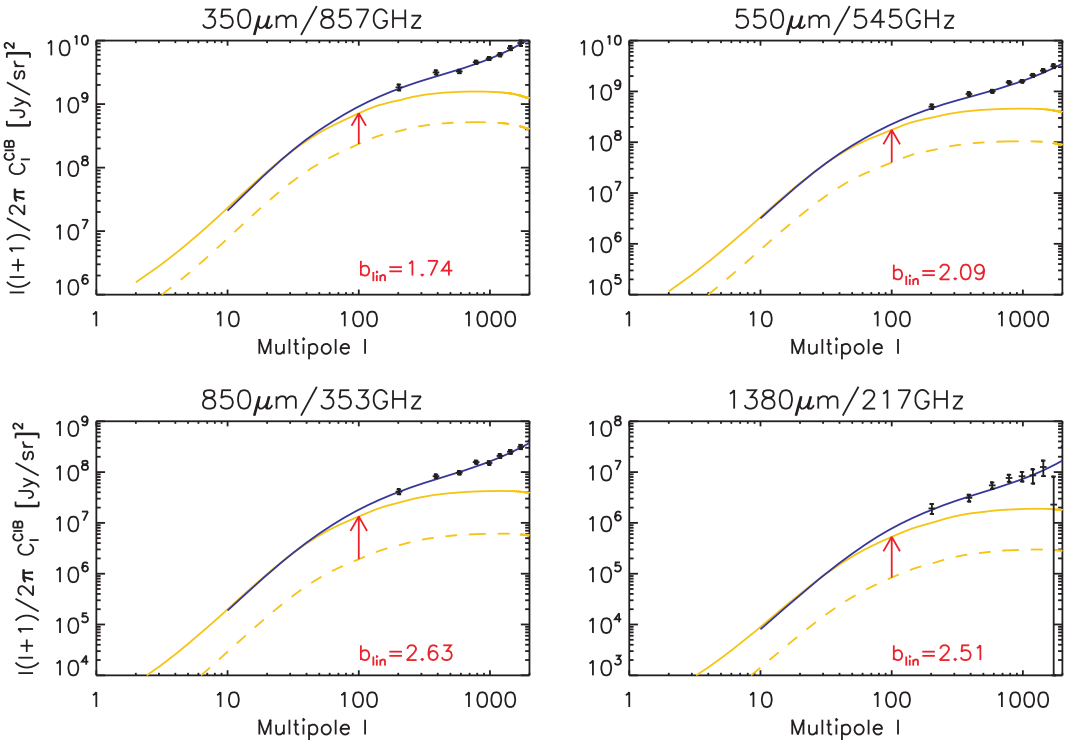

Figure 1. Angular power spectra of the CIB fluctuations at four frequencies of the *Planck*-HFI instrument, as predicted by the *Planck* Team (blue continuous line) and by our non-biased models (dashed yellow line). For each frequency, we provide in red the linear bias which gives the best agreement between the two models, and plot our models taking into account this bias (solid yellow line). The data points correspond to measurements obtained by the *Planck* Team (*Planck* Collaboration 2011b).

it at each frequency, we compute the value of $b_{\rm lin}$ that gives the best agreement between our linear CIB power spectrum and those obtained from the *Planck* data (*Planck* Collaboration 2011b). We choose to fit the two spectra in the range of multipoles $\ell \in [10, 50]$, where most of the ISW signal resides. This is illustrated in Fig. 1 where we plot the biased and non-biased CIB linear spectra from our framework and compare them to the ones from the *Planck* Collaboration (2011b) at their four frequencies. Overall, the two sets of spectra show good agreement over the multipoles of interest; the spectra deviate at higher ℓ (starting from $\simeq 100$) due to the rise of non-linearities that we did not account for in our linear model – namely the small-scale correlations between galaxies inside the same haloes. The linear bias we obtain this way increases with the wavelength: this is coherent with the fact that as we go further deep into the infrared, the galaxies probed are more luminous at higher z. They reside in more massive and rarer haloes and are therefore more biased.

2.2 Correlation with the ISW

In the CMB anisotropies, the temperature contribution due to the ISW effect is an integral over the conformal time of the growth rate of the gravitational potentials:

$$\delta T_{\rm ISW}(\hat{\boldsymbol{n}}) = \int_{\eta_{\rm r}}^{\eta_0} {\rm d}\eta\, {\rm e}^{-\tau(\eta)}\, (\dot{\Phi} - \dot{\Psi})[(\eta_0 - \eta)\hat{\boldsymbol{n}}, \eta], \tag{5}$$

where $\eta_{\rm r}$ is some initial time deep in the radiation era, Φ and Ψ are the Newtonian gauge gravitational potentials (with the conventions used in Kodama & Sasaki 1984), $\tau(\eta)$ is the optical depth included to account for the possibility of late re-ionization and the dot denotes differentiation with respect to η.

We are interested in calculating the CIB–ISW cross-correlation function $C^{\rm cr}$ at a given frequency ν in direct space:

$$C^{\rm cr}(\theta_{\hat{\boldsymbol{n}}_1,\hat{\boldsymbol{n}}_2}, \nu) \equiv \langle \delta T_{\rm CIB}(\hat{\boldsymbol{n}}_1, \nu) \delta T_{\rm ISW}(\hat{\boldsymbol{n}}_2) \rangle. \tag{6}$$

After a decomposition into Legendre series, we get

$$C^{\rm cr}(\theta, \nu) = \sum_{l=2}^{\infty} \frac{2\ell + 1}{4\pi} C_\ell^{\rm cr}(\nu) P_\ell(\cos\theta), \tag{7}$$

where we do not include the monopole and dipole terms in the sum. Using equations (2) and (5), we follow a calculation similar to Garriga, Pogosian & Vachaspati (2004) in order to finally get the CMB–CIB cross-power spectrum at a frequency ν:

$$C_\ell^{\rm cr}(\nu) = 4\pi \frac{9}{25} \int \frac{{\rm d}k}{k} \Delta^2_{\mathcal{R}} T_\ell^{\rm ISW}(k) M_\ell(k, \nu), \tag{8}$$

where $\Delta^2_{\mathcal{R}}$ comes from the primordial curvature power spectrum $P_{\mathcal{R}} \equiv 2\pi^2 \Delta^2_{\mathcal{R}} / k^3$. The use of this primordial spectrum differs from previous works on CMB–galaxies cross-correlation, where the present matter power spectrum is usually introduced instead, and is then evolved backwards in order to find its correlation with the CMB. Conversely, in the Garriga et al. approach, the starting point is the primordial perturbations which are evolved to the present time. While it allows a full account of possible fluctuations in the DE in non-Λ models, it also avoids the frequently used Limber approximation, which is known to be somewhat inaccurate at the largest scales considered here.

ours *does* contain information about how the emitting objects populate dark matter haloes.

At this point, we need to compute the two main functions $T_\ell^{\rm ISW}$ and M_ℓ, which are defined as

$$T_\ell^{\rm ISW}(k) = \int_{\eta_0}^{\eta_{\rm r}} {\rm d}\eta\, {\rm e}^{-\tau(\eta)}\; j_\ell(k[\eta-\eta_0])\,(c_{\Psi\Phi}\dot{\psi} - \dot{\phi}) \qquad (9)$$

and

$$M_\ell(k,\nu) = c_{\delta\Psi}\int_{\eta_0}^{\eta_{\rm r}} {\rm d}\eta\; j_\ell(k[\eta-\eta_0])a(\eta)b_{\rm lin}(\nu)\bar{j}(\nu,\eta)\tilde{\delta}(k,\eta), \qquad (10)$$

where $j_\ell(\cdot)$ are the spherical Bessel functions, while $\tilde{\delta}$, ϕ and ψ are the time-dependent[2] parts of (respectively) the dark matter density contrast δ and the two Newtonian gravitational potentials Φ and Ψ. The two coefficients $c_{\Psi\Phi}$ and $c_{\delta\Psi}$ give the relations between δ, Φ and Ψ for adiabatic initial conditions:

$$c_{\delta\Psi} \equiv \frac{\delta}{\Psi} = -\frac{3}{2}, \qquad c_{\Psi\Phi} \equiv \frac{\Psi}{\Phi} = -\left(1+\frac{2}{5}R_\nu\right), \qquad (11)$$

where $R_\nu \equiv \rho_\nu/(\rho_\nu+\rho_\gamma)$, ρ_ν and ρ_γ being, respectively, the energy densities in relativistic neutrinos and photons.

2.3 Shape of the cross-correlation spectrum

To compute these expressions, we adapted for our analysis an already modified version of CMBFAST (Seljak & Zaldarriaga 1996), named CROSS_CMBFAST (Corasaniti, Giannantonio & Melchiorri 2005). For a given cosmology and emissivity function $\bar{j}(\nu,z)$ (see equations 2 and 3), our code calculates the $C_\ell^{\rm cr}$ from equation (8) and at the same time the predicted power spectrum of the CIB fluctuations described in equation (4) and already illustrated in Fig. 1. It also gives the standard CMBFAST outputs, including the CMB temperature power spectrum.

In Fig. 2, we present our predictions for the CIB–CMB cross-correlation, at several FIR wavelengths and for different instruments, namely *IRAS* at 100 μm, *Herschel*-SPIRE at 250, 350 and 500 μm and *Planck*-HFI at 350, 550, 850, 1380 and 2097 μm. We note that at 350 μm, the SPIRE- and *Planck*-predicted spectra differ slightly from each other, due to the difference in wavelength bandwidth of the two instruments.

In a fashion similar to previous galaxy–ISW cross-correlations (see the references in Section 1), we note that the cross-correlation peaks around $\ell \simeq 10$–30, and quickly vanishes at higher multipoles. Comparing the signal at the different wavelengths shows that the amplitude of the cross-correlation signal is maximum at a wavelength $\simeq$250 μm. This is not entirely surprising, since this wavelength roughly corresponds to the maximum of the observed CIB spectral energy distribution (SED; Dole et al. see 2006, for reference).

It should be also noted that these results are not exact at the highest ℓ values since the non-linear counterpart to the ISW effect, called the Rees–Sciama effect, contributes at those scales (see Schaefer, Kalovidouris & Heisenberg 2011, for a discussion). However, in our case the linear part of the ISW largely dominates at the observed peak in Fig. 2.

3 SIGNAL-TO-NOISE RATIO ANALYSIS

3.1 Ideal case

We now investigate the detection level of the ISW effect using CMB–CIB cross-correlation by performing a S/N analysis. Using the power spectra computed in the previous section, we can write for each given frequency ν the total S/N of the ISW detection as

$$\left[\frac{S}{N}\right]^2(\nu) = \sum_{\ell=2}^{\ell_{\rm max}}(2\ell+1)\frac{[C_\ell^{\rm cr}(\nu)]^2}{\left[C_\ell^{\rm cr}(\nu)\right]^2 + C_\ell^{\rm CIB}(\nu)\times C_\ell^{\rm CMB}}, \qquad (12)$$

where the total (or cumulative) S/N is summed over multipoles between $\ell = 2$ and $\ell_{\rm max} \leqslant 100$ where the signal has its major contribution (see previous section, Fig. 2).

In this section, we first consider the ideal situation where the CIB and CMB maps used for cross-correlation are noiseless and cover the whole sky; with these assumptions we obtain the highest possible S/N, the only limitation being the cosmic variance. In Fig. 3 we present our prediction for the CIB–CMB cross-correlation in the case of a full-sky CIB map provided[3] by the previously mentioned instruments and frequencies.

With these optimistic assumptions, we obtain high levels of detection for the CIB–CMB correlation which reach $\simeq 7\sigma$ (for detailed results, see Table 1). It should be mentioned that these results in the ideal case are independent of the previously discussed linear bias in Section 2.1 even if it boosts the correlation signal. This can be understood from equation (12) where the linear bias can be factorized from each term (one for $C_\ell^{\rm cr}$ and a squared one for $C_\ell^{\rm CIB}$) and therefore cancels out.

As evoked in Section 2.3, we see that the largest contribution to the S/N comes from multipoles lower than $\simeq$50. On the other hand, the most interesting feature of these results is that contrary to what could be intuited from Fig. 2, the total S/N peaks around 850 μm instead of 250 μm for the cross-correlation signal itself. The reason for this is actually quite subtle: it comes from the shape of the 'noise' term in the S/N expression in equation (12), as a function of ℓ, namely

$$[N_\ell]^2(\nu) \equiv \left(\left[C_\ell^{\rm cr}(\nu)\right]^2 + C_\ell^{\rm CIB}(\nu)C_\ell^{\rm CMB}\right)\Big/(2\ell+1).$$

For all the frequencies studied here, this 'noise' has roughly the same amplitude *relative* to its corresponding 'signal':

$$[S_\ell]^2(\nu) \equiv [C_\ell^{\rm cr}(\nu)]^2.$$

This is illustrated in Fig. 4, where we plotted in the left-hand panel all the $[S_\nu]^2$ terms with their respective maximum rescaled to unity. In the middle panel, we apply the same rescaling factor of each $[S_\nu]^2$ term to the corresponding $[N_\nu]^2$ term. By doing this, we can compare all frequencies without changing their associated S/N. On the resulting graph, we see that at $\ell = 100$ the rescaled noise amplitude is roughly the same, while the signal has the same shape at all frequencies, except for a small shift in ℓ. However, there is a major difference in the shape of the noise power spectrum from one frequency to another: its slope changes depending on the frequency, with the steepest one for *Planck* 850 μm. Therefore, its amplitude goes down more quickly than the others as ℓ approaches zero where

[2] The separation between time and space dependence in the terms δ, Φ and Ψ is allowed in our calculation since the time evolution of each Fourier mode only depends on the magnitude $k = ||\boldsymbol{k}||$. For example $\Phi(\boldsymbol{k},\eta) = \Phi(\boldsymbol{k},\eta_{\rm r})\phi(k,\eta)$.

[3] Only the *IRAS* 100-μm data are already available, and previous works have managed to extract the CIB component on small patches of sky (Miville-Deschênes, Lagache & Puget 2002), but the CIB has yet to be extracted over a large enough part to allow for an ISW detection.

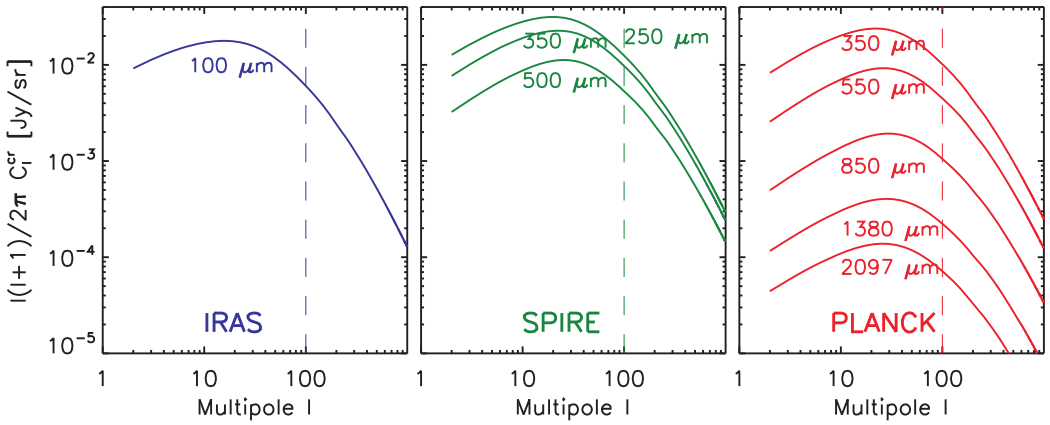

Figure 2. Theoretical angular cross-power spectrum of the CIB–CMB correlation calculated for *IRAS* at 100 μm (left-hand panel), for *Herschel*-SPIRE between 250 and 500 μm (central panel) and *Planck*-HFI between 350 and 2097 μm (right-hand panel). The linear bias, $b_{\rm lin}$, is fixed here to 1 at all frequencies in order to compare the non-biased CIB power spectra. The vertical dashed line on each panel marks the upper limit of the multipoles used in our analysis: this choice comes from the absence of ISW signal (see Fig. 3) and the rise of non-linearities at higher ℓ.

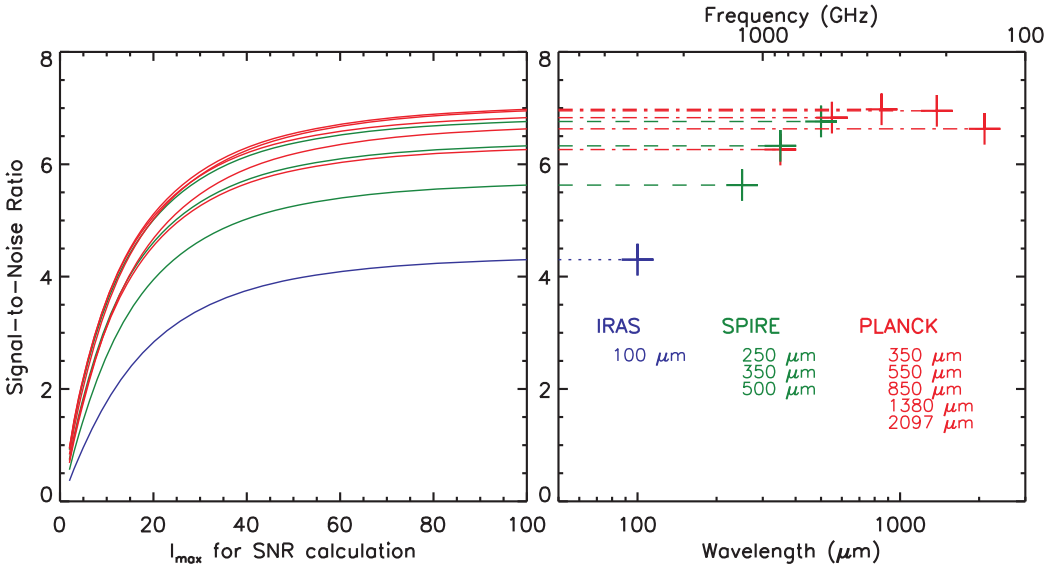

Figure 3. Left-hand panel: cumulated S/N as a function of $\ell_{\rm max}$ (defined in equation 12) for the CMB–CIB cross-correlation, at our chosen frequencies and instruments. Right-hand panel: total S/N with $\ell_{\rm max} = 100$ as a function of frequency/wavelength.

Table 1. Total S/N of the CIB–CMB cross-correlation for four of the CIB frequencies of *Planck*-HFI. The results are given for each frequency and for the joint cross-correlation, first for the ideal case discussed in Section 3.1 and then for two more realistic cases.

Frequency (GHz)	**857**	**545**	**353**	**217**
Wavelength (μm)	**350**	**550**	**850**	**1380**
Perfect single S/N	6.26	6.83	6.98	6.95
Joint S/N		7.12		
Realistic single S/N 1				
($f_{\rm sky} = 0.75, f_{\rm CMB} = 0.01, \mathcal{A}_{\rm fore.} = 0.01$)	5.36	5.73	5.39	3.56
Joint S/N		5.88		
Realistic single S/N 2				
($f_{\rm sky} = 0.15, f_{\rm CMB} = 0.01, \mathcal{A}_{\rm fore.} = 0.01$)	2.40	2.56	2.41	1.59
Joint S/N		2.63		

coincidentally the signal is strong, which then boosts the S/N at the low multipoles, and the total S/N.

In light of these results, the optimal frequency for ISW detection appears to be around 353 GHz/850 μm, with a maximum S/N reaching 7σ. However, in practice, the CIB extraction at this frequency might prove challenging since the CMB becomes dominant here, and increasingly so as we go down in frequency. Therefore, the possible residuals in our extracted CIB map have to be accounted for, and other sources of noise as well, which is the purpose of the next subsection.

3.2 More realistic S/N

We now carry a more realistic study by including several possible sources of contamination: first the signal is completely dominated on a large part of the sky by emissions from our own Galaxy. The contamination from this foreground in the Galactic plane is several orders of magnitude above the CIB level and prevents us from extracting the CIB, therefore reducing the 'usable' fraction of the sky by at least ∼25 per cent. Furthermore, the rest of the sky is also quite polluted – from a CIB point of view – by these foregrounds full of galactic dust. These will have to be removed from our maps although some residuals might remain in the final CIB map used

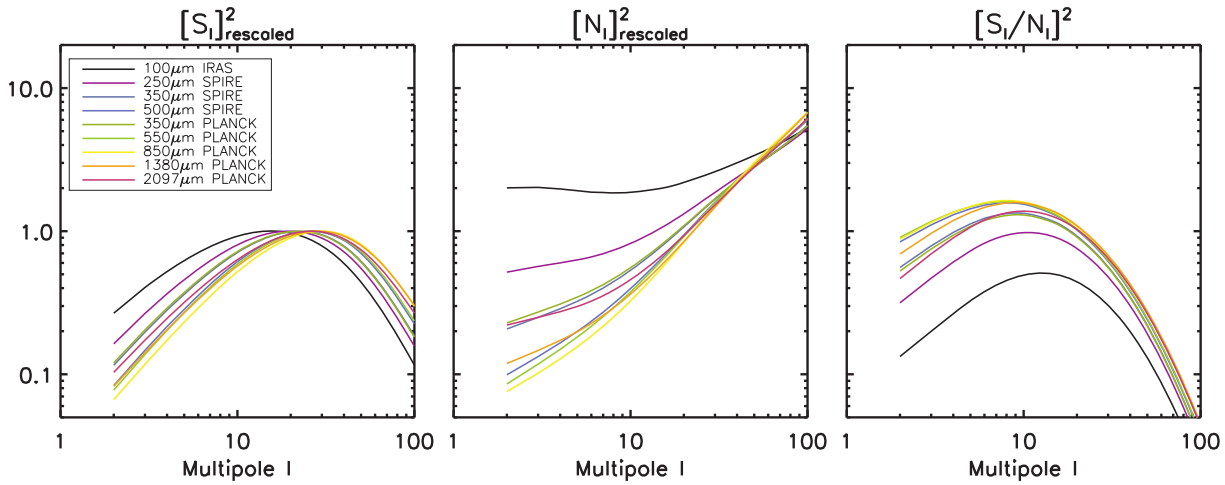

Figure 4. 'Signal' terms (left-hand panel, rescaled to unity) and 'noise' terms (middle panel, same rescale factor as the 'signal') of the S/N as functions of ℓ (see text for details) for our chosen frequencies and instruments. The quotient of the two terms, used in the calculation of the S/N itself, is shown in the right-hand panel: the main difference throughout the frequencies comes from the shape of the 'noise' term.

for the cross-correlation. There may even be a significant CMB residual in this map, due to an imperfect separation of components. Consequently, we need to assess the impact of these contaminants in our study.

To account for these effects on the detectability of the CIB–CMB cross-correlation, we use in the present section a more realistic formulation of the S/N by adding new elements in the noise term. It therefore becomes at a given frequency ν

$$\left[\frac{S}{N}\right]^2(\nu) = f_{\rm sky}\sum_{\ell=2}^{\ell_{\rm max}}(2\ell+1) \times \frac{\left[C_\ell^{\rm cr}(\nu)\right]^2}{\left[C_\ell^{\rm cr}(\nu)+N_\ell^{\rm cr}(\nu)\right]^2+\left[C_\ell^{\rm CIB}(\nu)+N_\ell^{\rm CIB}(\nu)\right]\left[C_\ell^{\rm CMB}+N_\ell^{\rm CMB}\right]}, \quad (13)$$

where $f_{\rm sky}$ is the fraction of the sky common to the CMB and the CIB maps, and $N_\ell^{\rm cr}$, $N_\ell^{\rm CIB}$ and $N_\ell^{\rm CMB}$ are the noise contributions, respectively, in the cross-, CIB and CMB signal. Since the CMB is expected to be only variance limited at the multipoles of interest, we take here $N_\ell^{\rm CMB}=0$. However, we still have to take into account the CIB contamination.

To do so, we first break the CIB noise power spectrum into several independent parts:

$$N_\ell^{\rm CIB}(\nu) = R_\ell^{\rm CMB}(\nu) + R_\ell^{\rm fore.}(\nu) + N_\ell^{\rm instr.}(\nu) + N_\ell^{\rm correl.}(\nu),$$

where these four different terms represent, from left to right, the power spectra of the CMB residual, the galactic foreground residuals, the instrumental noise and finally the noise due to correlation between residuals and the CIB (which appears when autocorrelating the final CIB map).

We quantify the CMB residual in the CIB map as a fraction, $f_{\rm CMB}$, of the total CMB map, which affects both the cross-correlation and CIB noise. This consequently defines the noise in the cross-signal,

$$N_\ell^{\rm cr}(\nu) = f_{\rm CMB}(\nu)\times C_\ell^{\rm CMB},$$

and the following two contributions:

$$R_\ell^{\rm CMB}(\nu) = f_{\rm CMB}^2(\nu)\times C_\ell^{\rm CMB,}$$
$$N_\ell^{\rm correl.}(\nu) = 2f_{\rm CMB}(\nu)\times C_\ell^{\rm cr}(\nu).$$

We then define the spectrum of the foreground residuals as the following power law:

$$R_\ell^{\rm fore.}(\nu) = \mathcal{A}_{\rm fore.}(\nu)\times C_{\ell=10}^{\rm CIB}(\nu)\left(\frac{\ell}{10}\right)^\alpha,$$

so that their amplitudes are defined relative to the real CIB signal through a chosen constant $\mathcal{A}_{\rm fore.}$, which defines the quantity

$$\mathcal{A}_{\rm fore.}(\nu) = R_{\ell=10}^{\rm fore.}(\nu)/C_{\ell=10}^{\rm CIB}(\nu),$$

i.e. the ratio between the foreground residuals and the CIB spectrum at the multipole $\ell=10$, approximately where the cross-signal is at its maximum. The slope of the spectrum α is fixed here for all frequencies; previous analysis of infrared maps (Wright 1998; Miville-Deschênes et al. 2007) found it to be $\simeq -3$ for foregrounds at high galactic latitudes. Finally, the instrumental noise power spectra, $N_\ell^{\rm instr.}$, at each frequency are taken from the first 10 months of *Planck* data in the *Planck* Collaboration (2011a), and extrapolated to the 30 months, i.e. the end of the fourth *Planck* full-sky survey.

In this section, we focus on four of the five previously described *Planck*-HFI frequencies, from 217 to 857 GHz: we discard the fifth, 143 GHz, as the CMB completely dominates the CIB signal there. We also put aside the *IRAS* frequency here because of its weaker significance, and the SPIRE frequencies since the instrument is not scheduled to ever cover very large regions of the sky (i.e. $f_{\rm sky}\ll 1$), dramatically decreasing the realistic S/N (see equation 13).

At this point, we get three free parameters at each of the four frequencies in our S/N analysis: $f_{\rm sky}, f_{\rm CMB}$ and $\mathcal{A}_{\rm fore.}$. The next step would be to explore this 3D parameter space at each frequency and compute the S/N at each point. Considering the very large number of possible combinations of parameters, it would not be practical to display the complete results of this exploration here. Therefore, we first choose to fix $f_{\rm sky}$ to two values of interest.

(i) $f_{\rm sky}=0.75$, which corresponds to an optimistic case where the only part of the sky that we discard is the Galactic plane; unfortunately, there are other highly contaminated regions where the component separation techniques might not be able to extract the CIB.

(ii) $f_{\rm sky}=0.15$, which is a low estimate of the area of the sky where the current data allow for an efficient CIB extraction. The methods currently employed are based on the use of H I maps as a

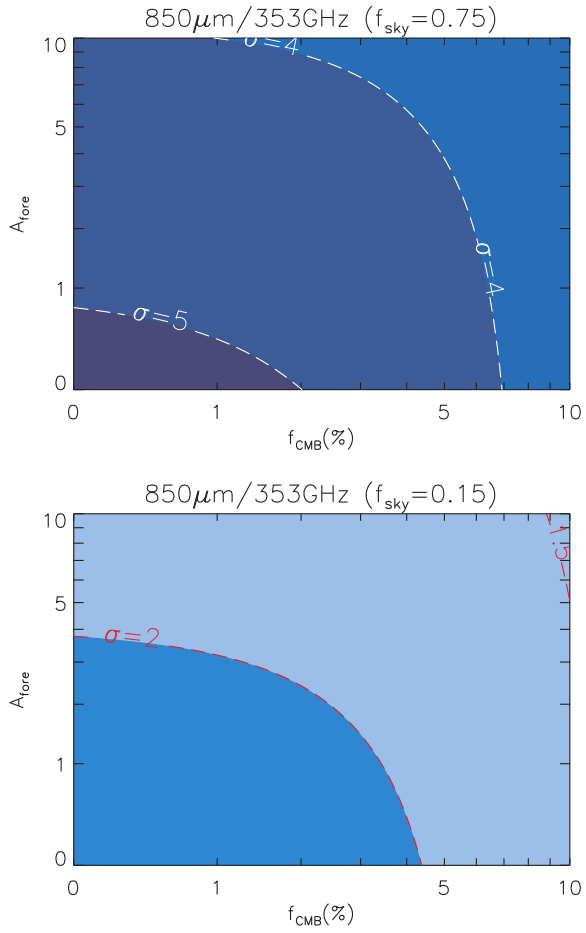

Figure 5. Total S/N of the CIB–CMB cross-correlation at 353 GHz, as a function of the CMB residuals (in percentage of the total CMB signal) and the foreground residuals (through the parameter $\mathcal{A}_{\rm fore.}$). Upper panel: $f_{\rm sky}$ = 0.75, the results go from less than 4 to more than 5, from the brightest coloured area to the darkest. Lower panel: $f_{\rm sky}$ = 0.15, the S/N goes from slightly less than 1.5 to more than 2, again from the brightest to the darkest area.

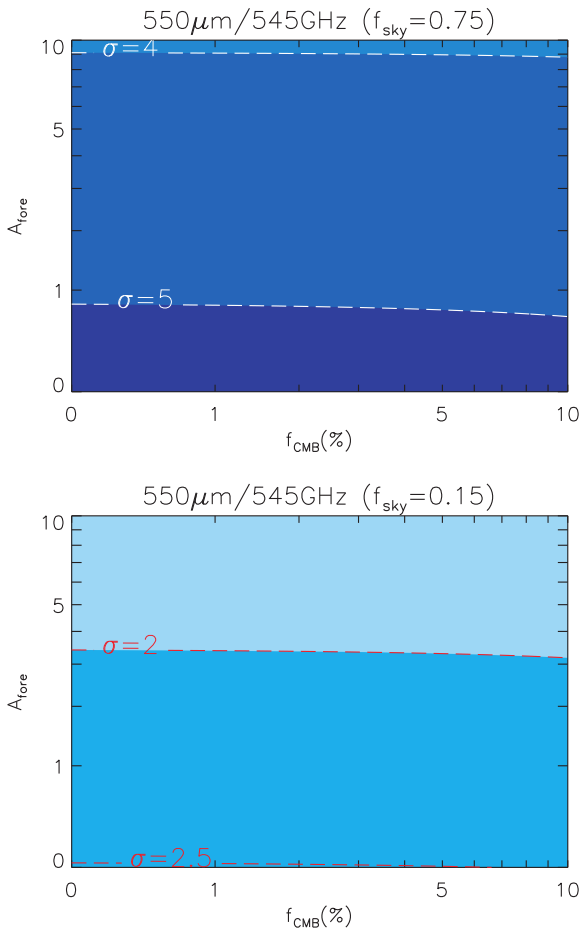

Figure 6. Total S/N of the CIB–CMB cross-correlation at 545 GHz as a function of the CMB residuals and the foreground residuals. Upper panel: $f_{\rm sky}$ = 0.75, the results go from slightly less than 4 to more than 5, from the brightest to the darkest area. Lower panel: $f_{\rm sky}$ = 0.15, the S/N goes from less than 2 to slightly more than 2.5.

tracer of the galactic dust, though it only remains valid for an H I column density lower than a specific threshold (see *Planck* Collaboration 2011b, for details on these methods).

Concerning our other two parameters we limit ourselves to reasonable values, with $f_{\rm CMB} \in [0, 0.1]$ and $\mathcal{A}_{\rm fore.} \in [0, 10]$.

We then focus on the frequency that gave the best S/N results in the ideal case, namely 850 μm/353 GHz, and study the effect of the noise on the cross-correlation detectability. The results are presented in Fig. 5 which shows the contour levels of the S/N in the ($f_{\rm CMB}$, $\mathcal{A}_{\rm fore.}$) parameter space. The influence of the CMB is clearly visible at this frequency, quickly reducing the S/N as its residual level increases. This effect is even more pronounced at 1380 μm/217 GHz, where the S/N is typically twice as low as in the ideal case (see Table 1), due to the fact that we get closer to the maximum of the SED of the CMB. It makes this frequency far less significant for the ISW detection than in the ideal case. The presence of instrumental noise – whose effect cannot be appreciated with Fig. 5 alone – becomes significant at the two lowest frequencies (217 and 353 GHz), again reducing their value in the cross-correlation. As expected, the galactic foreground residuals also decrease the S/N, though their influence is roughly the same at all frequencies as they are defined relative to the CIB spectrum in our analysis. Lastly, the biggest influence comes from the fraction of the sky through the $f_{\rm sky}$ parameter, as the total S/N scales as $\sqrt{f_{\rm sky}}$. This makes it a crucial requirement for future applications to have the largest possible coverage to minimize this effect.

Taking all these remarks into account and after some exploration of the parameter space, the optimal frequency that stands out in these more realistic scenarios is 545 GHz/550 μm. Indeed, it is weakly influenced by instrumental noise and CMB residuals and also has a higher 'original' S/N (in the ideal case) than the other remaining frequency 857 GHz/350 μm. Our analysis at 545 GHz is presented in Fig. 6.

3.3 Joint S/N

Until now we have only considered a detection at a single CIB frequency and its associated significance. In practice, we will have several cross-spectra at different frequencies, e.g. in the case of *Planck* where we will be able to extract the CIB at four different frequencies on a large fraction of the sky. This allows us to increase the total S/N of the ISW detection by combining the constraints from all available frequencies, though this will be limited by the possible intrinsic correlations between the CIB maps at different frequencies. Indeed, such correlations imply some redundancy in

the measured information, and therefore lessen the gain in the total significance of the combined detection.

We can expand the previous S/N formalism to express the theoretical joint significance of a set of n cross-correlations (i.e. CIB at n frequencies, each correlated to the same CMB):

$$\left(\frac{S}{N}\right)^2_{\rm Total} = X^{\rm T}\mathcal{M}^{-1}X, \tag{14}$$

with X ($X^{\rm T}$) being the column (row) vector of all the cross-correlations:

$$X^{\rm T} = \left(X^{\rm T}(\nu_1)\ \cdots\ X^{\rm T}(\nu_n)\right),$$

where $X^{\rm T}(\nu_i)$ contains the cross-spectrum at the frequency ν_i, from $\ell = 2$ to 100:

$$X^{\rm T}(\nu_i) = \left(C^{\rm cr}_{\ell=2}(\nu_i)\ \cdots\ C^{\rm cr}_{\ell=100}(\nu_i)\right).$$

The block matrix $\mathcal{M}$ is the covariance matrix, containing $n \times n$ blocks. Each one of them represents the covariance of two cross-spectra at different CIB frequencies, depending on the position of the block. At the ith line and jth column, the block $\mathcal{M}^{ij}$ is written as

$$\mathcal{M}^{ij} = \begin{pmatrix} \mathcal{M}^{ij}_{\ell=2} & & 0 \\ & \ddots & \\ 0 & & \mathcal{M}^{ij}_{\ell=100} \end{pmatrix}.$$

The diagonality of $\mathcal{M}^{ij}$ comes from the assumption that the different multipoles are uncorrelated. In the noiseless case discussed in Section 3.1, the elements of each block can be expressed as follows:

$$\begin{aligned}\mathcal{M}^{ij}_\ell &= {\rm Covar}\left(C^{\rm cr}_\ell(\nu_i), C^{\rm cr}_\ell(\nu_j)\right) \\ &= \frac{C^{\rm cr}_\ell(\nu_i)C^{\rm cr}_\ell(\nu_j) + C^{\rm CMB}_\ell C^{\rm crCIB}_\ell(\nu_i, \nu_j)}{2\ell+1}.\end{aligned}$$

We can see here the dependence on the aforementioned possible correlation between the CIB at frequency ν_i and the CIB at frequency ν_j, through the cross-spectrum $C^{\rm crCIB}_\ell(\nu_i, \nu_j)$. To perform a more advanced analysis, we can easily modify this expression to account for the possible sources of noise discussed in the previous section.

Once again, the large number of possible combinations of noise parameters makes it unpractical to present a complete study of the joint correlation. Instead, we focus on a few particular cases, motivated by what we found in Section 3.2. A summary of our results on single and joint correlations is presented in Table 1: we first go back to the ideal case to quantify the impact of the joint detection. We found a relatively small gain, as it increases the total S/N by a mere $\simeq 0.15$ compared to the maximum significance of a single detection. This can be attributed to the high correlations between the CIB at its different observed frequencies, which limit the usefulness of the joint cross-correlation.

Considering now more realistic situations, with the presence of instrumental noise, we once again choose to fix some of the parameters mentioned in Section 3.2, with $f_{\rm sky} = 0.75$ and 0.15. A reasonable confidence in component separation techniques allows us to hope for small enough residuals, so that we choose $f_{\rm CMB} = 0.01$ and $\mathcal{A}_{\rm fore.} = 0.01$. In these cases, the joint correlation has once again a limited interest (respectively, a $\simeq 0.15$ and $\simeq 0.07$ gain for $f_{\rm sky} = 0.75$ and 0.15) due to the correlations not only in both the CIB signals, but also in the astrophysical noise contributions – CMB and dust – between frequencies.

4 CONCLUSIONS

The topic of this paper is an investigation of the cross-correlation between the cosmological infrared and microwave backgrounds, and a study of its detectability under various observational situations. A non-zero correlation is expected to exist between the two backgrounds and their anisotropies through the ISW effect, caused by the time-evolving gravitational potentials that underlie the large-scale structures which are the sources of the CIB and of its anisotropies. Describing the CIB anisotropies as linearly biased tracers of the matter field fluctuations, we calculated the theoretical angular power spectrum of the CMB–CIB cross-correlation at several frequencies and for different instruments, taking into account their actual bandpasses. As is well known for CMB–galaxies cross-correlations, the signal peaks at low multipoles and quickly vanishes at higher ℓ. The linear bias introduced by our formalism was then obtained by confronting our predicted linear CIB power spectra with the data coming from the *Planck* mission. These observed CIB anisotropies were fitted by the *Planck* Collaboration (2011b) by an HOD model, to which we compared our own spectra at the low multipoles in order to get the desired bias at each different frequency.

Using an advanced S/N analysis which included the main sources of noise, both instrumental and astrophysical, and all their possible correlations, we pointed out the most promising frequency in the ideal case of noiseless full-sky maps (850 μm/353 GHz) with an expected significance as high as $\simeq 7\sigma$ for the cross-correlation signal. The same frequency turned out to be less optimal with more realistic assumptions about sky coverage and possible sources of noise (here CMB, dust residuals and instrumental noise). In this case, higher frequencies such as *Planck*-HFI's 545 and 857 GHz are favoured, with an expected significance ranging from 2.4 to 5.7 depending on the frequency, the levels of noise and the fraction of the sky available for analysis. We also found that a joint cross-correlation using all available frequencies is of minor interest, due to the high correlations between CIB anisotropies at the different frequencies. Nevertheless, our best results for $f_{\rm sky} = 0.75$ are higher than the significances of all current CMB–galaxies cross-correlation, with $\sigma > 5$, although a less optimistic estimate for the sky coverage quickly reduces our S/N. This stresses once again the requirement of good component separation techniques and foreground removals for future applications, in order to have the largest fraction of common clean sky, $f_{\rm sky}$, possible.

The results of this work will be valuable in the forthcoming years of analysis and exploitation of the *Planck* data. The formalism we developed provides us with an accurate forecast of the expected results of the CIB–CMB cross-correlation and allows us to constrain the requirements for a significant ISW detection. Regarding the use of the CIB itself, it presents some advantages over classical ISW studies: the underlying structures observed through the CIB span a large integrated range of redshifts and cover the whole sky, whereas the usual galaxy surveys used often have a limited depth and width in redshift or a small sky coverage – some of the main limiting factors in the ISW detection.

In current studies, the CIB is always considered in its integrated form at a given frequency, meaning that in this observed CIB, contributions from many redshift ranges are mixed together. An interesting further step would be to use the multiple observed frequencies to reconstruct the contributions from different redshift bands, in order to obtain several decorrelated CIB maps corresponding to these redshift slices. The resulting independent CIB maps could then be individually correlated with the CMB. Combining the independent detections could increase even more the total S/N of the

ISW detection, as it allows us to get rid of the correlation terms between CIB maps. Furthermore, each of these maps will then help in tracing the DE at a different time. Our preliminary calculations from predicted power spectra indicate encouraging enhancements in the S/N, although the details of the CIB decorrelation need further investigation and optimization, and will be presented in a future work.

Finally, let us note that as a background the CIB is likely to be lensed by large-scale structures in the local Universe: a dedicated study of the effects of lensing in a future work will be able to determine if the lensing could lead to a possible gain in the S/N of the ISW effect, or should be considered as a possible source of bias in the DE detection.

ACKNOWLEDGMENTS

We would like to thank Nabila Aghanim and Fabien Lacasa for valuable comments and fruitful discussions. We also thank Olivier Doré for his encouraging comments. ML and SI acknowledge financial support by the Doctoral Programme 'AAP 2010 contrats doctoraux Paris-Sud 11'.

REFERENCES

Abazajian K. N. et al., 2009, ApJS, 182, 543
Bass S. D., 2011, J. Phys. G: Nuclear Part. Phys., 38, 043201
Bassett B., Hlozek R., 2010, Baryon Acoustic Oscillations. Cambridge Univ. Press, Cambridge, p. 246
Béthermin M., Dole H., Lagache G., Le Borgne D., Pénin A., 2011, A&A, 529, A4
Boughn S., Crittenden R., 2004, Nat, 427, 45
Condon J. J., Cotton W. D., Greisen E. W., Yin Q. F., Perley R. A., Taylor G. B., Broderick J. J., 1998, AJ, 115, 1693
Cooray A., Sheth R., 2002, Phys. Rep., 372, 1
Corasaniti P., Giannantonio T., Melchiorri A., 2005, Phys. Rev. D, 71, 123521
Dole H. et al., 2006, A&A, 451, 417
Douspis M., Castro P. G., Caprini C., Aghanim N., 2008, A&A, 485, 395
Eisenstein D. J., Hu W., Tegmark M., 1998, ApJ, 504, L57
Eisenstein D. J. et al., 2005, ApJ, 633, 560
Garriga J., Pogosian L., Vachaspati T., 2004, Phys. Rev. D, 69, 063511
Giannantonio T., Scranton R., Crittenden R. G., Nichol R. C., Boughn S. P., Myers A. D., Richards G. T., 2008, Phys. Rev. D, 77, 123520
Granett B. R., Neyrinck M. C., Szapudi I., 2009, ApJ, 701, 414
Jarrett T. H., Chester T., Cutri R., Schneider S., Skrutskie M., Huchra J. P., 2000, AJ, 119, 2498
Knox L., Cooray A., Eisenstein D. J., Haiman Z., 2001, ApJ, 550, 7
Kodama H., Sasaki M., 1984, Progress Theor. Phys. Suppl., 78, 1
Lagache G., Puget J.-L., 2000, A&A, 355, 17
Matsuhara H. et al., 2000, A&A, 361, 407
Miville-Deschênes M.-A., Lagache G., Puget J.-L., 2002, A&A, 393, 749
Miville-Deschênes M.-A., Lagache G., Boulanger F., Puget J.-L., 2007, A&A, 469, 595
Padmanabhan T., 2003, Phys. Rep., 380, 235
Peacock J. A., Smith R. E., 2000, MNRAS, 318, 1144
Perlmutter S. et al., 1999, ApJ, 517, 565
Pietrobon D., Balbi A., Marinucci D., 2006, Phys. Rev. D, 74, 043524
Planck Collaboration, 2011a, preprint (arXiv:1101.2048)
Planck Collaboration, 2011b, preprint (arXiv:1101.2028)
Puget J.-L., Abergel A., Bernard J.-P., Boulanger F., Burton W. B., Désert F.-X., Hartmann D., 1996, A&A, 308, L5
Rassat A., Land K., Lahav O., Abdalla F. B., 2007, MNRAS, 377, 1085
Riess A. G. et al., 1998, AJ, 116, 1009
Sachs R. K., Wolfe A. M., 1967, ApJ, 147, 73
Sawangwit U., Shanks T., Cannon R. D., Croom S. M., Ross N. P., Wake D. A., 2010, MNRAS, 402, 2228
Schaefer B. M., Kalovidouris A. F., Heisenberg L., 2011, MNRAS, submitted (arXiv:1010.1096)
Seljak U., Zaldarriaga M., 1996, ApJ, 469, 437
Taburet N., Hernandez-Monteagudo C., Aghanim N., Douspis M., Sunyaev R. A., 2011, MNRAS, submitted (arXiv:1012.5036)
Wright E. L., 1998, ApJ, 496, 1

This paper has been typeset from a TEX/LATEX file prepared by the author.

Chapter 3

The impact of identified superstructures in the CMB

3.1 A new approach on the iSW effect

3.1.1 Narrowing the view

As of today, the cross-correlation of galaxy surveys with the CMB, extensively discussed in the previous chapter, is still considered as the standard way to probe the iSW effect. However, this method has yet to provide a definitive and unambiguous detection despite its robustness. As I mentioned previously in Sec. 2.1.4, current galaxy surveys are plagued by several shortcomings (low sky coverage and/or depth, not fully controlled systematics and biases) making them less than ideal for iSW studies and leading to inconsistent results across the literature.

In this clouded context, it is clear that cross-correlation studies could greatly benefit from another way of evidencing the iSW effect, an alternative method that could independently infirm or confirm its existence. We remember how in Chap. 2 we started from the cross-correlation of a single galaxy survey, projected on the 2D sky, with the map of the CMB. Then later we considered to further exploit a survey by taking advantage of their depth, decomposing it into slices of redshift. Following the same progression, we can imagine pushing the idea even further and consider using the full 3D information coming from a galaxy survey to "guide" us in our search for the iSW effect.

One possible application of this idea would be to locate the individual objects in the survey that are theoretically expected to leave the biggest imprint in the CMB, i.e. focus on the largest superstructures in the Universe (superclusters or supervoids) that

are not virialised instead of considering the whole the distribution of matter (and all the complications that could go with its analysis). In the linear regime, the shift in temperature experienced by photons (due to the iSW effect) is proportional to the size of the gravitational potential that they cross, so that the biggest structures are indeed expected to yield the biggest iSW effect.

However, it would be foolish to try to detect the imprint of a single superstructure on the CMB temperature map, as the small expected amplitude of the iSW effect (a few μK, cf. later in Sec. 3.5) is completely drowned in the noise, which in this case is none other than the primordial fluctuations of the CMB itself (of the order of 200 μK). However, this should not be a reason for abandoning the idea altogether: we can still exploit this approach by considering many of these superstructures and averaging the CMB over all their locations in the sky, in order to cancel the contribution from the random CMB fluctuations while enhancing the final iSW signature. It is already clear that the properties and the number of structures used will play a crucial rôle here, as well as the other sources of contamination that can pollute and bias the detection. The (historically) first application of this approach to real data will be described in the following section, along with its results and conclusions.

3.1.2 The stacking of superstructures in the CMB

Firstly, the aforementioned approach requires to have a list of identified superstructures to work with, but experiment has ever been dedicated to finding these specifically. In their pioneering work, (Granett et al., 2008, Gr08 thereafter) considered the Data Release 6 (DR6) of the Sloan Digital Sky Survey (SDSS), more precisely the catalogue of Luminous Red Galaxies (LRGs) – elliptical galaxies in massive galaxy clusters thought to be good (but sparse) tracers of matter on large scales (Eisenstein et al., 2001, Wake et al., 2008). The redshifts (estimated by photometry) of these galaxies span here $z = 0.4$ to 0.7 approximatively. On this sample of LRGs, Gr08 ran two numerical codes based on the Voronoi tessellation, VOBOZ (VOronoi BOund Zones, Neyrinck et al., 2005) and ZOBOV (ZOnes Bordering On Voidness, Neyrinck, 2008), respectively designed for void and cluster finding. With their first run, they found a large number of candidate structures (631 voids and 2836 clusters), but with many spurious detections arising from discreteness noise due to the high sensitivity of the algorithms. Therefore they chose to keep only the most "significant" structures using a criterium based on the comparison of the density contrasts of these identified objects with those of voids and clusters in a uniform Poisson point sample. In the end, their final catalogue contains the 50 most significant (according to their criterium) superclusters and 50 supervoids; it provides several informations for each structure, including (but not limited to) the position of

its centre on the celestial sphere, its physical volume and its density contrast. These clusters and voids have mean effective radii respectively around 38 and 109 Mpc, and mean redshifts of 0.50 and 0.53. This catalogue of 100 structures has been made publicly available by the authors; It should be noted however that they never released the full results of their algorithms, including the supposedly less significant detections of structures.

Once the superstructures are identified, the immediate next step is to choose the CMB map to work with: Gr08 used the ILC map from the WMAP five-year data, as well as the raw maps from the Q, V and W frequency band. The use of frequency maps is particularly important to test the one of the expected features of the iSW signal: its achromatic nature, as it does not depend on the energy of the photons experiencing it.

From here, the protocol is relatively simple and can be summarised as follows:

- Retrieve the locations of the superstructures on the sky from the considered catalogue;
- In the CMB map, cut square patches of CMB at these locations (the patches have to be large enough to include the entirety of each structure);
- Stack the patches together, i.e. compute the average of all these images.

This approach assumes that in each stacked patch, the corresponding superstructure produces an iSW signal at the centre of the image, but well hidden behind a veil of CMB fluctuations. However, since these primordial CMB anisotropies are uncorrelated to the position of structures, we expect their contamination to average out when stacking a large enough number of patches, so that only the (mean) iSW signal remains at the centre of the final image.

The output of this method as it was originally applied by Gr08 is reported in Fig. 3.1, extracted from the original Gr08 article. It contains the results of the stacking of three sets of structures: the 50 clusters of the Gr08 catalogue, the 50 voids, and finally a combination of these 100 structures where the opposite of the patches is used for the voids (to get a positive signal in the end). In each of the resulting images, a signal appears quite clearly at the centre: a cold spot for the voids, and a hot spot for the clusters (and the combination) as expected from the iSW that these structures should produce. To obtain the results of Fig. 3.1, they also added the addition step of rotating the align each structure's major axis with the vertical direction: indeed, such structures are often quite irregular in shape, and closer to ellipsoids rather than to spheres. The purpose of this rotation is however purely cosmetic, and tries to visually enhance the

signal in the images: the aperture photometry itself is invariant by rotation of the patches.

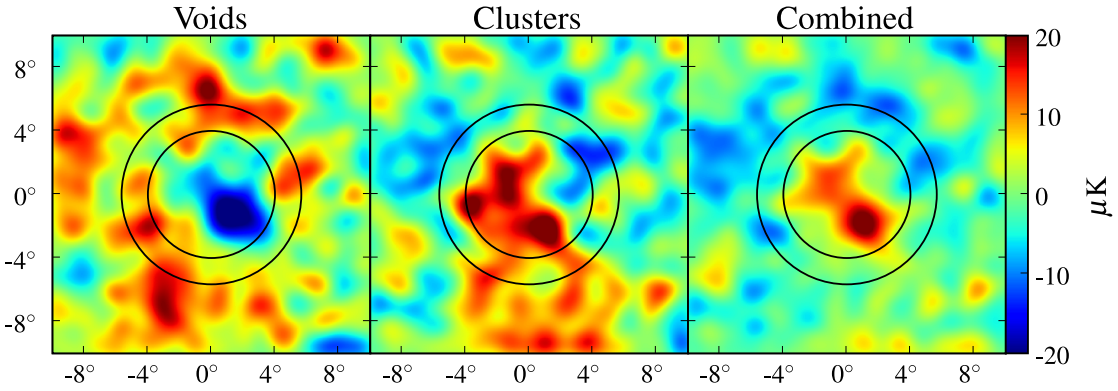

FIGURE 3.1: Figure 1 of Granett et al. (2008). Stacked patches of the CMB (WMAP five-year ILC) averaged at the location of 50 supervoids (left) and 50 superclusters (centre), themselves identified in the SDSS LRG catalogue. The stacked image for the combined sample is shown on the right. The patches of CMB were rotated so as to align each structure's major axis with the vertical direction. These images are smoothed with a Gaussian kernel with FWHM 1.4°. The inner circle (4° radius) and equal-area outer ring mark the extent of the compensated filter used in Gr08 analysis to highlight the visible hot (for the clusters and the combination) and cold (for the voids) spots at the centre of these images.

3.1.3 The Gr08 results: protocol, results and caveats

Although these images seem quite convincing, a simple look will not tell us anything about the amplitude of these apparent signals, or their significance. In order to first associate a number to them, the standard procedure chosen by Gr08 was to apply a top-hat filter on the stacked image, also called "aperture photometry". For a given aperture angle θ, this consists in averaging all the pixels in the image that are contained within a disk of radius θ, and subtracting from it the mean of the pixels inside the surrounding ring of equal area, i.e. between a radius of θ and $\theta\sqrt{2}$ (see the black circles of Fig. 3.1 for illustration). This procedure guaranties that the obtained value is not affected by a local fluctuation of temperature which could artificially boost the measured signal. In their study, Gr08 reported photometry amplitudes of -11.3 μK, 7.9 μK and 9.6 μK for the voids, clusters, and combined signal respectively, using a top-hat filter with a radius of 4°.

Having such figures is a step in the right direction, but it is not sufficient to determine if it is particularly exceptional or quite common: we need therefore some reference to compare this numbers to. A way to proceed used in Gr08 is to perform the same stacking protocol on random locations in the same CMB map, drawing each time as many positions as the number of structures used in the original stacked image. This

procedure is repeated many (several thousands) times while the aperture photometry of each "random stack" is computed. We end up with a distribution of values that we expect to be close to Gaussian, since the dominant signal comes from the primordial CMB anisotropies which constitutes a Gaussian field itself[1]. The photometry values previously obtained for the "true" stacking are then compared to this distribution, and their significance can therefore be determined (cf. an example in Fig. 3.10).

It should be noted that Gr08 also used an alternative approach to derive the distribution of random stacks: they kept the same fixed locations on sky – those of the "real", identified structures – and then repeated the stacking procedure many times but with a randomly generated CMB (using a theoretical power spectrum agreeing with the then latest WMAP parameters). The new distribution did not show any deviation from the one obtained previously; if it had, this would have indicated that the measured signal in the real stacked images could be due (at least partly) to a fortuitous correlation of the primordial CMB fluctuations for this particular arrangement of locations in the sky. Using the CMB map from the 5-year data release of WMAP, Gr08 found that for 50 randomly located patches of CMB, the 4°-aperture photometry has a zero mean[2] and a standard deviation of $3.1\,\mu$K, and $2.2\,\mu$K for 100 random positions. This led to a claim by Gr08 of a $2.6\,\sigma$ signal in the stacked image for their 50 voids, $3.7\,\sigma$ for their 50 clusters, resulting in a combined $4.4\,\sigma$ signal, which they attributed to the iSW effect of these structures.

Taken at face value, this result would effectively be one of the strongest detection of the iSW effect to date. Gr08 also claimed that it showed some tension with respect to the ΛCDM paradigm: they tried to estimate the expected iSW effect from this kind of superstructures by measuring the signal that a large cosmological N-body simulation (here the Millennium run, Springel et al., 2005) produces using ray-tracing techniques. However, the volume of the simulation is only large enough for 1 or 2 supervoids and superclusters only (with the same typical size as those of the Gr08 catalogue) and therefore might not be representative of the variety of the 100 structures of the Gr08 catalogue. The maximum iSW signal then gives $4.2\,\mu$K, about $2\,\sigma$ lower than measured in the stacked data. Although this estimate is quite crude, Gr08 noted nonetheless at that time that this higher-than-expected results seemed to follow a trend found in several previous iSW measurements (from cross-correlation studies) that were also somewhat higher than predicted by ΛCDM (see e.g. Ho et al., 2008).

I take the opportunity from this last point to mention a few caveats in the Gr08 analysis and in their stacking procedure. First of all, the "iSW landscape" has quite changed since

[1] This is true as far as we can discern for now, since the current constraints on the presence of primordial non-Gaussianities in the CMB are compatible with zero (see Planck Collaboration, 2013b).

[2] Which is quite expected from the nature of the CMB fluctuations.

TABLE 3.1: Adapted from Table 1 of Granett et al. (2008). For the stacked signal that they measured by photometry and its significance, it shows the dependence on the number of structures N (i.e. N voids and N clusters stacked) and the aperture radius.

N	Aperture radius	Photometry (μK)	Significance (σ)
30	4.0°	11.1	4.0
50	4.0°	9.6	4.4
70	4.0°	5.4	2.8
50	3.0°	8.4	3.4
50	3.5°	9.3	4.0
50	4.0°	9.6	4.4
50	4.5°	9.2	4.4
50	5.0°	7.8	3.8

the publication of their paper in 2008. Recent works, such as Hernández-Monteagudo et al. (2013b) and the dedicated iSW paper from the *Planck* cosmology results (Planck Collaboration, 2013c), have yielded results with slightly lower significances but in better agreement with ΛCDM (all within $1\,\sigma$), including the results from new probes of the iSW effects such as the iSW-lensing bispectrum. In this updated context, the Gr08 result is now the one that stands out as inconsistent, casting some doubts on the iSW origin of the reported signal. Moreover, confronting the stacking results to theory might require more than a single set of N-body simulation; a more thorough comparison between these and ΛCDM predictions requires a more advanced work on the theoretical side. This particular point will be discussed in more detail in Sec. 3.5.

A few other issues can also be discussed regarding the Gr08 study: the 100 structures that they used were extracted from a much larger catalogue of candidate structures that they first identified. However this "proto-catalogue" has never been released by the authors. I trust their claim that their selection of 100 structures was only based on the properties of these objects and not linked to their measured impact on the CMB. However, some elements in their study seem to point towards the possible existence of selection biases, especially in the light of a particular test that they performed: Gr08 tried to change the number of objects stacked and the aperture of the top-hat filter, and observed that any deviation from their "golden numbers" (50 voids and clusters, 4° aperture) resulted in a decrease of the significance of the results (see Table 3.1). This could be attributed to real physical effects, since it is reasonable to believe that the measured signal can be influenced by the addition (dilution of the mean iSW signal by lowly contributing objects) or the subtraction (increased noise due to the limited number of objects) of structures in the stacking.

However, all of the aforementioned remarks and difficulties called for a more in-depth analysis of the stacking procedure – a task that I chose to tackle. As I will show in the

next sections of this chapter, I even went beyond and did not confine myself to the sole catalogue of Gr08 and its intriguing results.

3.2 My revised and improved stacking protocol

Now, in 2013, the beautiful products of the *Planck* mission have been released: the first and foremost way to improve stacking studies will be to use this new CMB data to improve and validate our stacking studies. I actually conducted two separate works on the topic: one that used WMAP 7-year data (the latest at that time) which led to the publication of a paper (Ilić et al., 2013), and another inside the *Planck* collaboration itself where I was the leader of the stacking section in the iSW-dedicated cosmological paper (Planck Collaboration, 2013c). Although the CMB data is different, the protocol that I devised is largely the same for both new studies and the catalogues of structures used are identical. I will therefore describe the general framework of my method in the following, underlying any substantial difference when needed.

3.2.1 Data and core of the protocol

***Planck* data:** For my *Planck* related work, I have made use of the foreground-cleaned CMB map provided by the data processing centres (as described in the *Planck* component separation paper Planck Collaboration, 2013a). In particular, I used the so-called "official" CMB map which was cleaned using the SMICA component separation technique based on spectral matching. In addition to this, I also performed my analyses on six foreground-cleaned frequency maps (from 44 to 353 GHz) constructed by subtracting a linear combination of internal templates using SEVEM, an other component separation method considered and used in the *Planck* collaboration. (Planck Collaboration, 2013a, contains a description of both methods). We remember that the use of frequency maps is crucial in iSW studies as the signal is expected to be achromatic. Also, to minimize the presence of foreground contamination in the maps, I used the official *Planck* mask, also described in Planck Collaboration (2013a), which excludes regions with larger Galactic and point-source contamination.

WMAP data: In my other stacking study, I used the maps of the CMB released by the WMAP team after seven years of observation (Jarosik et al., 2011) in contrast to the five-year data used by Gr08 in their study. Just as for the *Planck* data, I also took the individual channel maps at the three frequencies that are the least contaminated by foregrounds (the Q, V and W bands at 41, 61 and 94 GHz respectively). At the

same time and in order to assess the possible impact of foregrounds, I also did my analyses with the foreground reduced maps released by the WMAP team in the same frequency channels. A galactic mask was also used here: the KQ75 from the WMAP team, the extended mask for temperature analysis removing about 22% of the sky along the galactic plane and around point sources.

My stacking procedure: The first protocol that I devised consisted in the following steps. The CMB map considered is cleared of its the cosmological monopole and dipole, accounting for the considered sky mask. Using as inputs the galactic longitudes and latitudes of the structures studied, a code I wrote based on the HEALPix3 package cuts a patch in the CMB map centred around each structure. I chose the patches to have a 6 arcmin/pixel resolution (small enough to oversample aand keep the details of the CMB maps used) and to be squares of 301×301 pixels, i.e. $30^\circ \times 30^\circ$ patches (large enough to encompass any of the considered objects). Concurrently, the code cuts identical square patches at the same locations in the associated mask map; it computes the final stacked image as the average image of all CMB patches weighted by their corresponding "mask patches". The originality of my work is that I extract two main products from the stacked images:

- The radial temperature profile starting from the centre of the image, by computing the mean temperature of the pixels in rings of fixed width and increasing angular radius. Considering the characteristics of my stacked images, it is calculated here for 150 radii between 0° and 15°, with a width of 0.1°;
- The aperture photometry profile, using the previously mentioned top-hat filter approach: At each chosen angle, we compute the photometry as the difference between the mean temperature of the pixels inside the disk of the given angular radius and the temperature of the pixels in the surrounding ring of same area. I compute this profile for 150 angles between 0° and $(15/\sqrt{2}) \sim 10.6^\circ$.

This differs from the original approach of Gr08 by adding a new dimension to the results: as we will see, the temperature profile gives us a precious insight on the origin and feature of any potential signal found in the photometry profile, which is itself useful (among other things) for a better identification of the scale of these signals.

On a more technical note, the summation of square pixels contained inside a disk can lead to calculation errors due to omitted fractions of pixels close to the boundaries of the disk. To reduce these as much as possible, I upscaled the 301×301 stacked images into 1204×1204 images, each pixel of the original image divided into 16 sub-pixels with

the same value. Statistical errors for these two profiles are estimated by computing the standard deviation of each sample mean of pixels. The stacked images themselves are useful mostly for illustration purposes, but I mainly focused on the analysis of these two profiles in my work, looking for any remarkable signal.

Of course, spotting a signal in the stacked images and/or their associated profiles is not enough to conclude about a possible detection of the iSW effect. We have to take great care in assessing the significance of our results: to do so I devised a systematic way to compute the significance adopting a Monte Carlo approach. It is quite similar to the Gr08 approach in the sense that I pick many sets (at least 10000) of N random positions on the sky (N being the number of structures used in the stacking whose significance we want to assess). However, for each random set I perform the same analyses as for the data, i.e. I produce not only a stacked image but also compute its full radial temperature and photometry profiles. I store all these profiles in memory and end up with thousands of temperature profiles and photometry profiles. After this, for every angular size of the profiles, we compare the results from the stack of real objects to the statistical distribution of results from the random stacks. In practical terms, we calculate the signal-to-noise ratio (S/N) of the data temperature and photometry profiles, at each angle considered.

With my protocol in place, I chose to apply it first on the catalogue of structures from Gr08, using their original study of these objects as a basis of comparison. In the following, I therefore use the catalogue (the 50 supervoids in particular) as a "fiducial stack" for a series of tests to check the robustness of my method.

3.2.2 Gr08 catalogue: preparation of the maps

Let us start this section with a picture: an example of a stacked image from the aforementioned procedure is shown in Fig. 3.2. I obtained it using the catalogue of 50 voids from the Gr08 catalogue and stacking in the WMAP V map. Although a cold spot seems to appear quite clearly, we can note that the picture looks a bit different from the original image of Gr08 (the left panel of Fig. 3.1). The main reason for this is that Gr08 rotated all the CMB patches before stacking in order to align the major axis of all the structures, as mentioned at the end of Sec. 3.1.2. Since Gr08 did not release the information about the orientation of their objects, I could not reproduce their work exactly. However this should not be a source of worry, as the relevant quantities that I derive from these images (i.e. temperature and photometry profiles) are rotationally invariant. Another difference between Fig. 3.2 and Fig. 3.1 is that the latter was smoothed with a

Gaussian kernel with FWHM 1.4° for aesthetic purposes, whereas mine is in its original resolution.

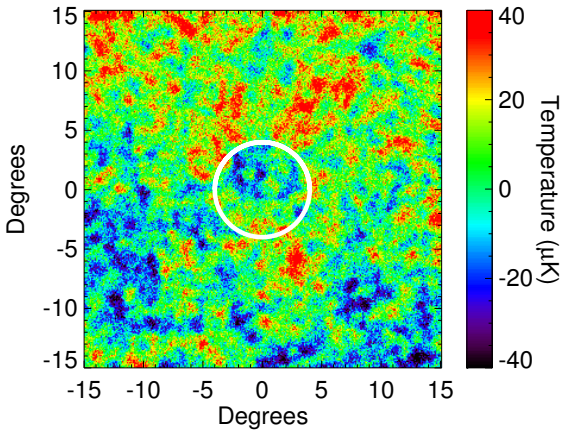

FIGURE 3.2: Image resulting from my stacking procedure at the location of the 50 voids of Gr08, here using the V band CMB map of WMAP. The cold spot reportedly due to the iSW effect is visible roughly at the centre of the image with an angular radius of about 4° (highlighted by the white circle). Note the North-South temperature gradient, discussed in Sec. 3.2.2.3.

3.2.2.1 About resolutions

This leads me to an important point: for a given experiment (both WMAP and *Planck*), all the CMB maps that I use inherently have different resolutions. Indeed, the angular resolution of a telescope is proportional to the observed wavelength: the CMB maps obtained at higher frequencies will therefore have finer resolutions. Another consequence of using maps at multiple frequencies is that each one of them will contain different types and levels of foregrounds which may contaminate my stacking measurements and produce inconsistent results across frequencies. Consequently, I chose to first assess the impact of these properties of each map, using my fiducial stacking as a basis.

In order to have a consistent stacking analysis through all the considered maps and frequencies, I "standardised" these maps by smoothing them at the same resolution, lower or equal to the lowest one of them. The beam sizes of the maps we considered span from 30 to 12 arcminutes for the WMAP Q-V-W bands, and 28 to 4 arcminutes for the *Planck* maps from 44 to 353 GHz. I chose therefore to smooth all the maps using a common Gaussian kernel with a FWHM of 30 arcminutes. Fig. 3.3 shows the effect of such smoothing for the three WMAP maps through the temperature and photometry profiles of the fiducial stacking. The stacks at each frequency, both raw and smoothed, give roughly the same results with only percent-level differences especially for the photometry profiles, which are the most useful products here. The degradation of the V and W maps to the lower resolution of the Q map naturally smooths the measured

profiles and reduces their dispersion around the results of the Q band, which is the desired effect. We note identical behaviours when smoothing the different frequency maps from *Planck*. Otherwise, this procedure does not modify significantly their amplitude and angular dependence, so that we can adopt this choice of a new common resolution for all maps and experiments, facilitating the comparison of results across frequencies.

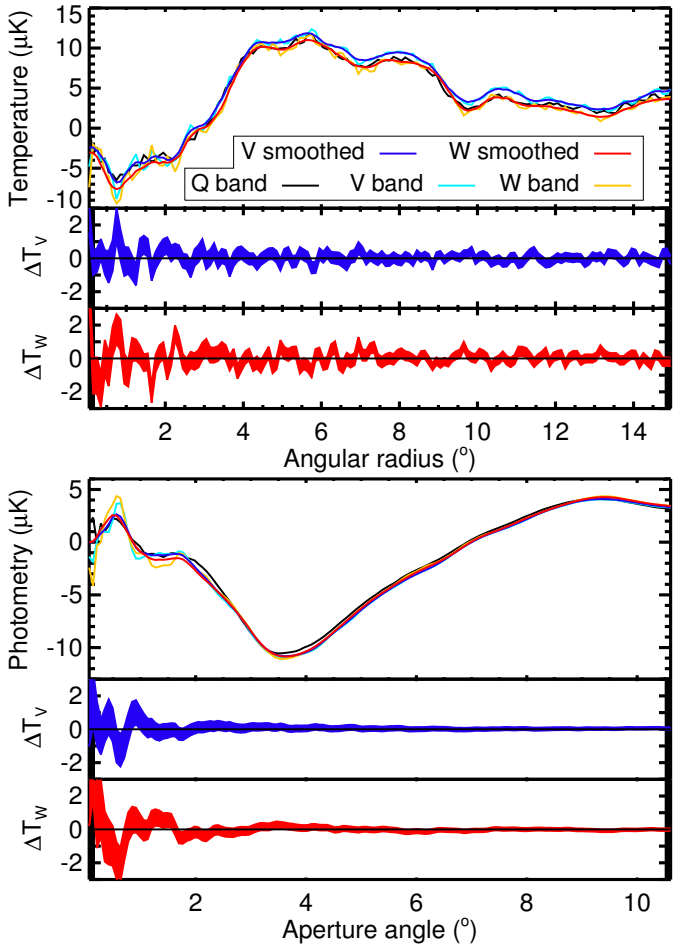

FIGURE 3.3: *First plot*: radial temperature profiles (*top* panel) of the stacking of Gr08 voids, done on WMAP Q, V and W maps (both in native resolution and smoothed by a 30.6 arcminutes kernel). The differences in the profiles between the smoothed and original maps are plotted below the main plot (*middle*: V band, *bottom*: W band). The width of the shaded curves corresponds to the statistical errors on the profile measurements. *Second plot*: Same graphs and legend as above but for the aperture photometry profiles of the stacking of Gr08 voids.

The corresponding photometry profiles using the *Planck* frequency maps are shown in Fig. 3.4, and the equivalent of the stacked images of Fig. 3.1 with the official *Planck* CMB map are displayed in Fig. 3.5. We keep in mind that the smoothing procedure with a $\sim$ 30 arcminute beam blurs the information and details contained below this scale. Therefore we should not devote too much attention to any feature in the profiles at angles lower than this value. Of important note is that the flux measured is quite constant across all the considered frequencies, which (at this point in the analysis)

supports the idea that the signal originally pointed out by Gr08 is indeed due to the iSW effect induced by structures.

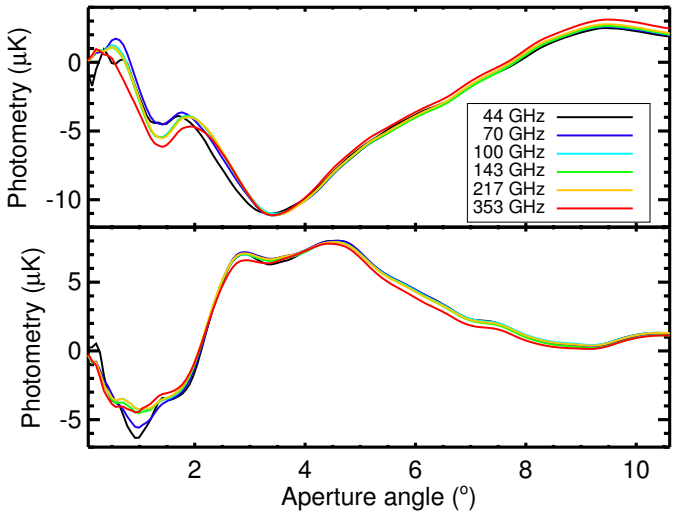

FIGURE 3.4: Aperture photometry profiles measured in the stacked patches centred on the Gr08 supervoids (top) and superclusters (bottom), using the SEVEM-cleaned *Planck* frequency maps. As we can see, these are almost identical for all frequencies except for small differences at low angular scales ($< 2°$): these are most likely due to small-scale artefacts of foreground remaining after the component separation. The interpretation of these profiles will be discussed later in Sec. 3.2.3.

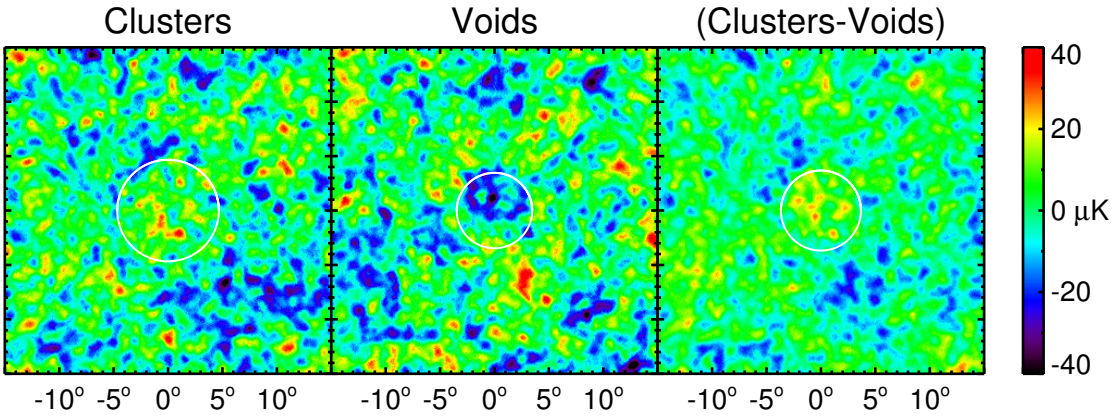

FIGURE 3.5: Stacked regions of the *Planck* CMB map (smoothed at 30 arcminutes) corresponding to the locations of the superstructures identified by Gr08. From left to right we show the images resulting from stacking of the 50 superclusters, the 50 supervoids, and the difference of both. The black circles superimposed indicate the angular radius at which the signal-to-noise ratio is maximal.

3.2.2.2 Effects of foregrounds

One other potential source of concern comes from the influence of foregrounds present in the CMB maps, as they might mimic the expected iSW signal in the stacked images (radio point sources for example could produce such effect with their flat spectrum). The *Planck* data that I used (both the frequency maps and the output from component

separation) and the foreground-cleaned WMAP maps are supposed to be free of such contaminants. However, no component separation technique can be considered as absolutely perfect: residuals always exist. To assess their possible impact, I performed the stacking of the Gr08 voids first on raw and then foreground cleaned CMB maps at all frequencies of WMAP. I then looked for differences between the two results, either in the amplitude or in the shape of the signal. Results are illustrated in Fig. 3.6: we obtain systematic offsets of a few micro-kelvins in the radial temperature profiles and less in the photometry profiles. This indicates that the foreground removal (by the WMAP team) ends up removing an almost uniform background in my stacked images, which does not influence much the aperture photometry of the stacked image. It does not mean of course that these removed foregrounds are uniform background across the sky, but rather that the number of stacked patches is sufficient to smooth the contribution of the foregrounds to the final stacked image. I still used the foreground cleaned maps for my analyses, so that any measurement of a potential iSW signal would be as close as possible to its true underlying amplitude. However, this test allowed to conclude that possible residuals in the cleaned maps should not be of any concern since we expect them to have the same "flat" behaviour in the stacked images as the foregrounds themselves.

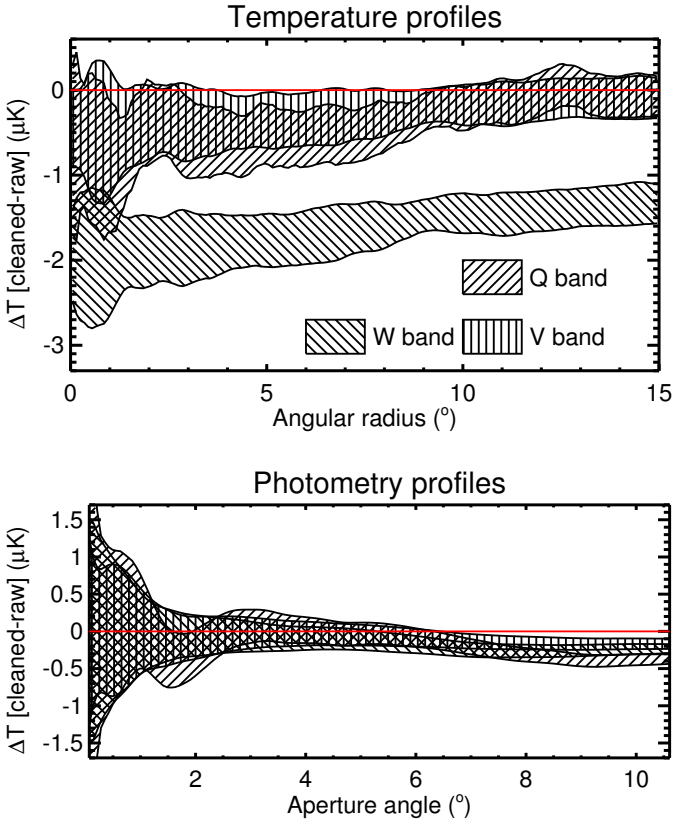

FIGURE 3.6: For the Gr08 stacking, differences in the temperature (*top*) and photometry (*bottom*) profiles between foreground cleaned maps and raw maps, for the three frequency bands considered. The width of the shaded curves corresponds to statistical errors on the profile measurements. The quasi-flat offsets observed in the temperature profiles do not affect substantially the photometry.

3.2.2.3 Unforeseen features

Another map-related problem showed up during my investigations: I observed that a clear temperature gradient appeared in many of my stacked images (already visible in Fig. 3.2), roughly on a North-South axis with hotter high latitudes. Foregrounds as a possible source of this can be excluded, because the gradient appears in both raw and foreground cleaned maps, and also – to a lesser extent – because we would expect foreground contamination to be hotter close to the galactic plane. This feature is not seen (or reported) in the work of Gr08, because of the rotation they performed on the CMB patches (see the beginning of Sec. 3.2.2) which randomised and erased this gradient.

The choice of map (foreground-cleaned or not) did not influence this gradient, ruling out the foregrounds as culprits. To have a better insight on the origin and feature of this large scale gradient, I decomposed the CMB maps on the spherical harmonics and to analyse the individual contribution of each multipole. This approach was motivated by the methods used in other works in the literature dedicated to the study of large scale anomalies in the CMB (e.g. Bennett et al., 2011, Planck Collaboration et al., 2013). This idea proved fruitful as it appears that the measured gradient is mainly caused by the first few multipoles of the CMB maps we use, especially by the $\ell = 6$ multipole map. In the region of the sky covered by the SDSS (where all the superstructures we considered are located), these multipoles combine to yield indeed a strong North-South gradient (see Fig. 3.7 for WMAP) which will be present at some level in every patch of CMB, and therefore in the final stacked image. As shown in Fig. 3.8, subtracting the contribution of these multipoles does remove the gradient in the stacked image but has an almost negligible effect in the photometry profile. Indeed, the removed contribution has a shape close to simple tilted plane (see Fig. 3.8) which does not affect the aperture photometry.

In the present work, I used both maps with and without these few multipoles removed and did not see any significant difference in the stacking results, except in very particular cases (that I mention later in this chapter). This gradient should therefore not be a source of particular worry in this context, although it should be kept in mind as it always at least add an offset in the measured temperature profiles.

3.2.3 Application to Gr08: significance and analysis

In all the stacking results shown so far, a signal appears in the photometry profile with a maximum (in absolute value) at an angular scale of about 3.5° for the Gr08 voids (see

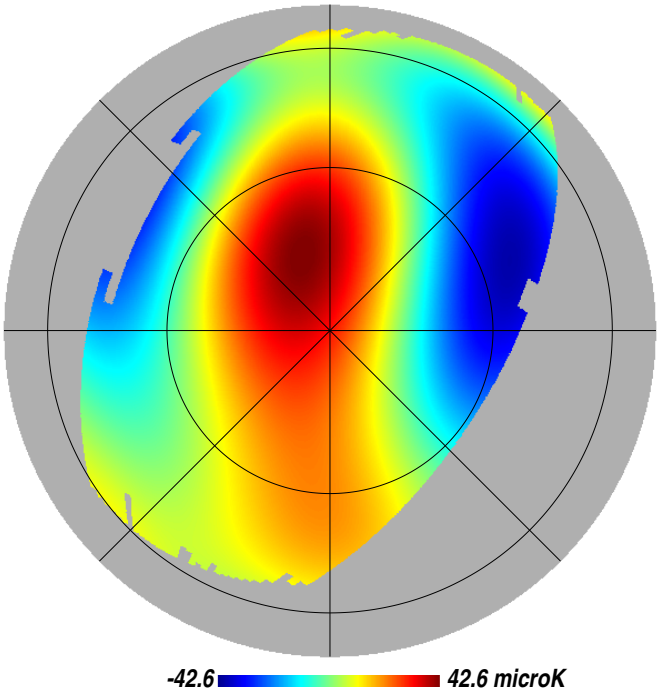

FIGURE 3.7: Orthographic projection of the $\ell = 2$ to 6 multipoles map extracted from the foreground reduced WMAP Q map, in galactic coordinates. Only half of the map is visible (centred on the galactic North pole), with a mask showing only the area covered by the main SDSS. A graticule grid has been superposed with a 45° step in longitude and 30° in latitude. The border of the image corresponds to the galactic plane, while the point at the very bottom is the galactic centre.

Fig. 3.3 and 3.4) and around 4.5° for the clusters (see Fig. 3.4), the preferred size changing only very slightly between frequencies. These figures mark the first departure from the Gr08 results as my analysis highlights a smaller/higher scale for the voids/clusters. Before trying to further interpret those results, one must remember that these profiles by themselves are not enough: we need to compute their significance.

I described the procedure for such a computation at the end of Sec. 3.2.1: I applied it to assess the significance of the stacking of the Gr08 structures, as illustrated in Fig. 3.9 (using there the CMB of *Planck*). For this particular example, I used more than 15000 sets of 50/100 random positions, enough to sample the distribution of temperature and photometry profiles. This is verified in Fig. 3.10 where the histogram of the "random" photometry values at a given angular size follows closely a Gaussian distribution.

Using the same catalogue as Gr08, I find results in reasonable agreement with their original study (see Fig. 3.9), with only slightly different amplitude (of order $\sim \mu$K) and significance, and small shifts in the preferred scales (less than 1°). These differences can be imputed to our use of different CMB maps (WMAP 7 and *Planck* vs. WMAP 5) which may have different levels of foreground residuals, and to a lesser extent to light differences in the practical application of the stacking procedure (profile calculations,

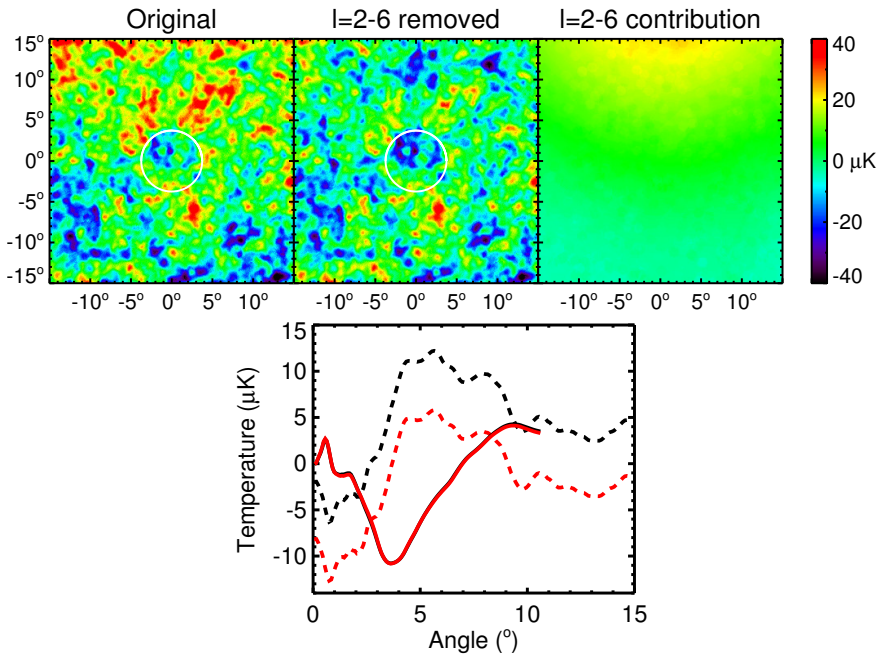

FIGURE 3.8: The three images represent the stacking of the Gr08 voids done (from left to right) on the cleaned WMAP V map, on the same map without its $\ell = 2-6$ multipoles, and on these multipoles only. The temperature (dotted curves) and photometry (solid) profiles shown on the rightmost plot are obtained from the first (black curves) and second (red) stacked image. The temperature offset induced by the removed multipoles does not affect the photometry.

significance estimation, etc.). While we can argue its cosmological origin, the signal is clearly not a simple oddity peculiar to WMAP 5 CMB maps: as mentioned before, it is essentially identical across frequencies as expected of the iSW effect. However, I found an important fact in the temperature profile of the stacked image of the 50 voids and its significance. Indeed, in the top panel of Fig. 3.9 we see that the central cold spot of the signal (below 3.5°) does not particularly stand out compared to random stacks (1-2 σ significance only). On the other hand, I measured around the spot a wide hot ring with a constant significance (around 1.5 σ) at scales between 3.5° and 10°, also clearly visible in the stacked images (see e.g. Fig. 3.5). This ring has the effect of rising the mean temperature of the stacked image in the region delimited by a circle of $\sim 9°$ radius: this has a visible impact in the photometry profile at higher scales, with a significance rising again around 9°.

Interpreting it in the light of the iSW effect, this would imply the presence of much larger overdensities surrounding the already large supervoids. Considering the filamentary structure of our Universe, this situation is unlikely and the source of this hot ring remains unknown. This peculiarity leads us to question whether the measured central cold spot – physically interpreted as an iSW signal – is really remarkable: it might as well be due to random fluctuations of the CMB, of which the significance in the photometry profile was coincidentally strengthened by a surrounding hot region in the stacked image. In

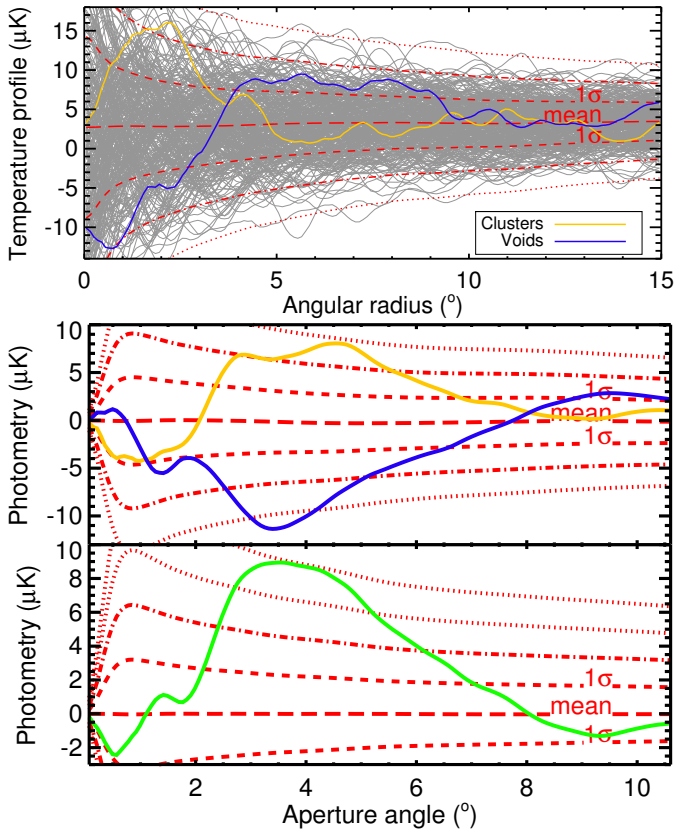

FIGURE 3.9: Temperature (top) and photometry (middle and bottom) profiles of the stacked patches (from the *Planck* CMB map) at the location of the 50 supervoids and 50 superclusters of Gr08. The lower panel shows the combined photometry profile (i.e., the average cluster profile minus the average void profile). The significance is represented by 1, 2, 3 σ level curves These curves represent the dispersion of the thousands of stacks of 50 CMB patches chosen at random positions (for illustration, on the top panel, we represent in grey a few hundreds of those random profiles).

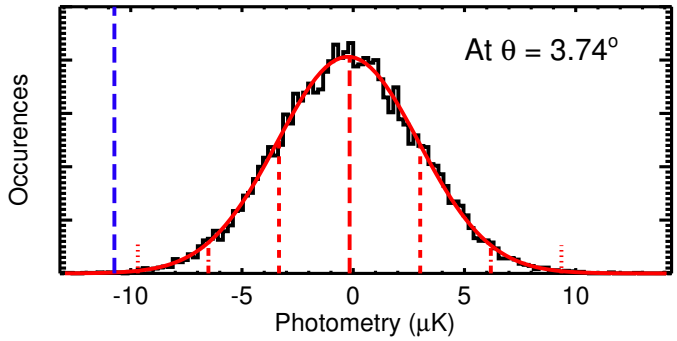

FIGURE 3.10: Distribution of photometry values for a single aperture (here 3.74°) from 14000 stacks of 50 random positions. The mean, 1, 2 and 3 σ values are marked the same way as in Fig. 3.9. The blue long-dashed line shows the value obtained from the fiducial stacking of the 50 voids. The best fitting Gaussian (red solid curved) follows closely the distribution.

a similar line of thought, the temperature profiles from the stacked clusters does not present such peculiarity, although we note that its most prominent photometry signal is

quite wide and has a lower significance. But more importantly, the photometry profile peaks at angular scales more than twice as large as those of the underlying clusters (which have a mean radius of 38 Mpc and a mean angular scale of $\sim 1.7°$).

Reaching any definitive conclusions on these particular results (and the scale of the measured signals) would require a complementary rigorous investigation through theory and/or numerical simulations of the iSW effect expected from such sets of superstructures with their large distribution of sizes. This is beyond the scope of this chapter, but this problem is treated in Chapter 4 of this thesis. However, we can try to account for the size of each structure inside the stacking procedure itself, which is the purpose of the next subsection.

3.2.4 Refining the stacking analysis

A quick look at Fig. 3.11 is worth a thousand word: in all the stacking that I performed so far, I actually mixed together structures with a relatively large variety of angular sizes on the sky. Combined with the fact that these objects have also different physical sizes and redshifts (therefore different iSW signatures), it is hard to draw any conclusion from the size of the signal measured by photometry. To account for this, I revised my stacking protocol in order to include a rescaling of the structures according to their effective radii. In practical terms, this meant cutting each CMB patch with the same number of pixels but with a tailored resolution so that the corresponding object always occupies the same surface on the image (hence also in the final stacked image).

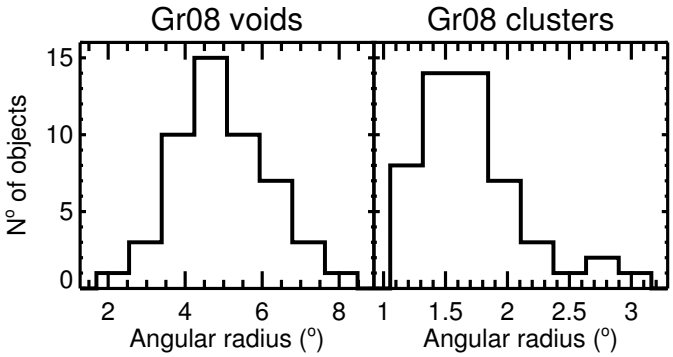

FIGURE 3.11: Histogram of the angular sizes of the 50 voids (*left panel*) and 50 clusters (*right*) of the Gr08 catalogue. Note that the x axis is not the same in both panels.

The resolution of the extracted patches now depends on the size of the corresponding structures: I chose to cut square patches with a side several times[3] the size of the effective radius of the structure it contains. Naturally, I also adapted my protocol for

[3]This was done in anticipation of a potentially large scale of the stacked signal, especially in the light of the "non-rescaled" results from the Gr08 clusters in Sec. 3.2.3.

the estimation of the significance: each random patch is first subjected to the same rescaling as the one done on the identified void patches. We can guess that this will have the effect of mixing different scales in the original CMB map, and will most likely amplify the variance of these random stacks compared to the previous estimation.

I begin with the fiducial stacking of the voids of Gr08: a comparison between the stacked images and profiles is illustrated in Fig. 3.12. The signal which was identified above still appears after rescaling, with the best significance at scales between 0.7 and 0.9 times the void effective radii.[4] Such angles are not entirely surprising, as we could expect the signal to show a size smaller than the objects themselves. We intuit that the iSW effect should fade close to the border of the voids; combined to the irregular geometry of the objects, it is conceivable that it would make the cold spot noticeably smaller than the underlying structure. However, a strong disagreement is found in the rescaled stacking of the superclusters, where the photometry prefers a scale that is 2.6 times the effective radius of the structures ! This mismatch could be a result of an underestimation of the structure extent by the ZOBOV and VOBOZ algorithms (as already suggested by Gr08) or because larger potential hills and valleys (responsible for the iSW effect and mainly generated by the Dark Matter) underlie the detected superstructures (composed of baryonic matter). Nevertheless, the factor of 2.6 for the case of superclusters seems hard to explain entirely with this argument. Another culprit could be found in the LRG subsample of the SDSS itself that was used for the identification of these structures; these LRGs are known to be biased tracers of matter (see e.g. Tegmark et al., 2006), so that the structures identified could be substantially larger than they appear. In any case, reconciling these measured signals with their associated structures would imply that some important corrections are needed in the characterising of these objects.

I also noted that the significance of these signals is found to be slightly lower (~ 0.5 less in the S/N), although this is partly due to the increased variance of the signal (cf. the wider significance contours in the profiles) induced by the rescaling as expected above. But it is also a consequence of the lower amplitude measured for the signal, at odds with our expectations of the rescaling procedure. This could be a further hint that random CMB fluctuations actually contribute notably to the signal seen in the stacked image. As a take-away message, the use of the rescaling certainly shows that it is a crucial step to reveal possible inconsistencies in the results from the stacking of structures. But in spite of all these comments, the Gr08 catalogue still yield results that remain at a high significance. One of the possible ways to gather some insight on those results would be

[4] It should be noted that these results differ slightly from those reported my published paper (Ilić et al., 2013), the reason being that I made a mistake in the calculation of the physical radius of the Gr08 voids (by a factor of ~ 0.7). The purple points in Fig. 3.13 were affected as well. This does not alter fundamentally my conclusions and I intend to submit an erratum to the editor of the paper very shortly.

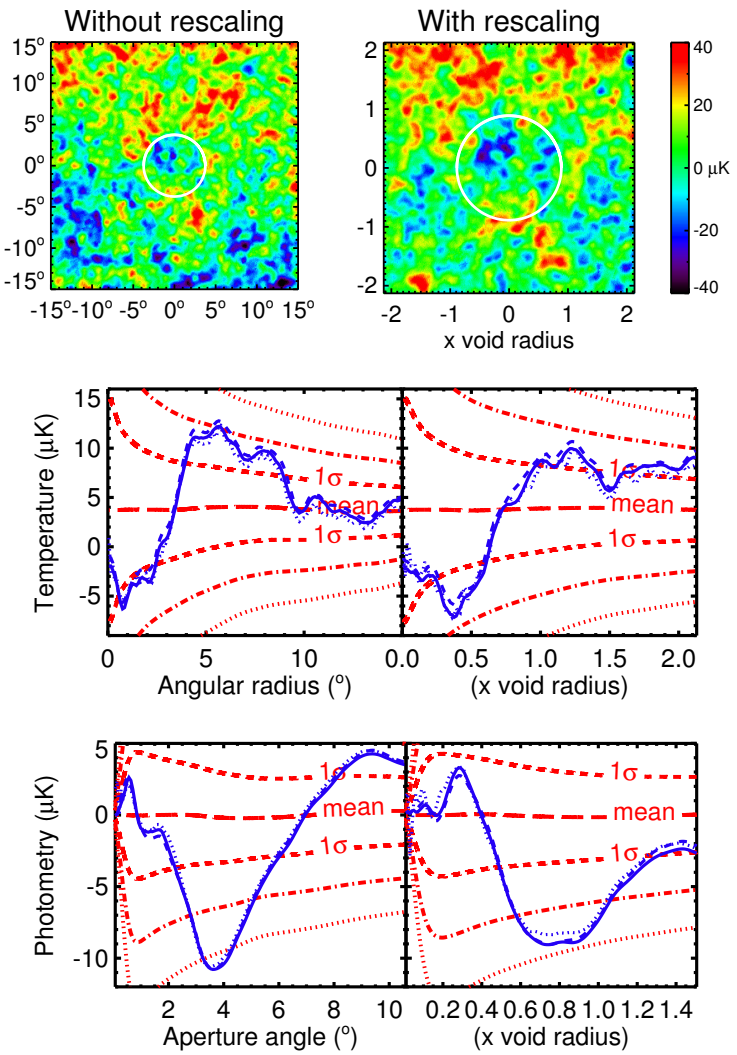

FIGURE 3.12: *Top*: Stacked images of Gr08 voids, without (*left*) and with (*right*) a rescaling of the CMB patches proportional to the void sizes. *Middle and bottom*: Respectively the temperature and photometry profiles for the original (*left*) and rescaled (*right*) stacking of Gr08 voids (same conventions as Fig 3.9).

to look for alternative objects to study, instead of being confined to the analysis of those only 100 structures.

3.3 Analysis of additional voids

Luckily, a few other works dedicated to the identification of structures were published since the original Gr08 paper, with publicly available catalogues. In this section, I describe these new datasets and perform a similar stacking analysis with these new objects.

3.3.1 The catalogues of Pan et al. and Sutter et al.

Two catalogues in particular held my attention: both are based on the same survey for the identification of structures, here the SDSS DR7 release. Of important note is that these two catalogues contain only voids, but these are actually more adapted for stacking studies. Indeed, emission of astrophysical origin is less likely to contaminate the iSW signal from these objects.

The first catalogue that I considered was published by Pan et al., 2012 (Pan12 thereafter), who used the VoidFinder algorithm as described by Hoyle and Vogeley (2002) to identify and catalogue 1055 voids with redshifts lower than $z = 0.1$. They provide for each void all the information that I need for my stacking studies and even more: the position on the sky, the physical radius (defined as the radius of the maximal sphere enclosing the void), an effective radius (as voids are often found to be elliptical) defined as the radius of a sphere of the same volume, its physical distance to us, its volume and mean density contrast. The largest void is just over 47 Mpc in effective radius while their median effective radius is of about 25 Mpc. Some are both very close to us and relatively large (more than 30 Mpc in radius) resulting in large angular sizes on the sky, up to 15 degrees and above.

The second (and most recent) catalogue that I studied was released by Sutter et al., 2012 (Sut12 thereafter). Using their own modified version of the already mentioned void finding algorithm ZOBOV, they took particular care of accounting for the effects of the survey boundary and masks. I should mention here that since its first release in July 2012, the catalogue has been subjected to regular updates (contrary to the Pan12 catalogue) and modifications reflecting improvements in the detection algorithm, bug corrections, and inclusion of additional void data. In the latest version of their catalogue, they found a total of 1495 voids which they divided into six redshift subsamples: four extracted from the main SDSS (*dim1, dim2, bright1* and *bright2*) and two from the SDSS LRG sample (*lrgdim* and *lrgbright*). The redshifts of these voids span $z \sim [0, 0.4]$ while their sizes range approximatively from 5 to 150 Mpc. This catalogue stands out by the amount of information provided about its voids: position of the barycentre, redshift, effective radius, locations of member galaxies, one-dimensional radial profiles of stacked voids, two-dimensional density projections and other statistical information about their distribution.

As a summary, we plot the properties of the voids from these two catalogues (including also the 50 voids of Gr08) in Fig. 3.13, including their redshifts, effective radii and corresponding angular sizes. More details about all the subsamples can be found in

Table 3.2. It is now time to take a closer look at these catalogues and see if they can give us any precious results and knowledge about the iSW effect.

TABLE 3.2: Summary of all the void catalogues considered in the stacking procedure.

(Sub)sample Name	Redshift Range	Number of Voids
Sut12	$0.003 < z < 0.43$	**1495**
dim1	$0.003 < z < 0.048$	218
dim2	$0.05 < z < 0.1$	419
bright1	$0.1 < z < 0.15$	341
bright2	$0.15 < z < 0.20$	176
lrgdim	$0.16 < z < 0.35$	291
lrgbright	$0.36 < z < 0.43$	50
Gr08	$0.43 < z < 0.69$	**50**
Pan12	$0.009 < z < 0.1$	**1055**

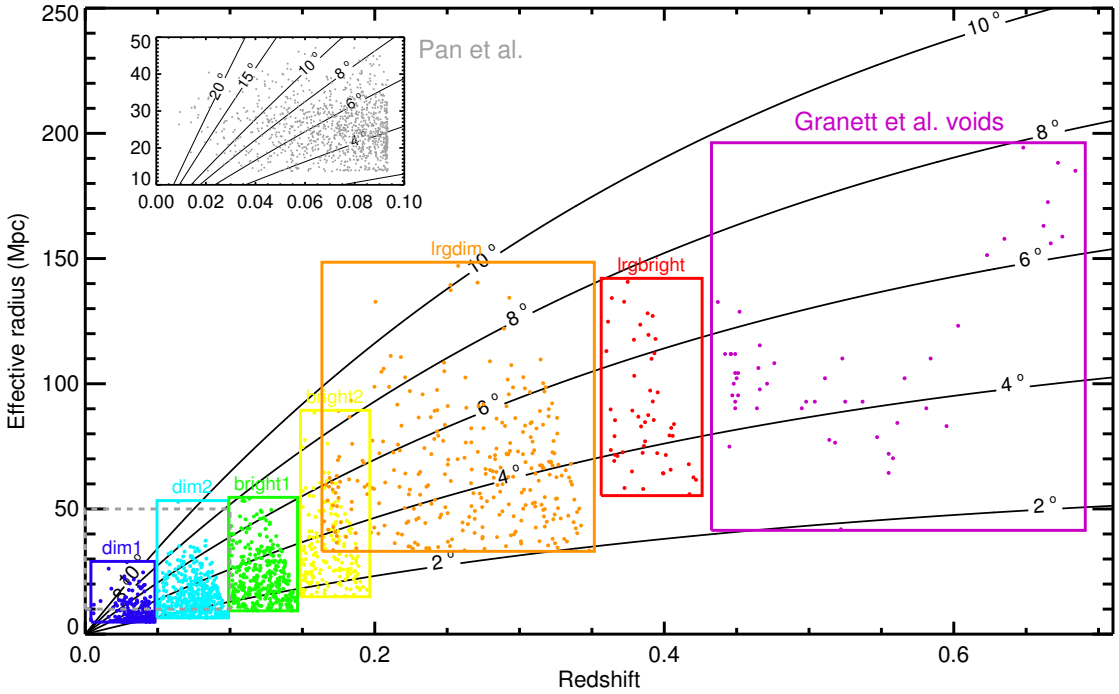

FIGURE 3.13: Effective radii (in Mpc) as a function of redshift for all the voids used in this work. The two catalogues of Granett et al. and Pan et al, and the six subsamples of Sutter et al. are delimited by boxes labelled by their names. The black curves are here to indicate the angular size (in degrees) of a structure in the redshift-radius plane.

3.3.2 New objects, new results

For the study of these two new catalogues, I kept the same protocol that I used for the Gr08 catalogue, i.e. the same method of cutting and stacking the patches of CMB, the same computation of the temperature and photometry profiles, as well as the same estimation of their significance and the same rescaling procedure.

As a first (and relatively crude) approach, I tried to stack these voids "as such" by subsamples, i.e. stacking the voids in each of the six samples of Sut12, and not trying any division of the Pan12 catalogue. Results for the photometry profiles and their significance are shown in Fig. 3.14.

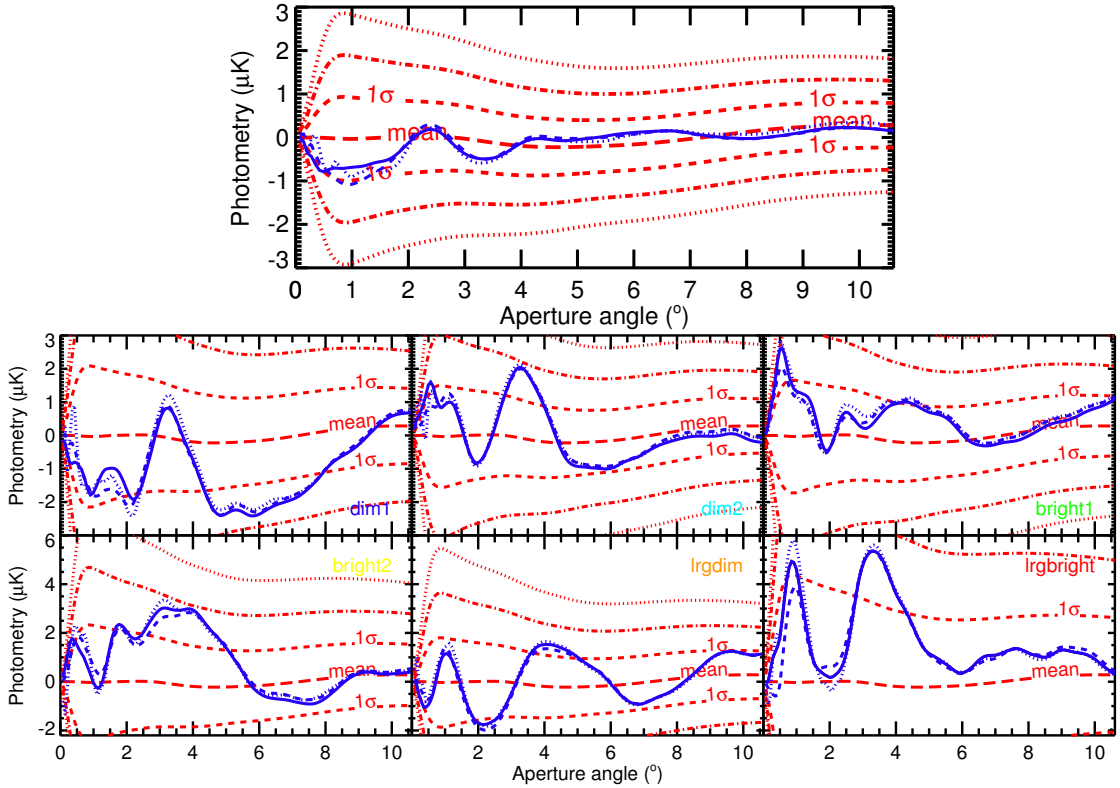

FIGURE 3.14: *Top panel*: Photometry profiles from the stacking of Pan12 voids (same conventions as Fig 3.9). *Bottom panel*: Photometry profiles from the stacking of Sut12 voids and its six subsamples (same conventions).

The stacking of the 1055 voids of Pan et al. gives a faint signal below the $1\,\sigma$ level at about 1° which does not allow any interpretation. Such lack of results may have been expected and could be due to the high number of voids in the sample and their very wide distribution of angular sizes. I considered the idea of dividing this catalogue into subsamples based on redshift, radius, and/or angular sizes; however after several attempts, it did not yield any significant result, and I faced a number of issues regarding possible a posteriori selection effects and the hassle of finding appropriate bins of size for the subsamples. Indeed, a smaller number of structures implies a narrower range of sizes and redshifts, but it also greatly reduces the signal-to-noise ratio.

This issue was partially addressed for the Sut12 catalogue when I chose to analyse separately the six redshift subsamples – a simple division based on redshift but in principle free from selection effects. But as it can be seen in Fig. 3.14, only one of the subsamples (dim1) yields a negative signal in the photometry with a significance higher than $1\,\sigma$, the other profiles either spanning between 0-$1\,\sigma$ or being entirely positive (lrgbright). An

explanation for this apparent lack of significant results may be found again by considering the dispersion in the angular radii of the voids. Even if the subsamples from Sut12 contain significantly more objects compared to the Gr08 sample (and therefore should strengthen the signal), their sizes on the sky are also more scattered (as can be seen in Fig. 3.13). Mixing such a variety of void sizes will necessarily dilute the associated iSW signal over the same range of scales, and might drastically reduce its significance.

This preliminary analysis strongly suggests that it is necessary to take into account the size of each individual void in the stacking procedure in order to improve the significance of the results, i.e. use the rescaling procedure that I already performed with the Gr08 catalogue. As we have seen earlier, if the rescaling process does not at least increase the absolute amplitude of any previously detected signal, then any subsequent significance estimation is very unlikely be higher than without rescaling. Indeed, since the variance will also necessarily increase, this will in turn further decrease the S/N. Therefore I chose to first produce an overview of the rescaled photometry profiles for Sut12 and Pan12 in Fig. 3.15.

Again, no signal of particular importance arises from this new analysis of Pan12 voids, with amplitudes which do not depart much from the original stacking except at very small angular sizes, in all likelihood due to random fluctuations and unrelated to the underlying voids. Concerning the Sut12, signals seem to arise in several of the rescaled profiles, especially around a scale equal to 0.5-0.55 times the voids effective radii, with a clear departure from the results without rescaling for some of them, e.g. the lrgdim subsample. However, some of the other subsamples (bright1, lrgbright) do not apparently benefit from the rescaling procedure. I identified the two most promising subsamples, i.e. dim1 and lrgdim, and evaluated the significance of their rescaled profiles. The results, shown in Fig. 3.16, are close to the expectations from Fig. 3.15: the dim1 subsample yields a signal at ~ 0.52 times the void effective radius, with a significance similar (albeit a bit smaller) to the the results without rescaling (around $1.36\,\sigma$). This is coherent with the fact that the amplitude of the signal remained almost at the same level (illustrated by the corresponding dashed line in Fig. 3.15) whereas the rescaling procedure slightly increased the variance of the random stacks used in the S/N estimation. Remembering that we are still looking for an iSW signal, I can note that the apparently significant signals at small aperture angles ($\sim 0.15\times$ and $0.3\times$) are not constant across frequencies and therefore are probably not related to an iSW effect. Regarding the lrgdim subsample, it gives a $\sim 2.35\,\sigma$ signal around 0.57 times the void radius, a clear improvement over the non-rescaled results which was expected considering the stronger amplitude of the rescaled signal. For both subsamples, we note that the amplitude of the highlighted signal stays remarkably constant across frequencies, whereas as mentioned before the other potentially significant features of the profiles are not achromatic.

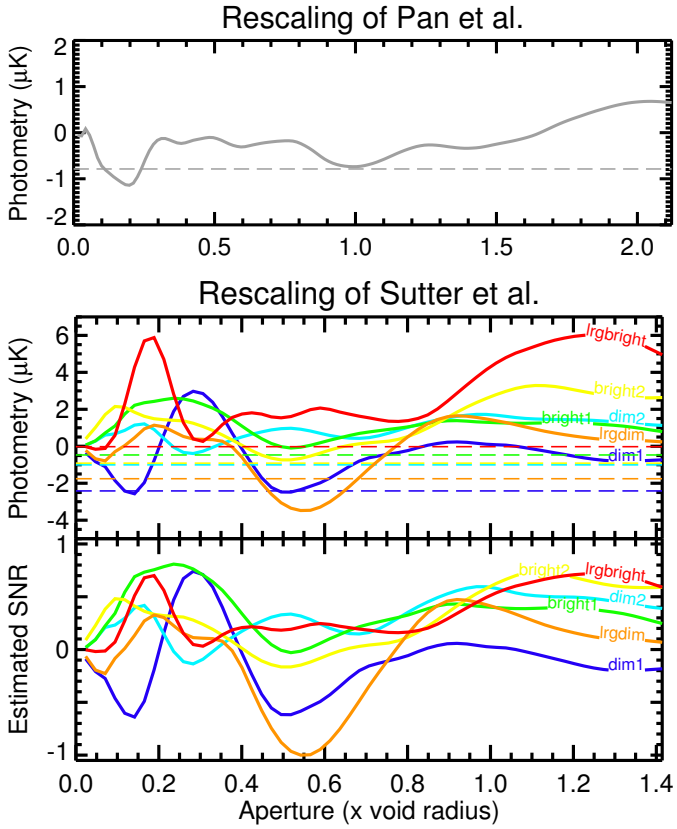

FIGURE 3.15: Summary of the photometry profiles extracted from the rescaled stacks of Pan12 (top) and Sut12 (middle), performed in the WMAP V band cleaned map. The coloured dashed lines indicate for each sample the lowest amplitude measured in the original stacked image (without rescaling the voids). These allow to roughly estimate if the rescaling procedure did improve the detection of any previously detected signal. The bottom panel shows the previous profiles multiplied by $\sqrt{N_v}$, with N_v the respective number of voids in each subsample. They are then normalized to the strongest signal (*lrgdim*). These curves provide an estimate of their potential significance as the noise in the stacked image is expected to scale as $1/\sqrt{N_v}$ approximately.

Interestingly, the highlighted scales show up consistently around (if not slightly above) half the effective radius of the considered voids, but this will be discussed more extensively in the following subsection. For now, I noted that the rescaling procedure was very fruitful in enhancing the photometry signals, and highlighted a seemingly consistent scale for several subsamples. Inspired by these observations, I wondered if the data from the Sut12 catalogue may be used in a more efficient way to further explore this hint of a signal.

3.3.3 Further improvement of the protocol

From the previous subsection, I gathered that in some of the Sut12 subsamples, an iSW-like signal seems to appear around 0.5-0.6 times the voids effective radii, and that it is especially significant in the *lrgdim* sample. A possible explanation may come from

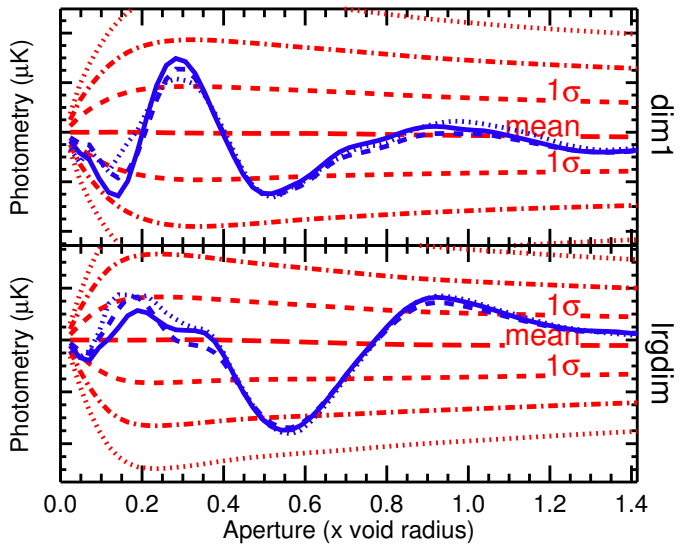

FIGURE 3.16: Photometry profiles and significance for the rescaled stacks of two Sutter et al. subsamples, *dim1* and *lrgdim* (same conventions as Fig 3.9).

the presence in this particular subsample of some of the largest voids in the whole Sut12 catalogue (as can be seen in Fig. 3.13) which are expected to yield the strongest iSW effect according to linear theory. We could argue that the *lrgbright* sample also contains many large voids but does not show such significant signal: however this could be explained by its small number of objects (50) and the consequently high level of noise from primordial CMB fluctuations in the stacked image.

This indicates that instead of considering each subsample separately, a better approach may be to combine them all and stack the voids starting from the largest ones. Indeed, in theory the noise should scale as usual roughly as the inverse square root of the number of stacked voids, but the stacked iSW signal is also expected to drop at some point due to the addition of smaller and less contributing voids. By starting from the largest voids, we intend to select the supposedly largest iSW contributions in order to keep the stacked signal from dropping too fast and effectively to boost the S/N of the detection. I carried out this analysis on the 1495 voids of Sut12, first focusing on the whole photometry profiles and increasing progressively the number of stacked voids. As expected, a negative signal consistently appears around an aperture of 0.54 times the voids effective radii. As intuited before, its amplitude gradually decreases as we include smaller and smaller voids in the stacking. In order to estimate the significance of this signal, I focused on the value of the photometry at this particular aperture scale: in the top half of Fig. 3.17, we show these values as a function of the increasing number of stacked voids. Similarly to the previous section, we estimate the significance of these values by repeating the analysis many times after randomly shifting the stacked positions. Therefore we can compute the S/N of these results, shown on the bottom half of Fig. 3.17. We note once again that the photometry is stable across frequencies and

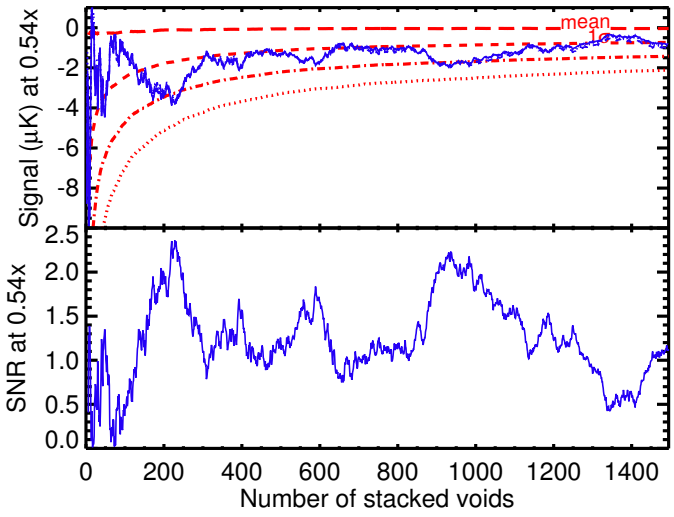

FIGURE 3.17: *Top:* Photometry values of the stacked and rescaled voids from the Sutter et al. catalogue, at an aperture of 0.54 times their effective radii, as a function of the number of voids (sorted by decreasing size). Significance contours are computed using random stacks produced from the WMAP V band cleaned map. Legend is identical to previous plots of photometry profiles (see Fig 3.9). *Bottom:* For the stacking performed in the WMAP V map, S/N of the above photometry values computed using the significance contours.

consistently negative for practically any number of stacked voids, but the shape of this curve and its significance are hard to interpret. The significance first rises up to $\sim 2.3\,\sigma$ for the first 200 stacked voids, a behaviour that would be expected from an iSW signal that progressively takes over the CMB noise. After this, the S/N quickly decreases and then oscillates between $\sim$ 1-2 σ before dropping after stacking more than 1300 voids. Although this significance appears to vary quite significantly, the stability of the signal itself (always negative and at the same scale) may indicate that this variability is due to random CMB fluctuations.

The scale of the detected signal clearly differs from the large sizes that were obtained with the Gr08 catalogue. What is encouraging here is that a physical explanation can be found for these smaller scales in the geometry of the voids from these subsamples. Indeed as noted by Sut12, the majority of them present a shape similar to a prolate ellipsoid with an ellipticity close to 2. Since the orientation of these voids is a priori random, we can intuit that stacking such ellipsoids (and their associated iSW signature) will eventually give a circular signal, with a smaller typical scale, closer to half the major axis of the ellipsoids.

Following this, I selected two particular numbers of voids with a high significance observed in Fig. 3.17, namely 231 and 983 voids, and performed the same photometry/significance analysis as usual. The results are shown in Fig. 3.18: both profiles highlight

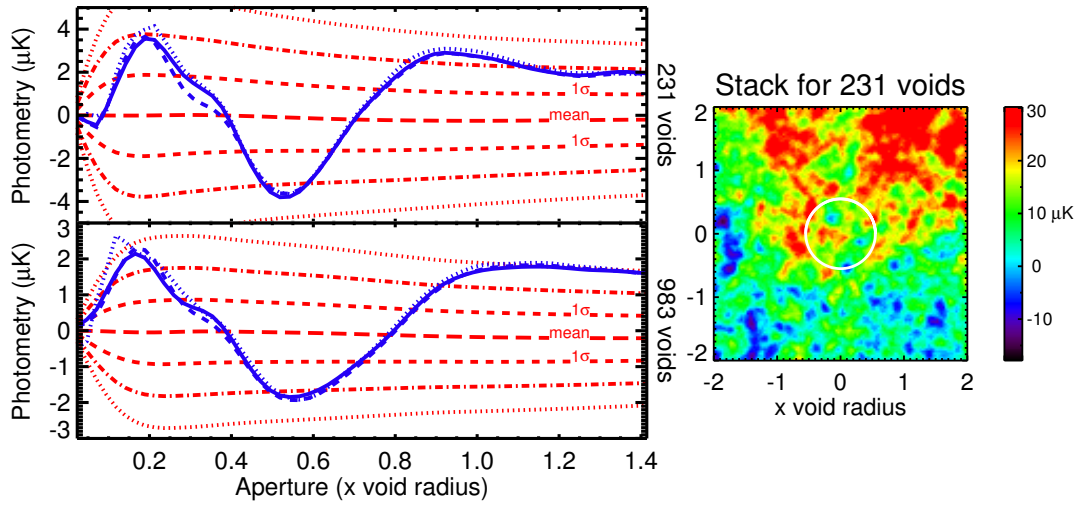

FIGURE 3.18: On the left, photometry profiles and significance of the rescaled stacking of the 231 (top) and 983 (bottom) largest voids from the Sutter et al. catalogue (same conventions as Fig 3.9). On the right, stacked images of the 231 largest voids with a rescaling of the CMB patches proportional to the void sizes.

a scale again equal to 0.54 times the voids effective radii where the signal reaches significances equal to $2.38\,\sigma$ and $2.20\,\sigma$ for the 231 and 983 voids respectively. Despite the bigger number of voids, the small drop in significance may again be caused by CMB fluctuations and/or the inclusion of small voids. Another notable feature appears in both photometry profiles, namely one hot significant signal at smaller scales ($\sim$ 0.2x) and one at larger scales ($>$ 0.9x). The former and its associated scale seem to coincide with an angular size close to 1°. It is directly related to the curious fact that the minimal temperature spots do not appear at the centre of the stacked image (see Fig. 3.18). Were the stacks centred on the coldest spot, I would not have obtained this positive signal in the photometry profiles at small angles. The origin of this hot central spot is undetermined, but could be due to several contributions of which the background CMB fluctuations, the irregular shape of the underlying voids, and the possible mismatch between the position of the void barycentres and their most underdense zones. Concerning the signal at larger scales, what comes to mind is the possible influence of large scale fluctuations through the low multipoles of the CMB, already glimpsed at in 3.2.2.3 with the large North-South gradient. Thus I redid the stacking of the same sets of voids on new maps with a few more low multipoles removed (from $\ell = 2$ to 20). The results then showed that these multipoles indeed have a non-negligible contribution to our photometry profiles: removing them reduces noticeably the measured amplitude at large scales but keeps almost intact the rest of the signal. Although it does not account for the entirety of the large scale signal, it does reduce its significance to less remarkable levels.

In summary, contrary to the Gr08 catalogue, the rescaling process had positive results

on the much larger catalogue of Sut12, highlighting a particular scale around half the void sizes in all the tests performed, in better agreement with our intuitive arguments. Although the maximum observed significance only reaches around $2.5\,\sigma$ and the signal depends quite significantly on the number of stacked voids and their size, the persistent nature of the signal seems to bolster the case for iSW detection. Lastly, the Pan12 catalogue did not benefit from the rescaling process, and I wish to mention that I also explored the same incremental approach used with the Sut12 catalogue but it did not yield any significant results. I hypothesise that this is caused by the narrow range of small sizes of these voids, whose faint iSW signal is likely to be dominated by CMB fluctuations.

To further elaborate on the possible conclusions that we can deduce from the present work, there are a couple of effects that can make the interpretation of the results even more difficult and that we should keep in mind. I will mention a few of them in the next section.

3.4 Precautions

3.4.1 Selection effects

The results from the previous section highlight the difficulty of getting a clear detection of a signal, at least when using the various catalogues as such. With this in mind, one could be tempted to amplify the signals hinted at by isolating the voids that contribute most in the stacking of a particular sample. I experimented with this idea, working with one of the best S/N from the results of the previous section: the rescaled stacking of the *lrgdim* subsample. From the 291 voids of the original set, I kept only the half (146) that contributes the most to the minimum of the photometry profile at the scale of 0.56 times the voids radii. The resulting photometry profile is plotted in Fig. 3.19 and indeed shows a dramatic increase in the amplitude of the signal. From there, the crux of the matter is to assess the significance of this new result. When using the same procedure as usual (many stacks of 146 random positions), I obtained a surprisingly high S/N, above $11\,\sigma$. This value clearly overestimates the real significance, as it ignores the selection that we performed on the sample. It is therefore required that I revise our protocol as follows. I first generate many sets of 291 random positions. Then for each set, I select and stack only the half that contributes most to the photometry profile at the same scale of 0.56 times the voids radii. Once I draw enough such random stacks, I keep the rest of the procedure identical. The corrected significance (Fig. 3.19) drops down to a level of ~ 2 comparable with (even lower than) the initial S/N in the original stack (Fig. 3.16).

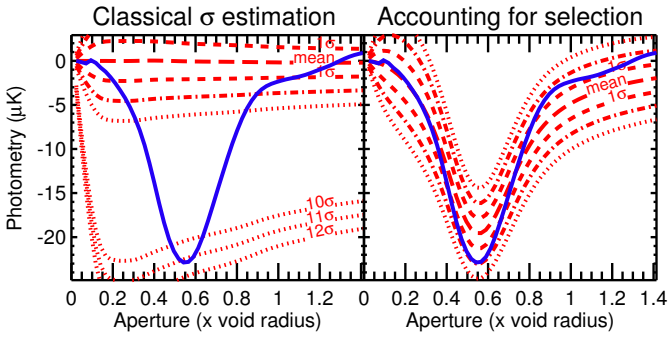

FIGURE 3.19: Photometry profile for the rescaled stacking of half the Sutter et al. *lrgdim* subsample (146 voids out of 291), chosen so that the amplitude at 0.56 times the voids radii is the strongest (see text for details). *Left:* the significance is estimated with stacks of 146 random positions. *Right:* the significance accounts for the selection effect. The difference between the two significances is obvious and very pronounced.

Therefore, such an a posteriori selection cannot be used to improve the S/N of the final stacked signal.

Actually, after playing a while and taking a closer look at these selection effects, I noticed that with only one set of a few hundred random positions, one can obtain a strong – but completely artificial – signal at almost any desired scale (Fig. 3.20) by selecting the appropriate half of it. This further illustrates, and warns us about the risk of a posteriori selections, and does put into perspective any apparently significant signal we obtained. The results from the new catalogues can be considered safe, as the only form of selection comes from the division of the Sut12 voids into redshift subsamples already performed a priori by the authors. The Gr08 results are probably also safe, although their 50 voids come originally from a ten times larger sample and were selected according to a density contrast criterium. This selection was also made by the authors prior to looking at CMB data. It is not clear however whether that selection might have helped increase the S/N artificially. Of further interest is the observation made by the Gr08 that either increasing or decreasing by a few tens the amount of voids in their selected sample does make the significance drop (mentioned in Sec. 3.1.3). This may either indicate a possible selection effect – thus casting doubt on the iSW nature of the signal – or be an expected effect due to the addition of noise-dominated voids (when increasing the number of voids) or the deletion of contributing voids (when decreasing it).

3.4.2 Alignment & overlap effects

When interpreting my results, another important issue arises due to the number and location of the voids studied. In principle, each one of them leaves an imprint in the CMB temperature. These hundreds of voids are confined in the area covered by the SDSS. Since the angular size of these objects often exceeds several degrees, they are

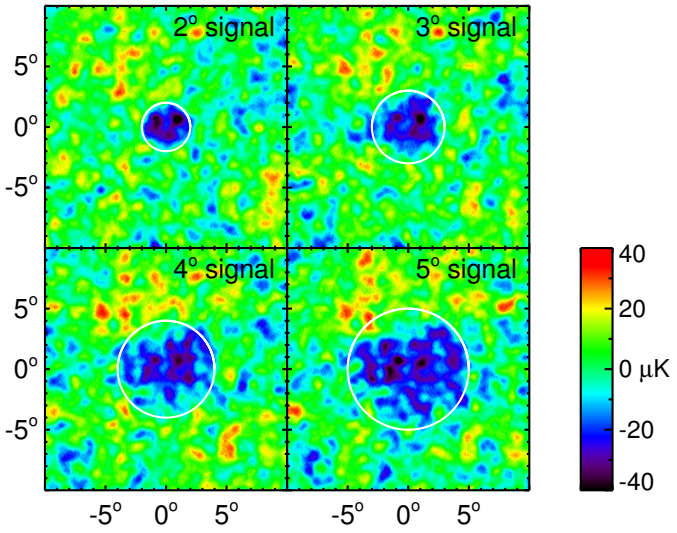

FIGURE 3.20: Illustration of selection effects: from a single set of around 200 random positions, we are able to construct a false "iSW-like" signal at any desired scale (here for angular radii of 2, 3, 4 and 5°) by selecting and stacking each time the appropriate half of the same set.

bound to fill this area and overlap. As a consequence, the stacking of a chosen set of voids contains in fact contributions from many others. Some structures may also be very close to each other on the sky, further complicating the interpretation of signals.

I devised two ways of quantifying these issues:

- First, for each individual sample, we compute both the total area covered by all the voids and the area where at least 2 voids overlap; we then compute the ratio of these quantities, which represents the "self-contamination" of each sample.
- Then, for every possible pair of samples, we compute the fraction of the area of the first sample shared by the second sample area – a measure of the contamination between samples.

The results of this study showed that every sample presents moderate to high contamination from other samples and self-contaminates itself quite strongly. The contamination is less pronounced for the Gr08 sample due to the small number of voids. Still, many voids from other catalogues will contribute to the stacking of the Gr08 voids, making it further difficult to interpret its relatively high significance results. This is true for every catalogue of voids identified in the same area: the level of overlap is very high and it would be difficult to determine which are the objects that produce the actual iSW signal. Moreover, the proximity of the voids may artificially amplify some detections due to the possibility of repeated stacking on the location of a significant signal/void.

Both aspects of this study showed that contribution from other samples is indeed frequent in the stacking of these voids. Supposedly, we can expect the contribution to cancel out for large numbers of stacked patches, although this argument may be weakened by the fact that voids represent a much larger fraction of the volume of the Universe than large overdensities (as shown by the large scale N-body simulations in the literature). In any case, the probability of measuring a false signal (due to a fortuitous event) may be heightened by the overlapping of so many voids. An accurate simulation of the expected signature from such a collection of overlapping structures will help quantify these contaminations and their effects on a possible iSW effect detection.

3.4.3 Spurious detections?

I would also like to stress that the superstructure data sets should be considered with caution. A quick comparison between the Sut12 and the Pan12 catalogues reveals that although they share a common interval in redshift (between $z = 0$ and 0.1), the structures identified by the two catalogues are very different. Whether it is by their radius, redshift, or position in the sky, the two sets of structures are quite hard to match: this mismatch may very well be due only to the different void finding algorithms used in the two works, although the fact remains that they were both based on the same survey (SDSS DR7) and should have more pronounced similarities.

On another note, during my work on the stacking of these superstructures, several updates of the Sut12 catalogue were released. The changes were stated as having no impact on the conclusions of the associated paper (Sutter et al., 2012). However, a detailed examination showed that modifications ranged from minor to more consequent ones. Numerous additional small voids were detected thanks to an improved void finding algorithm; quite a few voids were removed from one version to the other, and many others have seen modifications in their redshifts, sizes and positions on sky, up to the point where one of the subsample was almost completely different (*lrgbright*). These updates did consequently have a significant impact on the stacking of the voids, especially through the inclusion of the new small voids. For instance, with the July version, my procedure yielded a $\sim 2.5\,\sigma$ detection of a negative signal at about 2.4° in the *bright2* subsample prior rescaling, while in the latest version of the same subsample the photometry shows a positive excess with almost $2\,\sigma$ significance. Conversely, rescaling the voids improved the detection of a negative photometric decrement only with the latest version of the catalogue. While the present status of the catalogue should be considered as robust (according to a private communication I had with P. M. Sutter), the fact mentioned above makes it rather difficult to interpret without ambiguity the signals that I obtained.

The next-generation of galaxy surveys (such as LSST, Pan-STARRS or Euclid) will help alleviating some of these concerns: thanks to a better control of the systematics and observational biases, the use of these future surveys will hopefully allow a better identification of the structures confined within their boundaries. Combined with the much larger volumes surveyed by these future missions (i.e. with improved depth and sky coverage), the upcoming catalogues of structures will contain a large number of trustworthy objects. The stacking studies will certainly benefit from such new catalogues, and improve both the significance and our confidence in the results. The depth in redshift will also help investigating the influence of alignments such as those that I described in the previous subsection. Moreover, the increased precision of these surveys will allow to derive additional information on the structures such as their density/velocity profiles. This will in turn enable further cosmological tests and studies, such as the Alcock-Paczynski test (based on the geometry of the structures, see e.g. Sutter et al., 2012), or the exploitation of mass profiles to constraint the matter growth rate.

3.5 What does ΛCDM has to say on the matter ?

Up to this point in the present chapter, we have mainly looked at the results from the stacking procedure as such, trying to estimate their significance, in hope of finding "some kind of signal". Indeed, we only mentioned briefly the iSW signal expected from the kind of structures studied here, and made few links with theoretical calculations. In this last section, I assess where my results stand with respect to several works in the current literature that tried various approaches to tackle the prediction of the expected iSW contribution from superstructures.

3.5.1 Too small or too large signal ?

Before getting to the expected amplitude of the signal, let us focus on the size of the signature itself first. As I mentioned in the previous sections of this chapter, there seems to be a gap on this particular point between the stacking results of the Gr08 catalogue and the Sut12 one. The former yields a signal for the superclusters which has a size significantly larger than the underlying structures (2.6 times their mean angular radius), and a more reasonable scale for the supervoids (with a maximum of significance around x0.9 their size). On the other hand, the latter produce a signal with a typical scale of about half the size of the voids, which may seem more natural using some simple arguments about the iSW effect and the geometry of the structures (cf. 3.3.3 for more details).

Nonetheless, a recent study by Cai et al. (2013) comforts these intuitions: they constructed large N-body simulations following a ΛCDM cosmology and identified the voids in the manner of Sut12 and Gr08. They subsequently computed the iSW signature resulting from the stacking of their simulated voids which highlighted an optimal scale around 0.6 times the effective radius of the voids for the analysis by aperture photometry. The similarity between this predicted scale and the signal I observed in the Sut12 void subsamples is encouraging. In contrast, using a different approach Hernández-Monteagudo and Smith (2012) generated matter density maps (from both Gaussian and N-body simulations) that followed the redshift distribution of Gr08, from which they derived full-sky iSW maps. After performing a stacking in these maps at the locations of the density peaks/troughs, they found that the scales highlighted by aperture photometry ranged from 1° to 20°, with a maximum around 7° – seemingly in better agreement with the Gr08 results, in the sense that it explains why the highlighted scale tends towards higher values. These somewhat contradictory predictions does not allow to conclude on the agreement of my results with theory, although none of the aforementioned works is really dedicated to compute the exact expected signal from such structures – a task that will be at the centre of the next chapter.

3.5.2 Is $\sim 10\,\mu$K too much ?

The question of the supposed size of the iSW signal seems not solved yet. However, both the aforementioned studies concur on one point: the amplitude of the Gr08 signal (about 9.6μK) is significantly higher that what is expected. Using their N-body simulations of a ΛCDM universe, Cai et al. (2013) predict a photometry signal barely at the level of $0.1\,\mu$K, while the Gaussian simulations of Hernández-Monteagudo and Smith (2012) yield a maximum signal of $\sim 2\,\mu$K. They are joined in their conclusions by the work of Flender et al. (2013) who developed a theoretical model that goes beyond the linear approximation in order to compute the expected signal of the Gr08 objects, only to find a $3\,\sigma$ discrepancy between predicted (around $2.2\,\mu$K) and measured signals.

Up to now, the predictions from the literature seems therefore to reach a consensus on this matter; however, all of the results from these works are quite hard to directly compare to any of the stacking results from a particular catalogue. Indeed, these works consider the general features of the Gr08 structures (*mean* size, *mean* redshift, etc.) without considering the properties of each individual structure, their own expected signature, the influence of their relative locations on the sky, etc. This complicates the comparisons between these predictions and the results from an actual catalogue such as the Sut12 one. In this context, I felt that it would be necessary to be able to compute

an exact modelling of the impact of single superstructures on the CMB temperature, which is precisely the the aim of the next chapter.

3.6 Related personal publications

• Ilić et al. (2013), "Detecting the integrated Sachs-Wolfe effect with stacked voids", A&A, 556, A51

• Planck Collaboration (2013c) "Planck 2013 results. XIX. The integrated Sachs-Wolfe effect", submitted to A&A

A&A 556, A51 (2013)
DOI: 10.1051/0004-6361/201321150

Astronomy & Astrophysics

Detecting the integrated Sachs-Wolfe effect with stacked voids

Stéphane Ilić, Mathieu Langer, and Marian Douspis

Institut d'Astrophysique Spatiale, UMR 8617, Université Paris Sud & CNRS, Bât. 121, 91405 Orsay, France
e-mail: stephane.ilic@ias.u-psud.fr

Received 22 January 2013 / Accepted 19 May 2013

ABSTRACT

The stacking of cosmic microwave background (CMB) patches has been recently used to detect the integrated Sachs-Wolfe effect (iSW). When focusing on the locations of superstructures identified in the Sloan Digital Sky Survey (SDSS), Granett et al. (2008a, ApJ, 683, L99, Gr08) found a signal with strong significance and an amplitude reportedly higher than expected within the ΛCDM paradigm. We revisit the analysis using our own robust protocol, and extend the study to the two most recent and largest catalogues of voids publicly available. We quantify and subtract the level of foreground contamination in the stacked images and determine the contribution on the largest angular scales from the first multipoles of the CMB. We obtain the radial temperature and photometry profiles from the stacked images. Using a Monte Carlo approach, we computed the statistical significance of the profiles for each catalogue and identified the angular scale at which the signal-to-noise ratio (S/N) is maximum. We essentially confirm the signal detection reported by Gr08, but for the other two catalogues, a rescaling of the voids to the same size on the stacked image is needed to find any significant signal (with a maximum at $\sim 2.4\sigma$). This procedure reveals that the photometry peaks at unexpectedly large angles in the case of the Gr08 voids, in contrast to voids from other catalogues. Conversely, the photometry profiles derived from the stacked voids of these other catalogues contain small central hot spots of uncertain origin. We also stress the importance of a posteriori selection effects that might arise when intending to increase the S/N, and we discuss the possible impact of void overlap and alignment effects. We argue that the interpretation in terms of an iSW effect of any detected signal via the stacking method is far from obvious.

Key words. cosmic background radiation – dark energy – large-scale structure of Universe

1. Introduction

Among the many sources of secondary anisotropies of the cosmic microwave background (CMB) temperature (for a recent review, Aghanim et al. 2008), the integrated Sachs-Wolfe (henceforth iSW, Sachs & Wolfe 1967) effect is particularly interesting in connexion with the acceleration of cosmic expansion. In principle, in a universe not dominated by cold matter, the energy of CMB photons is redshifted or blueshifted while they travel across cosmic over-densities or underdensities, respectively, owing to the stretching-out of the gravitational potentials created by the structures. Since the amplitude of this effect is expected to be rather small and shows mostly on the largest angular scales (due to a line-of-sight cancellation, Kofman & Starobinskii 1985), it has been suggested, first in the context of studies of the Rees-Sciama effect (Crittenden & Turok 1996), to cross-correlate the CMB temperature fluctuations with the distribution of tracers (e.g. galaxies) of gravitational potentials. After the first attempts to detect the iSW effect by that method (Boughn et al. 1998; Boughn & Crittenden 2002), many studies have been published using the latest galaxy survey data. Often based on similar data and comparable techniques, the claims for detection range remarkably from a "negligible" to a $\sim 4.5\sigma$ statistical significance (for a discussion, see Dupé et al. 2011, and Giannantonio et al. 2012).

This puzzling situation calls for clarification. Discussions of the cross-correlation methods and techniques set aside, it would be invaluable to have another way to unveil the iSW effect. One such way would be to measure it directly in the CMB maps at the locations of the gravitational potentials that are responsible for it. Unfortunately, its amplitude with respect to the primary CMB anisotropies does not allow us to detect it structure by structure. However, stacking techniques can be profitably adopted to enhance the signal-to-noise ratio (S/N). With the help of the *Wilkinson* Microwave Anisotropy Probe (WMAP) five year maps (Hinshaw et al. 2009), such a technique has been applied by Granett et al. (2008a) to the supervoids and superclusters they identified in the catalogue of luminous red galaxies (LRGs) in the Data Release 6 (DR6) of the Sloan Digital Sky Survey (SDSS) (see also Granett et al. 2008b). Their super-structure identification method uses the VOBOZ (VOronoi BOund Zones, Neyrinck et al. 2005) and ZOBOV (ZOnes Bordering On Voidness, Neyrinck 2008) Voronoi tessellation-based, publicly available numerical codes. Focusing on the most significant (in terms of the density contrast) 50 supervoids and 50 superclusters, Granett et al. (2008a) report a combined mean temperature deviation of 9.6 μK, at a significance just above 4σ, which they interpret as a signature of the iSW effect. However, Hernández-Monteagudo & Smith (2012) pointed out that when considering several aperture scales (ranging from 1° to 20°), a combined χ^2 analysis yields a detection at a level of only $\sim 2\sigma$.

Using the Millennium simulation (Springel et al. 2005) and measuring the iSW effect that is expected in a standard ΛCDM universe, Granett et al. (2008a) find that it is $\sim 2\sigma$ lower (at 4.2 μK) than what they obtained from the WMAP data. Other studies have also measured a somewhat higher iSW effect than expected (e.g. Giannantonio et al. 2008, 2012; Ho et al. 2008), although with small statistical significance. The high significance and the stronger-than-expected amplitude of the iSW effect detected through stacking have stimulated a number of investigations. For instance, Hunt & Sarkar (2010) argue that LRGs need to be unnaturally underbiased tracers of matter if we want to attribute the signal measured by Granett et al. (2008a) to the iSW effect in the standard ΛCDM model. Nadathur et al. (2012) carefully analyse possible biasing effects

A&A 556, A51 (2013)

arising from the strategy adopted by Granett et al. (2008a), but show that even when those selection effects are taken into account, the signal from supervoids expected within standard ΛCDM is still at odds by $>3\sigma$ with the value measured by Granett et al. (2008a, for similar conclusions reached with numerical simulations of the iSW effect, see Flender et al. 2013). On the other hand, Pápai & Szapudi (2010) describe the superstructures by uncompensated density profiles from Gaussian statistics and find that large temperature deviations, $\Delta T \sim 10\,\mu$K, can be obtained. Moreover, building on this result, Pápai et al. (2011) re-assessed the statistical significance of those values and estimated that the discrepancy between the observations and the theoretical ΛCDM predictions is 2σ. However, as noted in Nadathur et al. (2012), the latter interpretation would imply voids with unphysical underdensities $\delta < -1$. Finally, we note that Granett et al. (2009) analysed again the WMAP 5 CMB data with a template fitting method and confirmed the 4σ significance of the signal found previously. Furthermore, they also reconstructed an iSW map from the very same LRG sample they used for their previous superstructure identification. On that reconstructed map, however, the combined voids and clusters associated temperature deviation was only $0.08 \pm 0.1\ \mu$K, casting doubt on the suggestion that the signal is indeed due to the linear iSW effect.

Should we conclude that the large CMB temperature deviations measured in association with superstructures signal a tension with the ΛCDM model? In this paper, we would like to take a further step towards answering that question. Since the study of Granett et al. (2008a), new CMB maps have been released and other superstructure catalogues have been published. We do the stacking analysis with the new data and look for the iSW signal that could be associated with the large scale structure. We pay particular attention to the bias introduced into the results by selection effects and illustrate it with an explicit example. We begin by introducing the data used for this study. In Sect. 3, we outline the methodology we adopted, stressing the assessment of the statistical significance of our results. The latter are detailed in Sect. 4, and in Sect. 5 we discuss the importance of a posteriori selection effects that may artificially boost the statistical significance, as well as other sources of uncertainty that cloud the interpretation of the results. Finally, we conclude in Sect. 6. We use the parameters from WMAP 7 (Komatsu et al. 2011) best-fit cosmology for all relevant calculations.

2. The data

2.1. Cosmic microwave background

In the present study, we have used the maps of the cosmic microwave background released by the WMAP team after seven years of observation (Jarosik et al. 2011), in contrast to the five-year data used by Granett et al. (2008a, Gr08 thereafter) in their study. We took the individual channel maps at the three frequencies that are the less contaminated by foregrounds (the *Q*, *V*, and *W* bands at 41, 61, and 94 GHz, respectively). We also used the hit map of the WMAP mission, i.e. the map that contains for each pixel the number of times it was observed in the satellite lifetime. The impact of foregrounds and the associated possibility of false signals is often a source of uncertainty in iSW studies. We therefore consider and assess their possible influence by redoing our analyses on the foreground reduced maps released by the WMAP team in the same frequency channels[1].

2.2. Granett et al. (2008)

The first catalogue of superstructures (clusters and voids) that we considered was created and studied by Gr08. Since it was already explored with WMAP 5-year data, it will serve us as a "fiducial" set when testing all the steps of our own stacking procedure. This will also be the opportunity to revisit the work of Gr08 with the newer seven-year data from WMAP.

The catalogue is based on the LRG sample of the SDSS DR6 (Adelman-McCarthy et al. 2008), which is composed of 1.1 million LRGs in the range $0.4 < z < 0.75$ (with a median $z = 0.52$), covers 7500 square degrees on the sky, and occupies a volume of $\sim 5\ h^{-3}$ Gpc^3. In this survey, Gr08 searched for clusters and voids respectively using the two publicly-available structure-finding algorithms VOBOZ and ZOBOV based on Voronoi tessellation. They detected 631 voids and 2836 clusters above a 2σ "significance level", defined as the probability of obtaining the same density contrasts as those of voids and clusters in a uniform Poisson point sample.

From these results, they kept and released the 50 most significant clusters and 50 voids only, which they used in their CMB stacking analysis. The catalogue of these 100 superstructures contains all the information needed for their analysis. For each structure it provides the position of its centre on the celestial sphere, the mean and maximum angular distances on the sky between the galaxies in the structure and its centre, its physical volume, and three different measures of its density contrast (either calculated from all its Voronoi cells, from only its over/underdense cells, or from only its most over/underdense one).

After conversion to physical distances (see details in Sect. 2.5), we note that these voids have a mean effective radius of about 78 Mpc and a mean redshift of ~0.5, corresponding to angular sizes on the sky of about 3.5 degrees.

2.3. Pan et al. (2012) void catalogue

Pan et al. (2012) published a catalogue of cosmic voids and void galaxies identified in the seventh data release (DR7) of the SDSS. Using the VoidFinder algorithm as described by Hoyle & Vogeley (2002), they identified and catalogued 1055 voids with redshifts lower than $z = 0.1$. For each void they provide its position on the sky (also, but not useful for us, its 3D position in the survey), its physical radius (defined as the radius of the maximal sphere enclosing the void), an effective radius (as voids are often found to be elliptical) defined as the radius of a sphere of the same volume, its physical distance to us, its volume, and mean density contrast.

The filling factor of the voids in the sample volume is 62%. The largest void is just over 47 Mpc in effective radius, while their median effective radius is about 25 Mpc. Some of them are both very close to us and relatively large (more than 30 Mpc in radius) resulting in large angular sizes on the sky, up to 15 degrees and above.

2.4. Sutter et al. (2012) void catalogue

The most recent catalogue considered in the present study was released by Sutter et al. (2012)[2]. Using their own modified version of the void finding algorithm ZOBOV, Sutter et al. also built a void catalogue from the SDSS DR7, taking particular care to

[1] All maps can be downloaded from the LAMBDA website http://lambda.gsfc.nasa.gov

[2] Catalogue published on-line at http://www.cosmicvoids.net, version 21/02/2013.

Table 1. Summary of the void catalogues.

(Sub)sample name	Redshift range	Number of voids
Sutter et al.	$0.003 < z < 0.43$	1495
dim1	$0.003 < z < 0.048$	218
dim2	$0.05 < z < 0.1$	419
bright1	$0.1 < z < 0.15$	341
bright2	$0.15 < z < 0.20$	176
lrgdim	$0.16 < z < 0.35$	291
lrgbright	$0.36 < z < 0.43$	50
Granett et al.	$0.43 < z < 0.69$	50
Pan et al.	$0.009 < z < 0.1$	1055

account for the effects of the survey boundary and masks. In the latest version of their catalogue, they found a total of 1495 voids, which they divided into six distinct subsamples of increasing redshift: four from the main SDSS (named *dim1*, *dim2*, *bright1*, and *bright2*) and two from the SDSS LRG sample (*lrgdim* and *lrgbright*). The redshifts of these voids span $z \sim [0, 0.4]$, while their sizes range approximatively from 5 to 150 Mpc. A summary of the six subsamples and their contents is provided in Table 1, together with the contents of the other two catalogues described in Sects. 2.2 and 2.3.

This catalogue stands out by the amount of information provided about its voids: position of the barycentre, redshift, effective radius (with the same definition as in the Pan et al. catalogue), locations of member galaxies, one-dimensional radial profiles of stacked voids, two-dimensional projections of stacked voids, and other statistical information about their distribution. Since its first release in July 2009, the catalogue has been subjected to regular updates and modifications reflecting improvements in the detection algorithm and bug corrections, along with inclusion of additional void data.

2.5. Using the void catalogues

The only indispensable information that we extract from these catalogues is the positions on the sky of the observed structures (most frequently the position of their barycentre), which is essential to apply the stacking procedure. They are most often provided in celestial coordinates (RA, Dec) that we easily convert into galactic coordinates in order to use them in the framework of the HEALPix[3] suite. For more advanced analysis and interpretations, we first require the redshift of these structures, which is a parameter that is directly given in the considered catalogues, except for that of Pan et al., which we obtained from the physical distance to the voids. Finally we also make use of the physical radius of the structures, through its relation to the angular size on the sky (see Sect. 5.2). When provided, we use the effective radius of the structure (Pan et al., Sutter et al.), which we translate into an angular size using the available redshift information. For the Gr08 catalogue, we derive the effective radius – with the same definition as in the two other catalogues – from the provided volume, and then also convert it to an angular size. This is somewhat of a compromise between the two angular sizes already provided by Gr08: the mean radius between the centre of the void and all its Voronoi cells (possibly an underestimate of the void size on the sky), and the maximum radius between the centre and the farthest cell (possibly an overestimate).

[3] http://healpix.jpl.nasa.gov

Of the Gr08 catalogue, we only use the voids and disregard the clusters, for the sake of consistency with the other two catalogues, but also because voids are more adapted to stacking studies; indeed, emission of an astrophysical origin is less likely to contaminate the iSW signal from these objects. As a summary, we plot the properties of the voids from all catalogues in Fig. 1, including their redshifts, effective radii, and corresponding angular sizes.

3. Methodology

3.1. Initial procedure

The analysis of these three different catalogues requires us to have a robust and well defined procedure for a systematic analysis of all the structures considered. First, the standard stacking procedure that we apply in this study consists in the following steps, for each superstructure sample or subsample:

- We first take a CMB map of the WMAP data at a given frequency, either raw or foreground cleaned, from which we remove the cosmological monopole and dipole;
- We construct the associated weight map by taking a galactic mask (here the KQ75 from the WMAP team, the extended mask for temperature analysis that removes ∼22% of the sky along the galactic plane and around point sources) and multiplying it by the hit map associated with the survey;
- We retrieve the galactic longitudes and latitudes of the structures we study;
- We use a custom code based on the HEALPix package to cut a patch in the CMB map centred on each structure. We choose the patches to have a 6 arcmin/pixel resolution (small enough to oversample any of the CMB maps used) and to be squares of 301×301 pixels, i.e. $30^\circ \times 30^\circ$ patches;
- At the same time, we cut identical square patches at the same locations in the associated weight map;
- The final stacked image is then constructed as the average image of all CMB patches weighted by their corresponding weight patches.

Two main products are then extracted from the stacked image:

- the radial temperature profile starting from the centre of the image, by computing the mean temperature of the pixels in rings of fixed width and increasing angular radius. Considering the characteristics of our stacked images, it is calculated here for 150 radii between 0° and 15°, with a width of $\Delta\theta = 0.1^\circ$;
- the aperture photometry profile, using a compensated filter approach. At each angle θ, we compute the photometry as the difference between the mean temperature of the pixels inside the disk of angular radius θ and the temperature of the pixels in the surrounding ring of same area, i.e. the ring enclosed between circles of radii θ and $\theta\sqrt{2}$. With this procedure, we obtained this profile for 150 angles between 0° and $(15/\sqrt{2}) \sim 10.6^\circ$.

The summation of square pixels contained inside a disk can lead to calculation errors due to omitted fractions of pixels close to the boundaries of the disk. To reduce these as much as possible, we upscale the 301×301 stacked image into a 1204×1204 one – each pixel of the original image is divided into 16 sub-pixels of the same value. Statistical errors for these two profiles are estimated by computing the standard deviation of each calculated mean of pixels. We mainly focus on the analysis of these two

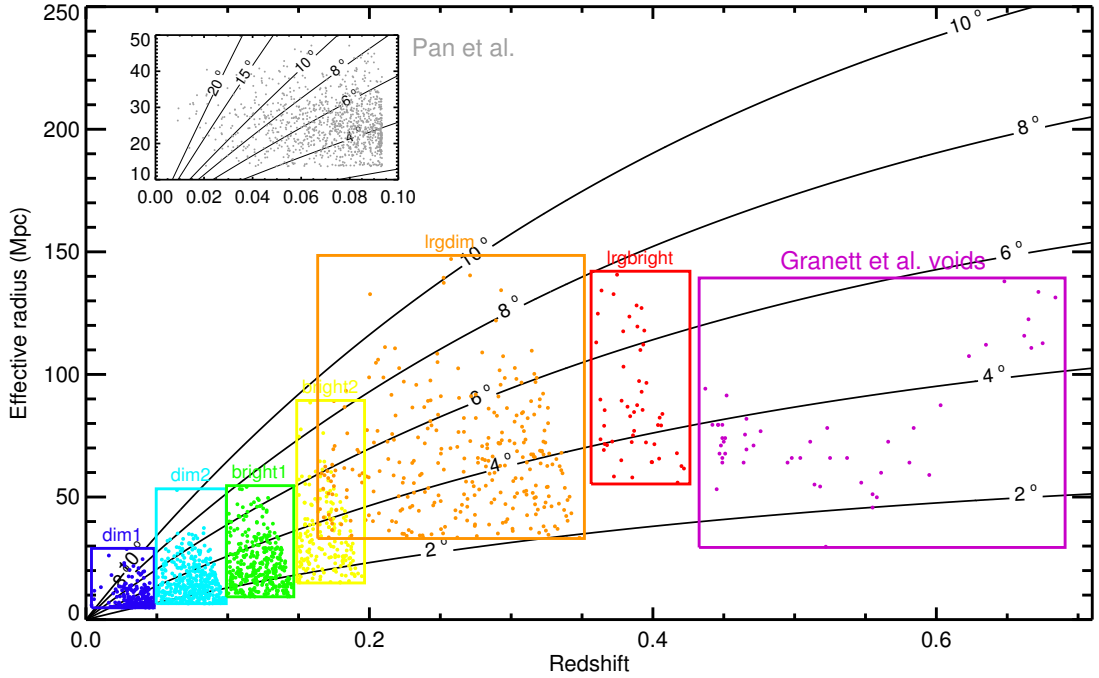

Fig. 1. Effective radii (in Mpc) as a function of redshift for all the voids used in this work. The two catalogues of Granett et al. and Pan et al, and the six subsamples of Sutter et al. are delimited by boxes labelled by their names. The black curves are here to indicate the angular size (in degrees) of a structure in the redshift-radius plane.

profiles (the image itself is useful for illustration purposes only), where we look for any remarkable signal whose significance we assess below (see Sect. 3.3).

We note that the size of the CMB patches is chosen large enough to enclose any of the structures studied and to properly compute their photometry (based on the effective angular radius that has to be smaller than ∼10.6°), with the exception of 11 voids (out of 1495) in the Sutter et al. catalogue and 21 in the Pan et al. one (out of 1055); we omit these voids in the stacking.

3.2. Choice of maps

Each of the three CMB maps that we use (WMAP Q, V, and W) inherently has a different resolution and contains different types and levels of foregrounds that may contaminate them. Before progressing any further, we assess the impact of the properties of each map, using our fiducial stacking (i.e. using the Gr08 void positions) as a basis.

3.2.1. Effects of resolution

We perform the fiducial stacking of the Gr08 voids on the three raw CMB maps from the Q, V, and W frequency bands, the beam sizes of which are, respectively, 30.6, 21 and 13.2 arcmin; an example of a stacked image is shown in Fig. 2. To have a consistent stacking analysis through all the considered frequencies, we need to "standardise" those maps by first smoothing them at the lowest resolution of the three (the Q band map) in order to lose as little information as possible. We then redo the fiducial analysis, and the resulting profiles are plotted in Fig. 3.

The stacks at each frequency, both raw and smoothed, give roughly the same results with only percent-level differences especially for the photometry profiles – the most useful products here. The degradation of the V and W maps to the lower resolution of the Q map naturally smooths the measured profiles and reduces their dispersion around the results of the Q band,

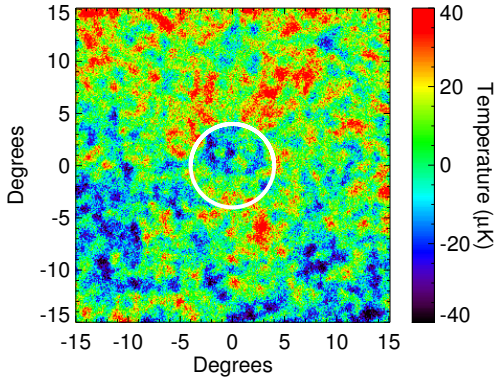

Fig. 2. Image resulting from our stacking procedure at the location of the 50 voids of Gr08, here using the V band CMB map of WMAP. A cold spot, reportedly due to the iSW effect, is visible roughly at the centre of the image with an angular radius of about 4° (underlined by the 4° radius white circle centred on the image).

which is the desired effect. Otherwise, this procedure does not significantly modify their amplitude and angular dependence, so that we may adopt hereafter this new common resolution for all frequencies.

In all cases, a signal appears in the photometry profile with a maximum (in absolute value) on an angular scale of about 3.5°, the preferred size changing only very slightly between frequencies. We keep in mind that the smoothing procedure with a ∼30.6 arcminute beam blurs the information and details contained below this scale, therefore we should not devote too much attention to any feature in the profiles at angles lower than this value.

3.2.2. Assessment of the effects of the foregrounds

One other source of concern comes from the influence of foregrounds present in the CMB maps, because they might mimic

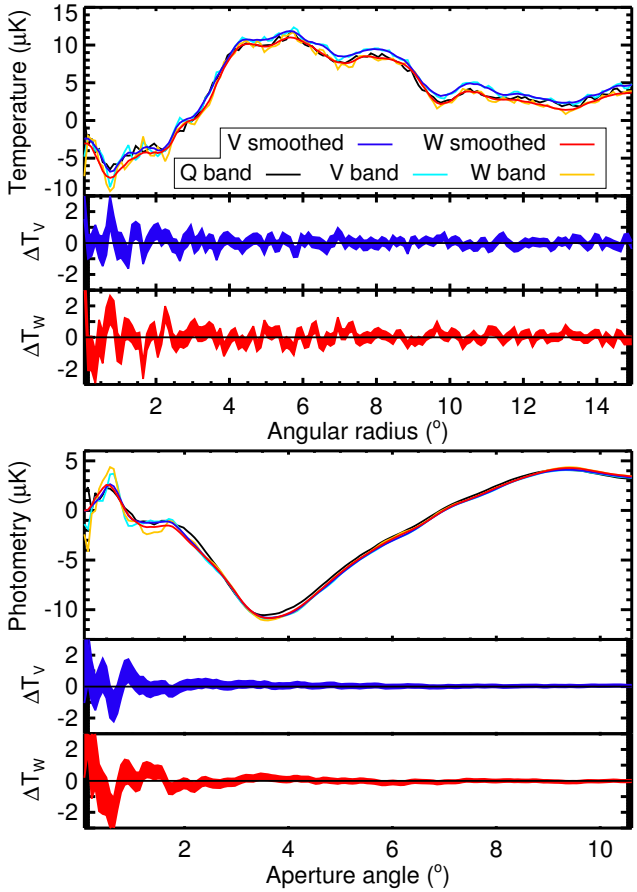

Fig. 3. *First plot*: radial temperature profiles (*top panel*) of the stacking of Gr08 voids, done on WMAP Q, V, and W maps (both in native resolution and smoothed by a 30.6 arcminutes kernel). The differences in the profiles between the smoothed and original maps are plotted below the main plot (*middle*: V band; *bottom*: W band). The width of the shaded curves corresponds to the statistical errors on the profile measurements. *Second plot*: same graphs and legend as above but for the aperture photometry profiles of the stacking of Gr08 voids.

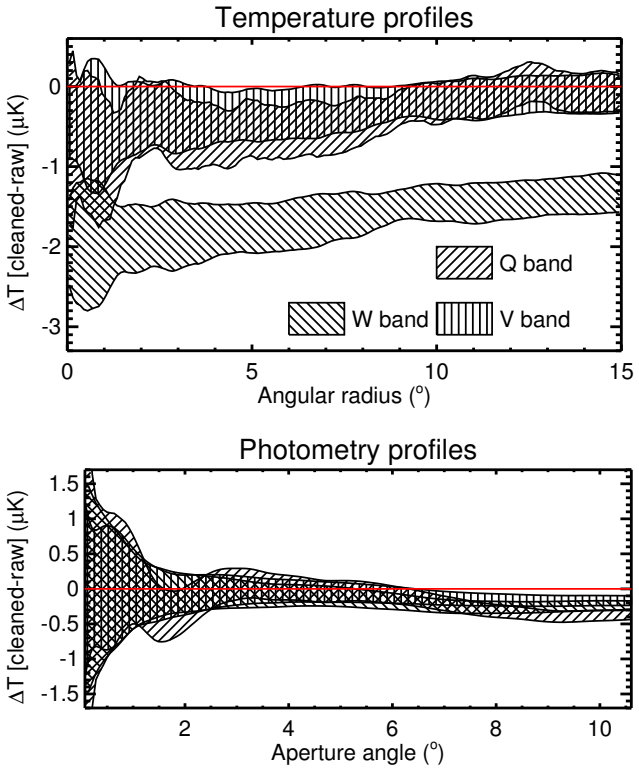

Fig. 4. For the Gr08 stacking, differences in the temperature (*top*) and photometry (*bottom*) profiles between foreground-cleaned maps and raw maps, for the three frequency bands considered. The width of the shaded curves corresponds to statistical errors on the profile measurements. The quasi-flat offsets observed in the temperature profiles do not affect the photometry substantially.

the expected iSW signal in the stacked images. To assess their possible impact, we performed the stacking of the Gr08 voids first on raw and then on foreground cleaned CMB maps at all frequencies. We then look for differences between the two results, either in the amplitude or in the shape of the signal.

Results are illustrated in Fig. 4: we obtain systematic offsets of a few micro-kelvins in the radial temperature profiles and less in the photometry profiles. This indicates that we mainly remove an almost uniform background, which does not influence the aperture photometry of the stacked image much. As a precaution we then use the foreground cleaned maps for our analyses. Possible residuals in the cleaned maps should not be of any concern since they would have the same "flat" behaviour in the stacked images.

3.2.3. Analysis of the temperature gradient

Another map-related problem showed up during our investigations, when we observed that a clear temperature gradient appeared in many of our stacked images with the new catalogues, roughly on a north-south axis with hotter high latitudes (see an example in Fig. 5). Foregrounds can be excluded as a possible source of this, because the gradient appears in both raw and foreground-cleaned maps, and also to a lesser extent because it is contrary to our intuition about foreground contamination since we would expect hotter temperatures closer to the galactic plane. One may wonder why this gradient was not observed by Gr08, but this can be explained by their rotating the CMB patches before stacking them in order to align the major axes of the voids. Since the voids are randomly oriented a priori, introducing such rotations is enough to erase any systematic gradient. In our study, we did not have any access to the information on the orientation of the voids (it is not included in the Gr08 catalogue) so we did not rotate the CMB patches. A systematic gradient in the final image is clearly observed (see Figs. 2 and 5).

After discarding foregrounds as culprits, we looked for "intrinsic" causes of this gradient. This led us to decompose the CMB maps on the spherical harmonics and to analyse the individual contribution of each multipole. This approach proved fruitful since it appears that the measured gradient is mainly caused by the first few multipoles of the CMB maps we use, especially by the $\ell = 6$ multipole map. In the region of the sky covered by the SDSS (where all the superstructures we considered are located), these multipoles combine to yield indeed a strong north-south gradient (see Fig. 6), which will be present at some level in every patch of CMB, hence in the final stacked image.

Visually speaking, subtracting the contribution of these multipoles out of the CMB maps does effectively remove the gradient in the stacked image. But on the other hand, the effect is almost negligible in the photometry profile of the Gr08 voids: indeed, the removed contribution most often has the shape of a simple tilted plane (see Fig. 5 for an example), which does not affect the aperture photometry since it is equivalent to a

A&A 556, A51 (2013)

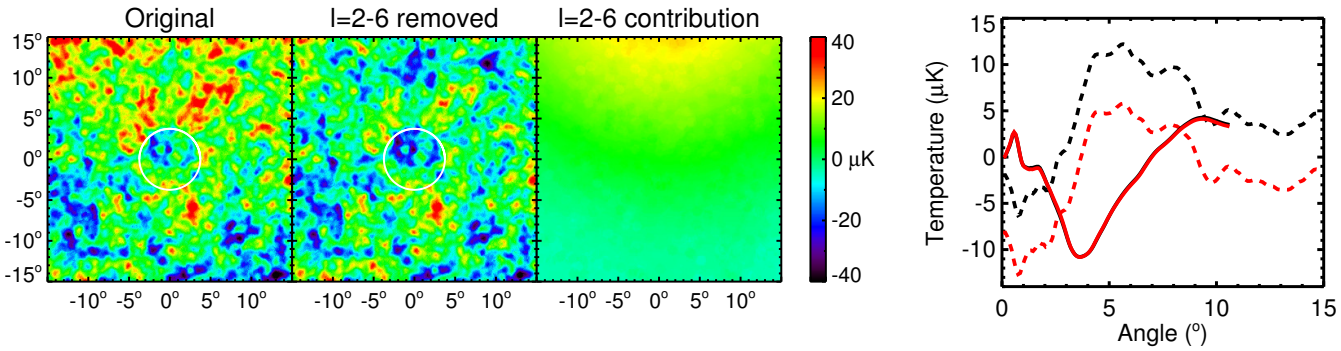

Fig. 5. Stacking of the Gr08 voids done (from *left to right*) on the cleaned WMAP *V* map, on the same map without its $\ell = 2$–6 multipoles, and on these multipoles only. The temperature (dotted curves) and photometry (solid) profiles shown in the rightmost plot are obtained from the first (black curves) and second (red) stacked images. The temperature offset induced by the removed multipoles does not affect the photometry.

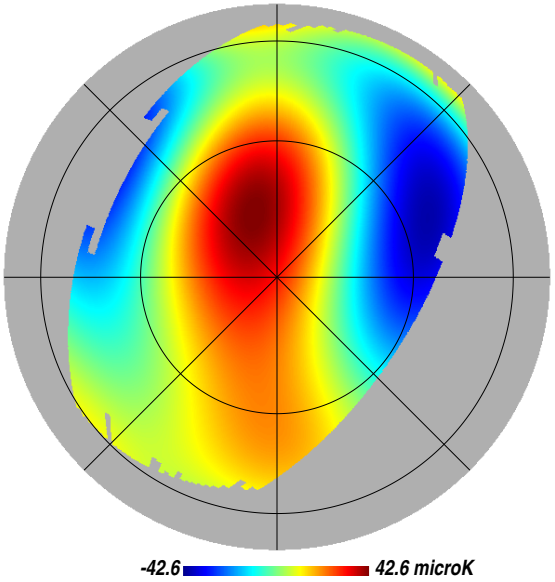

Fig. 6. Orthographic projection of the $\ell = 2$ to 6 multipoles map extracted from the foreground reduced WMAP Q map, in galactic coordinates. Only half of the map is visible (centred on the galactic north pole), with a mask showing only the area covered by the main SDSS. A graticule grid has been superposed with a 45° step in longitude and 30° in latitude.

constant background in the calculation. Indeed this gradient affects very low multipoles ($\ell \sim 2$–6) that correspond to angular scales larger than ∼30°, well above the angular sizes considered in the stacked profiles ($\theta < 15°$). For this reason, we will keep using the original CMB maps in our studies, which will also prevent the possible removal of relevant information in the stacked images. However since the other two catalogues that we use contain voids with larger angular sizes, we should keep the influence of this gradient in mind in the remainder of the analysis. We should also remember that all the temperature profiles will be affected by a systematic offset as shown in Fig. 5.

3.3. Significance estimation

When taken alone, the stacked images and their associated profiles are not enough to conclude anything about a possible detection of the iSW effect. Any peculiar feature that seems to stand out could very well be a random event well within statistical fluctuations. As a consequence, we have to take great care in assessing the significance of our results.

We have devised a systematic way to compute the significance adopting a Monte Carlo approach. We consider the stack of N_v voids, identified in the data, whose significance we try to estimate. We pick many sets (at least 10 000) of N_v random positions on the sky confined within the area covered by the SDSS. For each random set, we perform the same analyses as for the data voids; i.e., we produce a stacked image of the N_v patches extracted from the same CMB maps, and compute its radial temperature and photometry profiles. We store all these profiles in memory and end up with thousands of temperature profiles (called here $T^i_{\rm sim}(\theta)$) and photometry profiles ($P^i_{\rm sim}(\theta)$). After this, for each angular size of the profiles, we compare the results from the stack of data voids to the statistical distribution of results from the random stacks. In practical terms, we calculate the S/N of the data temperature ($T_{\rm data}(\theta)$) or photometry ($P_{\rm data}(\theta)$) profiles, at each angle θ considered, as follows:

$$S/N_{T,P}(\theta) = \frac{\left|(T,P)_{\rm data}(\theta) - {\rm Avg}[(T^i,P^i)_{\rm sim}(\theta)]\right|}{{\rm StdDev}[(T^i,P^i)_{\rm sim}(\theta)]} \quad (1)$$

where the average and the standard deviation are evaluated over the collection of random stacks. We then obtain two S/N angular profiles for the considered stack: one of its temperature and one of its photometry.

An application of this procedure is illustrated in Figs. 7 and 8 where we assess the significance of our fiducial stack (Gr08 voids) in the CMB of WMAP *V* band. For this particular example, we used more than 14 000 sets of 50 random positions, which seems enough to sample the distribution of temperature and photometry profiles. Indeed this is hinted at by Fig. 8 where the histogram of photometry values at a given angular size follows a Gaussian distribution closely. We discuss the interpretation of this data in Sects. 4 and 5. The procedure for this estimation of the significance is robust and is used in the next section for all our results.

4. Results

We apply the procedure described in the previous section to all our stacks in order to estimate their significance. We show the results for the photometry of the stacks for each catalogue and subsample, with an assessment of the significance (Figs. 7, 9, and 10).

4.1. Revisiting Gr08

The work of Gr08 reported a 3.7σ signal ($-11.3\,\mu$K) in the stacking of their voids on a scale of 4°. With the same dataset we

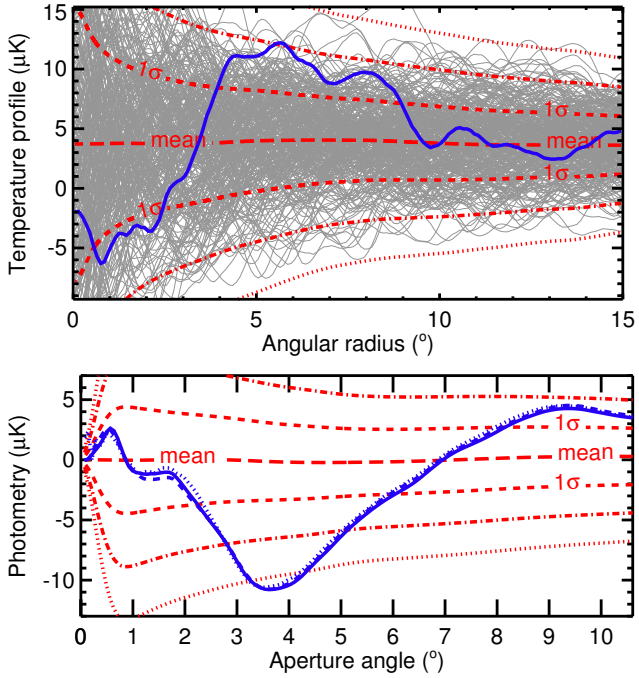

Fig. 7. *Top panel*: mean profile (long red dashes) from all 14 000 random stacks and the 1σ (dashed), 2σ (dash-dotted), and 3σ (dotted) limits of the distribution of profiles. For illustration, the thin grey curves are the temperature profiles of just a few hundred stacks of 50 random positions. The blue solid curve is the result from the fiducial stacking of Gr08 voids. Every stacking here is carried out in the WMAP *V* CMB map, smoothed at 30.6′. *Bottom panel*: same legend as before for the photometry profiles. The results from the *V* (solid blue) and *W* (dashed blue) band are also shown. Similarly to Gr08, the signal from their voids stands out at more than 3σ on an angular scale of 4°.

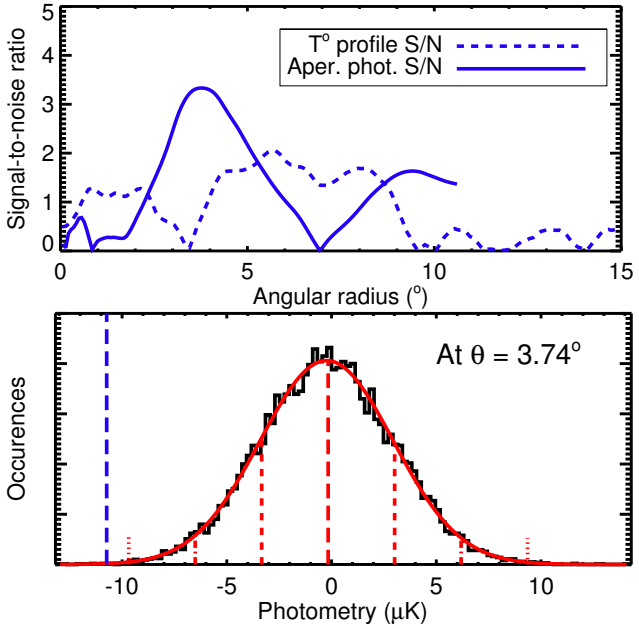

Fig. 8. *Top panel*: signal-to-noise ratio (as defined in Eq. (1)) of the temperature (dashed blue) and photometry (solid blue) profiles of our fiducial stack in WMAP *V* CMB map. A ~3.3σ signal stands out in the photometry at a scale of 3.74°. *Bottom panel*: distribution of photometry values for an aperture angle of 3.74°, from 14 000 stacks of 50 random positions. The mean, 1, 2, and 3σ values are marked the same way as in Fig. 7. The blue long-dashed line shows the value obtained from the fiducial stacking. The best fitting Gaussian (red solid curved) follows closely the distribution.

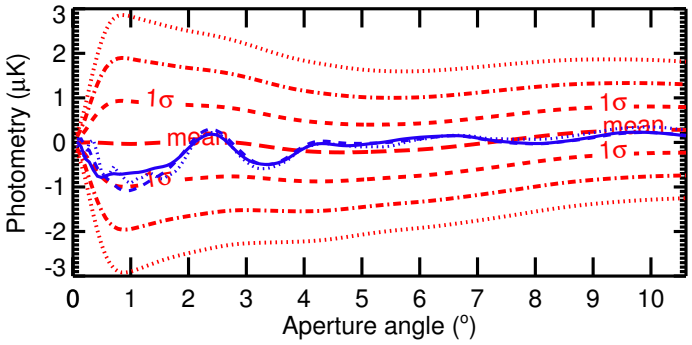

Fig. 9. Photometry profiles from the stacking of Pan et al. voids (same conventions as Fig. 7).

find a reasonable agreement (Fig. 8) with a preferred scale of ~3.7° with an $S/N \sim 3.3$ ($-10.8\,\mu$K). These differences can be imputed to our use of WMAP 7 maps instead of the WMAP 5 ILC map for Gr08 and, to a lesser extent, to light differences in the stacking procedure, profile calculations, or significance estimation. While we can argue about its cosmological origin, the signal seems to be persisting and is essentially identical across frequencies (see Fig. 7) as expected for the iSW effect. However, we found an important feature in the temperature profile of the stacked image and its significance. Indeed, in the top panel of Fig. 7 we see that the central cold spot of the signal (below 3.5°) does not particularly stand out compared to random stacks (1σ significance only). On the other hand, we measure a wide hot ring with around the spot a higher significance (up to 2σ) on scales between 3.5° and 10°, clearly visible in the middle image of Fig. 5. The impact of this ring is even visible in the photometry profile on higher scales, with a significance reaching almost 2σ around 9°.

Interpreting it in the light of the iSW effect, this would imply the presence of much higher overdensities surrounding the already large supervoids. Considering the filamentary structure of our Universe, this situation is unlikely, and the source of this hot ring remains unknown. This peculiarity leads us to question whether the measured central cold spot – physically interpreted as an iSW signal – is really remarkable. It might as well be due to random fluctuations of the CMB, of which the significance in the photometry profile is coincidentally strengthened by a surrounding hot region in the stacked image.

One could find an argument in favour of the iSW interpretation by noting the good match between the preferred scale in the S/N (~3.7°) and the mean effective angular radius of the Gr08 voids (~3.5°). As a matter of fact, the same argument can be turned around to rebut this interpretation. We intuit that the iSW effect should fade close to the border of the voids, making the cold spot noticeably smaller than the underlying structure. However, the presence of the wide hot ring around the central cold spot artificially pulls the preferred scale towards higher values, making it difficult to interpret the apparent match of scales. In a similar line of thought, note that the same analysis performed on the Gr08 superclusters gives a photometry profile that peaks on angular scales more than twice as large as those of the underlying clusters (Planck Collaboration 2013).

Before any definitive answer on this matter can be reached, this discussion requires a complementary rigorous investigation, through theory and/or numerical simulations, of the iSW effect

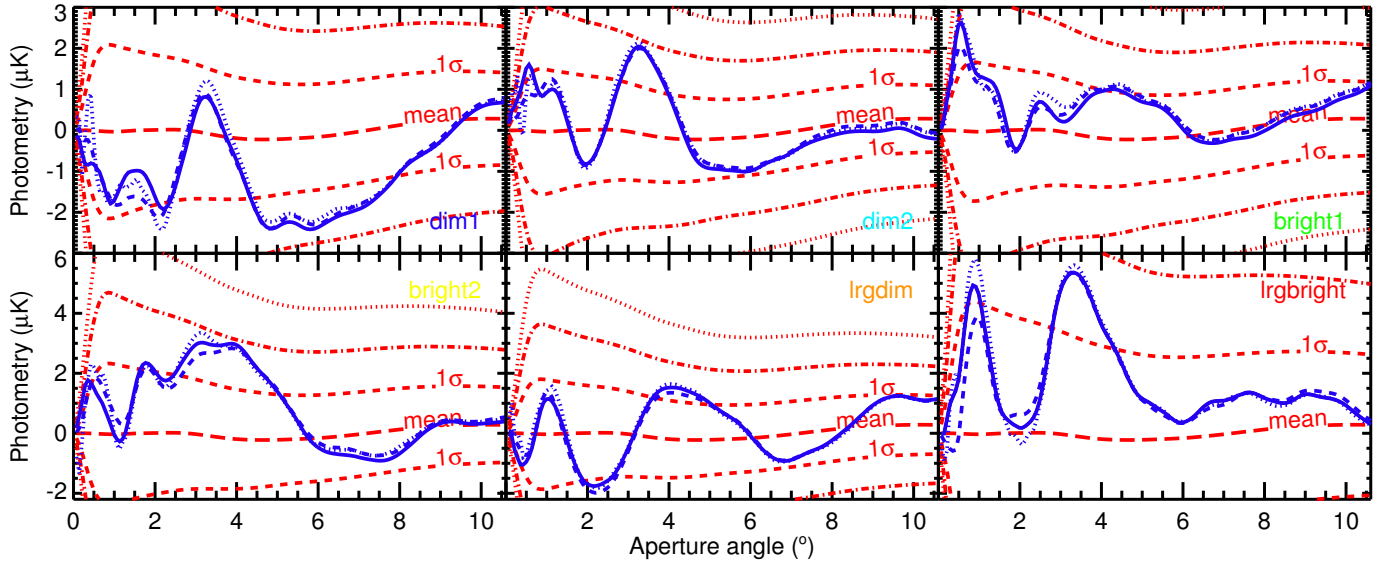

Fig. 10. Photometry profiles from the stacking of Sutter et al. voids and its six subsamples (same conventions as Fig. 7).

expected from such superstructures, which is beyond the scope of this paper.

4.2. Other catalogues

The two other catalogues used in our analysis yield mixed results, with no significance on the same level as the Gr08 catalogue. While discouraging, one has to remember that according to current theoretical predictions, we expect this iSW signal to be difficult to detect.

The stacking of the 1055 voids of Pan et al. gives a faint signal below the 1σ level at about 1° (Fig. 9), which does not allow any interpretation. This may be due to the high number of voids in the sample, which has a very wide distribution of angular sizes. We considered the idea of dividing this catalogue into subsamples based on redshift, radius, and/or angular sizes. After several attempts, it did not yield any significant result, and we faced a number of issues that include the hassle of finding appropriate bins of size for the subsamples and possible a posteriori selection effects. Indeed, a smaller number of structures implies a narrower range of sizes and redshifts, but it can also greatly reduce the S/N.

We still addressed this issue partially by separately analysing the six subsamples of Sutter et al. (Fig. 10) – a simple division based on redshift but in principle free of selection effects. From this analysis, only one of the subsamples (*dim1*) yields a negative signal in the photometry with a significance higher than 1σ. The other profiles are either entirely positive (*lrgbright*), or their significance is below 1σ. An explanation for this apparent absence of significant results may be found by considering the dispersion in the angular radii of the voids. The subsamples from Sutter et al. contain significantly more objects compared to the Gr08 sample, but their sizes on the sky are much more scattered (see Fig. 1). Mixing such a variety of void sizes necessarily dilutes the associated iSW signal over the same range of scales, drastically reducing its significance.

This preliminary analysis strongly suggest that we need to take the size of each individual void into account in the stacking procedure to improve the significance of the results.

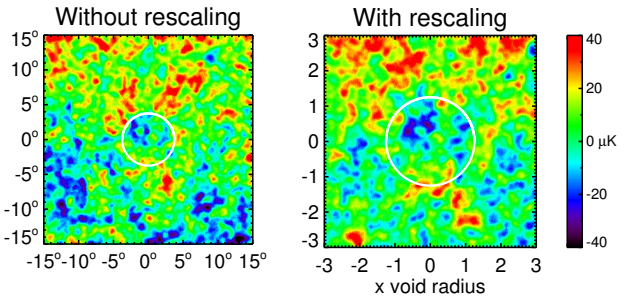

Fig. 11. Stacked images of Gr08 voids, without (*left*) and with (*right*) a rescaling of the CMB patches proportional to the void sizes.

4.3. Rescaling tests

In light of the results above, we adopted another approach in order to enhance the significance of the signal. We kept each subsample in its entirety and did the stacking analysis again, but this time rescaling the voids according to their effective radii. In practical terms, this means cutting the CMB patches so that each void occupies the same space on the stacked image.

We keep the same protocol as described in Sect. 3.1, but we change the resolution of the extracted patches, so that for each patch, it now depends on the size of the corresponding void. Each time, we cut a square patch with a side six times the size of the void effective radius it contains. Naturally, we also adapt our protocol for the estimation of the significance: The sets of random positions are still drawn the same way, but each random patch is first subjected to the same rescaling as done on the identified void patches. This will have the effect of mixing different scales in the original CMB map, and will most likely amplify the variance of these random stacks compared to those of Sect. 3.3.

We begin with the fiducial stacking of the voids of Gr08. A comparison between the stacked images is illustrated in Fig. 11 while the different profiles are shown in Fig. 12. The signal identified in Sect. 4.1 still appears after rescaling, with the best significance around scales between 1 and 1.3 times the void effective radii. This value somehow seems a little too high since, as stated above, we expect this value to be around or smaller than one (due to the irregular geometry of the voids). The significance of the signal is also found to be lower ($S/N \sim 2.8$ versus $\sim$3.3).

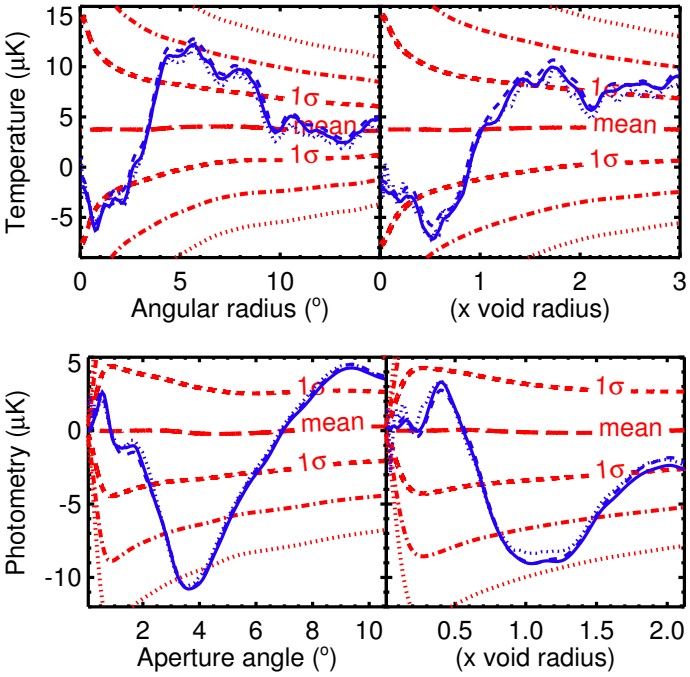

Fig. 12. Temperature (*top*) and photometry (*bottom*) profiles for the original (*left*) and rescaled (*right*) stacking of Gr08 voids (same conventions as Fig. 7).

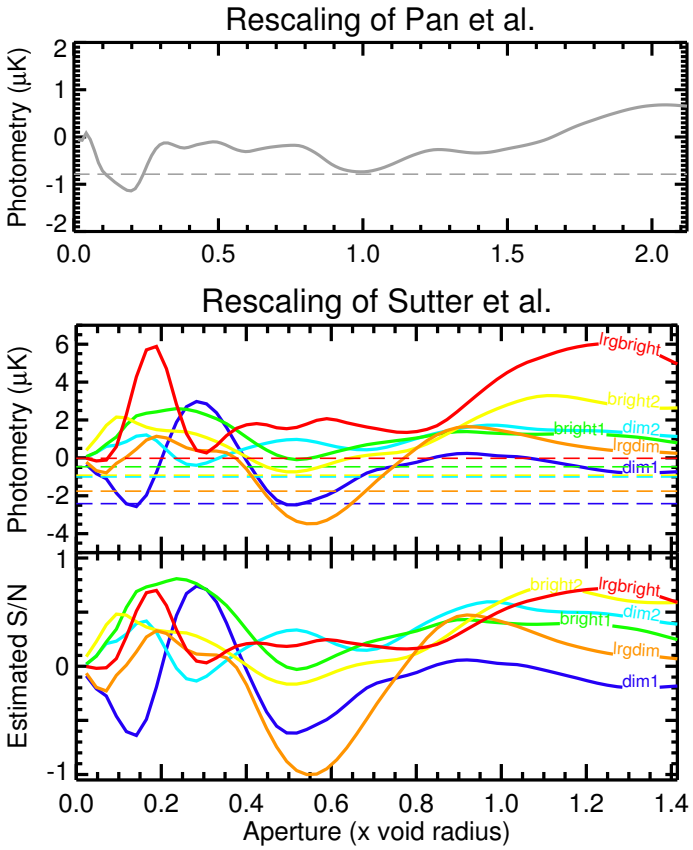

Fig. 13. Summary of the photometry profiles extracted from the rescaled stacks of Pan et al. (*top*) and Sutter et al. (*middle*), performed in the WMAP *V* band cleaned map. The coloured dashed lines indicate for each sample the lowest amplitude measured in the original stacked image (without rescaling the voids). These allow to roughly estimate if the rescaling procedure did improve the detection of any previously detected signal. The bottom panel shows the previous profiles multiplied by $\sqrt{N_v}$, with N_v the respective number of voids in each subsample. They are then normalized to the strongest signal (*lrgdim*). These curves provide an estimate of their potential significance as the noise in the stacked image is expected to scale as $1/\sqrt{N_v}$ approximately.

This is partly due to the increased variance of the signal (cf. the wider $1/2/3\sigma$ limits in the profiles) induced by the rescaling. But it is also a consequence of the lower amplitude measured for the signal, at odds with our expectations of the rescaling procedure. This could be a further hint that random CMB fluctuations actually contribute notably to the signal seen in the stacked image. On the other hand, the temperature profile of the rescaled stack is closer to expectations, with a higher significance cold spot in the centre (cf. first paragraph of Sect. 4.1 for comparison).

From this first test, we understand that if the rescaling process does not at least improve the absolute amplitude of any previously detected signal, then any subsequent significance estimation is very unlikely to yield an improvement since the necessarily larger variance decreases the S/N further. Therefore we first produced an overview of the photometry profiles obtained from the rescaled stacks of Sutter et al. and Pan et al. voids (top of Fig. 13). Again, no signal of particular importance arises from this new analysis of Pan et al. voids (except at very small angular sizes, most likely due to random fluctuations and not in relation to any underlying structure). Concerning the Sutter et al. catalogue, signals seem to arise in several of the rescaled profiles, especially on a scale equal to 0.5–0.55 times the voids effective radii, with a clear departure from the previous (without rescaling) results for some of them, such as the *lrgdim* subsample. However, some of the other subsamples (*bright1*, *lrgbright*) do not benefit from the rescaling procedure.

We identified the two most promising subsamples, *dim1* and *lrgdim*, and we evaluated the significance of their rescaled profiles. The results, shown in Fig. 14, are close to our expectations. The *dim1* subsample yields a signal at ∼0.52 times the void effective radius, with a significance similar (albeit a bit smaller) to the results without rescaling (around 1.36σ). This is coherent with the fact that the amplitude of the signal remained almost at the same level (illustrated by the corresponding dashed line in Fig. 13), whereas the rescaling procedure slightly increased the variance of the random stacks used in the S/N estimation. We

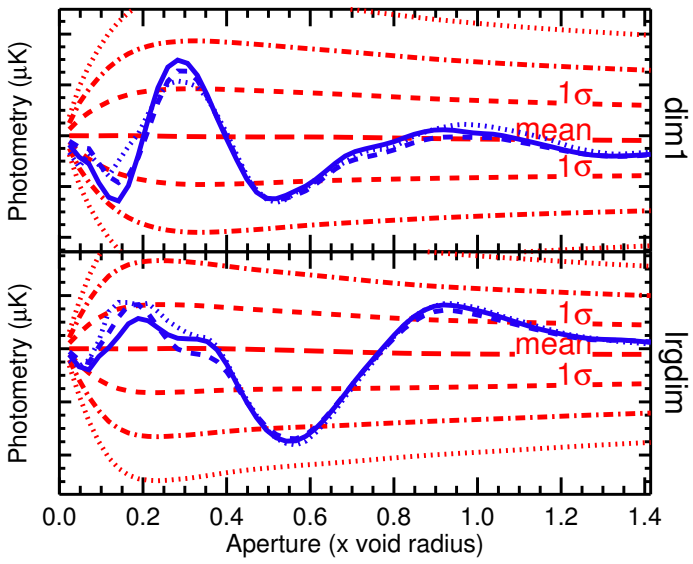

Fig. 14. Photometry profiles and significance for the rescaled stacks of two Sutter et al. subsamples, *dim1* and *lrgdim* (same conventions as Fig. 7).

A&A 556, A51 (2013)

note that the apparently significant signals at small aperture angles (~0.15× and 0.3×) are not constant across frequencies and therefore are probably not related to an iSW effect. Regarding the *lrgdim* subsample, it gives a ~2.35σ signal around 0.57 times the void radius, a clear improvement over the non-rescaled results that was expected considering the stronger amplitude of the rescaled signal. For both subsamples, we note that the amplitude of the highlighted signal stays remarkably constant across frequencies, whereas the other potentially significant features of the profiles (on smaller scales notably) are not achromatic.

Interestingly, we observe that the analysis of both subsamples presents an iSW-like signal at a scale slightly above half the effective radius of the considered voids. Although this clearly differs from the results obtained with the Gr08 catalogue, a physical explanation can be found in the geometry of the voids from these subsamples. Indeed, as noted by Sutter et al. (2012), the majority of them present a similar shape to a prolate ellipsoid with an ellipticity close to two. Since the orientation of these voids is a priori random, we can intuit that stacking such ellipsoids (and their associated iSW signature) will eventually give a circular signal, on a smaller typical scale, closer to half the major axis of the ellipsoids. An accurate estimation of this scale would require an extensive analysis of the individual geometry of the considered voids, and their associated iSW signature. Nonetheless, a recent study by Cai et al. (2013)[4] comforts our intuition. They constructed large N-body simulations following a ΛCDM cosmology and identified the voids in the manner of Sutter et al. (2012) and Gr08. They subsequently computed the iSW signature resulting from the stacking of their simulated voids, which highlighted an optimal scale around 0.6 times the effective radius of the voids for the analysis by aperture photometry. The similarity between this predicted scale and the signal we observe in the Sutter et al. void subsamples is encouraging. In contrast, we should note that using a different approach, Hernández-Monteagudo & Smith (2012) generated matter density maps (from both Gaussian and N-body simulations) that followed the redshift distribution of Gr08, from which they derived full-sky iSW maps. After performing a stacking in these maps at the locations of the density peaks/troughs, they found that the scales highlighted by aperture photometry ranged from 1° to 20° – with a maximum around 7°, but a small amplitude of ~2 μK.

4.4. Alternative approach with rescaling

From the previous sections, we gathered that in some of the Sutter et al. subsamples, an iSW-like signal seems to appear around 0.5–0.6 times the voids effective radii and that it is especially significant in the *lrgdim* sample. A possible explanation may come from the presence in this particular subsample of some of the largest voids in the whole Sutter et al. catalogue (as can be seen in Fig. 1), which are supposed to yield the strongest iSW effect. The *lrgbright* sample also contains many large voids, but because of its small number of objects (50), the level of noise from primordial CMB fluctuations is still high, hence the absence of a significant signal in the stacked image.

This indicates that instead of considering each subsample separately, a better approach may be to combine them all and stack the voids starting from the largest ones. Indeed, in theory

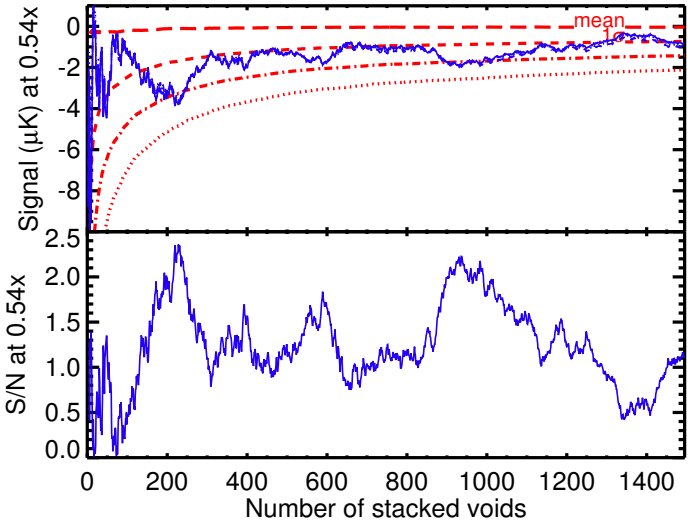

Fig. 15. *Top*: photometry values of the stacked and rescaled voids from the Sutter et al. catalogue, at an aperture of 0.54 times their effective radii, as a function of the number of voids (sorted by decreasing size). Significance contours are computed using random stacks produced from the WMAP V band cleaned map. Legend is identical to previous plots of photometry profiles (see Fig. 7). *Bottom*: for the stacking performed in the WMAP V map, S/N of the above photometry values computed using the significance contours.

the noise should scale as usual roughly as the inverse square root of the number of stacked voids, but the stacked iSW signal is also expected to drop at some point due to the addition of smaller and less contributing voids. By starting from the largest voids, we intend to select the supposedly largest iSW contributions in order to keep the stacked signal from dropping too fast and effectively to boost the S/N of the detection. We carried out this analysis on the 1495 voids of Sutter et al., first focusing on the whole photometry profiles and increasing progressively the number of stacked voids. As expected, a negative signal consistently appears around an aperture of 0.54 times the voids effective radii. As intuited before, its amplitude gradually decreases as we include smaller and smaller voids in the stacking. To estimate the significance of this signal, we focus on the value of the photometry at this particular aperture scale. In the top half of Fig. 15, we show these values as a function of the increasing number of stacked voids. Similarly to the previous section, we estimate the significance of these values by repeating the analysis many times after randomly shifting the stacked positions. Therefore we can compute the S/N of these results, shown in the bottom half of Fig. 15. We note once again that the photometry is stable across frequencies and consistently negative for practically any number of stacked voids, but the shape of this curve and its significance are hard to interpret. The significance first rises up to ~2.3σ for the first 200 stacked voids, a behaviour that would be expected from an ISW signal that progressively takes over the CMB noise. After this, the S/N quickly decreases and then oscillates between about 1σ and 2σ before dropping, after stacking more than 1300 voids. Although this significance appears to vary quite significantly, the stability of the signal itself (always negative and on the same scale) may indicate that this variability is due to random CMB fluctuations.

We selected two particular numbers of voids with a high significance observed in Fig. 15, namely 231 and 983 voids, and performed the same photometry/significance analysis as in Sect. 4.3. The results are shown in Fig. 16: both profiles highlight

[4] We note that Cai et al. have withdrawn their paper since their observational results were based on an older version (August 2012) of the Sutter et al. void catalogue which was plagued by a few issues – see http://www.cosmicvoids.net. The theoretical conclusions of Cai et al. based on their numerical simulations remain however valid.

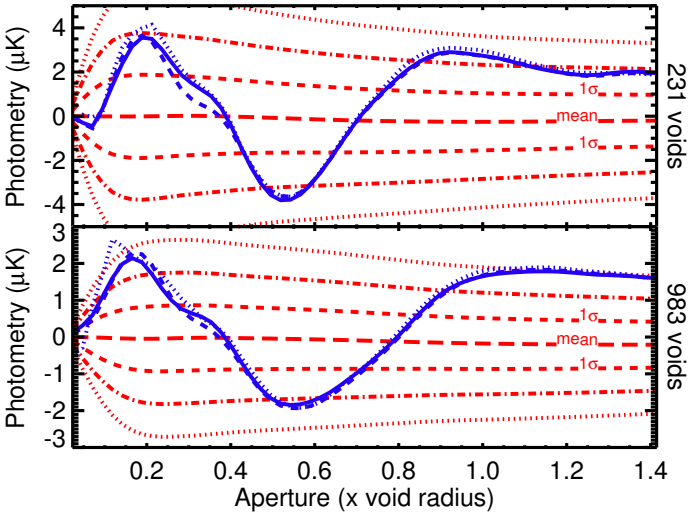

Fig. 16. Photometry profiles and significance of the rescaled stacking of the 231 (*top*) and 983 (*bottom*) largest voids from the Sutter et al. catalogue (same conventions as Fig. 7).

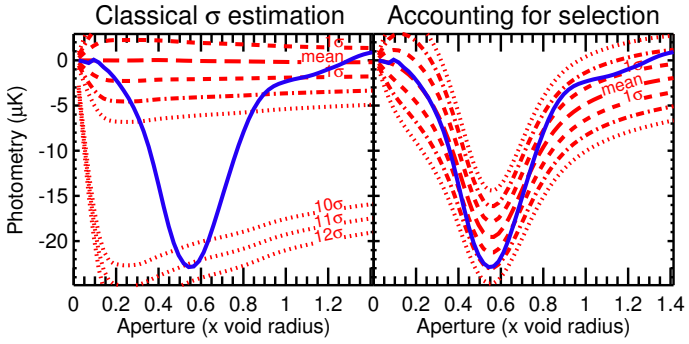

Fig. 17. Photometry profile for the rescaled stacking of half the Sutter et al. *lrgdim* subsample (146 voids out of 291), chosen so that the amplitude at 0.56 times the voids radii is the strongest (see text for details). *Left*: the significance is estimated with stacks of 146 random positions. *Right*: the significance accounts for the selection effect. The difference between the two significances is obvious and very pronounced.

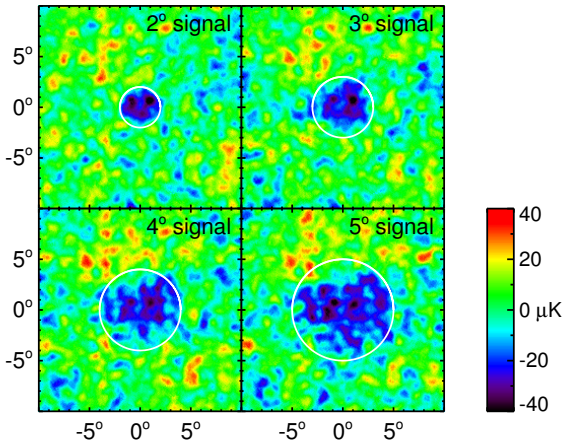

Fig. 18. Illustration of selection effects. From a single set of around 200 random positions, we are able to construct a false "iSW-like" signal on any desired scale (here for angular radii of 2, 3, 4 and 5°) by selecting and stacking each time the appropriate half of the same set.

a scale again equal to 0.54 times the voids effective radii where the signal reaches significances equal to 2.38σ for the 231 voids and 2.20σ for the 983 voids. Despite having more voids, the small drop in significance may again be caused by CMB fluctuations and/or the inclusion of small voids. Another notable feature appears in both photometry profiles, namely one hot significant signal on smaller scales (~0.2×) and one on larger scales (>0.9×). The former and its associated scale seem to coincide with an angular size close to 1°. It is directly related to the curious fact that the minimal temperature spots do not appear at the centre of the stacked image. Were the stacks centred on the coldest spot, we would not have obtained this positive signal in the photometry profiles at small angles.

The origin of this hot central spot is undetermined, but could be due to several contributions of which the background CMB fluctuations, the irregular shape of the underlying voids, and the possible mismatch between the position of the void barycentres and their most underdense zones. Concerning the signal on larger scales, what comes to mind is the possible influence of large scale fluctuations through the low multipoles of the CMB, already glimpsed in 3.2.3. Thus we redid the stacking of the same sets of voids on new maps with a few low multipoles removed from $\ell = 2$ to 20. The results then showed that these multipoles indeed make a non-negligible contribution to our photometry profiles: removing them noticeably reduces the measured amplitude on large scales but keeps the rest of the signal almost intact. Although it does not account for the entirety of the large scale signal, it does reduce its significance to less remarkable levels.

In summary, the introduction of a rescaling in the stacking procedure yielded different results depending on the considered samples of voids. Concerning the Gr08 catalogue, the rescaling gave a more coherent shape to the temperature profile of the stacked image: a significant cold spot and a less significant hot ring. However, it highlighted a tension between the scale preferred by the aperture photometry and the actual smaller size of the stacked objects, and also slightly (but counterintuitively) reduced the significance of the detected signal. These may be hints that this signal is not entirely an iSW effect produced by voids, but is partly due to random CMB fluctuations. This would explain both the scale discrepancy (CMB fluctuations and voids are uncorrelated) and the lower S/N (the noise from the CMB is "distributed" across all scales by the rescaling).

On the other hand, the rescaling process had positive results on the much larger catalogue of Sutter et al., highlighting a particular scale around half the void sizes in all the tests performed, in apparent agreement with both intuitive arguments and theoretical works in the literature. Although the maximum observed significance only reaches around 2.3σ and the signal depends quite significantly on the number of stacked voids and their size, the persistent nature of the signal seems to bolster the case for iSW detection.

Lastly, we note that the Pan et al. catalogue did not benefit from the rescaling process, and wish to mention that we also explored the same approach used with the Sutter et al. catalogue (gradual stacking starting with the largest voids), but it did not yield any significant results. We hypothesise that this is caused by the narrow range of small sizes of these voids, whose faint iSW signal is likely to be dominated by CMB fluctuations.

5. Discussion

5.1. Selection effects

To further elaborate on the possible conclusions that we can deduce from the present work, there are a couple of effects that can

A&A 556, A51 (2013)

make the interpretation of the results even more difficult and that we should keep in mind. We now mention a few of them.

The results from the previous section highlight the difficulty of getting a clear detection of a signal, at least when using the various catalogues as such. With this in mind, one could be tempted to amplify the signals hinted at by isolating the voids that contribute most. We experiment with this idea and apply it to the best S/N from our new results in Sect. 4.3, i.e. the rescaled stacking of the *lrgdim* subsample. From the 291 voids of the original set, we keep only the half (146) that contributes the most to the minimum of the photometry profile on the scale of 0.56 times the voids radii. The resulting photometry profile is plotted in Fig. 17 and indeed shows a dramatic increase in the amplitude of signal. From there, the crux of the matter is to assess the significance of this new result. When using the same procedure as in Sect. 3.3 (many stacks of 146 random positions), we obtain a surprisingly high S/N, above 11σ. This value clearly overestimates the real significance, since it ignores the selection that we performed on the sample. We need to revise our protocol as follows. We first generate many sets of 291 random positions. Then for each set, we select and stack only the half that contributes most to the photometry profile on the same scale of 0.56 times the voids radii. Once we draw enough such random stacks, we keep the rest of the procedure identical. The corrected significance (Fig. 17) drops down to a level of about two, comparable with (even lower than) the initial S/N in the original stack (Fig. 10). Such an a posteriori selection cannot be used to improve the S/N of the final stacked signal.

Actually, taking a closer look at these selection effects, we notice that with only one set of a few hundred random positions, one can obtain a strong – but completely artificial – signal on almost any desired scale (Fig. 18) by selecting the appropriate half of it. This further illustrates, and warns us about the risk of a posteriori selections, and does put any apparently significant signal we obtained into perspective. Our results from the new catalogues can be considered safe, since the only form of selection comes from the division of the Sutter et al. voids into redshift subsamples that has already been performed a priori by the authors. The Gr08 results are probably also safe, although their 50 voids come originally from a ten times larger sample (see Sect. 2.2) and were selected according to a density-contrast criterium. This selection was also made by the authors prior to looking at CMB data. It is not clear, however, whether that selection might have helped increasing the S/N artificially. Of further interest is the observation made by the Gr08 that either increasing or decreasing by a few tens the amount of voids in their selected sample does make the significance drop. This may either indicate a possible selection effect – thus casting doubt on the iSW nature of the signal – or be an expected effect due to the addition of noise-dominated voids (when increasing the number of voids) or the deletion of contributing voids (when decreasing it).

5.2. Alignment and overlap effects

When interpreting our results, another important issue arises due to the number and location of the voids studied. In principle, each one of them leaves an imprint in the CMB temperature. These hundreds of voids are confined in the area covered by the SDSS. Since the angular size of these objects often exceeds several degrees, they are bound to fill this area and overlap. As a consequence, the stacking of a chosen set of voids in fact contains contributions from many others. Some structures may also be very close to each other on the sky, further complicating the interpretation of signals.

Table 2. Summary of the overlapping study for the void samples.

		Fraction of the surface occupied by...							
		Gr08	Pan	Sut-1	Sut-2	Sut-3	Sut-4	Sut-5	Sut-6
...in common with ...	Gr08		14.3%	26.3%	27.3%	28.1%	28.2%	27.1%	21.6%
	Pan	100%		99.3%	100%	100%	100%	100%	100%
	Sut-1	88.3%	47.8%		91.3%	91.9%	93.2%	90.3%	92.1%
	Sut-2	86.0%	45.1%	85.4%		94.8%	94.5%	92.3%	95.9%
	Sut-3	82.1%	41.9%	79.9%	88.1%		90.1%	87.0%	90.1%
	Sut-4	70.6%	35.8%	69.3%	75.0%	77.0%		74.7%	76.5%
	Sut-5	85.4%	45.1%	84.6%	92.4%	93.7%	94.2%		95.1%
	Sut-6	36.3%	24.1%	46.0%	51.2%	51.8%	51.4%	50.7%	
		Fraction of overlapping zones							
		13.5%	81.8%	82.2%	81.5%	67.9%	49.9%	86.4%	25.3%

Notes. First part (top): each column indicates for each samples the fraction of its surface that is contaminated by every other sample. Second part (bottom line): shows for each sample the fraction of its covered surface where 2 or more voids overlap.

We devise two ways of quantifying these issues:

- First, for each individual sample, we compute both the total area covered by all the voids and the area where at least two voids overlap; we then compute the ratio of these quantities, which represents the "self-contamination" of each sample.
- Then, for every possible pair of samples, we compute the fraction of the area of the first sample shared by the second sample area – a measure of the contamination between samples.

The results are compiled in Table 2. We can see that each sample shows moderate to high contamination with other samples and overlaps itself quite strongly. The results are lower for the Gr08 sample due to the small number of voids. Still, the first row of Table 2 shows that many voids from other catalogues will contribute to the stacking of the Gr08 voids, making it more difficult to interpret its relatively high significance results. This is true for every catalogue of voids identified in the same area. The level of overlap is very high, and it would be difficult to determine which are the objects that produce the actual iSW signal. Moreover, the proximity of the voids may artificially amplify some detections due to the possibility of repeated stacking on the location of a significant signal/void.

Both aspects of this study show that contribution from other samples is indeed frequent in the stacking of these voids. Supposedly, we can expect the contribution to cancel out for large numbers of stacked patches, although this argument may be weakened by the fact that voids represent a much larger fraction of the volume of the Universe than high overdensities. In any case, the probability of measuring a false signal (due to a fortuitous event) may be heightened by the overlapping of so many voids. An accurate simulation of the expected signature from such a collection of overlapping structures will help quantify these contaminations and their effects on a possible iSW effect detection.

5.3. Spurious detections?

We would also like to stress that the superstructure data sets should be considered with caution. While writing this paper, several updates of the Sutter et al. catalogue were released. The changes were stated as having no impact on the conclusions of the associated paper (Sutter et al. 2012). A detailed examination

showed that modifications ranged from minor to more consequent. Numerous additional small voids were detected thanks to an improved void finding algorithm. Quite a few voids were removed from one version to the next, and many others have seen modifications in their redshifts, sizes, and positions on sky, up to the point where one of the subsample was almost completely different (lrgbright). These updates did, however, have a significant impact on the stacking of the voids, especially through inclusion of the new small voids. For instance, with the July version, our procedure yielded a $\sim 2.5\sigma$ detection of a negative signal at about 2.4° in the bright2 subsample prior rescaling, while in the latest version of the same subsample the photometry shows a positive excess with almost 2σ significance. Conversely, rescaling the voids improved the detection of a negative photometric decrement only with the latest version of the catalogue. While the present status of the catalogue should be considered as robust (Sutter, priv. comm.), we feel that the fact mentioned above makes it rather difficult to interpret without ambiguity the signal obtained.

6. Conclusion

In this paper, we revisited the stacking of voids in CMB maps as a potential probe of dark energy through the expected iSW effect from these structures. Previous work by Granett et al. (2008a, Gr08) measured a 3.7σ signal in WMAP 5 ILC map using a catalogue of 50 selected supervoids extracted from the SDSS (DR6). We devised a complete protocol for a stacking procedure from a careful choice of maps to a rigorous estimation of the significance. We first applied it to the catalogue of voids of Gr08 and did not find any significant difference, if not a little weaker signal and associated S/N (by 0.4σ). We then extended the analysis to two new void catalogues by Pan et al. (2012) and Sutter et al. (2012). The first did not yield any significant result, most likely owing to the limited range of redshift and radii of the sample.

The second new catalogue, however, hinted at more significant signals (although not nearly as strong as the Gr08 results) with a trend for the preferred scale in the signal, which seemed to point to half the mean size of the voids used in the stacking. This was not found with the Gr08 voids, for which the highest significance scale was close to the mean void size. We note, however, in favour of our results from the Sutter et al. catalogue that because of the irregular geometry of the stacked voids, we expect the preferred characteristic scale to in fact be noticeably smaller than the void themselves. Additionally, we showed that the rescaled signal from the Gr08 voids prefers a scale that is larger than the size of these objects, a feature that is rather hard to explain physically, unless these central voids are surrounded by unrealistically high overdensities. These results are in close agreement with the analysis performed by Planck Collaboration (2013) using the recently released CMB data.

The rescaling of the CMB patches (according to the void sizes) prior to stacking proved to be a mandatory step toward obtaining a significant signal in the photometry profiles, especially in light of our results with the incremental stacking of the largest voids of the Sutter et al. catalogue. However, an unexpected signal with moderately high significance was found on small scales in these same profiles (and to a lesser extent with the Gr08 voids), which could be attributed to random CMB fluctuations, the void irregular shapes, and uncertainties in the position of the voids actual centres. A similarly high signal was also measured on high scales; however, we showed that a large portion of it originated in large scale fluctuations ($2 < \ell < 20$) in the CMB map, unrelated to the smaller scales that we are investigating.

Along with these results, we also addressed the risks of possible selection effects that could easily lead to an overestimation of the significance. We also stressed that the surface density of the voids within the SDSS area make them overlap significantly, making it even more difficult to formulate clear expectations about, and interpretations of, the measured signals. Finally, it is known that voids are actually difficult to identify with certainty and that one must proceed with caution when analysing such void samples. Another instance of this is that while being identified in the same SDSS DR7 set, the void subsamples *dim1* and *dim2* of Sutter et al. lie within the same redshift range as the voids identified by Pan et al., but they cover quite a different range in size and are distributed differently in redshift. We argue, therefore, that, combined with the unavoidable overlap of voids along a line of sight mentioned above, any claim of a detection of an iSW-like signal by the stacking of voids and/or claim of an oddity with respect to ΛCDM would be premature.

Acknowledgements. We are happy to acknowledge discussions with C. Hernández-Monteagudo and J. M. Diego at an early stage of this work. We also thank N. Aghanim and F. Lacasa for stimulating discussions. Clarifying exchanges with the authors of Cai et al. (2013) and with P. M. Sutter are also acknowledged. Some of the results in this paper have been derived using the HEALPix (Górski et al. 2005) package. The work of S. Ilić is funded by the Doctoral Programme "AAP 2010 contrats doctoraux Paris-Sud 11".

References

Adelman-McCarthy, J. K., Agüeros, M. A., Allam, S. S., et al. 2008, ApJS, 175, 297
Aghanim, N., Majumdar, S., & Silk, J. 2008, Rep. Prog. Phys., 71, 066902
Boughn, S. P., & Crittenden, R. G. 2002, Phys. Rev. Lett., 88, 021302
Boughn, S. P., Crittenden, R. G., & Turok, N. G. 1998, New Astron., 3, 275
Cai, Y.-C., Neyrinck, M. C., Szapudi, I., Cole, S., & Frenk, C. S. 2013 [arXiv:1301.6136]
Crittenden, R. G., & Turok, N. 1996, Phys. Rev. Lett., 76, 575
Dupé, F.-X., Rassat, A., Starck, J.-L., & Fadili, M. J. 2011, A&A, 534, A51
Flender, S., Hotchkiss, S., & Nadathur, S. 2013, JCAP, 2, 13
Giannantonio, T., Scranton, R., Crittenden, R. G., et al. 2008, Phys. Rev. D, 77, 123520
Giannantonio, T., Crittenden, R., Nichol, R., & Ross, A. J. 2012, MNRAS, 426, 2581
Górski, K. M., Hivon, E., Banday, A. J., et al. 2005, ApJ, 622, 759
Granett, B. R., Neyrinck, M. C., & Szapudi, I. 2008a, ApJ, 683, L99
Granett, B. R., Neyrinck, M. C., & Szapudi, I. 2008b [arXiv:0805.2974]
Granett, B. R., Neyrinck, M. C., & Szapudi, I. 2009, ApJ, 701, 414
Hernández-Monteagudo, C., & Smith, R. E. 2012, MNRAS, submitted [arXiv:1212.1174]
Hinshaw, G., Weiland, J. L., Hill, R. S., et al. 2009, ApJS, 180, 225
Ho, S., Hirata, C., Padmanabhan, N., Seljak, U., & Bahcall, N. 2008, Phys. Rev. D, 78, 043519
Hoyle, F., & Vogeley, M. S. 2002, ApJ, 566, 641
Hunt, P., & Sarkar, S. 2010, MNRAS, 401, 547
Jarosik, N., Bennett, C. L., Dunkley, J., et al. 2011, ApJS, 192, 14
Kofman, L. A., & Starobinskii, A. A. 1985, SvA Lett., 11, 271
Komatsu, E., Smith, K. M., Dunkley, J., et al. 2011, ApJS, 192, 18
Nadathur, S., Hotchkiss, S., & Sarkar, S. 2012, JCAP, 2012, 042
Neyrinck, M. C. 2008, MNRAS, 386, 2101
Neyrinck, M. C., Gnedin, N. Y., & Hamilton, A. J. S. 2005, MNRAS, 356, 1222
Pan, D. C., Vogeley, M. S., Hoyle, F., Choi, Y.-Y., & Park, C. 2012, MNRAS, 421, 926
Pápai, P., & Szapudi, I. 2010, ApJ, 725, 2078
Pápai, P., Szapudi, I., & Granett, B. R. 2011, ApJ, 732, 27
Planck Collaboration 2013, A&A, submitted [arXiv:1303.5079]
Sachs, R. K., & Wolfe, A. M. 1967, ApJ, 147, 73
Springel, V., White, S. D. M., Jenkins, A., et al. 2005, Nature, 435, 629
Sutter, P. M., Lavaux, G., Wandelt, B. D., & Weinberg, D. H. 2012, ApJ, 761, 44

Astronomy & Astrophysics manuscript no. planck2013˙isw
March 22, 2013

Planck 2013 results. XIX. The integrated Sachs-Wolfe effect

Planck Collaboration: P. A. R. Ade[87], N. Aghanim[60], C. Armitage-Caplan[93], M. Arnaud[74], M. Ashdown[71,6], F. Atrio-Barandela[18], J. Aumont[60], C. Baccigalupi[86], A. J. Banday[97,9], R. B. Barreiro[68], J. G. Bartlett[1,69], N. Bartolo[33], E. Battaner[99], K. Benabed[61,95], A. Benoît[58], A. Benoit-Lévy[25,61,95], J.-P. Bernard[9], M. Bersanelli[36,50], P. Bielewicz[97,9,86], J. Bobin[74], J. J. Bock[69,10], A. Bonaldi[70], L. Bonavera[68], J. R. Bond[8], J. Borrill[13,90], F. R. Bouchet[61,95], M. Bridges[71,6,65], M. Bucher[1], C. Burigana[49,34], R. C. Butler[49], J.-F. Cardoso[75,1,61], A. Catalano[76,73], A. Challinor[65,71,11], A. Chamballu[74,15,60], L.-Y Chiang[64], H. C. Chiang[28,7], P. R. Christensen[82,39], S. Church[92], D. L. Clements[56], S. Colombi[61,95], L. P. L. Colombo[24,69], F. Couchot[72], A. Coulais[73], B. P. Crill[69,83], A. Curto[6,68], F. Cuttaia[49], L. Danese[86], R. D. Davies[70], R. J. Davis[70], P. de Bernardis[35], A. de Rosa[49], G. de Zotti[46,86], J. Delabrouille[1], J.-M. Delouis[61,95], F.-X. Désert[54], C. Dickinson[70], J. M. Diego[68], K. Dolag[98,79], H. Dole[60,59], S. Donzelli[50], O. Doré[69,10], M. Douspis[60], X. Dupac[41], G. Efstathiou[65], T. A. Enßlin[79], H. K. Eriksen[66], J. Fergusson[11], F. Finelli[49,51], O. Forni[97,9], P. Fosalba[62], M. Frailis[48], E. Franceschi[49], M. Frommert[17], S. Galeotta[48], K. Ganga[1], R. T. Génova-Santos[67], M. Giard[97,9], G. Giardino[42], Y. Giraud-Héraud[1], J. González-Nuevo[68,86], K. M. Górski[69,101], S. Gratton[71,65], A. Gregorio[37,48], A. Gruppuso[49], F. K. Hansen[66], D. Hanson[80,69,8], D. Harrison[65,71], S. Henrot-Versillé[72], C. Hernández-Monteagudo[12,79], D. Herranz[68], S. R. Hildebrandt[10], E. Hivon[61,95], S. Ho[26], M. Hobson[6], W. A. Holmes[69], A. Hornstrup[16], W. Hovest[79], K. M. Huffenberger[100], S. Ilić[60], T. R. Jaffe[97,9], A. H. Jaffe[56], J. Jasche[61], W. C. Jones[28], M. Juvela[27], E. Keihänen[27], R. Keskitalo[22,13], T. S. Kisner[78], J. Knoche[79], L. Knox[30], M. Kunz[17,60,3], H. Kurki-Suonio[27,44], G. Lagache[60], A. Lähteenmäki[2,44], J.-M. Lamarre[73], M. Langer[60], A. Lasenby[6,71], R. J. Laureijs[42], C. R. Lawrence[69], J. P. Leahy[70], R. Leonardi[41], J. Lesgourgues[94,85], M. Liguori[33], P. B. Lilje[66], M. Linden-Vørnle[16], M. López-Caniego[68], P. M. Lubin[31], J. F. Macías-Pérez[76], B. Maffei[70], D. Maino[36,50], N. Mandolesi[49,5,34], A. Mangilli[61], A. Marcos-Caballero[68], M. Maris[48], D. J. Marshall[74], P. G. Martin[8], E. Martínez-González[68], S. Masi[35], S. Matarrese[33], F. Matthai[79], P. Mazzotta[38], P. R. Meinhold[31], A. Melchiorri[35,52], L. Mendes[41], A. Mennella[36,50], M. Migliaccio[65,71], S. Mitra[55,69], M.-A. Miville-Deschênes[60,8], A. Moneti[61], L. Montier[97,9], G. Morgante[49], D. Mortlock[56], A. Moss[88], D. Munshi[87], P. Naselsky[82,39], F. Nati[35], P. Natoli[34,4,49], C. B. Netterfield[20], H. U. Nørgaard-Nielsen[16], F. Noviello[70], D. Novikov[56], I. Novikov[82], S. Osborne[92], C. A. Oxborrow[16], F. Paci[86], L. Pagano[35,52], F. Pajot[60], D. Paoletti[49,51], B. Partridge[43], F. Pasian[48], G. Patanchon[1], O. Perdereau[72], L. Perotto[76], F. Perrotta[86], F. Piacentini[35], M. Piat[1], E. Pierpaoli[24], D. Pietrobon[69], S. Plaszczynski[72], E. Pointecouteau[97,9], G. Polenta[4,47], N. Ponthieu[60,54], L. Popa[63], T. Poutanen[44,27,2], G. W. Pratt[74], G. Prézeau[10,69], S. Prunet[61,95], J.-L. Puget[60], J. P. Rachen[21,79], B. Racine[1], R. Rebolo[67,14,40], M. Reinecke[79], M. Remazeilles[60,1], C. Renault[76], A. Renzi[86], S. Ricciardi[49], T. Riller[79], I. Ristorcelli[97,9], G. Rocha[69,10], C. Rosset[1], G. Roudier[1,73,69], M. Rowan-Robinson[56], J. A. Rubiño-Martín[67,40], B. Rusholme[57], M. Sandri[49], D. Santos[76], G. Savini[84], B. M. Schaefer[96], F. Schiavon[49], D. Scott[23], M. D. Seiffert[69,10], E. P. S. Shellard[11], L. D. Spencer[87], J.-L. Starck[74], V. Stolyarov[6,71,91], R. Stompor[1], R. Sudiwala[87], R. Sunyaev[79,89], F. Sureau[74], D. Sutton[65,71], A.-S. Suur-Uski[27,44], J.-F. Sygnet[61], J. A. Tauber[42], D. Tavagnacco[48,37], L. Terenzi[49], L. Toffolatti[19,68], M. Tomasi[50], M. Tristram[72], M. Tucci[17,72], J. Tuovinen[81], G. Umana[45], L. Valenziano[49], J. Valiviita[44,27,66], B. Van Tent[77], J. Varis[81], M. Viel[48,53], P. Vielva[68]⋆, F. Villa[49], N. Vittorio[38], L. A. Wade[69], B. D. Wandelt[61,95,32], M. White[29], J.-Q. Xia[86], D. Yvon[15], A. Zacchei[48], and A. Zonca[31]

(Affiliations can be found after the references)

Received 2013; accepted 2013

ABSTRACT

Based on Cosmic Microwave Background (CMB) maps from the 2013 *Planck* Mission data release, this paper presents the detection of the Integrated Sachs-Wolfe (ISW) effect, i.e., the correlation between the CMB and large-scale evolving gravitational potentials. The significance of detection ranges from 2 to 4 σ, depending on which method is used. We investigate three separate approaches, which cover essentially all previous studies, as well as breaking new ground. (i) Through correlation of the CMB with the *Planck* reconstructed gravitational lensing potential (for the first time). This detection is made using the lensing-induced bispectrum between the low-ℓ and high-ℓ temperature anisotropies; the correlation between lensing and the ISW effect has a significance close to 2.5 σ. (ii) Through cross-correlation with tracers of large-scale structure, yielding around 3 σ significance, based on a combination of radio (NVSS) and optical (SDSS) data. (iii) Using aperture photometry on stacked CMB fields at the locations of known large-scale structures, which yields and confirms, over a broader spectral range, a 4 σ signal when using a previously explored catalogue, but shows strong discrepancies in amplitude and scale compared to expectations. More recent catalogues give more moderate results, ranging from negligible to 2.5 σ at most, but with a more consistent scale and amplitude, the latter being still slightly above what is expected from numerical simulations within ΛCMD. Where they can be compared, these measurements are compatible with previous work using data from *WMAP*, which had already mapped these scales to the limits of cosmic variance. *Planck*'s broader frequency coverage allows for better foreground cleaning, and confirms that the signal is achromatic, bolstering the case for ISW detection. As a final step we use tracers of large-scale structure to filter the CMB data, presenting maps of the ISW temperature perturbation. These results provide complementary and independent evidence for the existence of a dark energy component that governs the current accelerated expansion of the Universe.

Key words. Cosmology: observations – cosmic microwave background – large-scale structure of the Universe – dark engery – Galaxies: clusters: general – Methods: data analysis

⋆ Corresponding author: P. Vielva vielva@ifca.unican.es

1. Introduction

This paper, one of a set associated with the 2013 data release from the *Planck*[1] mission (Planck Collaboration I 2013), presents the first results on the integrated Sachs-Wolfe (ISW) effect using *Planck* data. The ISW effect (Sachs & Wolfe 1967; Rees & Sciama 1968; Hu & Sugiyama 1994) is a secondary anisotropy in the cosmic microwave background (CMB), caused by the interaction of CMB photons with the time-evolving potentials from large-scale structure (LSS, hereafter). Photons follow a geodesic that is weakly perturbed by the Newtonian gravitational potential, Φ, and experience a fractional shift in their temperature given by

$$\Theta = \frac{\Delta T}{T_{\rm CMB}} = \frac{2}{c^3}\int_{\eta_*}^{\eta_0} {\rm d}\eta\, \frac{\partial \Phi}{\partial \eta}, \quad (1)$$

where the integral is expressed in terms of the conformal time η, defined differentially by ${\rm d}\eta/{\rm d}a = 1/(a^2 H(a))$ with $H(a)$ the Hubble function and a the scale factor. The integration limits here go from the recombination time (η_*) to the present time (η_0).

The sensitivity of the ISW effect to gravitational potentials (that can extend over Gpc scales) results in the power of the ISW being concentrated on the largest scales. The largest scales for the CMB have been mapped out by the *Wilkinson Microwave Anisotropy Probe* (*WMAP*) to the statistical limit of cosmic variance. Some systematics (like foreground removal) can have an impact on the reconstruction of the CMB especially at the largest scales where our Galaxy can introduce significant residuals on the reconstructed CMB map. The superior sensitivity of *Planck* together with its better angular resolution and wider frequency coverage allows for a better understanding (and hence removal) of Galactic and extagalactic foregrounds, therefore reducing the possible negative impact of these residuals. *Planck* allows us to improve on previous measurements by having a better systematic control, an improved removal of foregrounds (that permits us to explore the achromatic nature of the ISW signal on a wider frequency range), and a better understanding of systematics affecting tracer catalogues.

For cosmological models where $\Omega_{\rm m} = 1$, gravitational potentials remain constant during linear structure formation, and the ISW signal is negligible (to first order, although second order nonlinear ISW is always expected around smaller over- and under-dense regions). In the presence of dark energy, decaying potentials due to the accelerated expansion rate, result in a net ISW effect which is positive when the CMB photons cross overdense regions and negative when the CMB photons cross underdense regions. Therefore, the ISW effect is an indicator of either non-zero curvature (Kamionkowski & Spergel 1994), any form of dark energy, such as a cosmological constant Λ (Crittenden & Turok 1996), modified gravity (Hu 2002), or a combination of these possibilities. By measuring the rate at which gravitational potentials in the LSS decay (up to redshift of around 2), the ISW effect can be used as an independent probe of cosmology and provides complementary and independent evidence for dark energy.

Detection of the ISW effect was first made possible with all-sky CMB maps from *WMAP*. Based on these data, many works can be found in the literature where the authors aim at making, and subsequectly improving, the measurement of the ISW effect through correlations with tracer catalogues: 2MASS (an infrared catalogue at low redshifts around 0.1, Afshordi et al. 2004; Dupé et al. 2011; Francis & Peacock 2009; Rassat et al. 2006), *HEAO* (an X-ray survey at low redshift, with the first positive claim for detection, Boughn & Crittenden 2004), Sloan Digital Sky Survey (SDSS, optical survey at intermediate redshifts, Bielby et al. 2010; Cabré et al. 2006; Fosalba et al. 2003; Fosalba & Gaztañaga 2004; Giannantonio et al. 2006; Granett et al. 2009; López-Corredoira et al. 2010; Padmanabhan et al. 2005; Sawangwit et al. 2010; Scranton et al. 2003; Xia 2009), the NRAO VLA Sky Survey (NVSS, radio catalogue with high-redshift sources, Boughn & Crittenden 2005; Hernández-Monteagudo 2010; Massardi et al. 2010; McEwen et al. 2007; Pietrobon et al. 2006a; Raccanelli et al. 2008; Schiavon et al. 2012; Vielva et al. 2006), and combined measurements with multiple tracers (Corasaniti et al. 2005; Gaztañaga et al. 2006; Giannantonio et al. 2008, 2012; Ho et al. 2008; Nolta et al. 2004). The significance of the ISW detections that can be found in the literature range between $0.9\,\sigma$ and $4.7\,\sigma$. There are a number of peculiarities related to some of the detection claims, as noted by Hernández-Monteagudo (2010) and López-Corredoira et al. (2010). They both found lower significance levels than some previous studies and pointed out the absence of the signal at low multipoles where the ISW effect should be most prominent and the presence of point source emission on small scales for radio surveys.

The main result that is obtained from an ISW detection is a constraint on the cosmological constant (or dark energy), Ω_Λ. The general consensus from the variety of ISW analyses is for a value of $\Omega_\Lambda \simeq 0.75$ with an error of about 20%, which provides independent evidence for the existence of dark energy (Fosalba et al. 2003; Fosalba & Gaztañaga 2004; Nolta et al. 2004; Corasaniti et al. 2005; Padmanabhan et al. 2005; Cabré et al. 2006; Giannantonio et al. 2006; Pietrobon et al. 2006b; Rassat et al. 2006; Vielva et al. 2006; McEwen et al. 2007; Ho et al. 2008). All tests on spatial flatness find an upper limit for Ω_K of a few percent (Nolta et al. 2004; Gaztañaga et al. 2006; Ho et al. 2008; Li & Xia 2010). Using a prior on spatial flatness, the dark energy equation of state parameter, w, was found to be close to -1 (Giannantonio et al. 2006; Vielva et al. 2006; Ho et al. 2008) and has been excluded from having a strong time evolution (Giannantonio et al. 2008; Li & Xia 2010).

The ISW effect is achromatic, conserving the Planck spectrum of the CMB and can be separated from other CMB fluctuations through cross-correlations with catalogues which trace the LSS gravitational potentials (see for instance Crittenden & Turok 1996). This cross-correlation can be studied in different ways: angular cross-correlations in real space between the CMB and the catalogues tracing the LSS; the corresponding angular cross-power spectrum of the Fourier-transformed maps; or through the covariance of wavelet-filtered maps as a function of wavelet scale. The studies using *WMAP* data mentioned above follow this survey cross-correlation techique.

An alternative approach, similar to the angular cross-correlation in real space, consists of stacking CMB fields centred on known superclusters or supervoids (Granett et al. 2008a,b; Pápai & Szapudi 2010). The advantage of this technique is that it allows for a detailed study of the profile of the CMB fluctuations caused by this secondary anisotropy.

A novel and powerful approach takes advantage of the fact that the same potentials that make CMB photons gain or loose energy along their path (ISW), create lensing distortions that can

[1] *Planck* (http://www.esa.int/Planck) is a project of the European Space Agency (ESA) with instruments provided by two scientific consortia funded by ESA member states (in particular the lead countries France and Italy), with contributions from NASA (USA) and telescope reflectors provided by a collaboration between ESA and a scientific consortium led and funded by Denmark.

be measured from the CMB map directly (e.g., Hu & Okamoto 2002). The interplay between weak gravitational lensing and the ISW effect causes a non-Gaussian contribution to the CMB, which can be measured through the lensing-induced bispectrum between small and large angular scales. The measurement of the lensing potential requires a large number of modes that could not be measured before the arrival of *Planck* data.

This paper presents new measurements of the ISW effect carried out with *Planck*. Even although our detections are not in every case as strong as some previously claimed significance levels, we believe that our results are an improvement over earlier studies. This is because we can use the additional power enabled by the frequency coverage and sensitivity of *Planck*. To establish this we carry out a comprehensive study of all the main approaches which have previously been taken to estimate the ISW signal. We also present new results in relation to the non-Gaussian structure induced by the ISW effect.

The paper is organized as follows: In Sect. 2 we describe the data used in this work (both for the CMB and large-scale structure). The first ever results on the estimation of the lensing-induced bispectrum are presented in Sect. 3. Cross-correlations with external surveys are investigated in Sect. 4, and in Sect. 5 we present the results for the stacking analysis on the temperature maps, as well as aperture photometry on super-clusters and super-voids. The recovery of the ISW all-sky map is described in Sect. 6. Finally, we discuss our main results and their cosmological implications in Sect. 7.

2. Data description

In this Section we describe the different data sets used in this paper. This includes *Planck* data (the CMB temperature and lensing potential maps, see Planck Collaboration I 2013; Planck Collaboration XII 2013; Planck Collaboration XVII 2013) we refer to the corresponding *Planck* papers for details) and external data sets (large-scale structure tracers) used in the ISW determination: the radio NVSS catalogue; optical Luminous Galaxies (CMASS/LOWZ) and the Main Galaxy Sample from the Sloan Digital Sky Survey (SDSS); as well as several superstructure catalogues.

2.1. Planck data

Planck data and products used in this paper are described in the following sections, in particular the foreground-cleaned CMB maps produced by the *Planck* component separation pipelines, and related products, such as dedicated component-separated frequency maps (Planck Collaboration XII 2013), as well as the *Planck* lensing map (Planck Collaboration XVII 2013).

2.1.1. CMB maps

For the present work we have made use of the *Planck* foreground-cleaned CMB maps provided by the data processing centres (as described in the *Planck* component separation paper Planck Collaboration XII 2013). In particular, to test robustness, some of the results are presented for different cleaned CMB maps, which were constructed using four different component separation techniques: `Commander-Ruler` (`C-R`, which uses physical parametrization); `NILC` (an internal linear combination technique); `SEVEM` (a template fitting method); and `SMICA` (which uses spectral matching). Since the contribution of the ISW signal is only important on large scales, low resolution maps, with `HEALPix` Górski et al. (2005) parameter $N_{\rm side} = 64$, and pixel size of about 55 arcmin, have been used for most of the analyses. One exception is the study of the correlation between the ISW and lensing signals, which requires the use of full-resolution maps ($N_{\rm side}$=2048, pixel size of 1.7 arcmin). The maps are degraded directly from the original full resolution down to the corresponding $N_{\rm side}$.

In addition, foreground-cleaned maps per frequency (from 44 to 353 GHz) at resolution $N_{\rm side} = 512$ were used for the stacking analysis presented in Sect. 5. These maps were constructed by subtracting a linear combination of internal templates using `SEVEM` (see the `SEVEM` Appendix of Planck Collaboration XII 2013, for a detailed description of the method). As an example the `SEVEM` CMB map is shown in Fig. 1 (left panel).

Finally, to minimize the presence of foreground contamination in the maps, we have used the official mask described in Planck Collaboration XII (2013), which excludes regions with larger Galactic and point-source contamination (the U73 mask). This mask is given at the full *Planck* resolution and is downgraded to the required levels. The downgrading procedure consists of the following steps: the mask (originally a map with zero and one values) is convolved with a Gaussian beam of FWHM three times the characteristic pixel size of the final $N_{\rm side}$ resolution; this convolved map is then degraded to the required $N_{\rm side}$, and, afterwards, a threshold of 0.75 is imposed (i.e., pixels with a value above this threshold are set to one, whereas the rest are set to zero).

2.1.2. Lensing potential map

Weak gravitational lensing distorts the CMB temperature anisotropy pattern. This effect is sensitive to the projected matter distribution in the large-scale structure at high redshifts, where structure growth is linear and the statistics close to Gaussian. Weak lensing causes correlations between different multipoles which are proportional to the lensing deflection field. These correlations can be exploited for reconstructing the density field and for measuring its statistical properties (Hu & Okamoto 2002; Okamoto & Hu 2003). The lensing effect in the CMB can be estimated by this homogeneity breaking, and in this way individual modes of the lensing potential at multipoles $\ell < 100$ can be reconstructed with a significance of around $0.5\,\sigma$, showing the necessity of a statistical treatment. Nevertheless the overall effect of the lensing is measured to better than $25\,\sigma$ (Planck Collaboration XVII 2013). The additional lensing effect in the temperature power spectrum is detectable with a significance of about $10\,\sigma$ (Planck Collaboration XV 2013).

With *Planck* data, we aim at detecting a correlation between the ISW effect and the lensing potential, where the latter is a tracer of the large-scale structure at high redshift. This correlation is restricted to $9\,\sigma$, even in the ideal case, limited by cosmic variance and the smallness of the ISW effect in comparison to the primary CMB (Lewis et al. 2011). The data products used in this study are the *Planck* lensing potential reconstruction, and specific lensing maps obtained from the component separation pipelines. The lensing potential is available as part of the first *Planck* data release. Its detailed development is described in the *Planck* lensing paper (Planck Collaboration XVII 2013). In Fig. 1 we reproduce (right panel) an optimally filtered version of the *Planck* lensing map, suitable for the ISW-lensing cross-correlation.

In addition to a direct correlation between the CMB sky and the reconstructed lensing map, we measure the bispectrum generated by weak lensing by applying a range of estimators: the

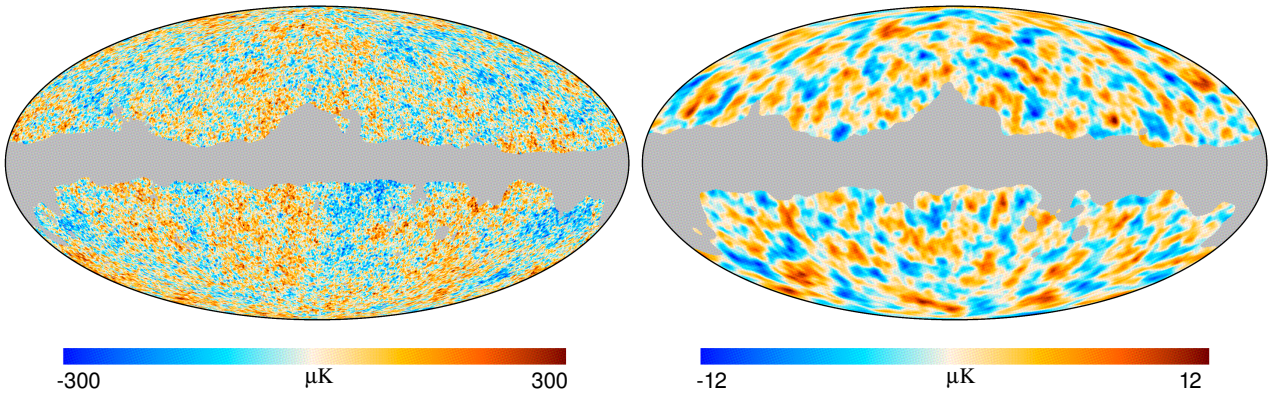

Fig. 1. *Left*: one of the CMB used in this paper, constructed using SEVEM (given at $N_{\rm side} = 64$). Other *Planck* CMB maps used in this work are Commader-Ruler, NILC and SMICA, in addition to clean SEVEM maps from 44 to 353 GHz. *Right*: *Planck* lensing map, optimally filtered to perform the ISW–lensing cross-correlation (given at $N_{\rm side} = 1024$).

KSW-bispectrum estimator; bispectra binned in multipole intervals; and a modal decomposition of the bispectrum. This measurement is made possible for the first time thanks to the *Planck* data. In addition, we will use information from the lensing field as a tracer for an ISW map reconstruction at high redshift (see Sect. 6).

2.2. External data sets

As described in the introduction, the achromatic nature of the ISW effect requires a tracer of the gravitational potentials from the large-scale structure, so that by cross-correlating the CMB temperature map with that tracer distribution the fluctuations due to the ISW effect are singled out. The prerequisites for a tracer catalogue to be used in ISW studies are: a large survey volume; well-understood biasing properties; and low or at least well-modelled systematics. The radio NVSS catalogue and the optical Luminous Galaxies (SDSS-CMASS/LOWZ) and Main Galaxy Sample (SDSS-MG) catalogues possess these qualities. Table 7 summarizes some basic properties of these catalogues. In addition, the redshift distributions of these catalogues are shown in Fig. 2. Notice that NVSS presents the widest redshift coverage. The SDSS-CMASS/LOWZ sample is peaked around $z \approx 0.5$, whereas the SDSS-MG sample peaks around $z \approx 0.3$.

Figure 3 shows the all-sky density projection for these maps, where the grey area indicates regions not observed by these surveys (or discarded for having contamination or low galaxy number density, see next subsections for details). In Fig. 4 we give the angular power spectra (blue points) of the surveys (corrected with a procedure similar to MASTER, e.g., Hivon et al. 2002), as well as the theoretical spectra (black lines) and their $1\,\sigma$ error bars (grey areas), estimated from the MASTER approach as well.

Besides the cross-correlation between CMB and LSS tracers (Sect. 4), we will present results from a different methodology in Sect. 5, where we use catalogues of super-structures to study the ISW through stacking of the CMB fluctuations on the positions of these super-structures. The relevant catalogues are described in Sect. 2.2.4.

2.2.1. NVSS radio catalogues

Luminous Active Galactic Nuclei (hereafter AGN) are known to be powerful radio sources, visible out to high redshifts. These sources are hence able to probe the cosmic density field during the entire redshift range from matter domination to accelerated expansion due to dark energy. If AGN are fair tracers of the underlying density field, these sources should likewise probe the spatial distribution of the large-scale potential wells that decay

Table 1. Major characteristics of the galaxy catalogues used as tracers of the gravitational potential. From left to right, the columns indicate: the number of galaxies per steradian; the fraction of the sky covered by each survey; the mean bias; and the median redshift. Notice that the bias for NVSS is not provided, since the assumed model has a bias which depends on redshift (see text for details).

Galaxy catalogue	$\bar{n}$	$f_{\rm sky}$	bias	$\bar{z}$
NVSS	1.584×10^5	0.73		1.17
SDSS-CMASS/LOWZ	5.558×10^5	0.22	2.03	0.45
SDSS-MG	9.680×10^6	0.22	1.20	0.32

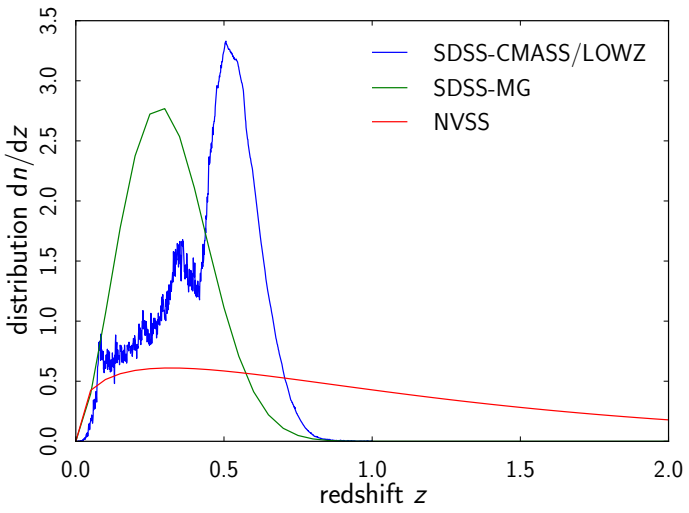

Fig. 2. Redshift distributions of the different surveys used in this work as LSS tracers, to be correlated with the *Planck* CMB maps. For ease of comparison, these distributions have been normalised to unity.

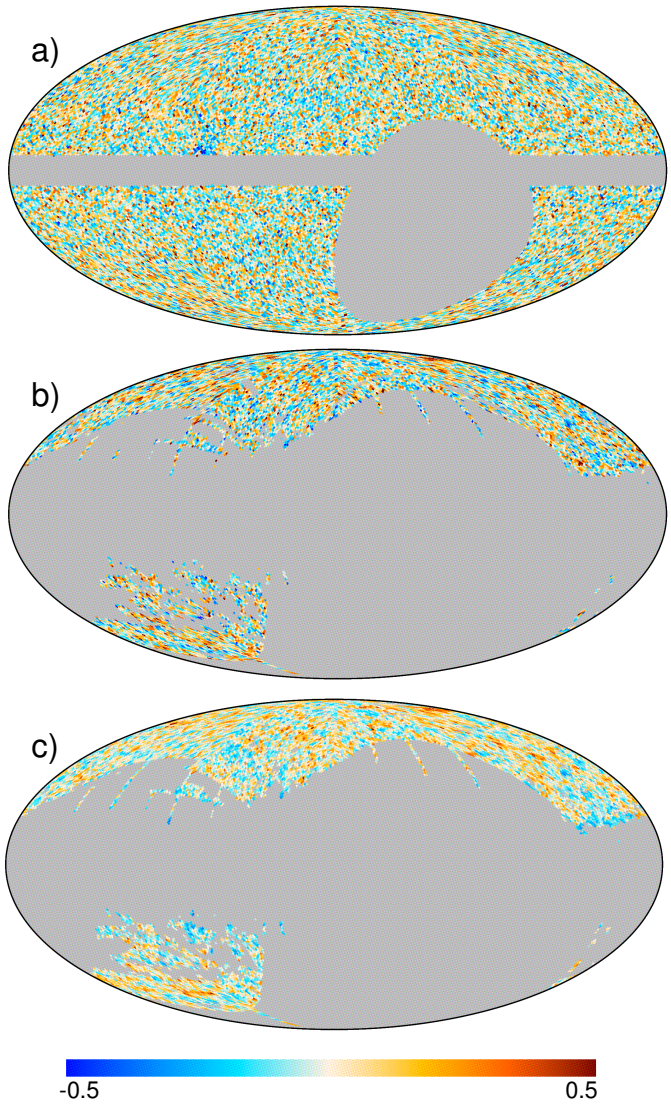

Fig. 3. Density contrast maps obtained from the galaxy catalogues at $N_{\rm side} = 64$. From top to bottom: NVSS; SDSS-CMASS/LOWZ; and SDSS-MG.

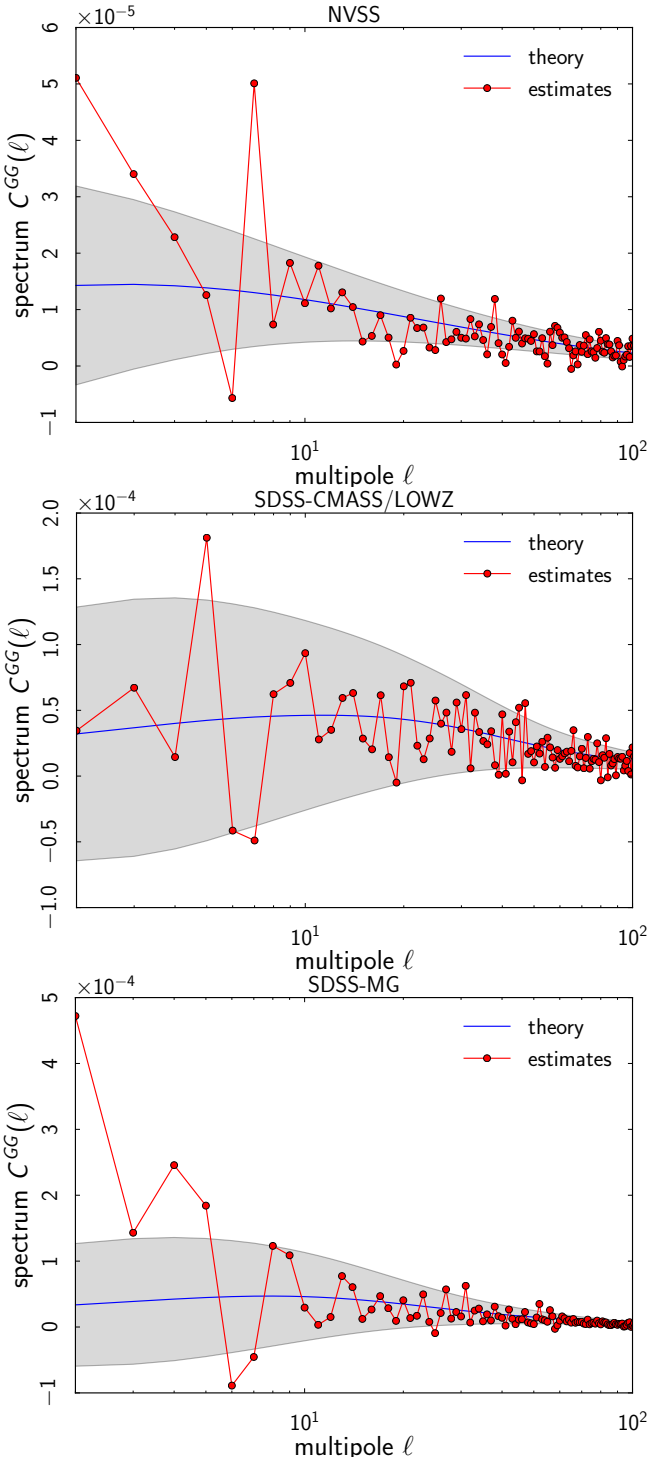

Fig. 4. Angular power spectra from the maps in Fig. 3. From top to bottom: NVSS; SDSS-CMASS/LOWZ; and SDSS-MG. The observed spectra are the red points, whereas the theoretical models are represented by the black lines (the grey areas correspond to the sampling variance).

at late times after the accelerated expansion sets in and generates the ISW effect.

We shall focus on a single radio survey, with the level of sensitivity and sky coverage required for ISW studies, namely the NRAO VLA Sky Survey (hereafter NVSS, Condon et al. 1998). This survey was conducted using the Very Large Array (VLA) at 1.4 GHz, and covers up to an equatorial latitude of $b_{\rm E} = -40°$, with an average noise level of 0.45 mJy beam^{-1}. It results in roughly 1.4×10^6 sources above a flux threshold of 2.5 mJy. Fig. 3 displays the number density map computed from the NVSS survey (top panel). The AGN population is known to be dominant in radio catalogues at 1.4 GHz in the high flux density regime. Condon et al. (1998) show that at this frequency, star-forming galaxies (SFGs) contribute about 30% of the total number of weighted source counts above 1 mJy, but their presence decreases rapidly as higher flux thresholds are adopted. The NVSS SFGs are nearby sources ($z < 0.01$), and hence may distort the ability of our radio template to probe the intermediate and high redshift density field.

We next address the presence of systematic effects in the NVSS survey. Two different antenna configurations were used while conducting the NVSS survey: the D-configuration (for $b_{\rm E} \in [-10°, 78°]$), and the DnC-configuration for large zenith angles ($b_{\rm E} < -10°$, $b_{\rm E} > 78°$). This change in the antenna configuration is known to introduce changes in the source number density above 2.5 mJy, as first pointed out by Blake & Wall

(2002). The NVSS map at 2.5 mJy is corrected for this declination systematic using the following procedure: the sky is divided into equatorial strips and the mean number of sources in each strip is re-normalised to the full sky mean (see e.g., Vielva et al. 2006). With this procedure the average number of sources in the NVSS map is the same as before the correction, and hence the shot noise level does not change. The number of strips into which the map is divided is 70, but the results are independent of this choice.

Regarding the galaxy bias, in this work we adopt the Gaussian bias evolution model of Xia et al. (2011). If $n(M,z)$ is the halo mass function and $b(M,z)$ is the bias of halos with comoving mass M, then the bias of the survey is given by a mass-weighted integral,

$$b(z) = \frac{\int_{M_{\rm min}}^{\infty} {\rm d}M\; b(M,z)\; M\; n(M,z)}{\int_{M_{\rm min}}^{\infty} {\rm d}M\; M\; n(M,z)} \,. \qquad (2)$$

This model depends on the minimum mass $M_{\rm min}$ of halos present in the survey. The upper limit in the mass is taken to be infinity because the effect of the high mass end on the bias is negligible. Marcos-Caballero et al. (2013) proposed a theoretical model for the NVSS angular power spectrum, which also takes into account the information of the redshift distribution given by CENSORS data (Brookes et al. 2008). The redshift distribution is parametrized by

$$\frac{{\rm d}n}{{\rm d}z} = n_0 \left(\frac{z}{z_0}\right)^{\alpha} e^{-\alpha z/z_0} \,, \qquad (3)$$

where $z_0 = 0.32$ and $\alpha = 0.36$. The parameter n_0 is a constant in order to have a distribution normalized to unity. This function is represented in Fig. 2. The bias follows the prescription of Eq. 2, with $M_{\rm min}$ equal to $10^{12.67}{\rm M}_{\odot}$, where the Sheth-Tormen (Sheth & Tormen 1999) mass function is adopted. Hereafter this model will be regarded as our fiducial model for NVSS.

2.2.2. SDSS Luminous Galaxies

For this analysis we use the photometric Luminous Galaxy (LG) catalogue from the Baryonic Oscillation Spectroscopic Survey (BOSS) of the SDSS III. The data used consist of two subsamples: CMASS; and LOWZ. Both samples are combined to form a unique LG map (see Fig. 3, second panel). Hereafter, these samples will be referred to as SDSS-CMASS, SDSS-LOWZ, and SDSS-CMASS/LOWZ, for the combination.

SDSS-CMASS

We use the BOSS targets chosen to have roughly constant stellar mass and known as the photometric "CMASS" sample. This sample is mostly contained in the redshift range $z = 0.4$–0.7, with a galaxy number density close to $110\,{\rm deg}^{-2}$, and is selected after applying the colour cuts explained in Ross et al. (2011).

While such color selection yields a catalogue of about 1,600 , 000 galaxies, further cuts needed to be applied in order to account for dust extinction (based on the maps by Schlegel et al. 1998 with the criterion $E(B-V) < 0.08$), for seeing in the r band (required to be $< 2.0''$) and for the presence of bright stars, similar to Ho et al. (2012). Finally, we neglected all pixels with a mask value inferred from the footprint below 0.9 on a `HEALPix` map of resolution $N_{\rm side}$=64. This procedure left about one million sources 10,500 deg^2. Photometric redshifts of this sample are calibrated using a selection of about 100,000 BOSS spectra as a training sample for the photometric catalogue. These LGs are among the most luminous galaxies in the Universe and therefore allow for a good sampling of the largest scales. Given the large number of such sources included in the sample, shot-noise does not dominate clustering errors. According to Ross et al. (2011), about 3.7 % of these objects are either stars or quasars, and this makes further corrections necessary, as explained at the end of this section.

SDSS-LOWZ

The photometric LOWZ sample is one of the two galaxy samples targeted by the BOSS of Sloan III. It selectd luminous, highly biased, mostly red galaxies, placed at an average redshift of $\langle z\rangle \sim 0.3$ and below the redshifts of the CMASS sample ($z < 0.4$). Our selection criteria in terms of the Sloan five model magnitudes *ugriz* follow those given in Sect. 2 of Parejko et al. (2013). With a total number of sources close to 600,000, this photometric sample contains a higher number density of galaxies in the southern part of the footprint than in the northern one (by more than 3 %), which seems to be at odds with ΛCDM predictions. However, most of this effect vanishes when we subtract the dipole in the effective area under analysis, in such a way that the low ℓ range of the auto power spectrum is consistent with a ΛCDM model and a constant bias $b \simeq 2$ (Hernandez-Monteagudo et al. 2013).

Both SDSS-CMASS and SDSS-LOWZ samples are further corrected for any scaling introduced by possible systematics like stars, mask value, seeing, sky emission, airmass and dust extinction. Following exactly the same procedure as in Hernandez-Monteagudo et al. (2013), we find that both LG samples are contaminated by stars, in the sense that the galaxy number density decreases in areas with higher star density, since the latter tend to "blind" galaxy detection algorithms.

2.2.3. Main SDSS Galaxy Sample

We use a sample of photometrically-selected galaxies from the SDSS-DR8 catalogue, which covers a total sky area of 14,555 deg^2 (Aihara et al. 2011). The total number of objects labelled as galaxies in this data release is 208 million. From this catalogue, and following Cabré et al. (2006), we define a subsample by selecting only objects within the range $18 < r < 21$, where this r-band model magnitude corrected for extinction. Following Giannantonio et al. (2008), we also restrict our subsample to objects with redshifts $0.1 < z < 0.9$, and with measured redsfhit errors such that $\sigma_z < 0.5z$. We rely on the photometric redshift estimates of the SDSS photo-z primary galaxy table, which have been obtained through a "kd-tree" nearest neighbour technique, by fitting the spectroscopic objects observed with similar colour and inclination angle. The total number of galaxies in our final sample is about 42 million, with redshifts distributed around a median value of around 0.35, as shown in Fig. 2. To avoid possible errors introduced by singularities in the photometric redshifts estimates, instead of using the real observed redshift distribution in our analysis we resort to the analytical function

$$\frac{dn}{dz} = \frac{\beta}{\Gamma\left(\frac{m+1}{\beta}\right)} \frac{z^m}{z_0^{m+1}} e^{-(z/z_0)^{\beta}} \,, \qquad (4)$$

which is fitted to the data, with parameters $m = 1.5, \beta = 2.3$ and $z_0 = 0.34$, which are identical to those found by Giannantonio et al. (2012). For the galactic bias we use the value $b = 1.2$,

which is found by Giannantonio et al. (2012) by fitting the ΛCDM prediction to the observed auto-correlation function of the galaxies, and we adopt their proposed mask.

2.2.4. SDSS, super-structures

Granett et al. (2008b) produced a sample[2] of 50 superclusters and 50 supervoids identified from the Luminous Red Galaxies (LRGs) in the SDSS (sixth data release, DR6, Adelman-McCarthy et al. 2008) that covers an area of 7500 deg^2 on the sky. They used publicly available algorithms, based on the Voronoi tessellation, to find 2836 superclusters (using VOBOZ, VOronoi BOund Zones, Neyrinck et al. 2005) and 631 supervoids (using ZOBOV, ZOnes Bordering On Voidness, Neyrinck 2008) above a $2\,\sigma$ significance level (defined as the probability of obtaining, in a uniform Poisson point sample, the same density contrasts as those of clusters and voids). The 50 superclusters and 50 supervoids they published in their catalogue correspond to density contrasts of about $3\,\sigma$ and $3.3\,\sigma$ respectively. They span a redshift range of $0.4 < z < 0.75$, with a median of around 0.5, and inhabit a volume of about $5\,h^{-3}$ Gpc^3. These superstructures can potentially produce measurable ISW signals, as suggested in Granett et al. (2008a,b). For each structure, the catalogue provides: the position on the sky of the centre; the mean and maximum angular distance between the galaxies in the structure and its centre; the physical volume; and three different measures of the density contrast (calculated from all its Voronoi cells, from only its over- or under-dense cells, and from only its most over- under-dense cell). For the present paper, we concentrate on using the supervoid catalogue by Granett et al. (2008b), as they can be compared with two other, more recent catalogues of voids.

The second catalogue of cosmic voids that we consider here is published by Pan et al. (2012)[3]. It has been built from the seventh data release (DR7) of the SDSS. Using the `VoidFinder` algorithm (Hoyle & Vogeley 2002), they identified 1055 voids with redshifts smaller than $z = 0.1$. Each void is listed with its position on the sky, its physical radius (defined as the radius of the maximal sphere enclosing the void), an effective radius defined as the radius of a sphere of the same volume, its physical distance to us, its volume and mean density contrast. The filling factor of the voids in the sample volume is 62 %. The largest void is just over 47 Mpc in effective radius, while the median effective radius of the void sample is roughly 25 Mpc. Some of the voids are both very close to us and relatively large (larger than 30 Mpc in radius), which results in large angular sizes of up to 15°.

The third void catalogue that we use has been released by Sutter et al. (2012) and also made publicly available.[4] Note that it is being updated regularly, and the results reported here are based on the 21 February 2013 version of the catalogue. Using their own improved version of `ZOBOV`, these authors identified 1495 voids distributed across the 0–0.44 redshift range. They subdivided their catalogue into six subsamples: *dim1*, *dim2*, *bright1* and *bright2*, constructed from the main SDSS; and *lrgdim*, *lrgbright* built from the SDSS LRG sample. For each void, the information provided includes the position of the centre, the redshift, the volume, the effective radius, and the density contrast.

[2] Available at `http://ifa.hawaii.edu/cosmowave/supervoids/`.

[3] Available at `http://www.physics.drexel.edu/~pan/`.

[4] Available at `http://www.cosmicvoids.net`.

3. ISW-lensing bispectrum

There is an interesting interplay between gravitational lensing of the CMB and the ISW effect, which manifests itself as a non-Gaussian feature. CMB-lensing can be described by a convolution of the CMB-temperature map T with the weak lensing potential ϕ,

$$T(\ell) \rightarrow T(\ell) - \int \frac{\mathrm{d}^2\ell'}{2\pi}\, \ell'(\ell-\ell')\,\phi(\ell-\ell')T(\ell'). \tag{5}$$

The CMB lensing can be measured by a direct estimate of the CMB bispectrum, because the bispectrum acquires first order terms proportional to the product of two power spectra $\tilde{C}_\ell^{\mathrm{TT}} C_\ell^{\mathrm{T}\phi}$, where $\tilde{C}_\ell^{\mathrm{TT}}$ is the lensed temperature power spectrum and $C_\ell^{\mathrm{T}\phi}$ is the temperature-potential cross-power spectrum. The potential field ϕ and the temperature field T are correlated, because ϕ, which deflects the CMB photons, also gives rise to the ISW effect in T (Hu & Okamoto 2002; Seljak & Zaldarriaga 1999; Verde & Spergel 2002; Giovi et al. 2003). This secondary bispectrum contains new information about the cosmological redshift, because it is generated mainly at redshifts larger than unity, and biases measurements of the primordial bispectrum. The term $C_\ell^{\mathrm{T}\phi}$ correlates the CMB temperature on small scales with the lensing potential on large scales, and causes the bispectrum to assume large amplitudes in the squeezed triangles configuration (see e.g., Goldberg & Spergel 1999; Seljak & Zaldarriaga 1999; Hu 2000; Giovi et al. 2003; Okamoto & Hu 2003; Giovi & Baccigalupi 2005; Lewis & Challinor 2006; Serra & Cooray 2008; Mangilli & Verde 2009; Hanson et al. 2009, 2010; Smith & Zaldarriaga 2011; Lewis et al. 2011).

Due to the rotational invariance of the sky, the CMB angular bispectrum $\langle a_{\ell_1 m_1} a_{\ell_2 m_2} a_{\ell_3 m_3}\rangle$ can be factorized as follows:

$$\langle a_{\ell_1 m_1} a_{\ell_2 m_2} a_{\ell_3 m_3}\rangle = \mathcal{G}^{m_1 m_2 m_3}_{\ell_1\ell_2\ell_3} b_{\ell_1\ell_2\ell_3}, \tag{6}$$

where $\mathcal{G}^{m_1 m_2 m_3}_{\ell_1\ell_2\ell_3} \equiv \int \mathrm{d}^2\Omega\; Y^{m_1}_{\ell_1}(\hat{\boldsymbol{n}}) Y^{m_2}_{\ell_2}(\hat{\boldsymbol{n}}) Y^{m_3}_{l_3}(\hat{\boldsymbol{n}})$ is the Gaunt-integral and $b_{\ell_1\ell_2\ell_3}$ is the so-called reduced bispectrum. In the case where the bispectral signal on the sky is due to the ISW-lensing effect, $b_{\ell_1\ell_2\ell_3} = A^{\mathrm{T}\phi} b^{\mathrm{lens-ISW}}_{\ell_1\ell_2\ell_3}$, where $A^{\mathrm{T}\phi}$ parametrizes the amplitude of the effect and

$$b^{\mathrm{lens-ISW}}_{\ell_1\ell_2\ell_3} = \left\{ \frac{\ell_1(\ell_1+1) - \ell_2(\ell_2+1) + \ell_3(\ell_3+1)}{2} C^{\mathrm{T}\phi}_{\ell_1} \tilde{C}^{\mathrm{TT}}_{\ell_3} + (5\ \text{permutations}) \right\}. \tag{7}$$

A more general expression for intensity and polarization can be found in Lewis et al. (2011). Estimation of the bispectrum then yields a measurement of $A^{\mathrm{T}\phi}$.

We can also define an alternative rotationally-invariant reduced bispectrum $B_{\ell_1\ell_2\ell_3}$ as $B_{\ell_1\ell_2\ell_3} = h^2_{\ell_1\ell_2\ell_3} b_{\ell_1\ell_2\ell_3}$, where

$$h^2_{\ell_1\ell_2\ell_3} \equiv \sum_{m_1 m_2 m_3} \left(\mathcal{G}^{m_1 m_2 m_3}_{\ell_1\ell_2\ell_3}\right)^2 = \frac{(2\ell_1+1)(2\ell_2+1)(2\ell_3+1)}{4\pi} \begin{pmatrix} \ell_1 & \ell_2 & \ell_3 \\ 0 & 0 & 0 \end{pmatrix}^2. \tag{8}$$

The interest in $B_{\ell_1\ell_2\ell_3}$ is that it can be directly estimated from the observed map using the expression

$$B^{\mathrm{obs}}_{\ell_1\ell_2\ell_3} = \int \mathrm{d}\Omega T_{\ell_1}(\Omega) T_{\ell_2}(\Omega) T_{\ell_3}(\Omega), \tag{9}$$

where the filtered maps $T_\ell(\Omega)$ are defined as

$$T_\ell(\Omega) \equiv \sum_m a_{\ell m} Y_{\ell m}(\Omega). \tag{10}$$

By basically combining the single-ℓ estimates $B^{\rm obs}/B^{\rm lens-ISW}$ for $A^{{\rm T}\phi}$ using inverse variance weighting, the ISW-lensing bispectrum estimator can be written as (see Planck Collaboration XXIV 2013, for more details)

$$\hat{A}^{{\rm T}\phi} = \frac{\langle B^{\rm lens-ISW}, (B^{\rm obs} - B^{\rm lin})\rangle}{\langle B^{\rm lens-ISW}, B^{\rm lens-ISW}\rangle}, \tag{11}$$

where the inner product is defined by

$$\langle B^i, B^j\rangle \equiv \sum_{\ell_1\le\ell_2\le\ell_3} \frac{B^i_{\ell_1\ell_2\ell_3} B^j_{\ell_1\ell_2\ell_3}}{V_{\ell_1\ell_2\ell_3}}. \tag{12}$$

Here, $B^{\rm lin}$ is a linear correction that has zero average but reduces the variance of the estimator in the presence of anisotropic noise and a mask. Furthermore, $V_{\ell_1\ell_2\ell_3} = g_{\ell_1\ell_2\ell_3} h^2_{\ell_1\ell_2\ell_3} C_{\ell_1} C_{\ell_2} C_{\ell_3}$, with g being a simple permutation factor ($g = 6$ when all ℓ are equal, $g = 2$ when two ℓ are equal and $g = 1$ otherwise). As in all expressions in this section, we have implicitly taken the beam and noise of the experiment into accout, e.g., C_ℓ should actually be $b^2_\ell C_\ell + N_\ell$ with b_ℓ the beam transfer function and N_ℓ the noise power spectrum.

In Eq. 11 we have also used the fact that, as discussed in detail in Planck Collaboration XXIV (2013), the full inverse covariance weighting can be replaced by a diagonal covariance term, $(C^{-1}a)_{\ell m} \rightarrow a_{\ell m}/C_\ell$, without loss of optimality, if the masked regions of the map are filled in with a simple diffusive inpainting scheme.

The normalization of the lensing-ISW estimator in the denominator of Eq. 11 can be replaced by (see e.g. Lewis et al. 2011)

$$F = \sum_\ell \left(F_\ell^{-1} + \frac{1 + r_\ell^{-2}}{2\ell + 1}\right)^{-1}, \tag{13}$$

where $r_\ell \equiv C_\ell^{{\rm T}\phi}/\sqrt{\tilde{C}_\ell^{\rm TT}\, C_\ell^{\phi\phi}}$ parameterizes the deviation from the Cauchy-Schwarz relation and F_ℓ is given in terms of the ISW-lensing bispectrum (see for example Lewis et al. 2011). The first term in Eq. 13 corresponds to the Fisher errors assuming Gaussian $a_{\ell m}$. However, contrary to the null hypothesis that is assumed, for example, in the primordial bispectra (Gaussianity), there is an actual non-Gaussian signal already present in the ISW-lensing bispectrum. This guarantees a larger variance for the estimators than are included in the additional terms present in the previous equations.

An important issue is the impact of the ISW-lensing bispectrum on estimates of the primordial non-Gaussianity. Assuming weak levels of non-Gaussianity and considering both the primordial bispectrum $B^{\rm prim}_{\ell_1\ell_2\ell_3}$ and the ISW-lensing bispectrum $B^{\rm lens-ISW}_{\ell_1\ell_2\ell_3}$, one can compute the expected bias Δ induced in the primordial bispectrum using the formula:

$$\Delta^{\rm prim} = \frac{\langle B^{\rm lens-ISW}, B^{\rm prim}\rangle}{\langle B^{\rm prim}, B^{\rm prim}\rangle} \tag{14}$$

with the inner product defined in Eq. 12. Predictions of this bias on the primordial $f_{\rm NL}$ for *Planck* resolution can be seen for example in Hanson et al. (2009), Mangilli & Verde (2009), Smith & Zaldarriaga (2011), and Lewis et al. (2011). The most important bias is introduced to the local shape and, considering $\ell_{\rm max} \sim 2000$, is expected to be $\Delta^{\rm local} \sim 7$ (Planck Collaboration XXIV 2013).

3.1. ISW-lensing estimators

There are several implementations of the optimal estimator given in Eq. 11. For their detailed description in the context of *Planck* see Planck Collaboration XXIV (2013); Planck Collaboration XVII (2013). We have applied four of these implementations to *Planck* data in order to constrain the ISW-lensing bispectrum. Three of them represent a direct bispectrum estimation: the KSW estimator (Komatsu et al. 2005; Creminelli et al. 2006), the binned bispectrum (Bucher et al. 2010), and the modal decomposition (Fergusson et al. 2010).The remaining approach is based on a previous estimation of the gravitational lensing potential field Lewis et al. (2011). These estimators differ in the implementation and approximations that are used in order to compute the expression given in Eq. 11, the direct computation of which is out of reach of current computing facilities. They will be reviewed in the next subsections.

3.1.1. Lensing potential reconstruction

The estimator given in Eq. 6 can be written in terms of the lensing potential amplitude reconstruction $\hat{\phi}$ as

$$\hat{A}^{{\rm T}\phi} \equiv \hat{S} = \frac{1}{N}\sum_{\ell m} C_\ell^{{\rm T}\phi} \frac{\tilde{T}_{\ell m}}{\tilde{C}_\ell^{\rm TT}} \frac{\hat{\phi}^*_{\ell m}}{N_\ell^{\phi\phi}}, \tag{15}$$

where $\hat{\phi}^*_{\ell m}$ can be estimated using a quadratic estimator (Okamoto & Hu 2003) and $N_\ell^{(0)}$ is given in terms of the ISW-lensing bispectrum (Lewis et al. 2011). Therefore, this estimator quantifes the amount of cross-correlation between the temperature map and the reconstruction of the lensing signal, and most of the correlation is found at multipoles below 100.

3.1.2. KSW-estimator

The KSW bispectrum estimator (Komatsu et al. 2005) for the ISW-lensing signal can be written as

$$\hat{A}^{{\rm T}\phi} = (F^{-1})\hat{S}, \tag{16}$$

where $\hat{S}$ can be computed from data as

$$\hat{S} \equiv \frac{1}{6}\sum_{\ell_1 m_1}\sum_{\ell_2 m_2}\sum_{\ell_3 m_3} \mathcal{G}^{m_1 m_2 m_3}_{\ell_1\ell_2\ell_3} b^{\rm lens-ISW}_{\ell_1\ell_2\ell_3} \times \Big[(C^{-1}a)_{\ell_1 m_1}(C^{-1}a)_{\ell_2 m_2}(C^{-1}a)_{\ell_3 m_3} - 3(C^{-1})_{\ell_1 m_1,\ell_2 m_2}(C^{-1}a)_{\ell_3 m_3}\Big]. \tag{17}$$

and (F^{-1}) is the inverse of the ISW-lensing Fisher matrix F of Eq. 13. Details on the implementation of the KSW estimator for the ISW-lensing signal can be found in Mangilli et al. (2013). In particular, Eq. 16 takes the form

$$\hat{A}^{{\rm T}\phi} = (F^{-1})(\hat{S}_{\rm cubic} + \hat{S}_{\rm linear}), \tag{18}$$

where $\hat{S}_{\rm cubic}$ is the term that extracts the amplitude information from the data contained in the bispectrum, while $\hat{S}_{\rm linear}$ is a zero-mean term that reduces estimator variance when the experimental setup breaks rotational invariance, i.e., in the presence of sky

cut and anisotropic noise. To estimate $\hat{A}^{T\phi}$ we used the KSW estimator with an implementation of the linear term truncated at ℓ_{max} as described in Munshi & Heavens (2010) and Planck Collaboration XXIV (2013).

3.1.3. Binned bispectrum

The binned bispectrum estimator (Bucher et al. 2010) achieves the required computational reduction in determining $A^{T\phi}$ by binning Eq. 11. In particular, the maximally filtered maps in Eq. 10 are replaced by

$$T_i(\Omega) = \sum_{\ell\in\Delta_i}\sum_{m=-\ell}^{+\ell} a_{\ell m}Y_{\ell m}(\Omega), \tag{19}$$

where the Δ_i are suitably chosen intervals (bins) of multipole values (chosen in such a way as to minimize the variance of the quantities to be estimated). These maps are then used in Eq. 9 to obtain the binned observed bispectrum, and analogously for $B^{\rm lin}$. The bispectrum template $B^{\rm lens-ISW}$ and inverse-variance weights V are also binned by summing them over all ℓ values in the bin. Finally these binned quantities are inserted in the general expression for $A^{T\phi}$ (Eq. 11), with the sum over ℓ replaced by a sum over bin indices i. Since most bispectrum shapes change rather slowly (with features on the scale of the acoustic peaks, like the power spectrum), the binned estimator works very well, increasing the variance only slightly, while achieving an enormous computational reduction (from about 2000 multipoles in each of the three directions to only about 50 bins).

3.1.4. Modal bispectra

Modal decomposition of bispectra has been introduced by Fergusson et al. (2010) as a way to compute reduced bispectra that uses a diagonalization ansatz such that the shape function in Fourier space can be separated, which reduces the dimensionality of the integration. At the same time it greatly reduces the complexity of estimating bispectra from data. The separation of the bispectrum shape function into coefficients $q_p^\ell(x)$ allows the derivation of a filtered map $M_p(\hat{n}, x)$,

$$M_p(\hat{n}, x) = \sum_{\ell m}\frac{q_p^\ell(x)a_{\ell m}}{C_\ell}Y_{\ell m}(\hat{n}), \tag{20}$$

from the coefficients $a_{\ell m}$ of the temperature map. With that expression, one can obtain a mode expansion coefficient β,

$$\beta_{prs} = \int {\rm d}\Omega \int x^2{\rm d}x\, M_p(\hat{n}, x)M_r(\hat{n}, x)M_s(\hat{n}, x). \tag{21}$$

With that decomposition, the estimator of the bispectrum assumes a particularly simple diagonal shape,

$$\hat{S} = \frac{6}{N}\Delta_\Phi^2\sum_{prs}\alpha_{prs}\beta_{prs}, \tag{22}$$

where the α_{prs} are the equivalent coefficients obtained by performing the modal decomposition of the theoretical bispectrum shape function. The relation between modal bispectra and wavelet bispectra is derived by Regan et al. (2013).

3.2. Results

The detection of the ISW effect via the non-Gaussian signal induced by the gravitational lensing potential is summarized in Table 2. We provide the estimates of the ISW-lensing amplitude $A^{T\phi}$, its uncertainty σ_A and the signal-to-noise obtained with the different estimator pipelines described in Sec. 3.1. The estimators have been applied to the official *Planck* CMB maps made using `C-R`, `NILC`, `SEVEM`, and `SMICA` (Planck Collaboration XII 2013). The quantity σ_A is obtained from 200 simulations representative of the analysed CMB data maps. These Monte Carlo simulations (FFP-6, see Planck Collaboration I 2013) account for the expected non-Gaussian ISW-lensing signal, according to the *Planck* best-fit model, and have been passed through the different component separation pipelines, as described in Planck Collaboration XII (2013). lensed simulations can be found in Planck Collaboration XVII (2013). The mask used in the analysis is the combined Galactic and point source common mask (U73, Planck Collaboration I 2013) with sky fraction $f_{\rm sky} = 0.73$.

The KSW and the $T\phi$ estimators show similar sensitivity, finding, respectively, $A^{T\phi} = 0.81 \pm 0.31$ and $A^{T\phi} = 0.70 \pm 0.28$ from the `SMICA` CMB map, which corresponds to a significance at about the $2.5\,\sigma$ level. The modal and binned estimators are slightly less optimal, but give consistent results, which is consistent with the imperfect overlap of the modal estimator templates with the ISW-lensing signal; the ISW-lensing bispectrum has a rapidly oscillating shape in the squeezed limit and both, binned and modal estimates, are better suited (and originally implemented) to deal with smooth bispectra of the kind predicted by primordial inflationary theories. Since the correlation coefficient of the binned and modal ISW-lensing templates relative to the actual ISW-lensing bispectrum (Eq. 8) is generally $0.8 < r < 0.9$ (to be compared with $r = 0.99$, achieved by both estimators for local, equilateral and orthogonal primordial templates, Planck Collaboration XXIV 2013), the corresponding estimator's weights are expected to be about 20 % suboptimal, consistent with observations.

The $T\phi$ estimator has also been applied to the specific *Planck* lensing baseline, i.e., the MV map, which is a noise-weighted combination of the 217 GHz and 143 GHz channel maps, previously cleaned from infrared contamination through subtraction of the 857 GHz map, taken as a dust template. From this map the lensing potential is recovered and then correlated with that potential field in order to estimate the amplitude $A^{T\phi}$. The official baseline adopts a more conservative high-pass filtering, such that as only multipoles $\ell \geq 10$ are considered, and the mask with $f_{\rm sky} = 0.7$ is used. In this case, the ISW-lensing estimate is 0.78 ± 0.32 (a $2.4\,\sigma$ detection, where the error bars are obtained from 1000 simulations), as reported in the first sub-row for $T\phi$ in Table 2. The full multipole range is considered in the second sub-row, obtaining about 7% better sensitivity.

Notice that, according to all the estimators, the `C-R` CMB map provides lower significance for ISW-lensing, since its resolution is slightly lower than that of the other maps. `NILC` and `SMICA` exhibit a somewhat larger detection of the ISW signal, since they are the least noisy maps.

In order to explore the agreement among the different estimators, we performed a validation test based on 200 lensed simulations processed through the `SMICA` pipeline. The results are summarized in Table 3. For each pair of statistics, we provide the difference in amplitudes estimated for the data ($\Delta A^{T\phi}$), the dispersion of the difference of amplitudes obtained from the simulations (s_A), the ratio between this dispersion and the largest

Table 2. Amplitudes $A^{T\phi}$, errors σ_A and significance levels of the non-Gaussianity due to the ISW effect, for all component separation algorithms (C-R, NILC, SEVEM, and SMICA) and all the estimators (potential reconstruction, KSW, binned, and modal). For the potential reconstruction case, an additional minimum variance (MV) map has been considered (see Planck Collaboration XVII 2013 for details).

Estimator		C-R		NILC		SEVEM		SMICA		MV	
$T\phi$	$\ell \geq 10$	0.52 ± 0.33	1.5	0.72 ± 0.30	2.4	0.58 ± 0.31	1.9	0.68 ± 0.30	2.3	0.78 ± 0.32	2.4
	$\ell \geq 2$	0.52 ± 0.32	1.6	0.75 ± 0.28	2.7	0.62 ± 0.29	2.1	0.70 ± 0.28	2.5		
KSW		0.75 ± 0.32	2.3	0.85 ± 0.32	2.7	0.68 ± 0.32	2.1	0.81 ± 0.31	2.6		
binned		0.80 ± 0.40	2.0	1.03 ± 0.37	2.8	0.83 ± 0.39	2.1	0.91 ± 0.37	2.5		
modal		0.68 ± 0.39	1.7	0.93 ± 0.37	2.5	0.60 ± 0.37	1.6	0.77 ± 0.37	2.1		

Table 3. For each pair of estimators we provide the mean difference among the amplitudes estimated from the data ($\Delta A^{T\phi}$), the dispersion of the differences between the amplitudes estimated from the simulations (s_A), the ratio of this dispersion to the larger of the corresponding sensitivities (η), and the correlation coefficient (ρ).

		KSW	binned	modal
$T\phi$	$\Delta A \pm s_A$	-0.11 ± 0.10	-0.21 ± 0.21	-0.07 ± 0.21
	η	0.32	0.56	0.56
	ρ	0.95	0.84	0.84
KSW	$\Delta A \pm s_A$		-0.10 ± 0.19	0.04 ± 0.19
	η		0.52	0.51
	ρ		0.86	0.87
binned	$\Delta A \pm s_A$			0.14 ± 0.15
	η			0.41
	ρ			0.92

of the corresponding sensitivities (η, according to Table 2), and the correlation coefficient (ρ). As can be seen from the Table, the agreement among estimators is good and the discrepancies are only around $0.5\,\sigma$, which is the expected scatter, given the correlation between the weights of different estimators discussed above. Overall, the bispectrum estimators provide a larger value of the amplitude $A^{T\phi}$, as compared to the $T\phi$ estimator.

We have also explored the joint estimation of the two bispectra that are expected to be found in the data: the ISW-lensing; and the residual point sources. A detailed description of the non-Gaussian signal coming from point sources can be found in Planck Collaboration XXIV (2013). The joint analysis of these two signals performed with the KSW estimator, and the binned, and modal estimators has shown that the ISW-lensing amplitude estimation can be considered almost completely independent of the non-Gaussian signal induced by the residual sources, and that the two bispectra are nearly perfectly uncorrelated.

There is not a unique way of extracting a single signal-to-noise value from Table 2. However, all the estimators show evidence of ISW-lensing at about the $2.5\,\sigma$ level.

Finally, we estimate that the bias introduced by the ISW-lensing signal on the estimation of the primordial local shape bispectrum (Eq. 14) is $\Delta^{\rm prim} \simeq 7$, corresponding to the theoretical expectation, as described in detail in Planck Collaboration XXIV (2013).

4. Cross-Correlation with surveys

The ISW effect can be probed through several different approaches. Among the ones already explored in the literature, the classical test is to study the cross-correlation of the CMB temperature fluctuations with a tracer of the matter distribution, typically a galaxy or cluster catalogue. As mentioned in the introduction, the correlation of the CMB with LSS tracers was first proposed by Crittenden & Turok (1996) as a natural way to amplify the ISW signal, otherwise very much subdominant with respect to the primordial CMB fluctuations. Indeed, this technique led to the first reported detection of the ISW effect (Boughn & Crittenden 2004).

Several methods have been proposed in the literature to study statistically the cross-correlation of the CMB fluctuations with LSS tracers, and, they can be divided into: real space statistics (e.g., the cross-correlation function, hereinafter CCF); harmonic space statistics (e.g., the cross-angular power spectrum, hereinafter CAPS); and wavelet space statistics (e.g., the covariance of the Spherical Mexican Hat Wavelet coefficients, or SMHWcov from now on). These statistics are equivalent (in the sense of the significance of the ISW detection) under ideal conditions. However, ISW data analysis presents several problematic issues (incomplete sky coverage, selection biases in the LSS catalogues, foreground residuals in the CMB map, etc.). Hence, the use of several different statistical approaches provides a more robust framework for studying the ISW-LSS cross-correlation, since different statistics may have different sensitivity to these systematic effects, The individual methods are described in more detail in Sect. 4.1.

Besides the choice of specific statistical tool, the ISW cross-correlation can be studied from two different (and complementary) perspectives. On the one hand, we can determine the amplitude of the ISW signal, as well as the corresponding signal-to-noise ratio, by comparing the observed cross-correlation to the expected one. On the other hand, we can postulate a null hypothesis (i.e., that there is no correlation between the CMB and the LSS tracer) and study the probability of obtaining the observed cross-correlation. Whereas the former answers a question regarding the compatibility of the data with the ISW hypothesis (and provides an estimation of the signal-to-noise associated with the observed signal), the latter tells us how incompatible the measured signal is with the no-correlation hypothesis, i.e., against the presence of dark energy (assuming that the Universe is spatially flat). Obviously, both approaches can be extended to account for the cross-correlation signal obtained from several surveys at the same time. These two complementary tests are described in detail in Sect. 4.2, with the results presented in Sect. 4.3.

4.1. Cross-correlation statistics

Let us denote the expected cross-correlation of two signals (x and y) by ξ_a^{xy}, where a stands for a distance measure (e.g., the angular distance θ between two points in the sky, the multipole ℓ of the harmonic transformation, or the wavelet scale R). For

simplicity, we assume that the two signals are given in terms of a fluctuation field (i.e., with zero mean and dimensionless).

This cross-correlation could represent either the CCF, the CAPS or the SMHWcov. It has to be understood as a vector of $a_{\rm max}$ components, where $a_{\rm max}$ is the maximum number of considered *distances*. Obviously, when $x \equiv y$, ξ_a^{xy} represents an auto-correlation. The specific forms for ξ_a^{xy} and $\mathbf{C}_{\xi^{xy}}$ for the different cross-correlation statistics (CAPS, CCF, and SMHWcov) are given below.

4.1.1. Angular cross-power spectrum

The angular cross-power spectrum (CAPS) is a natural tool for studying the cross-correlation of the CMB fluctuations and tracers of the LSS. Under certain conditions, it provides a statistical tool with uncorrelated (full-sky coverage) or nearly uncorrelated (binned spectrum for incomplete sky coverage) components. Even the unbinned CAPS, estimated on incomplete signals, can be easily worked out, since the correlations are mostly related to the geometry of the mask. This is the case for the CAPS obtained through `MASTER` approach (e.g., Hivon et al. 2002; Hinshaw et al. 2003). Another approach is to work in the map domain, making use of a quadratic maximum likelihood (QML henceforth) estimator (Tegmark 1997) for the CAPS (Padmanabhan et al. 2005; Schiavon et al. 2012). Such approach is optimal, i.e., leads to unbiased estimates for the CAPS with minimum error bars.

Pseudo angular power spectrum

Let us denote the CAPS between the CMB field $T(p)$ and an LSS tracer $G(p)$ map (where $p = (\theta, \phi)$ represents a given pixel) as: $C_\ell^{\rm TG}$ (i.e., $\xi_a^{xy} \equiv C_\ell^{\rm TG}$ for this cross-correlation estimator). In the full-sky case, an optimal estimator of the CAPS is given by:

$$\hat{C}_\ell^{\rm TG} = \frac{1}{2\ell+1} \sum_{m=-\ell}^{+\ell} t_{\ell m} g_{\ell m}^*, \tag{23}$$

where $t_{\ell m}$ and $g_{\ell m}$ are the spherical harmonic coefficients of the CMB and the LSS maps, respectively. This CAPS can be seen as a vector with $\ell_{\rm max}$ components, where $\ell_{\rm max}$ is the maximum multipole considered in the analysis. Here we adopt $3N_{\rm side}-1$, which suffices for ISW analysis, since it is know that most of the ISW signal is contained within $\ell \lesssim 80$ (Afshordi 2004; Hernández-Monteagudo 2008). When a mask $\Pi(p)$ is applied to the maps, it acts as a weight that modifies the underlying harmonic coefficients. Now, we have $\tilde{t}_{\ell m}$ and $\tilde{g}_{\ell m}$, where

$$\begin{aligned} \tilde{t}_{\ell m} &= \int\int {\rm d}(\cos\theta)\, {\rm d}\phi\, T(\theta,\phi)\, \Pi(\theta,\phi)\, Y_{\ell m}^*(\theta,\phi), \\ \tilde{g}_{\ell m} &= \int\int {\rm d}(\cos\theta)\, {\rm d}\phi\, G(\theta,\phi)\, \Pi(\theta,\phi)\, Y_{\ell m}^*(\theta,\phi), \end{aligned} \tag{24}$$

and $Y_{\ell m}(\theta,\phi)$ are the spherical harmonic functions. In these circumstances, the estimator in Eq. 23 is not longer optimal, and is referred to as pseudo-CAPS. A nearly optimal estimator is given by decoupling the masked CAPS (denoted by $\tilde{C}_\ell^{\rm TG}$) through the masking kernel B (e.g., Xia et al. 2011):

$$\hat{C}_\ell^{\rm TG} = \mathsf{B}^{-1} \tilde{C}_\ell^{\rm TG}, \tag{25}$$

where

$$B_{\ell\ell',{\rm G}} = \frac{2\ell+1}{4\pi} \sum_{\ell''} J_{\ell''}^{\rm G} \begin{pmatrix} \ell & \ell' & \ell'' \\ 0 & 0 & 0 \end{pmatrix}^2, \tag{26}$$

with $J_{\ell''}^G$ the cross-angular power spectrum of the T and G masks.

The estimator in Eq. 25 is nearly optimal because $\tilde{C}_\ell^{\rm TG}$ has to be understood as the mean value over an ensemble average of skies. Let us point out that when more than a single CAPS is considered, for instance when one is interested in the cross-correlation of the *Planck* CMB map with more than one LSS tracer map, the CAPS estimator can be seen as a single vector with $N\ell_{\rm max}$ components, with N being the number of surveys.

It can be shown that the element $C_{\ell\ell',ij}$ of the covariance matrix of the CAPS estimator in Eq. 25 (for the case of a masked sky and for N surveys) is given by

$$C_{\ell\ell',ij} = K_{\ell,ij} K_{\ell',ij} \frac{\left(M_{ij}\right)_{\ell\ell'}^{-1}}{(2\ell'+1)}, \tag{27}$$

where

$$K_{\ell,ij} = \left[C_\ell^{{\rm TG}_i} C_\ell^{{\rm TG}_j} + C_\ell^{\rm T} \left(C_\ell^{{\rm G}_i{\rm G}_j} + N_\ell^{{\rm G}_i{\rm G}_j} \delta_{ij} \right) \right]^{1/2}, \tag{28}$$

and $\left(M_{ij}\right)_{\ell\ell'}^{-1}$ is the (ℓ,ℓ') element of the inverse matrix of M for surveys i and j fixed, such as

$$M_{\ell\ell',ij} = \frac{2\ell+1}{4\pi} \sum_{\ell''} H_{\ell''}^{ij} \begin{pmatrix} \ell & \ell' & \ell'' \\ 0 & 0 & 0 \end{pmatrix}^2, \tag{29}$$

Here $H_{\ell''}^{ij}$ is the angular cross-power spectrum of the two joint masks, i.e., the masks resulting from the multiplication of the T with G_i and G_j, respectively. The quantities C_ℓ^{xy} are expected or fiducial spectra, N_ℓ^{yy} is the Poissonian noise of the y survey (deconvolved by any beam or pixel filter), and δ_{ij} is the Kronecker delta. In Eq. 28, the instrumental noise associated with the CMB data has been ignored, since the *Planck* sensitivity is such that the noise contribution on the scales of interest is negligible. When more than one survey has poor sky coverage, then the complexity of the correlations is not well reflected by the previous expression. Therefore, in this paper, we will compute $C_{\ell\ell',ij}$ from coherent CMB and LSS Monte Carlo simulations. For each simulation, we generate four independent, Gaussian, and white realizations (at $N_{\rm nside} = 64$), which are afterwards properly correlated using the expected auto- and cross-correlations of the signals. Corresponding Poissonian shot noise realizations are added to each survey map. The resulting four maps are masked with the corresponding masks (i.e., one for the CMB and one for mask for each survey).

The computation of the CAPS in Eq. 25 is extremely fast (especially for the resolutions used in the study of the ISW). However, as stated above, it is only a *nearly* optimal estimator of the underlying CAPS. Moreover, its departure from optimality is largest at the smallest multipoles (largest scales), where the ISW signal is more important.

The QML angular power spectrum

The QML method for the power spectrum estimation of temperature CMB anisotropies was introduced by Tegmark (1997) and later extended to polarization by Tegmark & de Oliveira-Costa (2001). For an application to temperature and polarization to *WMAP* data see Gruppuso et al. (2009) and Paci et al. (2013). The same method was employed to measure the cross-correlation between the CMB and LSS in Padmanabhan et al. (2005), Ho et al. (2008), and Schiavon et al. (2012). The QML method is usually stated to be optimal, since it provides unbiased estimates and the smallest error bars allowed by the Fisher-Cramér-Rao inequality. As a drawback, from the computational

point of view, the QML is a very expensive approach. Let us denote the QML estimator of the CAPS between the CMB map T and an LSS tracer G (at multipole ℓ) by $Q_\ell^{\rm TG}$ (i.e., $\xi_a^{xy} \equiv Q_\ell^{\rm TG}$ for this cross-correlation estimator).

A detailed description of the algebra of the QML is given in Schiavon et al. (2012). We briefly recall here the basics of the CAPS estimator, which is given by:

$$\hat{Q}_\ell^{\rm TG} = \sum_{\ell' X'} (F^{-1})_{\ell\ell'}^{{\rm TG}\ X'} \left[\boldsymbol{x}^{\rm T} \mathsf{E}_{\ell'}^{X'} \boldsymbol{x} - {\rm Tr}(\mathsf{N}\mathsf{E}_{\ell'}^{X'}) \right], \tag{30}$$

where X represents any of the following spectra: $X = \{{\rm T}, {\rm TG}, {\rm G}\}$. The vector $\boldsymbol{x}$ has $2N_{\rm pix}$ elements (with $N_{\rm pix}$ being the total number of pixels allowed by the joint CMB and LSS mask): the first set of $N_{\rm pix}$ corresponds to the CMB map, and the second one accounts for the LSS map. The $F_{\ell\ell'}^{{\rm TG}\ X'}$ is the Fisher matrix defined as

$$F_{\ell\ell'}^{{\rm TG}\ X'} = \frac{1}{2} {\rm Tr}\left[\mathsf{C}^{-1} \frac{\partial \mathsf{C}}{\partial C_\ell^{\rm TG}} \mathsf{C}^{-1} \frac{\partial \mathsf{C}}{\partial C_{\ell'}^{X'}} \right], \tag{31}$$

and the E matrix is given by

$$\mathsf{E}_\ell^X = \frac{1}{2} \mathsf{C}^{-1} \frac{\partial \mathsf{C}}{\partial C_\ell^X} \mathsf{C}^{-1}. \tag{32}$$

The object $\mathsf{C} = \mathsf{S}(C_\ell^X) + \mathsf{N}$ is the global covariance matrix, including the signal S and noise N contributions, with C_ℓ^X being the fiducial theoretical angular power spectrum. The uncertainties in the QML estimates are given by the inverse of the Fisher matrix, which includes the correlation among different multipoles. The error associated with the shot noise of the galaxy surveys is modelled in the galaxy submatrix of N.

The results presented on this paper are based on $\hat{C}_\ell^{\rm TG}$, whereas $\hat{Q}_\ell^{\rm TG}$ is used as a cross-check, applied to a lower resolution version of the maps of $N_{\rm side} = 32$. In addition the maximum multipole considered in this case is $\ell_{\rm max} = 2N_{\rm side}$, which has been already verified as a conservative limit for the QML.

4.1.2. Cross-correlation function

The cross-correlation function (CCF) is a suitable tool for studying the ISW effect via cross-correlation of the CMB fluctuations and tracers of the LSS, and it has been one of the most extensively used in this context (e.g., Boughn & Crittenden 2002; Giannantonio et al. 2008; Xia et al. 2009). On the one hand, the signal only appears at very large scales and, therefore, it is sufficient to work at resolutions at which the low performance of the CCF (in terms of computational time) is not a serious handicap. On the other hand, neither the CMB nor the LSS data are available with full sky coverage and, in some cases, the geometry of the masks is very complicated: the CCF adapts perfectly to the effects of partial sky coverage, since it is defined in real space. As a drawback, the Poissonian noise of the galaxy tracer appears at the smallest angular scales, where the signal-to-noise of the ISW effect is higher for this estimator. Therefore, a proper characterization of the shot noise is especially important for the CCF, in order to obtain a good estimation of the uncertainties.

Let us denote the CCF between the CMB map T and an LSS tracer G (at an angular distance of θ) as $C^{\rm TG}(\theta)$ (i.e., $\xi_a^{xy} \equiv C^{\rm TG}(\theta)$ for this cross-correlation statistic). The CCF estimator is defined as

$$\hat{C}^{\rm TG}(\theta) = \frac{1}{N_\theta} \sum_{i,j} T_i G_j, \tag{33}$$

where the sum runs over all pixels with a given angular separation. For each angular bin centred around θ, N_θ is the number of pixel pairs separated by an angle within the bin. Only the pixels allowed by the joint CMB and LSS mask are considered. The angular bins used in this work are: $\theta_1 \in [0, 1]^\circ$; $\theta_2 \in (1, 3]^\circ$; $\theta_3 \in (3, 5]^\circ$; ...; and $\theta_{61} \in (119, 121]^\circ$. The choice of binning does not affect the results significantly.

The covariance of the CCF estimator can be easily derived from the one already computed for the CAPS in Eq. 27. It is sufficient to know that the CCF can be expressed in terms of the CAPS as

$$C^{\rm TG}(\theta) = \sum_{\ell=0}^{\ell_{\rm max}} \frac{2\ell+1}{4\pi} C_\ell^{\rm TG} P_\ell(\cos\theta), \tag{34}$$

where $P_\ell(\cos\theta)$ are the Legendre polynomials. Hence, it is straightforward to prove that the covariance between the θ and θ' components of the CCF for the surveys i and j, respectively, is given by

$$C_{\theta\theta',ij} = \sum_\ell \sum_{\ell'} \frac{(2\ell+1)}{4\pi} \frac{(2\ell'+1)}{4\pi} P_\ell(\cos\theta) P_{\ell'}(\cos\theta') C_{\ell\ell',ij}. \tag{35}$$

4.1.3. Wavelet covariance

Wavelets provide an interesting alternative to more traditional tools (e.g., CCF or CAPS) for studying the CMB-LSS correlation. They exploit the fact that the ISW signal is mostly concentrated at scales of a few degrees (e.g., Afshordi 2004). Wavelets are ideal kernels to enhance features with a characteristic size, since the wavelet analysis at an appropriate scale R amplifies those features over the background. Therefore, wavelets could provide most of the signal-to-noise of the ISW effect by just analysing a narrow range of scales. They were first proposed for the ISW detection by Vielva et al. (2006), where the Spherical Mexican Hat Wavelet (SMHW, Martínez-González et al. 2002) was proposed as the filtering kernel. The basic idea of this approach is to estimate the covariance of the SMHW coefficients (SMHWcov) as a function of the wavelet scale (see e.g., Vielva et al. 2006, for details). Other wavelet kernels can be considered, such as needlets (Pietrobon et al. 2006a), directional wavelets (McEwen et al. 2007), or steerable wavelets (McEwen et al. 2008).

Let us denote the SMHWcov between the CMB map T and a LSS tracer G (at a wavelet scale R) as $\Omega^{\rm TG}(R)$, i.e., $\xi_a^{xy} \equiv \Omega^{\rm TG}(R)$ for this cross-correlation statistic). The SMHWcov estimator is defined as

$$\hat{\Omega}^{\rm TG}(R) = \frac{1}{N_{\rm pix}} \sum_i \omega_{{\rm T}_i}(R)\, \omega_{{\rm G}_i}(R), \tag{36}$$

where $\omega_T(R)$ and $\omega_G(R)$ are the SMHW coefficients for the CMB and the LSS at scale R, respectively (note that wavelet coefficients are forced to have zero mean on the observed sky). The scales considered in our study are $R = \{60, 90, 120, 150, 200, 250, 300, 350, 400, 500, 600\}$ in arcminutes.

As for the CCF, the covariance of the SMHWcov estimator can be easily derived from the one already computed for the CAPS in Eq. 27. It is sufficient to know that the SMHWcov can be expressed in terms of the CAPS as

$$\Omega^{\rm TG}(R) = \sum_{\ell=0}^{\ell_{\rm max}} \frac{2\ell+1}{4\pi} C_\ell^{\rm TG} \omega_\ell^2(R), \tag{37}$$

where $\omega_\ell(R)$ is the SMHW window function at the scale R. Hence, it is straightforward to prove that the covariance between the R and R' components of the SMWHcov for surveys i and j, respectively, is given by:

$$C_{RR',ij} = \sum_\ell \sum_{\ell'} \frac{(2\ell+1)}{4\pi} \frac{(2\ell'+1)}{4\pi} \omega_\ell^2(R)\, \omega_{\ell'}^2(R')\, C_{\ell\ell',ij}. \quad (38)$$

4.2. Cross-correlation tests

For any of the cross-correlation estimators described above, we aim two different statistical tests. First, if the observed cross-correlation is given by $\hat{\xi}_a^{xy}$, then, a simple χ^2 can be proposed to estimate the amplitude A, such that $A\xi_a^{xy}$ is the closest solution to $\hat{\xi}_a^{xy}$:

$$\chi^2(A) = \left[\hat{\xi}_a^{xy} - A\xi_a^{xy}\right]^{\mathrm{T}} \mathsf{C}_{\xi^{xy}}^{-1} \left[\hat{\xi}_a^{xy} - A\xi_a^{xy}\right], \quad (39)$$

where $\mathsf{C}_{\xi^{xy}}$ is the covariance matrix (of dimension $a_{\max} \times a_{\max}$) of the expected cross-correlation ξ_a^{xy}, i.e., $\mathbf{C}_{\xi^{xy}{}_{i,j}} \equiv \left\langle \xi_{a_i}^{xy} \xi_{a_j}^{xy} \right\rangle$. It is straightforward to show that the best-fit amplitude A and its dispersion are given by

$$A = \left[\hat{\xi}_a^{xy}\right]^t \mathsf{C}_{\xi^{xy}}^{-1} \xi_a^{xy} \left[\left[\xi_a^{xy}\right]^t \mathsf{C}_{\xi^{xy}}^{-1} \xi_a^{xy}\right]^{-1}, \quad (40)$$

$$\sigma_A = \left[\left[\xi_a^{xy}\right]^t \mathsf{C}_{\xi^{xy}}^{-1} \xi_a^{xy}\right]^{-1/2}.$$

An analogy with Eq. 39 can be defined for the null hypothesis case:

$$\chi^2{}_{\mathrm{null}} = \left[\hat{\xi}_a^{xy}\right]^{\mathrm{T}} \mathsf{D}_{\xi^{xy}}^{-1} \hat{\xi}_a^{xy}, \quad (41)$$

where $\mathsf{D}_{\xi^{xy}}$ is the covariance of the cross-correlation of the two signals, in the absence of an intrinsic dependence, i.e., when $\xi_a^{xy} \equiv 0$. The ISW signal is very weak and, therefore it is a good approximation to assume that that $\mathsf{D}_{\xi^{xy}} \approx \mathsf{C}_{\xi^{xy}}$.

For Gaussian statistics, $\chi^2{}_{\mathrm{null}}$ already provides the direct probability of the observed cross-correlation $\hat{\xi}_a^{xy}$ under the null hypothesis. However, several non-idealities (sky coverage, systematics, foregrounds residuals, etc.) forces is to use alternative approaches to estimate the probability. One of the most common options is to perform the cross-correlation of survey signal y with realistic simulations of the CMB, x, and compute a joint statistics (e.g., $\chi^2{}_{\mathrm{null}}$) for each simulation. The probabiltiy value associated with the data will come then then be the fraction of simulations having a value of $\chi^2{}_{\mathrm{null}}$ equal to or larger than the one obtained for the data. Both, $\mathsf{C}_{\xi^{xy}}$ and $\mathsf{D}_{\xi^{xy}}$ can be derived either analytically or numerically (via simulations).

The latter approach is computationally expensive, but, in some cases, could provide a more accurate defence against certain systematics, in particular the incomplete sky coverage. There are several options to perform such kind of simulations. The standard approach is the one mentioned above, i.e., cross-correlation of the LSS map with CMB simulations. This is a very robust approach, since it is usually hard to reproduce the systematics present in the LSS tracers, but incomplete because the LSS is fixed, resulting in a lack of randomness. An alternative method is to use a jack-knife test, which unfortunately tends to underestimate the errors. Finally, one can produce simulations of both the CMB and the LSS, assuming perfect knowledge of the properties of both signals, in particular of the LSS field (which, as mentioned above, is almost never the case). Comprehensive discussions of these approaches are given in Cabré et al. (2007) and Giannantonio et al. (2008).

Table 4. Expected significance A/σ_A of the CMB-LSS cross-correlation. Values obtained from each survey independently, as well as jointly, are given for all the estimators (CAPS, CCF, and SMHWcov).

$\hat{\xi}_a^{xy}$	NVSS	SDSS CMASS/LOWZ	SDSS MG	all
CAPS	3.0	1.9	0.6	3.2
CCF	3.0	1.9	0.6	3.1
SMMHWcov	3.0	1.9	0.5	3.1

4.3. Results

In this section we present the results obtained from the cross-correlation of the galaxy catalogues described in Sect. 2.2 (NVSS, SDSS-CMASS/LOWZand SDSS-MG) with the four *Planck* CMB maps presented in Sect. 2.1.1 (`C-R`, `NILC`, `SEVEM`, and `SMICA`). All these maps are analysed at a `HEALPix` resolution of $N_{\mathrm{side}} = 64$. The cross-correlation estimators described in the previous section are applied to all cases. This comprehensive analysis will help to achieve a robust estimation of the ISW.

As already mentioned the covariance among all the components of the estimators are obtained from coherent Gaussian simulations of the CMB and the three galaxy catalogues. Since we are only considering large-scale effects (above about 1°), the same set of CMB simulations are equally valid for the four CMB maps, since they are nearly identical on such scales(see Planck Collaboration XII 2013, for details). We have used 70,000 coherent Monte Carlo simulation sets (as described in Sect. 4.1.1) to compute the correlations; this is enough to characterize the covariance.

The expected signal-to-noise ratio for the ISW effect detection is summarized in Table 4. Values for all the cross-correlation estimators are given. We consider the case of a survey-by-survey detection, as well as the joint analysis of all the surveys. A signal-to-noise of about $3\,\sigma$ is expected for the joint analysis, which is actually dominated by the NVSS cross-correlation. This is expected, since, firstly, NVSS covers a much larger fraction of the sky compared to other surveys, and secondly, it extends over a redshift interval ideal for the detection of the ISW signal (e.g. Afshordi 2004).

The differences among estimators are not significant, indicating that none of them is clearly optimal compared with the others. To explore this agreement further, we have analysed an extra set of 1,000 CMB and LSS clustered simulations, and have compared, simulation by simulation, the ISW amplitude estimation derived for each cross-correlation estimator (C_ℓ^{TG}, $C^{\mathrm{TG}}(\theta)$ and $\Omega^{\mathrm{TG}}(R)$). In Table 5 we summarize the comparison. We only report values for the joint fit to the ISW amplitude for the three surveys. Similar results are found survey by survey. For each pair of estimators, we provide the mean difference among the amplitude estimations (ΔA), the dispersion of these differences (s_A), the ratio (η) of this dispersion to the expected sensitivity (i.e., the inverse of the signal-to-noise numbers given in the last column of Table 4), and the correlation coefficient (ρ). It is clear that the agreement between estimators is very high and that differences are, on average, lower than half the statistical uncertainty imposed by the sampling variance.

We have fitted the observed cross-correlations to the expected ISW signal (C_ℓ^{TG}, $C^{\mathrm{TG}}(\theta)$, and $\Omega^{\mathrm{TG}}(R)$, see Fig. 5), following Eq. 41, i.e., allowing for a free amplitude of the expected signal. Results are summarized in Table 6. Overall, the ISW detection is at about the $3\,\sigma$ level and, as expected, it is clearly

Table 6. Amplitudes A, errors σ_A and significances A/σ_A of the CMB-LSS cross-correlation (survey by survey and all together) due to the ISW effect, for all component separation algorithms (C-R, NILC, SEVEM, and SMICA) for the CAPS, CCF, and SMHWcov estimators.

LSS data	$\hat{\xi}_a^{xy}$	C-R		NILC		SEVEM		SMICA	
NVSS	CAPS	0.86 ± 0.33	2.6	0.91 ± 0.33	2.8	0.90 ± 0.33	2.7	0.91 ± 0.33	2.7
	CCF	0.80 ± 0.33	2.4	0.84 ± 0.33	2.5	0.83 ± 0.33	2.5	0.84 ± 0.33	2.5
	SMHWcov	0.89 ± 0.34	2.6	0.93 ± 0.34	2.8	0.89 ± 0.34	2.6	0.92 ± 0.34	2.7
SDSS-CMASS/LOWZ	CAPS	0.98 ± 0.52	1.9	1.09 ± 0.52	2.1	1.06 ± 0.52	2.0	1.09 ± 0.52	2.1
	CCF	0.81 ± 0.52	1.6	0.91 ± 0.52	1.8	0.89 ± 0.52	1.7	0.90 ± 0.52	1.7
	SMHWcov	0.80 ± 0.53	1.5	0.89 ± 0.53	1.9	0.87 ± 0.53	1.6	0.88 ± 0.53	1.7
SDSS-MG	CAPS	1.31 ± 0.57	2.3	1.43 ± 0.57	2.5	1.35 ± 0.57	2.4	1.42 ± 0.57	2.5
	CCF	1.00 ± 0.57	1.8	1.11 ± 0.57	2.0	1.10 ± 0.57	1.9	1.10 ± 0.57	1.9
	SMHWcov	1.03 ± 0.59	1.8	1.18 ± 0.59	2.0	1.15 ± 0.59	2.0	1.17 ± 0.59	2.0
all	CAPS	0.84 ± 0.31	2.7	0.91 ± 0.31	2.9	0.88 ± 0.31	2.0	0.90 ± 0.31	2.9
	CCF	0.77 ± 0.31	2.5	0.83 ± 0.31	2.7	0.82 ± 0.31	2.6	0.82 ± 0.31	2.7
	SMHWcov	0.86 ± 0.32	2.7	0.92 ± 0.32	2.9	0.89 ± 0.32	2.8	0.91 ± 0.32	2.9

Table 5. For each pair of estimators we provide the mean difference among the amplitude estimations (ΔA), the dispersion of these differences (s_A), the ratio (η) of this dispersion to the expected sensitivity (i.e., the inverse of the signal-to-noise numbers given in the last column of Table 4), and the correlation coefficient (ρ).

		CCF	SMHWcov
CAPS	$\Delta A \pm s_A$	-0.01 ± 0.12	0.06 ± 0.07
	η	0.36	0.21
	ρ	0.93	0.98
CAPS	$\Delta A \pm s_A$		0.08 ± 0.14
	η		0.42
	ρ		0.92

dominated by the NVSS signal. There are only small differences among estimators and CMB maps (as expected from the above discussion), indicating that this is a robust result. Notice that all the estimated amplitudes are compatible with unity, within the error bars (especially for NVSS and SDSS-CMASS/LOWZ). This is an additional validation of how CMB and LSS are modelled. Values of A deviating significantly from unity would indicate some tension between the observed cross-correlation and the model (in particular on the LSS modelling, which is more complex). The CAPS-QML, applied to the SEVEM and NVSS (i.e., the survey with the highest signal-to-noise), yields a value of $A = 0.73 \pm 0.33$, which is compatible with the CAPS, when applied to the same $N_{\rm side} = 32$ and $\ell_{\rm max} = 2N_{\rm side}$ resolution ($A = 0.84 \pm 0.34$). Preliminary tests indicate that running the CAPS-QML at $N_{\rm side} = 64$ resolution could increase the sensitivity for detecting the ISW effect with NVSS by $\approx 20\%$.

Our results indicate a somewhat smaller signal-to-noise with respect to some previous analyses on *WMAP* data, where several (and in some case quite similar) surveys were also considered. For instance, Ho et al. (2008) and Giannantonio et al. (2012) found $3.7\,\sigma$ and $4.4\,\sigma$ detections, respectively. Compatibility with the former is below $1\,\sigma$, whereas there is more tension (around $1.5\,\sigma$) with the latter. A fraction of around $0.3\,\sigma$ of these differences could be explained in terms of the comological parameters adopted to defined the theoretical expectations. In particular, the lower values of H_0 and Ω_Λ found by *Planck* (Planck Collaboration XVI 2013) with respect to *WMAP* (e.g., Larson et al. 2011), imply a sensitivity for the ISW $\approx 10\%$ smaller. The rest of the differences come either from the LSS side, or from the error characterization, which depends on the presence of a correlated signal between CMB and LSS simulations (see for instance Cabré et al. 2007, for a discussion). Survey modelling is another important aspect: besides systematic errors associated with the galaxy identification and redshift estimation procedures, there are complicated aspects, such as the bias characterization. As was mentioned already, a strong point of our results, is the excellent compatibility between the ISW amplitude estimates with respect to the expected value. Whereas our estimation deviates by about $0.5\,\sigma$ from the expected value, the Giannantonio et al. (2012) result exceeds it by about $1\,\sigma$ and Ho et al. (2008) is around $2\,\sigma$ above.

Nevertheless, the value of the ISW effect that we measure by means of NVSS (that because of to its large sky coverage, redshift range, and density of galaxies is probably the best current catalogue for studying the ISW effect) is significant, and in agreement with previously published results using *WMAP*.

We have also studied the ISW signal from the point of view of its compatibility with the null hypothesis. We have considered in this analysis only the NVSS catalogue, since it provides the largest detection of the ISW effect and, therefore, is the best of the existing surveys for challenging the null hypothesis. Probability values are summarized in Table 7. As mentioned in Sect. 4.2, there is not a unique way of computing the null hypothesis. Our approach follows Eq. 41, where $\mathsf{D}_{\xi^{xy}}$ was computed out of 90,000 CMB simulations that have been cross-correlated with the LSS data. This matrix is used to compute $\chi^2_{\rm null}$ from the data. This value is then compared to its distribution for the null hypothesis, obtained from 1,000 realistic CMB simulations (FFP-6) uncorrelated with NVSS, which have been processed in the same way as the *Planck* data set. CAPS provides the smallest probability value, but the null hypothesis is rejected at about 10% only; this result is not unexpected, since an expected result since the ISW effect is weak.

The fact that the CAPS statistic provides tighter limits with respect to the CCF and SMHWcov could have been anticipated. In our implementation, the CAPS explores the maximum angular range allowed for a given map, whereas the CCF and the SMHWcov approaches are only evaluated at certain angles/scales. This limitation is not an issue in the analysis devoted

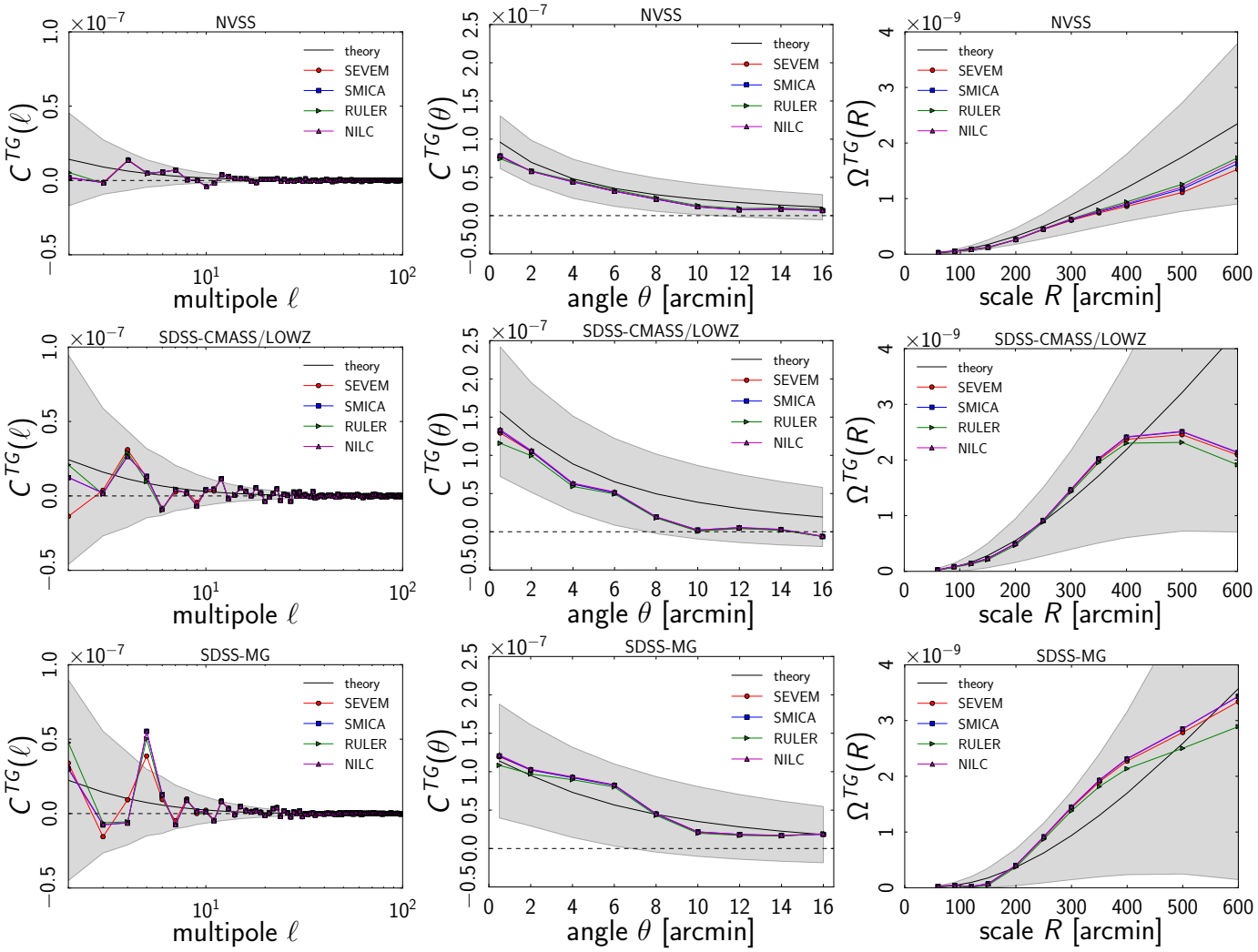

Fig. 5. Observed and expected cross-correlation signal versus multipole ℓ, for several surveys and different cross-correlation estimators. Columns from left to right correspond to: CAPS; CCF; and SMHWcov. Rows from top to bottom represent: NVSS; SDSS-CMASS/LOWZ; and SDSS-MG. On each panel we show the expected cross-correlation (black line) and the $\pm 1\,\sigma$ region (grey area). Observed cross-correlations for the different CMB maps are provided: `C-R` and `NILC` as green and magenta triangles, respectively; `SEVEM` as red circles; and `SMICA` as blue squares.

Table 7. Probability values of the CMB-LSS cross-correlation for the NVSS survey under the null hypothesis, for the four component separation methods (`SMICA`, `SEVEM`, `C-R` and `NILC`) and for the CAPS, CCF, and SMHWcov estimators.

LSS data	$\hat{\xi}_a^{xy}$	`C-R`	`NILC`	`SEVEM`	`SMICA`
NVSS	CAPS	0.09	0.10	0.10	0.09
	CCF	0.33	0.34	0.40	0.33
	SMHWcov	0.20	0.23	0.27	0.19

to estimating the ISW amplitude, since these angles/scales are suitable for detecting the ISW. However, in order to discard the null hypothesis, the longer the number of "distances" the better.

5. Stacking of large-scale structures

An alternative approach for measuring the ISW effect in *Planck* maps is to look for an ISW signal directly at the positions of positive and/or negative peaks in the potential. Since the expected (and observed) signal is very weak, for individual structures, a stacking technique needs to be applied. Using the *WMAP* data, it has been shown that CMB maps show hot spots and cold spots in the direction of superclusters and supervoids, respectively (Granett et al. 2008a,b, GR08 hereafter), which appear to be barely consistent with the predictions of standard ΛCDM (see also Hernandez-Monteagudo & Smith 2012). These structures, which are not yet virialized, are evolving while the CMB photons travel across them and this should contribute to the ISW effect. We apply here the same approach to the different *Planck* maps, using the catalogues of superstructures introduced in Sect. 2.2.4, and we test for the robustness of our findings. We first discuss our method and the results obtained using the catalogue provided by GR08, and then present the results obtained with the other catalogues.

5.1. Method

Our analysis is performed on the `SMICA` CMB map, although we have checked that results are compatible for the other three

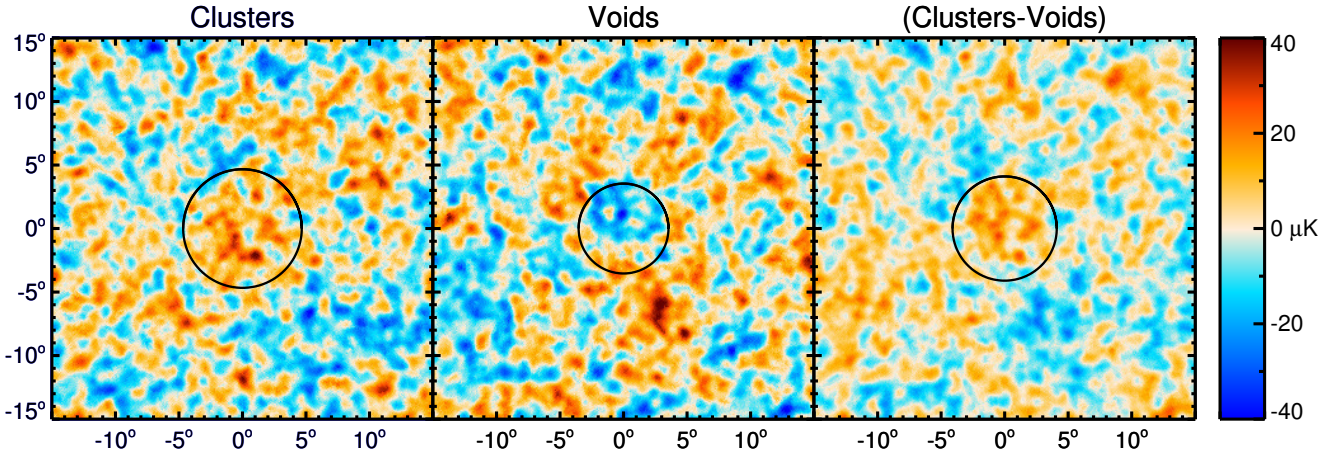

Fig. 6. Stacked regions of *Planck* maps corresponding to the locations of the superstructures identified by GR08. From left to right we show the images resulting from stacking of the 50 superclusters, the 50 supervoids, and the difference of both. The black circles superimposed indicate the angular radius at which the signal-to-noise ratio is maximal. See Fig. 7 for the corresponding temperature and photometry profiles, as well as their statistical significance.

Planck maps. We have also used the cleaned frequency maps from SEVEM (see Sect. 2.1.1) for some of the tests. We first remove the monopole and dipole of the maps (outside the U73 mask), and then apply a compact source mask based on the Planck Legacy Point Source Catalogue (Planck Collaboration XII 2013) to remove the contamination from individual point sources.

For the purpose of comparison with the results of GR08, we smooth the CMB maps with a common Gaussian kernel of 30′ FWHM. We then project them onto patches around each position in the supervoid and supercluster catalogue. The GR08 structures have a relatively small size on the sky (a few degrees), but the other two catalogues considered here contain many larger and closer voids, covering larger angular sizes. Thus we work with 30° × 30° CMB patches and choose the pixel size to be 6′, so that all voids considered are fully enclosed. We then co-add (stack) the maps, taking into account the mask used. On the stacked images, we calculate both the radial temperature profile and the aperture photometry, to characterize the signal around density structures. The temperature profile is obtained by computing the mean of the pixels in rings of fixed width and increasing angular radius; in practice, it is calculated for 150 radii between 0° and 15°, with a width of $\Delta\theta = 0.^\circ1$. The photometry profile is obtained by applying a compensated filter that subtracts the average temperature of a ring from the average temperature within the disk whose radius θ is the inner radius ring, and where the outer radius is chosen to be $\theta\sqrt{2}$, so that the disc and ring have the same area. This should enhance fluctuations of typical angular size θ against fluctuations at smaller or larger scales. Aperture photometry results are also provide for at 150 angles, this time between 0° and $15/\sqrt{2} \approx 10.^\circ6$. In addition to the monopole and dipole, we also removed from the CMB maps the contribution of large scale angular modes, namely $\ell = 2$–10. These modes correspond to angular scales much larger than those of the structures under investigation, and for our purposes their only effect is to introduce gradients in the stacked images; the high-pass filter essentially stops such gradients getting into the stacked map (which is equivalent to removing gradients at the end). The contribution of the large-scale angular modes has no impact on the aperture photometry profiles, and introduces only an offset in the temperature profiles (Ilić et al. 2013).

In order to estimate the significance of the resulting photometry and temperature profiles, we follow a Monte Carlo approach based on stacked CMB images chosen at random positions. In detail, we compute the photometry and the temperature profiles for 16 000 sets of 50 CMB patches randomly distributed over the SDSS area. We then compare the profiles obtained from the stacking at the location of the GR08 superstructures to these random profiles, in order to compute their signal-to-noise ratio.

5.2. Results

We show in Fig. 6 the stacked images of the 50 supervoids and 50 superclusters of GR08 in the *Planck* map. The corresponding temperature and photometry profiles, along with their significance levels, are shown in Fig. 7. The first thing to say is that, although the signatures are fairly weak, the sign of the effect certainly seems to be correct. Using the same catalogue and the *Planck* CMB map, we find reasonable agreement with GR08. The maximal photometric decrement, $-10.8\,\mu$K (essentially identical with the $-11.3\,\mu$K found by GR08), induced by supervoids is obtained for a preferred scale of about $3.^\circ5$ (4° in GR08) and a signal-to-noise of 3.3 ($3.7\,\sigma$ in GR08), as shown in Fig. 7. Superclusters produce a photometric increment of about $8.5\,\mu$K (slightly above the $7\,\mu$K in GR08), with a significance of $3.0\,\sigma$ (compared with $2.6\,\sigma$ in GR08) at a slightly larger angle of $4.^\circ7$. Finally, the stack of the combined sample (clusters minus voids) gives a temperature deviation of $8.7\,\mu$K, with a signal strength of $4.0\,\sigma$ at $4.^\circ1$, which is consistent with the values reported in GR08. The values of statistical significance for our aperture aperture photometry results are closely related to those for the temperature profiles. Indeed, as shown in the top panel of Fig. 7, the temperature profile for the void stack shows a roughly $2\,\sigma$ deficit at small angular radii and a roughly $2\,\sigma$ excess extending to large radii. Since the aperture photometry is essentially an integral of the temperature profile with a compensated filter, it picks up enhanced significance because of the shape of the temperature profile.

As noted previously by several authors (e.g., Hernandez-Monteagudo & Smith 2012), the amplitude and shape of the photometric profile found for voids and clusters is in tension (around $2\,\sigma$) with the values expected from pure ISW within ΛCDM.

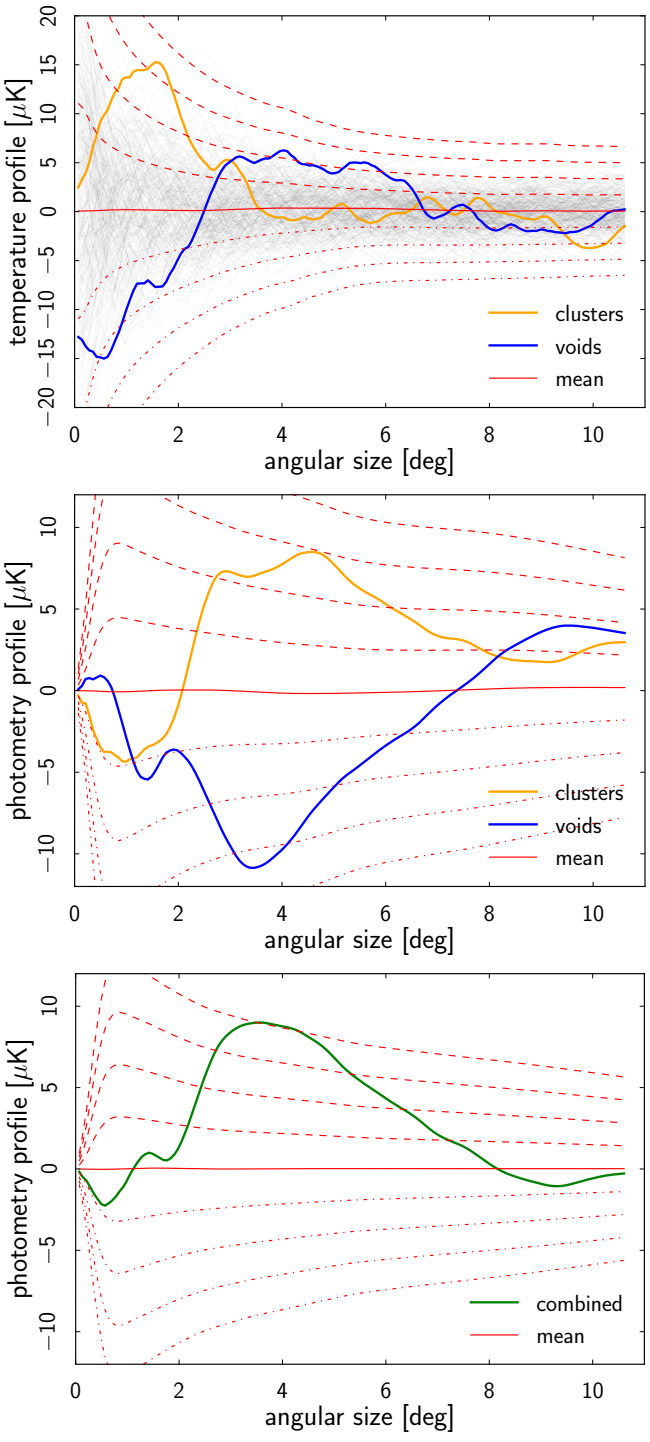

Fig. 7. Temperature (top) and photometry (middle and bottom) profiles of the stacked CMB patches at the location of the 50 supervoids and 50 superclusters of GR08. The lower panel shows the combined photometry profile (i.e., the average cluster profile minus the average void profile). The significance is represented by 1, 2, 3, and 4 σ level curves (dashed and dotted lines represent positive and negative error bars, respectively). These curves represent the dispersion of the 16 000 stacks of 50 CMB patches chosen at random positions (for illustration, on the top panel, we represent in grey 300 of those random profiles).

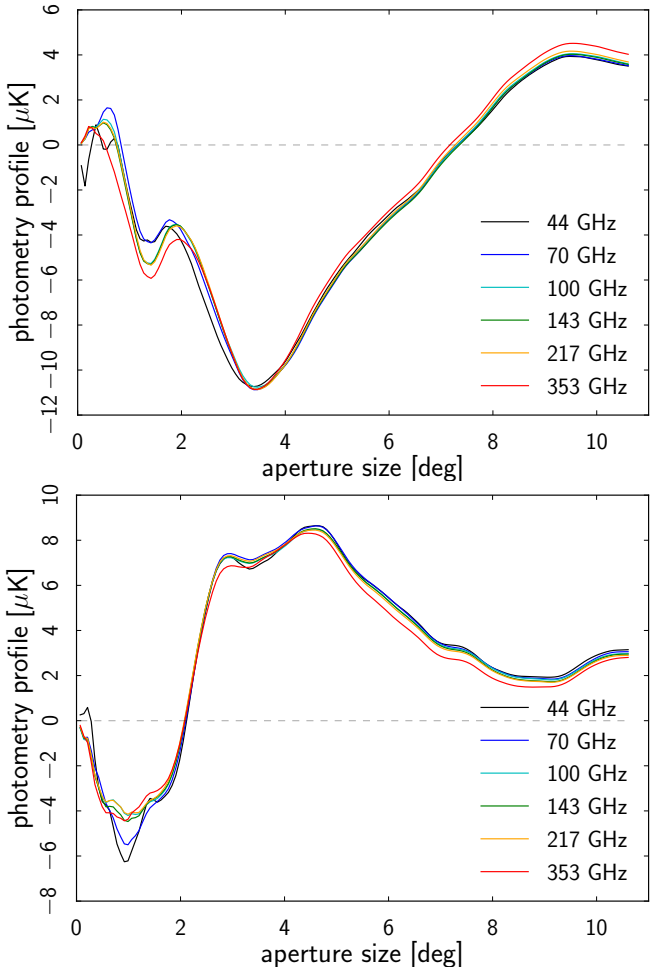

Fig. 8. Independence of the signal on the SEVEM frequency channels. The aperture photometry profiles measured in the stacked patches centred on supervoids (top) and superclusters (bottom) are virtually identical for all frequencies.

However, it is not straightforward to associate this entire signal with a pure ISW effect. As seen in the Fig. 6, many small-scale structures – both cold and hot – are present around the region delineated by the angular radius at which the signal-to-noise ratio of the aperture photometry is maximal. This small-scale structure contributes to the amplitude of the photometric decrement, but at a few tens of μK, which is incompatible with the ΛCDM predictions for the ISW effect. These are rather simply background CMB fluctuations, with their lingering presence due to the small number (50) of patches which are used to produce the stack.

It is intriguing that the angular sizes of the catalogued superstructures are smaller than the angular sizes suggested by the photometry profiles. This result is more apparent when we repeat the stacking analysis after rescaling each CMB patch by the effective radius of the structure it contains. Since the voids and super clusters identified by GR08 are roughly the same size, the photometric results are similar after rescaling ($-10\,\mu$K for voids and $7.9\,\mu$K for superclusters). However, the deviations have significance levels of $3.3\,\sigma$ and $2.7\,\sigma$ for supervoids and superclusters, respectively, at angular sizes of 1.3 (voids) and 2.6 (clusters) times the effective radius of the structures. This mismatch could be a result of underestimation of the structure extent the ZOBOV and VOBOZ algorithms (as already suggested by GR08) or

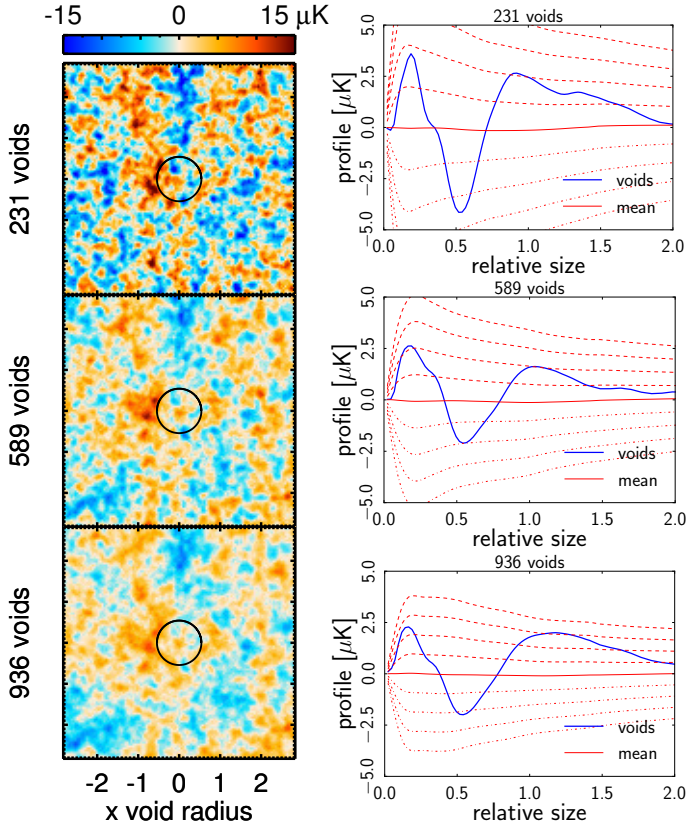

Fig. 9. Stacked images (left) and photometry profiles (right) obtained for the voids of Sutter et al. (2012). From top to bottom, we show results obtained from stacking the largest 231, 589, and 936 voids. The black circles superimposed indicate the angular radius at which the signal is maximal. The statistical dispersion is reduced as we stack more voids. However, the amplitude of the "cold spot" at about 0.5 times the effective void radius is mostly due to the surrounding "hot shell", which is easiest to see in the bottom panel. This is further demonstrated by the $3\,\sigma$ signal detected using aperture photometry, seen at radii above 1.2 times the effective radius (for the 936 void case). Dashed and dotted lines in the right-hand panels represent positive and negative error bars, respectively, from 1 to $4\,\sigma$.

because larger potential hills and valleys underlie the detected superstructures. Since structure in the potential is related to the density field through the Poisson equation, gravitational potential features are expected to cover larger scales than structures in the density field. Nevertheless, the factor of 2.6 for the case of superclusters seems large. It is also true that the GR08 superstructures were identified in the LRG subsample of the SDSS, and LRGs are known to be biased tracers of the matter density field (e.g., Tegmark et al. 2006). This bias could help explain why structures are larger than the scales identified by the *VOBOZ* algorithm, although the argument would go in the opposite sense for the voids. Another way of stating this is (Hunt & Sarkar 2010) that the relatively large effect decrement found for the GR08 voids can be only be attributed to the ISW effect only if the underdensities have been significantly underestimated or if the LRGs are under-biased.

It is therefore difficult to be confident that the signal is due entirely to the ISW effect. We know, however, that the ISW signal generated by superstructures is expected to be achromatic, since it generates a fractional perturbation of the CMB temperature. In order to check if the signal we measure is indeed independent of frequency, we applied the same technique to *Planck* individual SEVEM cleaned frequency maps from 44 to 353 GHz. Lower (higher) frequency maps may be contaminated by radio (IR) signals coming from our Galaxy and may thus introduce a bias in the measurement. Figure 8 shows the photometry profiles of supercluster- and supervoid-stacked maps at 44, 70, 100, 143, 217, and 353 GHz. The flux measured appears to be quite constant, which supports the idea that the signal is due to the ISW effect induced by structures. In the remainder of this section, we therefore apply our analysis only to the SMICA CMB map.

5.3. Discussion and alternative catalogues

It should be remembered that although the GR08 structures are considered to be good tracers of the cosmic matter distribution on scales larger than $10\,h^{-1}$ Mpc, they are also known for their sparsity at these redshifts ($z \approx 0.4$–0.7). This sparsity could lead to biased estimates of the properties of the reconstructed voids, in particular their sizes and depths could be biased. Moreover, some of the structures overlap on the sky, which could lead to systematic effects in the stacking analysis.

We thus turn to other samples, for example the catalogue of Pan et al. (2012), introduced in Sect. 2.2.4. The 1054 statistically significant voids it contains are larger than $10\,h^{-1}$ Mpc in radius and, with redshifts lower than 0.1, they are much closer to us than the structures of GR08. Direct stacking gives only a weak signal at about the $1\,\sigma$ level, which is difficult to reconcile with the previous results. This may be due to the inclusion of a large number of small voids that could dilute the signal. Also, unlike the voids of GR08, the voids of Pan et al. (2012) have a large scatter in angular sizes on the sky, from about 2° to 20° (e.g., Ilić et al. 2013). In order to try to enhance the signal, we repeated the stacking after rescaling the voids to their effective sizes. We also subdivided the catalogue into sub-samples based on redshift, radius, and/or angular size. However, none of these attempts yielded any statistically significant result, in agreement with Ilić et al. (2013).

Finally, we applied our procedure to the catalogue of voids published by Sutter et al. (2012). These cover a rather extended range of angular scales (about 2–10°), and so we rescaled all the CMB patches by the effective radius of each void. Stacking subsample by subsample (*dim1*, *dim2*, *bright1*, *bright2*, *lrgdim*, *lrgbright*), does not yield any significant signal. Similarly, when stacked together, the entire catalogue does not yield an ISW detection. However, since the ISW signal is expected to be stronger for the largest and closest voids (e.g., Flender et al. 2013) we tried starting from the largest void and adding them one by one, looking for the optimal number of voids, i.e., that for which the signal-to-noise ratio is maximal (see Fig. 10). We found that stacking 231, 589 or 936 voids gives roughly the same signal-to-noise ($2.5\,\sigma$, $2.0\,\sigma$ and $2.2\,\sigma$, respectively). However, the more voids we stack, the smaller the amplitude of the photometry signal (see Fig. 9, this being about $-2.0\,\mu$K for 936 voids, $-2.1\,\mu$K for 589 voids and $-4.1\,\mu$K for 231 voids, at an angular size of about 0.5 times the common rescaled radius. These amplitudes are lower than those found with the 50 GR08 voids, although above what is expected from numerical simulations (see e.g., Hernandez-Monteagudo & Smith 2012, for higher redshift and larger voids), but see also Cai et al. (2013).

The apparent angular size detected (about 0.5 times the effective void radius) in the photometry profile is smaller than that for the GR08 voids, but in agreement with expectations from simu-

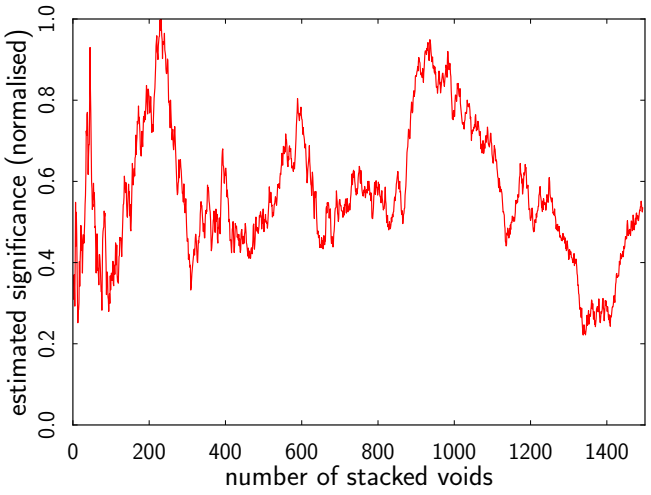

Fig. 10. Estimate of the optimal number of patches/voids to stack using the catalogue of Sutter et al. (2012). Starting from the largest void and adding one CMB patch at a time to the stack, we find at each step N the minimum of the aperture photometry profile, and we multiply this value by $\sqrt{N}$ to find the largest signal-to-noise, assuming that the noise scales roughly as $1/\sqrt{N}$. The vertical axis has been normalized to the best signal-to-noise, obtained for 231 voids.

lations (Cai et al. 2013), and consistent with the sizes detected using *WMAP* data (Ilić et al. 2013).

The profiles in Fig. 9 show hints (significance about $2\,\sigma$) of a positive excess below about 0.2 times the effective void radius. This may be partly because the ZOBOV algorithm uses galaxies as centres of the tessellation, meaning that the centre has to be slightly locally overdense. Fig. 9 also shows positive excess for larger apertures, partly caused by the large "hot ring" surrounding the cold feature in the stacked images, which raises the mean temperature of the stacked image for discs of radii around 0.8–1.2 times the void radius.

6. ISW map recovery

In recent years, some effort has been invested, not only to obtain the statistical cross-correlation signal between the CMB and LSS data, but also to recover a map of the ISW signal itself (Barreiro et al. 2008, 2013; Francis & Peacock 2010; Dupé et al. 2011). In particular, assuming the existence of a correlation between the CMB and the gravitational potential, it is possible to recover a map of the ISW fluctuations using a filtering method, given a tracer of the gravitational potential (e.g., the galaxy catalogues described in Sect. 2.2) and the CMB fluctuations. Given the weakness of the signal, the main objective of this section is to provide a qualitative image of the ISW fluctuations for visual inspection, and an additional consistency test of the validity of the assumed fiducial model, by comparing the statistical properties of the recovered and expected signals. In addition, this secondary anisotropy map could also be used to study the large-scale properties of the CMB, and its possible relation to some possible large-angle anomalies found in the *Planck* data (Planck Collaboration XXIII 2013).

6.1. Method

We have followed the methodology of Barreiro et al. (2008), which applies a linear filter to the CMB and to a gravitational potential tracer map, in order to reconstruct an ISW map, assuming that the cross- and auto-spectra of the signals are known. This technique has been recently applied to reconstruct the ISW map from the *WMAP* data and NVSS galaxy map (Barreiro et al. 2013). The filter is implemented in harmonic space and the estimated ISW map $\hat{s}_{\ell m}$ at each harmonic mode is given by (see Barreiro et al. 2008 for details)

$$\hat{s}_{\ell m} = \frac{L_{12}(\ell)}{L_{11}(\ell)} g_{\ell m} + \frac{L_{22}^2(\ell)}{L_{22}^2(\ell) + C_\ell^{\rm n}} \left(d_{\ell m} - \frac{L_{12}(\ell)}{L_{11}(\ell)} g_{\ell m} \right), \tag{42}$$

where $L(\ell)$ corresponds to the Cholesky decomposition of the covariance matrix between the considered tracer of the potential and the ISW signal, at each multipole, which satisfies $C(\ell) = L(\ell)L^{\rm T}(\ell)$. Here $d_{\ell m}$ and $g_{\ell m}$ are the CMB data and the gravitational potential tracer map, respectively, and $C_\ell^{\rm n}$ is the power spectrum of the CMB signal without including the ISW effect. If full-sky coverage is not available, the covariance matrix is obtained from the corresponding pseudo-spectra. It can be shown that the expected value of the power spectrum for the reconstructed signal is given by

$$\left\langle C_\ell^{\hat{\rm s}} \right\rangle = \frac{(C_\ell^{\rm gs})^2 \left(|C(\ell)| + C_\ell^{\rm g} C_\ell^{\rm n} \right) + |C(\ell)|^2}{C_\ell^{\rm g} \left(|C(\ell)| + C_\ell^{\rm g} C_\ell^{\rm n} \right)}, \tag{43}$$

where $|C(\ell)|$ is the determinant of the tracer-ISW covariance matrix at each multipole, and $C_\ell^{\rm gs}$ and $C_\ell^{\rm g}$ are the assumed cross-spectrum and gravitational potential tracer spectra, respectively. Note that the recovered ISW power spectrum will not contain the full ISW signal, since it can only account for the part of the ISW signal probed by the tracer being considered. It is also worth noting that in detail the expected cross-correlation depends on the assumed model. However, in practice, given the weakness of the signal, it would be difficult to distinguish between two mild variants of the standard ΛCDM model. Nevertheless this approach still provides a useful consistency check.

6.2. Results

We have applied the filter described above to two different cases: combining information from the CMB and the NVSS galaxy catalogue; and applying the filter to the CMB and the recovered lensing potential map described in 2.1.2. Results have been obtained for the four *Planck* maps, C-R, NILC, SEVEM, and SMICA. For simplicity, we show the reconstructions only for the SEVEM CMB map, since the four methods give very similar results. The resolution considered for both analyses is $N_{\rm side} = 64$.

For the first case, we are using the *Planck* fiducial model for the CMB and cross-power spectrum, while for the NVSS map we assume the model described in Sect. 2.2.1. We also take into account the presence of Poissonian noise. We have excluded the area obtained from combining the CMB mask at $N_{\rm side} = 64$ (described in Sect. 2.1.1) as well as the area which has not been observed by NVSS. The final mask keeps around 62% of the sky. Since the filter is constructed in harmonic space, we have used an apodized version of the mask in order to reduce the mask-induced correlations. In any case, the degradation introduced by the presence of a mask is small (Barreiro et al. 2008).

For the second case, the lensing map involved applying a high-pass filter, which removed all multipoles with $\ell < 10$. This

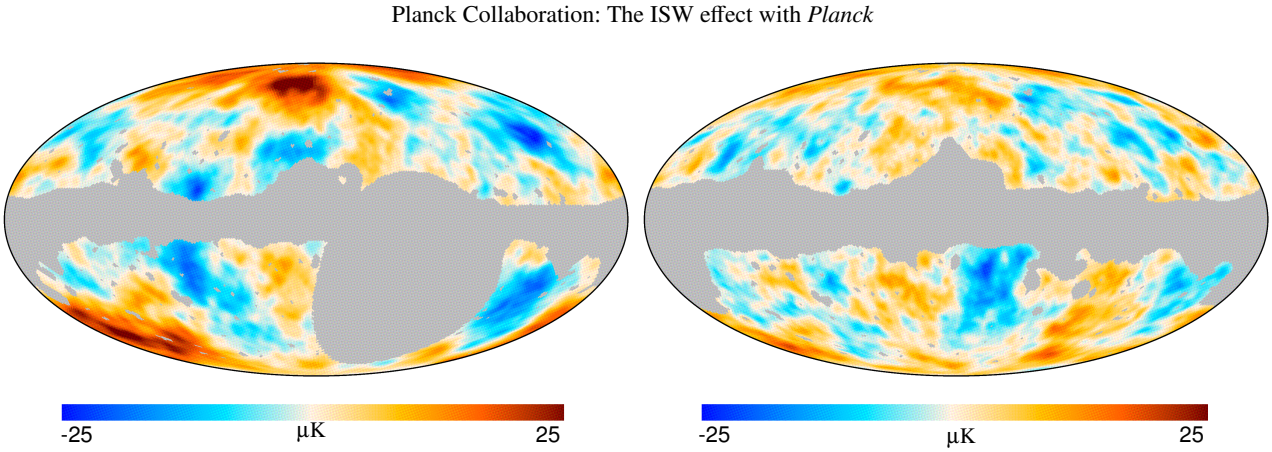

Fig. 11. Reconstructed ISW map from the *Planck* CMB and NVSS data (left) and from the *Planck* CMB and lensing potential maps (right). Note that the maps are not expected to look exactly the same, since each of them provides a partial reconstruction of the noisy ISW signal (see Sect. 6.2 for details).

filtering was done in harmonic space with the presence of a mask. To take this effect into account we used a direct estimation of the pseudo-power spectrum of these data for the power spectrum of the lensing map, after applying the corresponding apodized mask. We used the *Planck* fiducial model for the other power spectra involved, but setting to zero the cross-power for $\ell < 10$. A mask has been constructed by combining the CMB mask plus that provided for the lensing potential map (described in Planck Collaboration XVII 2013), which keeps around 67% of the sky. The corresponding apodized version of this mask was applied before reconstructing the ISW map. Note that the map given in Fig. 1 (right panel) corresponds, to a good approximation, to the first term of the right hand side of Eq. 42.

Figure 11 shows the reconstructed ISW map using the *Planck* CMB map and NVSS (left panel) and that obtained combining the CMB with the lensing potential map (right panel). There are similar structures present in both maps, but they are not expected to look exactly the same, since each of them provides only a partial reconstruction of the ISW signal. This is due to the fact that the reconstruction accounts for the part of the ISW effect probed by the considered tracer, which is different (although correlated) for each case. Moreover, due to the high-pass filter applied to the lensing potential map, the power at $\ell < 10$ for this case corresponds to the Wiener-filtered map of the CMB (to which the filter given by Eq. 42 defaults, if the cross-correlation is set to zero, as in this case), without additional information from the considered tracer.

For both cases, we have tested that the power spectrum of the recovered ISW signal, as well as that of the cross-power between the reconstructed ISW and the considered gravitational potential tracer, are consistent with the corresponding expected values. This indicates the compatibility between the assumed fiducial model and the underlying statistical properties of the data.

7. Conclusions

This paper presents the first study of the ISW effect using *Planck* data. We derived results based on three different approaches: the detection of the interplay between weak lensing of the CMB and the ISW effect, by looking at non-Gaussian signatures; the conventional cross-correlations with tracers of large-scale structure; and aperture photometry on stacks of the CMB field at the positions of known superstructures. A reconstruction of the ISW map inferred from the CMB and LSS tracers was also provided.

The correlation with lensing allows, for the first time, the detection of the ISW effect using only CMB data. This is an effective approach, because the gravitational potential responsible for deflecting CMB photons also generates ISW temperature perturbations. Using different estimators, we investigated the correlation of the *Planck* temperature map with a reconstruction of the lensing potential on the one hand, and the estimation of the ISW-lensing generated non-Gaussian signature on the other. We found that the signal strength is close to $2.5\,\sigma$, for several combinations of estimator implementation and foreground-cleaned CMB maps.

We computed cross-correlations between the *Planck* CMB temperature map, and tracers of large-scale structure, namely: the NVSS survey of radio sources; and the SDSS-CMASS/LOWZ, and SDSS-MG galaxy samples. As estimators we considered the angular cross-correlation function, the angular cross-spectra, and the variance of wavelet coefficients as a function of angular scale. We performed a comparison on different component-separation maps, where we considered `C-R`, `NILC`, `SEVEM`, and `SMICA`, and found remarkable agreement between the results, indicating that the the low multipoles are robustly reconstructed. Covariance matrices between the cross-correlation quantities were estimated for a set of Gaussian realizations of the CMB for the *Planck* fiducial model. For the ISW effect, we report detection significance levels of $2.9\,\sigma$ (NVSS), $1.7\,\sigma$ (SDSS-CMASS/LOWZ), and $2.0\,\sigma$ (SDSS-MG), which are consistent among the different estimators considered. Although these numbers are compatible with previous claims which used *WMAP* data, they are generally smaller. We believe that this discrepancy is mainly due to the different characterization of the surveys and treatment of uncertainties, since the measurement of the CMB fluctuations at the scales which contribute to the ISW detection are very similar for *Planck* and *WMAP*. Only a fraction of these differences (around $0.3\,\sigma$) could be understood in terms of the different cosmological models used by each experiment – in particular, the lower values of H_0 and Ω_Λ reported by *Planck* compared with *WMAP*.

A strength of our new study lies in the fact that the amplitudes derived for the expected signals are largely consistent with unity (i.e., the model expectation), which indicates good modelling of the surveys. The CMB and LSS cross-correlation has also been tested against the null hypothesis, i.e., whether the observed signal is compatible with a null correlation. As expected for such a weak signal, there is no strong evidence of incom-

patibility with the lack of correlation. In this respect, the CAPS approach seems to provide better constraints than the other estimators investigated here (CCF and the SMHWcov).

We explored the aperture photometry of stacked CMB patches at the positions of superstructures identified in the SDSS galaxy distribution. Our analysis of the Granett et al. (2008a) catalogue (50 supervoids and 50 superstructures) reproduced previous results, with similarly strong amplitude and significance levels (somewhat above and below $3\,\sigma$ for voids and clusters, respectively). While the most plausible source of this signal is the ISW effect associated with these structures, it shows some tension with expectations, both in terms of amplitude and scale. The same type of analysis was carried on the latest and much larger void catalogues of Sutter et al. (2012) (about 1 500 voids) and Pan et al. (2012) (about 1 000 voids). The results range from negligible to evidence at the 2–2.5 σ level, with a more moderate amplitude and a smaller scale, in better agreement with theoretical predictions found in the literature. The broad spectral coverage of *Planck* allows us to confirm the achromatic nature of these signals over the 44 to 353 GHz range, supporting their cosmological origin.

We reconstructed maps of the ISW effect using a linear filter, by combining the *Planck* CMB and a gravitational potential tracers. In particular, we considered both the NVSS catalogue and the reconstructed CMB lensing map as LSS tracers. Again we found good agreement between different component separation methods, as well as consistency between the expected and reconstructed auto- and cross-power spectra for the recovered ISW map.

We conclude that the ISW effect is present in *Planck* data at the level expected for ΛCDM-cosmologies, using a range of measurement methods, although there is a possible tension with the results from stacking of CMB fields centred on superstructures. Generally, our results are more conservative than previous claims using *WMAP* data, but the agreement with the expected signal is better. Future *Planck* data releases, including polarization information, as well as improved understanding of foregrounds, could improve on these results, in particular for ISW-lensing correlation and ISW-lensing map reconstruction.

Acknowledgements. The development of *Planck* has been supported by: ESA; CNES and CNRS/INSU-IN2P3-INP (France); ASI, CNR, and INAF (Italy); NASA and DoE (USA); STFC and UKSA (UK); CSIC, MICINN, JA and RES (Spain); Tekes, AoF and CSC (Finland); DLR and MPG (Germany); CSA (Canada); DTU Space (Denmark); SER/SSO (Switzerland); RCN (Norway); SFI (Ireland); FCT/MCTES (Portugal); and PRACE (EU). A description of the Planck Collaboration and a list of its members, including the technical or scientific activities in which they have been involved, can be found at http://www.sciops.esa.int/index.php?project=planck&page=Planck_Collaboration. The modal and KSW bispectrum estimator analysis was performed on the COSMOS supercomputer, part of the STFC DiRAC HPC Facility. We acknowledge the computer resources, technical expertise and assistance provided by the Spanish Supercomputing Network (RES) node at Universidad de Cantabria, and the support provided by the Advanced Computing and e-Science team at IFCA.

References

Adelman-McCarthy, J. K., Agüeros, M. A., Allam, S. S., et al. 2008, ApJS, 175, 297
Afshordi, N. 2004, Phys. Rev. D, 70, 083536
Afshordi, N., Loh, Y., & Strauss, M. A. 2004, Phys. Rev. D, 69, 083524
Aihara, H., Allende Prieto, C., An, D., et al. 2011, ApJS, 193, 29
Barreiro, R. B., Vielva, P., Hernandez-Monteagudo, C., & Martinez-Gonzalez, E. 2008, IEEE Journal of Selected Topics in Signal Processing, 2, 747
Barreiro, R. B., Vielva, P., Marcos-Caballero, A., & Martínez-González, E. 2013, MNRAS, 430, 259
Bielby, R., Shanks, T., Sawangwit, U., et al. 2010, MNRAS, 403, 1261
Blake, C. & Wall, J. 2002, MNRAS, 329, L37
Boughn, S. & Crittenden, R. 2004, Nature, 427, 45
Boughn, S. P. & Crittenden, R. G. 2002, Physical Review Letters, 88, 021302
Boughn, S. P. & Crittenden, R. G. 2005, New Astronomy Review, 49, 75
Brookes, M. H., Best, P. N., Peacock, J. A., Röttgering, H. J. A., & Dunlop, J. S. 2008, MNRAS, 385, 1297
Bucher, M., van Tent, B., & Carvalho, C. S. 2010, MNRAS, 407, 2193
Cabré, A., Fosalba, P., Gaztañaga, E., & Manera, M. 2007, MNRAS, 381, 1347
Cabré, A., Gaztañaga, E., Manera, M., Fosalba, P., & Castander, F. 2006, MNRAS, 372, L23
Cai, Y.-C., Neyrinck, M. C., Szapudi, I., Cole, S., & Frenk, C. S. 2013, ArXiv e-prints 1301.6136
Condon, J. J., Cotton, W. D., Greisen, E. W., et al. 1998, AJ, 115, 1693
Corasaniti, P.-S., Giannantonio, T., & Melchiorri, A. 2005, Phys. Rev. D, 71, 123521
Creminelli, P., Nicolis, A., Senatore, L., Tegmark, M., & Zaldarriaga, M. 2006, J. Cosmology Astropart. Phys., 5, 4
Crittenden, R. G. & Turok, N. 1996, Physical Review Letters, 76, 575
Dupé, F.-X., Rassat, A., Starck, J.-L., & Fadili, M. J. 2011, A&A, 534, A51
Fergusson, J. R., Liguori, M., & Shellard, E. P. S. 2010, Phys. Rev. D, 82, 023502
Flender, S., Hotchkiss, S., & Nadathur, S. 2013, Journal of Cosmology and Astroparticle Physics, 2013, 013
Fosalba, P. & Gaztañaga, E. 2004, MNRAS, 350, L37
Fosalba, P., Gaztañaga, E., & Castander, F. J. 2003, ApJ, 597, L89
Francis, C. L. & Peacock, J. A. 2009, ArXiv e-prints 0909.2494
Francis, C. L. & Peacock, J. A. 2010, MNRAS, 406, 14
Gaztañaga, E., Manera, M., & Multamäki, T. 2006, MNRAS, 365, 171
Giannantonio, T., Crittenden, R., Nichol, R., & Ross, A. J. 2012, MNRAS, 426, 2581
Giannantonio, T., Crittenden, R. G., Nichol, R. C., et al. 2006, Phys. Rev. D, 74, 063520
Giannantonio, T., Scranton, R., Crittenden, R. G., et al. 2008, Phys. Rev. D, 77, 123520
Giovi, F. & Baccigalupi, C. 2005, in IAU Symposium, Vol. 225, Gravitational Lensing Impact on Cosmology, ed. Y. Mellier & G. Meylan, 117–122
Giovi, F., Baccigalupi, C., & Perrotta, F. 2003, Phys. Rev. D, 68, 123002
Goldberg, D. M. & Spergel, D. N. 1999, Phys. Rev. D, 59, 103002
Górski, K. M., Hivon, E., Banday, A. J., et al. 2005, ApJ, 622, 759
Granett, B. R., Neyrinck, M. C., & Szapudi, I. 2008a, ApJ, 683, L99
Granett, B. R., Neyrinck, M. C., & Szapudi, I. 2008b, ArXiv e-prints 0805.2974
Granett, B. R., Neyrinck, M. C., & Szapudi, I. 2009, ApJ, 701, 414
Gruppuso, A., de Rosa, A., Cabella, P., et al. 2009, MNRAS, 400, 463
Hanson, D., Challinor, A., & Lewis, A. 2010, General Relativity and Gravitation, 42, 2197
Hanson, D., Smith, K. M., Challinor, A., & Liguori, M. 2009, Phys. Rev. D, 80, 083004
Hernández-Monteagudo, C. 2008, A&A, 490, 15
Hernández-Monteagudo, C. 2010, A&A, 520, A101
Hernandez-Monteagudo, C., Ross, A., Cuesta, A., et al. 2013, ArXiv e-prints
Hernandez-Monteagudo, C. & Smith, R. E. 2012, ArXiv e-prints 1212.1174
Hinshaw, G., Spergel, D. N., Verde, L., et al. 2003, ApJS, 148, 135
Hivon, E., Górski, K. M., Netterfield, C. B., et al. 2002, ApJ, 567, 2
Ho, S., Cuesta, A., Seo, H.-J., et al. 2012, ArXiv e-prints 1201.2137
Ho, S., Hirata, C., Padmanabhan, N., Seljak, U., & Bahcall, N. 2008, Phys. Rev. D, 78, 043519
Hoyle, F. & Vogeley, M. S. 2002, ApJ, 566, 641
Hu, W. 2000, Phys. Rev. D, 62, 043007
Hu, W. 2002, Phys. Rev. D, 65, 023003
Hu, W. & Okamoto, T. 2002, ApJ, 574, 566
Hu, W. & Sugiyama, N. 1994, Phys. Rev. D, 50, 627
Hunt, P. & Sarkar, S. 2010, MNRAS, 401, 547
Ilić, S., Langer, M., & Douspis, M. 2013, arXiv:1301.5849
Kamionkowski, M. & Spergel, D. N. 1994, ApJ, 432, 7
Komatsu, E., Spergel, D. N., & Wandelt, B. D. 2005, ApJ, 634, 14
Komatsu, E., Spergel, D. N., & Wandelt, B. D. 2005, Astrophys.J., 634, 14
Larson, D., Dunkley, J., Hinshaw, G., et al. 2011, ApJS, 192, 16
Lewis, A. & Challinor, A. 2006, Phys. Rep., 429, 1
Lewis, A., Challinor, A., & Hanson, D. 2011, J. Cosmology Astropart. Phys., 3, 18
Li, H. & Xia, J. 2010, J. Cosmology Astropart. Phys., 4, 26
López-Corredoira, M., Sylos Labini, F., & Betancort-Rijo, J. 2010, A&A, 513, A3
Mangilli, A. & Verde, L. 2009, Phys. Rev. D, 80, 123007
Mangilli, A., Wandelt, B., Elsner, F., & Liguori, M. 2013
Marcos-Caballero et al. 2013, in preparation
Martínez-González, E., Gallegos, J. E., Argüeso, F., Cayón, L., & Sanz, J. L. 2002, MNRAS, 336, 22
Massardi, M., Bonaldi, A., Negrello, M., et al. 2010, MNRAS, 404, 532

McEwen, J. D., Vielva, P., Hobson, M. P., Martínez-González, E., & Lasenby, A. N. 2007, MNRAS, 376, 1211
McEwen, J. D., Wiaux, Y., Hobson, M. P., Vandergheynst, P., & Lasenby, A. N. 2008, MNRAS, 384, 1289
Munshi, D. & Heavens, A. 2010, Mon.Not.Roy.Astron.Soc., 401, 2406
Neyrinck, M. C. 2008, MNRAS, 386, 2101
Neyrinck, M. C., Gnedin, N. Y., & Hamilton, A. J. S. 2005, MNRAS, 356, 1222
Nolta, M. R., Wright, E. L., Page, L., et al. 2004, ApJ, 608, 10
Okamoto, T. & Hu, W. 2003, Phys. Rev. D, 67, 083002
Paci, F., Gruppuso, A., Finelli, F., et al. 2013, ArXiv e-prints 1301.5195
Padmanabhan, N., Hirata, C. M., Seljak, U., et al. 2005, Phys. Rev. D, 72, 043525
Pan, D. C., Vogeley, M. S., Hoyle, F., Choi, Y.-Y., & Park, C. 2012, MNRAS, 421, 926
Pápai, P. & Szapudi, I. 2010, ArXiv e-prints 1009.0754
Parejko, J. K., Sunayama, T., Padmanabhan, N., et al. 2013, MNRAS, 429, 98
Pietrobon, D., Balbi, A., & Marinucci, D. 2006a, arXiv:astro-ph/0611797
Pietrobon, D., Balbi, A., & Marinucci, D. 2006b, Phys. Rev. D, 74, 043524
Planck Collaboration I. 2013, Submitted to A&A
Planck Collaboration XII. 2013, Submitted to A&A
Planck Collaboration XV. 2013, Submitted to A&A
Planck Collaboration XVI. 2013, Submitted to A&A
Planck Collaboration XVII. 2013, Submitted to A&A
Planck Collaboration XXIII. 2013, Submitted to A&A
Planck Collaboration XXIV. 2013, Submitted to A&A
Raccanelli, A., Bonaldi, A., Negrello, M., et al. 2008, MNRAS, 386, 2161
Rassat, A., Land, K., Lahav, O., & Abdalla, F. B. 2006, arXiv:astro-ph/0610911
Rees, M. J. & Sciama, D. W. 1968, Nature, 217, 511
Regan, D., Mukherjee, P., & Seery, D. 2013, ArXiv e-prints 1302.5631
Ross, A. J., Ho, S., Cuesta, A. J., et al. 2011, MNRAS, 417, 1350
Sachs, R. K. & Wolfe, A. M. 1967, ApJ, 147, 73
Sawangwit, U., Shanks, T., Cannon, R. D., et al. 2010, MNRAS, 402, 2228
Schiavon, F., Finelli, F., Gruppuso, A., et al. 2012, MNRAS, 427, 3044
Schlegel, D. J., Finkbeiner, D. P., & Davis, M. 1998, ApJ, 500, 525
Scranton, R., Connolly, A. J., Nichol, R. C., et al. 2003, ArXiv:astro-ph/0307335
Seljak, U. & Zaldarriaga, M. 1999, Phys. Rev. D, 60, 043504
Serra, P. & Cooray, A. 2008, Phys. Rev. D, 77, 107305
Sheth, R. K. & Tormen, G. 1999, MNRAS, 308, 119
Smith, K. M. & Zaldarriaga, M. 2011, MNRAS, 417, 2
Sutter, P. M., Lavaux, G., Wandelt, B. D., & Weinberg, D. H. 2012, arXiv e-prints 1207.2524
Tegmark, M. 1997, Phys. Rev. D, 55, 5895
Tegmark, M. & de Oliveira-Costa, A. 2001, Phys. Rev. D, 64, 063001
Tegmark, M., Eisenstein, D. J., Strauss, M. A., et al. 2006, Phys. Rev. D, 74, 123507
Verde, L. & Spergel, D. N. 2002, Phys. Rev. D, 65, 043007
Vielva, P., Martínez-González, E., & Tucci, M. 2006, MNRAS, 365, 891
Xia, J. 2009, Phys. Rev. D, 80, 103514
Xia, J.-Q., Baccigalupi, C., Matarrese, S., Verde, L., & Viel, M. 2011, J. Cosmology Astropart. Phys., 8, 33
Xia, J.-Q., Viel, M., Baccigalupi, C., & Matarrese, S. 2009, ArXiv e-prints 0907.4753

[1] APC, AstroParticule et Cosmologie, Université Paris Diderot, CNRS/IN2P3, CEA/lrfu, Observatoire de Paris, Sorbonne Paris Cité, 10, rue Alice Domon et Léonie Duquet, 75205 Paris Cedex 13, France
[2] Aalto University Metsähovi Radio Observatory, Metsähovintie 114, FIN-02540 Kylmälä, Finland
[3] African Institute for Mathematical Sciences, 6-8 Melrose Road, Muizenberg, Cape Town, South Africa
[4] Agenzia Spaziale Italiana Science Data Center, c/o ESRIN, via Galileo Galilei, Frascati, Italy
[5] Agenzia Spaziale Italiana, Viale Liegi 26, Roma, Italy
[6] Astrophysics Group, Cavendish Laboratory, University of Cambridge, J J Thomson Avenue, Cambridge CB3 0HE, U.K.
[7] Astrophysics & Cosmology Research Unit, School of Mathematics, Statistics & Computer Science, University of KwaZulu-Natal, Westville Campus, Private Bag X54001, Durban 4000, South Africa
[8] CITA, University of Toronto, 60 St. George St., Toronto, ON M5S 3H8, Canada
[9] CNRS, IRAP, 9 Av. colonel Roche, BP 44346, F-31028 Toulouse cedex 4, France
[10] California Institute of Technology, Pasadena, California, U.S.A.
[11] Centre for Theoretical Cosmology, DAMTP, University of Cambridge, Wilberforce Road, Cambridge CB3 0WA U.K.
[12] Centro de Estudios de Física del Cosmos de Aragón (CEFCA), Plaza San Juan, 1, planta 2, E-44001, Teruel, Spain
[13] Computational Cosmology Center, Lawrence Berkeley National Laboratory, Berkeley, California, U.S.A.
[14] Consejo Superior de Investigaciones Científicas (CSIC), Madrid, Spain
[15] DSM/Irfu/SPP, CEA-Saclay, F-91191 Gif-sur-Yvette Cedex, France
[16] DTU Space, National Space Institute, Technical University of Denmark, Elektrovej 327, DK-2800 Kgs. Lyngby, Denmark
[17] Département de Physique Théorique, Université de Genève, 24, Quai E. Ansermet,1211 Genève 4, Switzerland
[18] Departamento de Física Fundamental, Facultad de Ciencias, Universidad de Salamanca, 37008 Salamanca, Spain
[19] Departamento de Física, Universidad de Oviedo, Avda. Calvo Sotelo s/n, Oviedo, Spain
[20] Department of Astronomy and Astrophysics, University of Toronto, 50 Saint George Street, Toronto, Ontario, Canada
[21] Department of Astrophysics/IMAPP, Radboud University Nijmegen, P.O. Box 9010, 6500 GL Nijmegen, The Netherlands
[22] Department of Electrical Engineering and Computer Sciences, University of California, Berkeley, California, U.S.A.
[23] Department of Physics & Astronomy, University of British Columbia, 6224 Agricultural Road, Vancouver, British Columbia, Canada
[24] Department of Physics and Astronomy, Dana and David Dornsife College of Letter, Arts and Sciences, University of Southern California, Los Angeles, CA 90089, U.S.A.
[25] Department of Physics and Astronomy, University College London, London WC1E 6BT, U.K.
[26] Department of Physics, Carnegie Mellon University, 5000 Forbes Ave, Pittsburgh, PA 15213, U.S.A.
[27] Department of Physics, Gustaf Hällströmin katu 2a, University of Helsinki, Helsinki, Finland
[28] Department of Physics, Princeton University, Princeton, New Jersey, U.S.A.
[29] Department of Physics, University of California, Berkeley, California, U.S.A.
[30] Department of Physics, University of California, One Shields Avenue, Davis, California, U.S.A.
[31] Department of Physics, University of California, Santa Barbara, California, U.S.A.
[32] Department of Physics, University of Illinois at Urbana-Champaign, 1110 West Green Street, Urbana, Illinois, U.S.A.
[33] Dipartimento di Fisica e Astronomia G. Galilei, Università degli Studi di Padova, via Marzolo 8, 35131 Padova, Italy
[34] Dipartimento di Fisica e Scienze della Terra, Università di Ferrara, Via Saragat 1, 44122 Ferrara, Italy
[35] Dipartimento di Fisica, Università La Sapienza, P. le A. Moro 2, Roma, Italy
[36] Dipartimento di Fisica, Università degli Studi di Milano, Via Celoria, 16, Milano, Italy
[37] Dipartimento di Fisica, Università degli Studi di Trieste, via A. Valerio 2, Trieste, Italy
[38] Dipartimento di Fisica, Università di Roma Tor Vergata, Via della Ricerca Scientifica, 1, Roma, Italy
[39] Discovery Center, Niels Bohr Institute, Blegdamsvej 17, Copenhagen, Denmark
[40] Dpto. Astrofísica, Universidad de La Laguna (ULL), E-38206 La Laguna, Tenerife, Spain
[41] European Space Agency, ESAC, Planck Science Office, Camino bajo del Castillo, s/n, Urbanización Villafranca del Castillo, Villanueva de la Cañada, Madrid, Spain
[42] European Space Agency, ESTEC, Keplerlaan 1, 2201 AZ Noordwijk, The Netherlands
[43] Haverford College Astronomy Department, 370 Lancaster Avenue, Haverford, Pennsylvania, U.S.A.

[44] Helsinki Institute of Physics, Gustaf Hällströmin katu 2, University of Helsinki, Helsinki, Finland
[45] INAF - Osservatorio Astrofisico di Catania, Via S. Sofia 78, Catania, Italy
[46] INAF - Osservatorio Astronomico di Padova, Vicolo dell'Osservatorio 5, Padova, Italy
[47] INAF - Osservatorio Astronomico di Roma, via di Frascati 33, Monte Porzio Catone, Italy
[48] INAF - Osservatorio Astronomico di Trieste, Via G.B. Tiepolo 11, Trieste, Italy
[49] INAF/IASF Bologna, Via Gobetti 101, Bologna, Italy
[50] INAF/IASF Milano, Via E. Bassini 15, Milano, Italy
[51] INFN, Sezione di Bologna, Via Irnerio 46, I-40126, Bologna, Italy
[52] INFN, Sezione di Roma 1, Università di Roma Sapienza, Piazzale Aldo Moro 2, 00185, Roma, Italy
[53] INFN/National Institute for Nuclear Physics, Via Valerio 2, I-34127 Trieste, Italy
[54] IPAG: Institut de Planétologie et d'Astrophysique de Grenoble, Université Joseph Fourier, Grenoble 1 / CNRS-INSU, UMR 5274, Grenoble, F-38041, France
[55] IUCAA, Post Bag 4, Ganeshkhind, Pune University Campus, Pune 411 007, India
[56] Imperial College London, Astrophysics group, Blackett Laboratory, Prince Consort Road, London, SW7 2AZ, U.K.
[57] Infrared Processing and Analysis Center, California Institute of Technology, Pasadena, CA 91125, U.S.A.
[58] Institut Néel, CNRS, Université Joseph Fourier Grenoble I, 25 rue des Martyrs, Grenoble, France
[59] Institut Universitaire de France, 103, bd Saint-Michel, 75005, Paris, France
[60] Institut d'Astrophysique Spatiale, CNRS (UMR8617) Université Paris-Sud 11, Bâtiment 121, Orsay, France
[61] Institut d'Astrophysique de Paris, CNRS (UMR7095), 98 bis Boulevard Arago, F-75014, Paris, France
[62] Institut de Ciències de l'Espai, CSIC/IEEC, Facultat de Ciències, Campus UAB, Torre C5 par-2, Bellaterra 08193, Spain
[63] Institute for Space Sciences, Bucharest-Magurale, Romania
[64] Institute of Astronomy and Astrophysics, Academia Sinica, Taipei, Taiwan
[65] Institute of Astronomy, University of Cambridge, Madingley Road, Cambridge CB3 0HA, U.K.
[66] Institute of Theoretical Astrophysics, University of Oslo, Blindern, Oslo, Norway
[67] Instituto de Astrofísica de Canarias, C/Vía Láctea s/n, La Laguna, Tenerife, Spain
[68] Instituto de Física de Cantabria (CSIC-Universidad de Cantabria), Avda. de los Castros s/n, Santander, Spain
[69] Jet Propulsion Laboratory, California Institute of Technology, 4800 Oak Grove Drive, Pasadena, California, U.S.A.
[70] Jodrell Bank Centre for Astrophysics, Alan Turing Building, School of Physics and Astronomy, The University of Manchester, Oxford Road, Manchester, M13 9PL, U.K.
[71] Kavli Institute for Cosmology Cambridge, Madingley Road, Cambridge, CB3 0HA, U.K.
[72] LAL, Université Paris-Sud, CNRS/IN2P3, Orsay, France
[73] LERMA, CNRS, Observatoire de Paris, 61 Avenue de l'Observatoire, Paris, France
[74] Laboratoire AIM, IRFU/Service d'Astrophysique - CEA/DSM - CNRS - Université Paris Diderot, Bât. 709, CEA-Saclay, F-91191 Gif-sur-Yvette Cedex, France
[75] Laboratoire Traitement et Communication de l'Information, CNRS (UMR 5141) and Télécom ParisTech, 46 rue Barrault F-75634 Paris Cedex 13, France
[76] Laboratoire de Physique Subatomique et de Cosmologie, Université Joseph Fourier Grenoble I, CNRS/IN2P3, Institut National Polytechnique de Grenoble, 53 rue des Martyrs, 38026 Grenoble cedex, France
[77] Laboratoire de Physique Théorique, Université Paris-Sud 11 & CNRS, Bâtiment 210, 91405 Orsay, France
[78] Lawrence Berkeley National Laboratory, Berkeley, California, U.S.A.
[79] Max-Planck-Institut für Astrophysik, Karl-Schwarzschild-Str. 1, 85741 Garching, Germany
[80] McGill Physics, Ernest Rutherford Physics Building, McGill University, 3600 rue University, Montréal, QC, H3A 2T8, Canada
[81] MilliLab, VTT Technical Research Centre of Finland, Tietotie 3, Espoo, Finland
[82] Niels Bohr Institute, Blegdamsvej 17, Copenhagen, Denmark
[83] Observational Cosmology, Mail Stop 367-17, California Institute of Technology, Pasadena, CA, 91125, U.S.A.
[84] Optical Science Laboratory, University College London, Gower Street, London, U.K.
[85] SB-ITP-LPPC, EPFL, CH-1015, Lausanne, Switzerland
[86] SISSA, Astrophysics Sector, via Bonomea 265, 34136, Trieste, Italy
[87] School of Physics and Astronomy, Cardiff University, Queens Buildings, The Parade, Cardiff, CF24 3AA, U.K.
[88] School of Physics and Astronomy, University of Nottingham, Nottingham NG7 2RD, U.K.
[89] Space Research Institute (IKI), Russian Academy of Sciences, Profsoyuznaya Str, 84/32, Moscow, 117997, Russia
[90] Space Sciences Laboratory, University of California, Berkeley, California, U.S.A.
[91] Special Astrophysical Observatory, Russian Academy of Sciences, Nizhnij Arkhyz, Zelenchukskiy region, Karachai-Cherkessian Republic, 369167, Russia
[92] Stanford University, Dept of Physics, Varian Physics Bldg, 382 Via Pueblo Mall, Stanford, California, U.S.A.
[93] Sub-Department of Astrophysics, University of Oxford, Keble Road, Oxford OX1 3RH, U.K.
[94] Theory Division, PH-TH, CERN, CH-1211, Geneva 23, Switzerland
[95] UPMC Univ Paris 06, UMR7095, 98 bis Boulevard Arago, F-75014, Paris, France
[96] Universität Heidelberg, Institut für Theoretische Astrophysik, Philosophenweg 12, 69120 Heidelberg, Germany
[97] Université de Toulouse, UPS-OMP, IRAP, F-31028 Toulouse cedex 4, France
[98] University Observatory, Ludwig Maximilian University of Munich, Scheinerstrasse 1, 81679 Munich, Germany
[99] University of Granada, Departamento de Física Teórica y del Cosmos, Facultad de Ciencias, Granada, Spain
[100] University of Miami, Knight Physics Building, 1320 Campo Sano Dr., Coral Gables, Florida, U.S.A.
[101] Warsaw University Observatory, Aleje Ujazdowskie 4, 00-478 Warszawa, Poland

Chapter 4

Towards a full modelling of the iSW effect

As I explored the possible impact of individual structures on the CMB in the previous chapter, it appeared that evidencing the existence and characteristics of the Dark Energy with this method was challenging. The stacking studies that I presented there yielded promising, and interesting results – yet somewhat perplexing and uncertain, which did not allow to draw any definitive conclusions on the matter.

One of the missing elements to this puzzle is a clear idea, if not an exact prediction of the iSW signal expected from structures such as the ones that I considered, in the framework of the ΛCDM paradigm. Indeed, the theoretical studies performed so far in the literature and their predictions (see Sec. 3.5 of Chap. 3) often resort to simulations, approximations and the use of the linear regime of the evolution of structures. None of them addressed the problem from that particular angle, i.e. the exact modelling of objects similar to the observed ones and the computation of their associated iSW signal. The motivation for such endeavour arises quite clearly in the light of the previously discussed results, and is actually twofold. These "exact" predictions would first allow to verify the validity of current claims of a detected iSW signal, such as the results of Granett et al. (2008), especially when we consider the multiple discrepancies that are associated to it (size, amplitude, ...) and which I pointed out in the previous chapter. The new results that I presented, using more recent catalogues of structures, would also benefit from a validation from these kind of predictions. Secondly, such predictive work would constitute a formidable tool for exploring the range of iSW signals that can be generated by potential structures (with realistic features) in the Universe. Then, it

naturally follows that it could also be used to determine the requirements for a significant iSW detection through the means of stacking, in terms of sample size, the objects characteristics, positions, etc.

The structure of this chapter will revolve around these two axes of thought, preceded by a description of the process of elaborating a predictive tool and framework.

4.1 Computing the iSW effect from a structure: a step-by-step recipe

4.1.1 Modelling an inhomogeneity

The need for a precise description of a single structure and its evolution arises clearly from the introduction to this chapter. Similarly to the approach adopted in the previous chapter, I will focus on the study of cosmic voids, as they were at the core of my stacking studies and constitute a considerable amount of material and results, to which I will compare the present theoretical study. However, all the tools that I will discuss and develop here can be applied to overdensities as well – a task that I will perform in the near future.

We can find a good starting point by assuming a spherical symmetry for the voids that we are trying to describe. This constitutes a reasonable statement as voids are found to become more and more spherical as they evolve (Icke, 1984), this spherical form additionally being a stable one (Sato and Maeda, 1983). This assumption also works as a simplification to the current problem, without being too strong. Considering an isolated void – i.e. here an underdense region with spherical symmetry – my choice for its description then turned naturally to a particular metric of General Relativity (GR), namely the so-called Lemaître-Tolman-Bondi (LTB) metric.[1] It is the most general metric of GR for pressureless dust with spherical symmetry. The usual expression for this metric (adopting natural units, i.e. $c = 1$) is the following:

$$ds^2 = -dt^2 + A^2(r,t)dr^2 - B^2(r,t)d\Omega^2 \tag{4.1}$$

where $d\Omega^2 = d\theta^2 + \sin^2\theta d\phi$ is the standard metric on the 2-sphere. $A(r,t)$ and $B(r,t)$ are two almost arbitrary functions, as the Einstein equations impose a relation between

[1] It should be noted for the sake of historical accuracy that this metric might as well be called the Lemaître metric only, as he was the first to find this particular solution to the Einstein equations in 1933 (Lemaître, 1933) Tolman found it again independently but only in 1934 (Tolman, 1934), and it was later investigated by Bondi in 1947 (Bondi, 1947). However, to avoid a possible confusion with the FLRW metric, Tolman's name (and sometimes Bondi's) is often associated to Lemaître.

them (see e.g. Enqvist, 2008, for a derivation):

$$A^2(r,t) = \frac{{B_{,r}}^2}{1+2E(r)} \tag{4.2}$$

where $E(r)$ is a truly arbitrary function (as per usual GR conventions, the "$_{,r}$" and "$_{,t}$" subscripts indicate derivation with respect to the space and the time coordinates respectively). The function $B(r,t)$ is often renamed to $R(r,t)$, after which the metric is finally written as:

$$ds^2 = -dt^2 + \frac{{R_{,r}}^2}{1+2E(r)}dr^2 + R^2(r,t)d\Omega^2. \tag{4.3}$$

The evolution of the function at the core of the metric, $R(r,t)$, is then derived from the Einstein equations yielding:

$${R_{,t}}^2 = E(r) + \frac{2GM(r)}{R} - \frac{1}{3}\Lambda R^2 \tag{4.4}$$

where $M(r)$ is a new arbitrary function. A physical interpretation can be found for each function involved in this metric: the central function $R(r,t)$ acts as an analogue to the angular distance of the FLRW metric. The arbitrary function of space $M(r)$ can be assimilated to a sort of "mass function" as it is directly related to the T_{00} element of the stress-energy tensor (see Bondi, 1947, for more details), while on the other hand the $E(r)$ function can be interpreted as a "curvature profile". A last arbitrary function appears when integrating Eq. (4.4) but it can be safely fixed to any value, as the equation is also invariant with respect to a reparametrisation of the spatial coordinate r.

This metric has sparked a lot of interest in the literature in the last decade, as it was considered as an alternative to the classical FLRW description of our whole Universe (and not only a localised structure), without resorting to the addition of a cosmological constant (Célérier, 2000, Biswas et al., 2007, 2010, February et al., 2010, Clarkson and Regis, 2011). Indeed, if we place ourselves at the centre of a carefully tailored over/underdensity (and the associated LTB metric), it is possible to fit many of the current cosmological observables (CMB, BAO, supernovae, ...) without the need for invoking the "Λ" of the standard model. However, this theory is not without caveats, as it fails to reproduce – alone – some observables within reasonable error margins (most notably constraints from the kinetic SZ effect, see e.g Bull et al., 2012). It constitutes nonetheless a valuable tool to explore the limitations of the FLRW model and the possible influence on cosmological observations of a localised inhomogeneity in our vicinity.

4.1.2 Applying the LTB metric to cosmic voids

My use of the LTB metric here concerns less ambitious scales, with only one structure considered at a time. The last missing step here – besides fixing a few initial parameters and a gauge degree of freedom – is the choice of the features of the void that we want to model and study. This step is often done through the choice of a density profile $\rho(r)$ at a given time in the history of the structure. Indeed, the density in the LTB metric is related to the aforementioned function $M(r)$ of Sec. 4.1.1 as follows:

$$4\pi\rho(r) = \frac{M_{,r}(r)}{R^2 R_{,r}}. \tag{4.5}$$

The last degree of freedom of the LTB, the other arbitrary function $E(r)$, is then fixed by the combination of the chosen initial conditions and Eq. (4.4). The choice of this density profile is of course of no small matter, and will be discussed in more detail further on.

This LTB description of cosmic voids has been already explored multiple times in the past literature (among many others: Olson and Silk, 1979, Meszaros, 1993) to study several theoretical problems of voids, such as their evolution, stability, etc. My present work is also not the first interested in the topic of the exact iSW effect experienced by CMB photons when crossing cosmic voids (Panek, 1992, Baccigalupi et al., 1997, Rakić et al., 2006). It should be noted however that some of these works may not have fully considered the issue of the background that these voids are sitting in (often considered to be a classical FLRW background) and may have neglected the discontinuities that arise then at the border of the structures (Sakai et al., 1999, Inoue and Silk, 2006, Inoue and Silk, 2007). In my work, I assumed that the objects considered are compensated, meaning that these cosmic voids are surrounded by overdense "shells" – an assumption backed up by observations (see Pisani et al., 2013, for a recent exemple). In such case, the conditions of junction (the so-called Darmois-Israel conditions, Darmois, 1927, Israel, 1966, 1967) between the LTB metric describing the voids and the FLRW metric of the background can be reduced to two simple conditions (see e.g. Vanderveld et al., 2008, for details):

- the void needs to be exactly compensated, i.e. its mean density should be equal to the density of the background;
- the density of the void should be continuous as it reconnects to the background metric.

Once these conditions are satisfied, we have all the elements in place to compute the full history of an underdensity through the evolution of its metric, and follow (among

other variables) its density profile as a function of time. An example is shown in Fig. 4.1 where I computed the evolution of a void with an arbitrary profile and an initial density contrast of $\delta = 10^{-3}$ at its centre, from recombination ($z \sim 1100$) all the way to $z = 0$. As expected, the void gets deeper as time progresses, and matter builds up at its edges, creating a gradually denser and thinner shell. This phenomenon can be simply understood using only Newtonian physics: imagining the void as the sum of infinitesimally thin shells of growing radius, it appears clearly that the outer shells will expand slower than the inner ones as they contain more matter inside of them, and therefore are slowed by a stronger gravitational pull (accordingly to the Gauss theorem). The catching-up of the inner shells is then responsible for the apparition of the surrounding overdensity.

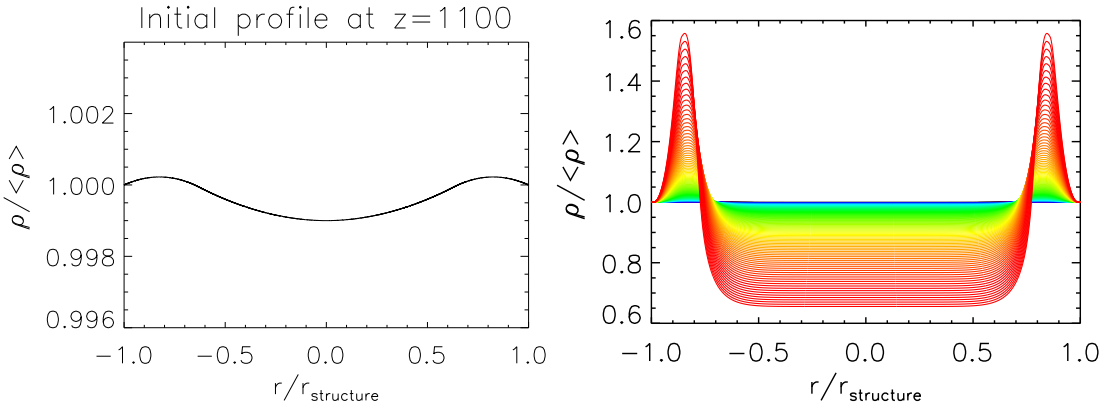

FIGURE 4.1: *Left panel:* Initial density profile (normalised to the mean density in the universe) of a compensated void at $z = 1100$ as a function of the LTB radial coordinate r (normalised to the void radius). This arbitrary profile was used as an input in my LTB framework. *Right panel:* Evolution of the density profile of the same void from $z = 1100$ (blue curve) to $z = 0$ (red curve), as computed by my code solving the LTB equations.

4.1.3 "Lighting up" the voids

While simulating the history of such cosmic voids and exploiting the results could be the subject of a dedicated study, I am more interested here in the effect of the evolution of these structures on the CMB, i.e. on crossing photons. Tracking the path of a photon, as well as its energy, through such voids requires to solve the geodesic equations of GR for this photon in the corresponding LTB metric at a chosen time/redshift. Then, we compare the energy of this photon to another one travelling simultaneously in the FLRW background without any interruption: the difference between the two then yields an estimate of the iSW effect caused by the considered void.

For a radial photon that crosses the void through its diameter, the geodesic equations are fairly simple. To obtain its equation of motion, we can even start from Eq. (4.3),

and equate the line element ds^2 to zero (also eliminating the $d\Omega^2$ term) which gives the following equation:

$$dt^2 = \frac{{R_{,r}}^2}{1+2E}dr^2 \tag{4.6}$$

and then:

$$\frac{dr}{dt} = \pm\frac{\sqrt{1+2E}}{R_{,r}}. \tag{4.7}$$

The "±" in Eq. (4.7) depends on whether the photon is travelling towards (−) or away (+) from the centre of the void.[2] The evolution of the energy of the photon is obtained through the geodesic equation for the time coordinate:

$$\frac{d^2t}{d\lambda^2} = -\Gamma^0_{\alpha\beta}\frac{dx^\alpha}{d\lambda}\frac{dx^\beta}{d\lambda} \tag{4.8}$$

After a few intermediate steps, we obtain the differential equation of the energy $\epsilon = dt/d\lambda$ of the photon:

$$\frac{d\epsilon}{dt} = -\frac{R_{,rt}}{R_{,r}}\epsilon \tag{4.9}$$

Once the complete evolution of the LTB metric – and its associated function $R(r,t)$ – has been computed, we have all the required elements at hand to compute the path of the photon. As an example, I performed this computation for a photon crossing the void described in Fig. 4.1 at some late redshift ($z < 1$), and illustrate in Fig. 4.2 the relative difference in its energy with respect to that of a background photon. While the influence of the cosmic void is visible along the path of the photon (with a maximal energy difference of $\sim 0.1\%$), the final difference is in fact tiny (with $\Delta T/T \sim 10^{-5} - 10^{-6}$) as expected from the weak nature of the iSW effect.

Diametral photons give us a valuable insight on the maximum magnitude of the iSW effect produced by the considered void (since it corresponds to the maximum distance a photon can travel under the influence of the void evolution). However, a complete and thorough analysis requires the full "iSW profile" of the void, i.e. including non-diametral photons with various impact parameters, so as to allow for a rigorous comparison with observations of the CMB and stacking results. For this task, we invoke once more the same geodesic equations for the photons, although now more complex due to the added degree[3] of freedom. We derive then from these a series of new equations of motion for

[2] We are able to deduce this from the fact that the term after ± in Eq. (4.7) is always positive: the angular distance $R(r,t)$ is always a growing function of r (no shell of matter crosses another one) hence $R_{,r} > 0$.

[3] Here, the angular coordinate θ: it is indeed unnecessary to use all three space coordinates thanks to the spherical symmetry of the problem. There always exists a plane, intersecting the centre of the metric, that contains all the motion of the photon.

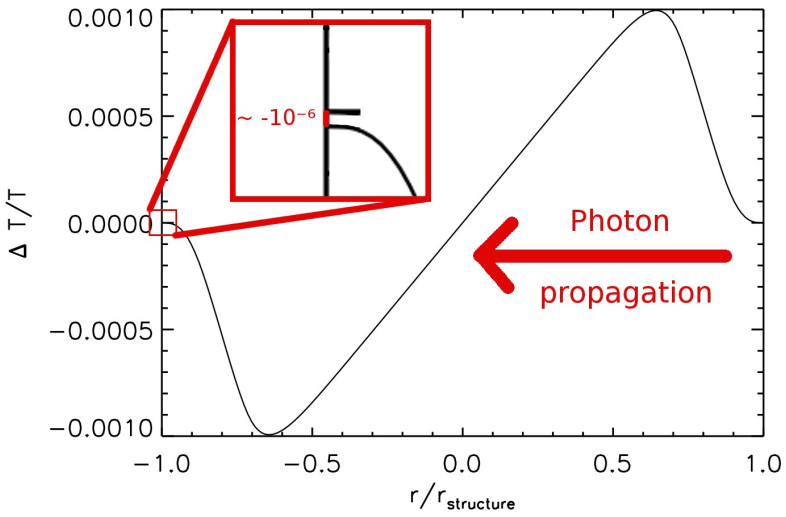

FIGURE 4.2: Relative temperature shift of a photon diametrally crossing the void of Fig. 4.1 (at some late redshift) with respect to a background photon. The shift is plotted as a function of the photon's distance to the centre and was computed by solving the geodesic equations of a diametral photon in the LTB metric.

the crossing photon (details can be found e.g. in Sakai and Inoue, 2008, Zhan, 2011):

$$\frac{dk_t}{dt} = -\frac{1}{k_t}\left(\frac{R_{,rt}\,R_{,r}}{E(r)+1}k_r + R_{,t}\,Rk_\theta^2\right) \tag{4.10}$$

$$\frac{dk_r}{dt} = -\frac{1}{k_t}\left(\left(\frac{R_{,rr}}{R_{,r}} - \frac{E_{,r}}{2(E(r)+1)}\right)k_r^2 - \frac{(E(r)+1)R}{R_{,r}}k_\theta^2\right) - \frac{2R_{,rt}}{R_{,r}}k_r \tag{4.11}$$

$$\frac{dk_\theta}{dt} = -\left(\frac{2R_{,t}}{R} + \frac{2R_{,r}}{R}\frac{k_r}{k_t}\right)k_\theta \tag{4.12}$$

$$\frac{dr}{dt} = \frac{k_r}{k_t} \tag{4.13}$$

$$\frac{d\theta}{dt} = \frac{k_\theta}{k_t} \tag{4.14}$$

with $k_\chi = d\chi/d\lambda$ ($\chi = t, r, \theta$). From this set of equations, we are able to trace the path and follow the energy of any photon crossing the considered void, allowing to reconstruct its iSW profile. An example of such reconstruction is illustrated in Fig. 4.3, where I represented the motion of photons crossing a void, as well as their temperature shift along the way (compared to a background photon evolving simultaneously). The "bending" of the photon trajectories is clearly visible here, as well as their temperature shift along the way, although the final residual shift (i.e. iSW effect) is tiny and is not visible. At this point of the study remains only the question of the tools used for solving the aforementioned equations and getting these results, which will be discussed in the next subsection.

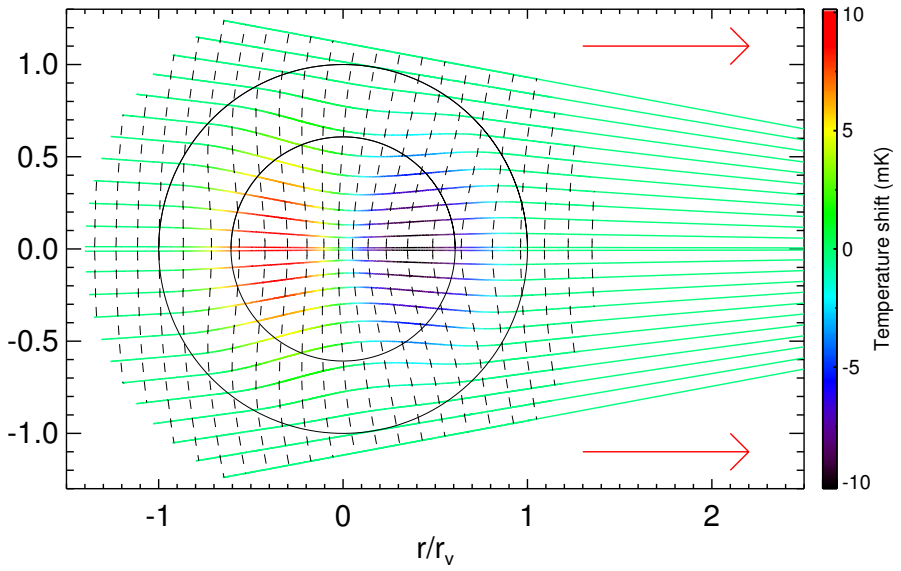

FIGURE 4.3: Paths of 24 photons (thick coloured solid lines) crossing a void with a 130-Mpc physical radius at $z = 0.44$ (N.B.: these are the properties of one of the Gr08 voids), plotted in comoving coordinates normalised by the void comoving radius. The colour of the paths indicates the temperature shift experienced by the crossing photons compared to background photons. Notice here the scale in mK: the final iSW effect (a few μK) is imperceptible here. The large and smaller black circles indicate respectively the radii of the void with or without its compensating overdense shell. The black dashed lines represent the same wavefront of photons at different times of its propagation. The red arrows indicate the direction of propagation of the photons.

4.1.4 Numerical implementation

To perform all the required calculations of this work, I implemented the equations described previously in two distinct codes that I wrote in the Interactive Data Language (IDL).

The first is dedicated to the computation of the LTB metric, its evolution and all its relevant functions, and including a precise control over the initial conditions (density profile, etc.) as well as the choice for the value of the cosmological parameters. I coded my own fourth-order Runge-Kutta algorithm (with an additional feature in the form of an adaptive step finding procedure) for solving the differential equations that govern the main function of the metric, $R(r, t)$. Such numerical method for solving equations implies a discretisation of $R(r, t)$ that needs to be carefully chosen in order to sample the function correctly over the relevant range of time and space coordinates. An emphasis on later times is important for t as the considered voids will often be located at low redshifts. On the other hand, a uniform sampling for r proved to be sufficient to obtain a satisfying degree of precision: after this, the problem becomes equivalent to solving the evolutions of independent, infinitesimal shells of matter enclosing a fixed amount of matter. However, some extra care had to be taken to check for any "shell-crossing" (i.e.

one inner shell catching up another outer one) that may happen for very underdense voids, that have a weak gravitational pull on the shells. It should be noted however that in a real situation, such crossings will probably not occur due to the presence of pressure forces not accounted for in the LTB metric – at least when baryons are considered.[4] The second code I devised solves the geodesic equations for either a single diametral photon, or the full iSW profile. It needs as an input the previously computed $R(r,t)$ to perform its calculations. The one and only free input parameter here is the redshift at which the considered void is located.

In the interests of accuracy, I performed several consistency tests for both codes. I first tested my codes against a "null case", i.e. by reproducing a void with a zero-density contrast profile that should yield results equivalent to the FLRW metric: in terms of density evolution, as well as its effect on photon propagation. Secondly, I studied the effect of refining the spatial grid of all the relevant functions in my codes by a factor of 10 to check the stability of the results when considering realistic voids.

My computed $R(r,t)$ function (the core function of the LTB metric) agrees with its analytical expected value in the "flat" case (which is simply $R(r,t) = (a(t)/a_0)r$) within a relative error of only $10^{-14} - 10^{-13}$. Then, choosing as a reference the values of $R(r,t)$ for the finest grid of r, the use of a $\times 10$ coarser grid resulted in an average relative change of 10^{-8} (10^{-4} at most). Regarding the computed propagation of photons in a "flat void", the results agree with the predictions of the FLRW metric within a margin of 10^{-10}, both for their path (straight line) and energy ($\propto 1+z$). Finally, concerning the stability of the results, I used one of the Gr08 voids (that I reproduced with the LTB metric) as a test case: the difference in the results between the two choices of grid sampling are illustrated in Fig. 4.4. Here, the temperature shift of crossing photons (central and off-centre) along their propagation is shown for the finest sampling scheme. The difference in the results between the two sampling methods (original minus finer) is then overplotted on the same graph. Generally, the differences are below the percent level, with a maximum of a few percents in the non-central case. An examination of Fig. 4.4 seems to indicate first that sudden differences appear near the edges of the voids ($r/r_V = \pm 1$), most likely caused by the density profile of the void, whose derivative is not continuous at the void edge (see Sec. 4.2.1 for more details on the choice of profile). Small differences add up along the path of the photons, with a more pronounced effect near the centre of the void: for diametral photons, this probably originates once again

[4] Strictly speaking, in a DM-only scenario, nothing would stop a shell from crossing another one: it would then be probably pulled back as it will then experience an additional gravitational pull from the shell it just passed, and so on. In reality, with the presence of baryons, such situation would most likely lead to a virialisation process and the formation of structures at the border of the void. In my case, it is actually more of a computing problem as the crossing of these infinitesimal shells produces a local infinite density that crashes the numerical code.

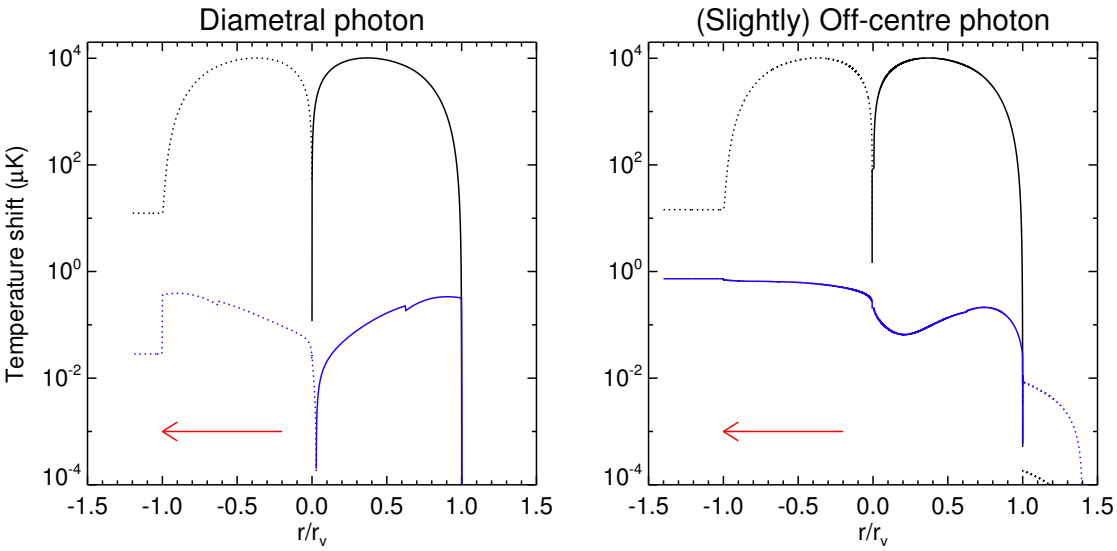

FIGURE 4.4: *Left panel:* Temperature shift (black curve) experienced by a photon crossing a void along a diameter (with properties as in Fig. 4.3) as a function of its distance to the void centre in terms of the comoving coordinate r normalised by the void comoving radius. This computation is performed with a "fine" spatial grid (see text) and acts as a reference. The differences/errors introduced by the use of a $\times 10$ coarser grid are illustrated by the blue curve. As the y-axis is in a logarithmic scale, negative parts of both curves are indicated the dotted portions. The red arrow indicates the direction of propagation of the photon. *Right panel:* Same legend for a non-radial photon, passing close to the void centre.

from a discontinuity at $r = 0$. For off-centre photons, the culprit most likely lies in the stiffness of the differential equation governing the propagation of the photons. Indeed, near the centre of the voids, the angular coordinate θ found in Eqs. (4.10) through (4.14) begins to vary very quickly, perturbing the numerical resolution of these equations.

Several of the aforementioned issues could be attenuated by introducing customised, non-uniform grid for the radial coordinate r (with a finer sampling at the edges for example), as well as using numerical solvers specialised in stiff differential equations – all of which I intend to implement in the near future. For the present work, these errors are acceptable: they affect the predicted iSW signal in a relatively small way ($1\,\mu$K and below), especially compared to the errors present in the stacking results (most notably due to the primordial CMB contamination) that I try to reproduce theoretically. As seen in the previous chapter, the way the temperature profiles are measured on the stacked images introduces errors with similar amplitude, which are themselves several times smaller than the influence of the variance of the CMB.

4.2 The predicted iSW effect from actual structures

As I mentioned, the main goal of the present chapter is to clarify some of the most puzzling results that I obtained when studying the impact of superstructures on the CMB temperature. One of the most important aspects that needed attention is the intriguing results that arose from my study of the Granett et al. (2008) catalogue of structures, where the features of the stacked signal (amplitude, scale, ...) showed inconsistencies with the expected signal, that is predicted in the literature so far.

Multiple interrogations arose from this study: is the apparent discrepancy with respect to these ΛCDM predictions a sign of new physics? Or is it only due to the fact that the current predictions, often based on N-body simulations or linear theory calculations (see previous chapter), are unsuited for the problem? Or even another possibility: could it be that the data has been incorrectly interpreted as a signature of the iSW effect?

My purpose in this section will be to answer these questions (and more) considering an approach not yet examined in the past literature, that is, not searching to compute the expected amplitude of the iSW signal directly, but rather reproducing first the considered structures with the help of the LTB metric, and then deducing their iSW signature.

4.2.1 Return to the Granett et al. catalogue

The first step to reproducing the objects of this catalogue is to consider all the information that it provides that is relevant to the problem at hand. Examining the data provided by the authors, I realised that the exploitable content was hardly exhaustive and that some assumptions had to be made. For each object, the catalogue provides:

- the redshift of the lowest-density galaxy in the void,
- the volume of the void,
- three different measures of its density contrast, either calculated from the mean of all its Voronoi cells (see Sec. 3.1.2 for details), from the mean of its underdense cells exclusively, or finally the density contrast of the single most underdense cell.

I first assumed (reasonably) that the lowest-density galaxy is located near the centre of the void, and therefore considered the given redshift as the "redshift of the void". Then, I converted the volume of the void to an effective radius (the radius of a sphere with the same volume) that I could work with in the LTB framework. Finally, I used two of the density contrast values: I considered again that the most underdense cell would be

near the centre of the void, and consequently identified its density contrast as the one that should be at the centre of the void. Lastly, I kept the mean of the underdense cells and associated it with the expected mean density contrast of the void but only in its underdense part, i.e. excluding the compensation (the overdense region) that forms at the edges of the voids in the LTB model.

Due to the non-analytic nature of the solutions of the equations governing the evolution of the LTB metric, reproducing the Gr08 voids with identical features at the same redshift required a trial-and-error approach. One of the first requirements was to find some adapted expression for the modelling of the voids in terms of their initial density profile. In my work, accounting for the few constraints extractable from the Gr08 catalogue, I chose a simple model for a void by dividing it into two regions:

- an inner part, exclusively underdense and with a density contrast strictly increasing along the radial coordinate, from some initial (negative) value δ_0 at the centre to $\delta = 0$ at the border of the region, at a radius of $r = R_1$,
- an outer region, modelling the initial overdense compensation and extending from $r = R_1$ to $r = R_2$.

To model these two regions, I used the following mathematical expressions respectively:

$$\delta(r) = Ar^n + B(r - R_1) + C \tag{4.15}$$

$$\delta(r) = A'(r - R_1)(r - R_2) \tag{4.16}$$

The four parameters of Eq. (4.15), i.e. A, B, C, and n, allow me to fix the values of δ and its derivative at $r = 0$ and $r = R_1$, giving enough control to reproduce a large spectrum of density profiles. In Eq. (4.16) however, the parameter A' is fixed by the fact that we require the void to be exactly compensated. In order to mimic the features of the actual Gr08 voids, an exploration of these initial parameters was necessary: eventually I was able to match the available data within a error margin of 0.1-0.5%. I also checked that the resulting profiles did not yield unrealistic features for the voids at the initial time ($z = 1100$), e.g. too large or too deep fluctuations that would be inconsistent with the Gaussian theory of structure formation.

Two other points require a particular attention here, the first one being that there are no constraints in the Gr08 data on the width of the (possible) compensation that (supposedly) surrounds the voids. I chose an initial width that yielded at the later times of interest ($z = 0.4 - 0.7$) an overdense shell roughly a third of the void radius at these times. The absence of precise measurements of such profiles in the literature forces us to rely on more theoretical studies (see e.g. Patiri et al., 2006, Figs. 4 and 5), that agree

reasonably with my choice. The second point of interest comes from the Gr08 data itself, more particularly from the reported values of mean density contrasts in underdense cells. I found these values to be somewhat small ($\delta \in [-0.48, -0.25]$) which, when coupled to the bigger reported contrasts at the centre ($\delta \in [-0.87, -0.64]$), has some implication on the shape of the density profiles. It requires them to rise quickly as a function of the radius, whereas they are expected to be rather flat near the void centre. Whether this indicates an issue of the data, or a unsuitable assumption on my part, remains an open question.

As a last note, I should point out that my choice of expression for the void profiles (with two distinct regions) results in a continuous function with, however, a discontinuity in its derivative at $r = R_1$. This may have some small effects on the results (as hinted at in Sec. 4.1.4) but should however be no reason for concern, as the $\delta(r)$ function appears mainly in an integrated form through the "mass function" $M(r)$ (mentioned in Sec. 4.1.1) in the LTB equations.

With these final remarks, my framework is then ready to provide its first predictions regarding the iSW effect produced by actual cosmic voids, or more precisely those of the Gr08 catalogue.

4.2.2 First computations and predictions

With all the required tools at hand, I was able to reproduce all the voids of the Gr08 catalogue, with nearly identical properties (radius, depth, etc.) at their redshift of observation. The first task that I chose to perform was to calculate the theoretical iSW effect associated to these voids using diametral photons – a fairly fast computation. I obtained for each void a value of the expected shift in temperature, and then averaged these 50 values to obtain the mean iSW effect that should be observed near the centre of the stacked image of the CMB patches corresponding to the location of these 50 voids.

The final value that I derived from this calculation is equal to $\Delta T_{\mathrm{iSW}} \simeq -11.44\,\mu\mathrm{K}$. Interestingly, when compared to the temperature decrement observed in the stacked image of the previous chapter (see e.g. the red dashed line of Fig. 3.8), which peaks around -10 to $-13\,\mu\mathrm{K}$ near the centre of the void, the predicted value appears quite close. On this point, my findings seem to differ from the trend observed in other theoretical results in the literature that predict smaller amplitude, as mentioned in Sec. 3.5. However, it would be premature to conclude anything yet as I only considered diametral photons at this point and not the full profile and shape of the predicted iSW effect (remember that the shape and size of the signal were of particular importance in the stacking studies). Nonetheless, I took advantage of the computed contributions of each of the 50 voids

considered and investigated the potential correlations between the amplitude of the predicted signal and the features of the considered voids: here, their radius, redshift, and mean density contrast (in their underdense region). I illustrate the results of these tests

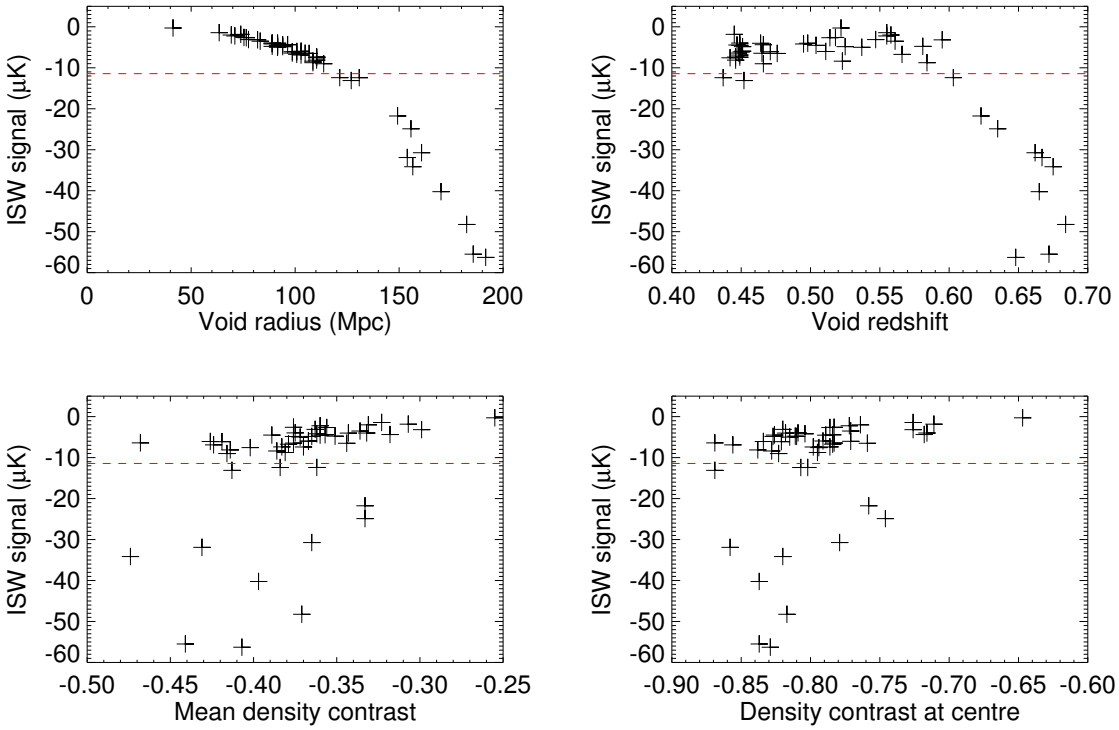

FIGURE 4.5: Total theoretical temperature shift experienced by a photon as a function of one of four features of the reproduced Gr08 void that it crossed diametrically: the void physical radius (top left), redshift (top right), mean density contrast (bottom left) and density contrast at the centre (bottom right). In each plot, the red dashed line corresponds to the average temperature shift for the 50 voids.

in Fig. 4.5. Overall, we cannot find here any obvious correlations, except for a clear one between the void sizes and their associated iSW amplitudes, as expected from our initial idea about the behaviour of the iSW effect: the larger the void, the longer the photon path, and the larger the associated iSW effect. One crucial point here is the fact that only a fifth (around 10) of the voids contribute for the majority of the predicted signal: these also happen to be the largest ones in the sample, as is expected. We find them again in the iSW-redshift graph, at the highest redshifts of the sample. This indicates a correlation between the size and distance of these voids that we already noticed and discussed in Chap. 3 when studying the Gr08 catalogue.

To come back to these ~ 10 most contributing voids, they appear to make up for at least half of the total iSW signal of the sample, as shown in Fig 4.6. Starting from here, I can identify these most (theoretically) contributing voids in the Gr08 catalogue, then go back to the data, and observe the effect of ignoring these voids in the stacking process. This supposedly should have a significant impact on the measured signal, but as I show in Fig. 4.7 by comparing temperatures profiles, we observe almost no modification of

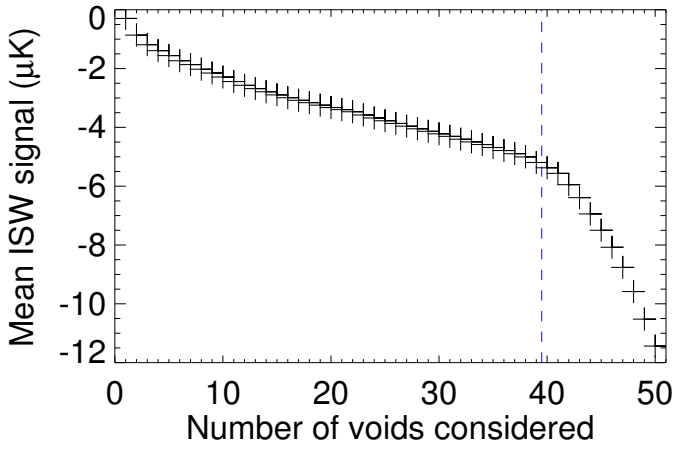

FIGURE 4.6: For the reproduced Gr08 voids, mean temperature shift (experienced by diametral photons) as a function of the number of voids considered in the average, starting from the smallest void. The black dashed line marks the point where the iSW contribution of the 10 biggest and most contributing voids start to add to the average.

the resulting iSW flux. This constitutes yet another counterintuitive fact regarding the analysis of the Gr08 voids and associated results. I will push the analysis even further in the next subsection by considering the full theoretical iSW profiles of these voids.

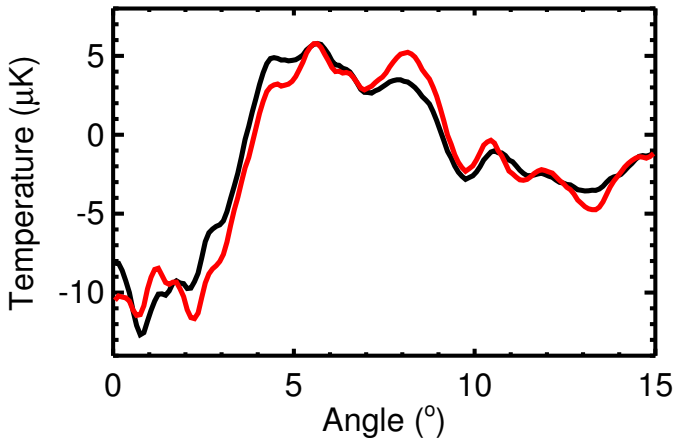

FIGURE 4.7: Temperature profiles of the images resulting from the stacking of the CMB patches (from WMAP V map) at the location of the 50 Gr08 voids (black curve) and at the location of only the 40 smallest voids (red curve). No significant difference can be reported.

4.2.3 Full modelling of the iSW profile

As mentioned earlier, the set of tools that I devised allows for the computation of the complete radial profile of the theoretical iSW temperature shift caused by any void. Applying these tools to the reproduced Gr08 voids, I was able to derive the iSW profile of each of those 50 objects, as well as their mean, which should tell us what to expect

from the results of the stacking of the same voids. In Fig. 4.8, I plotted the 50 individual profiles that I computed, the mean profile (red dashed line) and for the sake of comparison the stacked temperature profile of the Gr08 voids extracted in the previous chapter (blue line). There are several things to notice here: once again, the profiles of

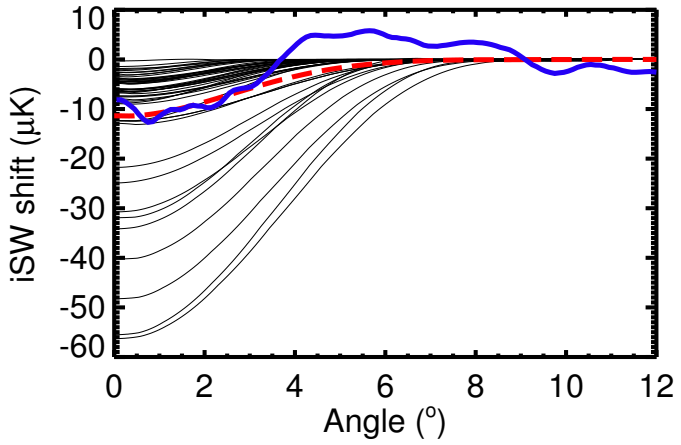

FIGURE 4.8: For the 50 simulated voids tailored to match the Gr08 ones, theoretical temperature shift (black curves) as a function of the angular distance to the void centre in the sky. The red dashed line indicates the mean of these 50 profiles. For the sake of comparison, the temperature profile of the stacked image computed from the actual CMB data is plotted in blue.

$\sim$ 10 voids seem to stand out significantly from the rest, as observed with the radial photons results. Interestingly enough, the mean signal that arises from the combination of all theoretical profiles follows quite closely the measured stacked temperature profile at the lowest angles (from 0° to $\sim$ 3°). However we also observe for larger scales a clear departure from the theoretical prediction. The signal becomes even positive with the presence of a "hot shell" (already discussed in the previous chapter) which does not find any equivalent or logical explanation in my computations. More generally the LTB voids that I simulated do not produce a positive iSW signal near the edges, although they all feature an overdense shell. This may originate from the compensated nature of the void: no matter the distance from the centre of the void, the mean density contrast of the region enclosed within this radius is always lower or equal to 0, causing the photons to constantly experience the effect of an underdensity, even when it is in the locally overdense shell of the void.

This point may prove to be critical because I showed in Chap. 3 that the hot signal surrounding the voids in the stacked image of Gr08 voids was responsible for the high significance of this detection. If it turns out that this hot signal is not physical (in the sense that it cannot be reproduced theoretically), it may prove to be therefore a simple statistical fluke, forcing us to reconsider the significance of the Gr08 stacking results.

But before concluding anything, we have to remember that in reality, all these signals come from different locations in the Universe and projected onto the celestial sphere. This may give rise to distortions in the mean iSW signal due to the proximity of some of these voids in the sky. To deal with this possible issue, I reconstructed the "theoretical iSW map" associated with my 50 theoretical voids (shown in Fig. 4.9), i.e. the temperature shift due to the iSW effect associated to each point in the sky, accounting for all the voids present on the corresponding line of sight. Then, I used the exact same tools that

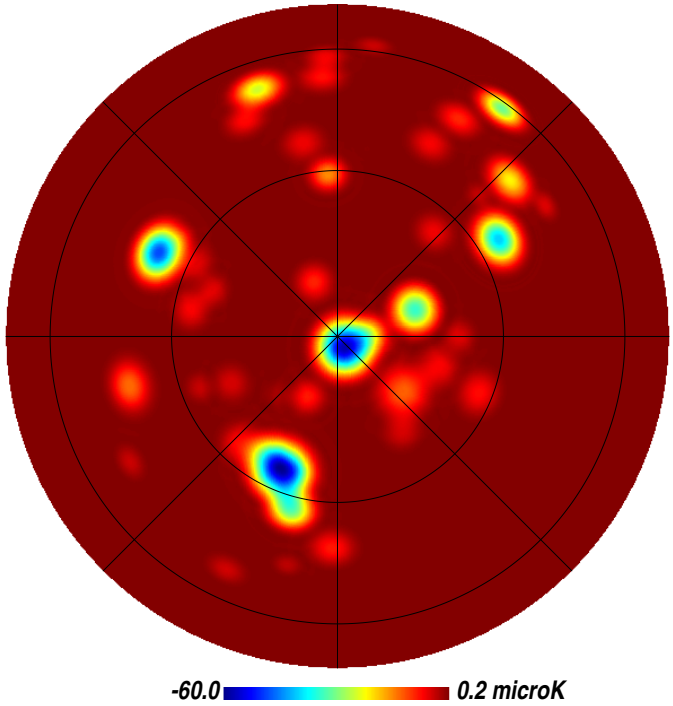

FIGURE 4.9: Orthographic projection of the map of the total theoretical temperature shift caused by the 50 voids of Gr08 as simulated using my LTB framework. Only half of the map is visible (centred on the galactic North pole) and a graticule grid has been superposed with a 45° step in longitude and 30° in latitude.

I have used in the previous chapter to perform stacking analyses on real CMB maps: a computation of the stacked image, as well as its temperature and photometry profile. The resulting profiles are plotted in Fig. 4.10. I also show there the results the same analysis with the inclusion of a rescaling of the patches prior to the final stacking, again similarly to what I did in Chap. 3. No huge surprise here as far as the temperature profile is concerned: we still see no sign of a positive signal, which is quite expected from the combination of the strictly negative profiles of Fig. 4.8. However, some small changes are visible in the amplitude of the signal: firstly, the whole profile is shifted towards negative values compared to the mean profile of Fig. 4.8. This is illustrated by the value of the temperature shift at the largest angles which no longer tends towards 0 ($\sim -4\,\mu$K instead). Secondly, the signal at the centre of the stack is itself slightly colder (by 2 or $3\,\mu$K), even accounting for the previous shift. Both of these effects are

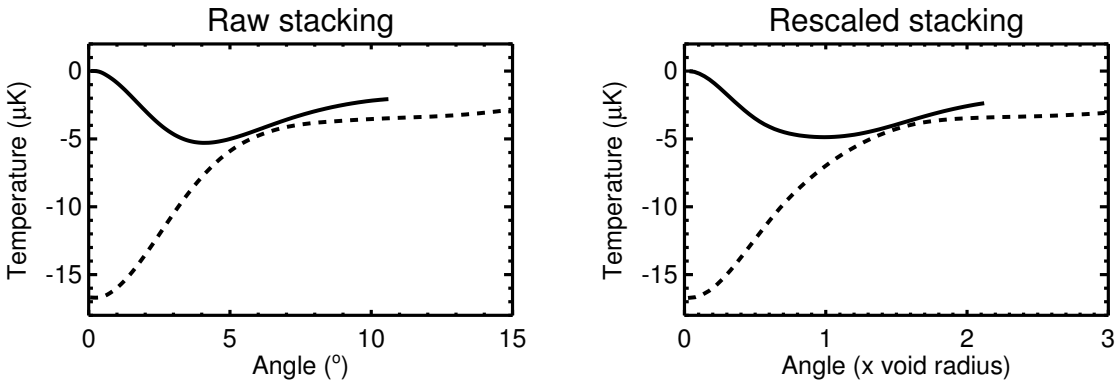

FIGURE 4.10: Temperature (dashed lines) and photometry (solid lines) profiles of the images obtained from the stacking procedure performed on the map of Fig. 4.9 at the location of the Gr08 voids, with (right panel) or without (left panel) rescaling the patches prior to stacking.

consequences of the proximity of the voids on the sky and the introduced overlaps when projecting their all-negative theoretical iSW profile. We note that similar observations can be made on the rescaled profile.

The analysis of the photometry profile yields some interesting results: the maximum (absolute) value of the signal is found around a 4° scale (around one void radius for the rescaled profile) with an amplitude of $\sim 5\,\mu$K, more than twice as low as the measured Gr08 value. This is again expected from my previous remarks on the absence of a "hot signal" at the edges of my predicted profiles. Based on the stacking results of Chap. 3, such signal would have a significance around $1.5\,\sigma$. Regarding the scale of the highlighted signal, my findings appear somewhat closer to the features of the measured photometry profile for Gr08 voids (see Fig. 3.12 for reference), as all of my simulated voids consistently produces as signal with the same extent as the void itself. As a consequence, these results differ from my conclusions using other catalogues of voids, as well as from predictions from other works in the literature (detailed in Sec. 3.5) which all found a signal with a smaller typical scale (typically ~ 0.6 times the voids radii). My assumptions of spherical symmetry and the choice of using the effective radius (computed from the void volume) to characterise my simulations of the Gr08 voids may have played a rôle in this inconsistency. Indeed, modelling a void this way could lead to an overestimate of its actual projected size on the sky, especially for ellipsoidal voids aligned with the line of sight, as they would therefore appear much more smaller than a sphere with equivalent volume. The arbitrary size that I fixed for the width of the compensating shell surrounding my simulated voids, which could artificially "expand" the size of the signal on the sky. Some of these hypotheses will be explored in the next and last section of this chapter. In the mean time, the results of the present section proved however that although all of its features cannot be reproduced (and might even be unphysical), the

actual stacked signal of the Gr08 voids and its amplitude are not entirely irreproducible and at odds with the ΛCDM model, as the original authors claimed so.

4.3 Exploring the limits of the LTB landscape

4.3.1 Assumptions and their consequences

In the previous section I showed an example of application of the LTB framework that I devised: I reproduced the features of the Gr08 voids as closely as possible, and subsequently computed their associated iSW profiles. However, given the relatively scarce information available about these voids, some assumptions on their nature had to be made to be able to work with them. This includes in particular the choice of working with spherically symmetric and compensated voids (whose radii I derived from their volume given in the Gr08 catalogue), as well as the arbitrary choice of the size of the compensated shell (and even its existence) surrounding each simulated void. The geometry of the simulated void cannot be changed without drastic modifications of the protocol, including a change in the choice of metric. However, an exploration of the initial parameters of the LTB model can teach us how our assumptions affect the computed results.

Using one of the reproduced Gr08 void as a basis, I studied the rôle of its compensation in the resulting iSW effect by varying its width at the initial time of the LTB simulation (in my case, $z \sim 1100$). As illustrated by the density profiles in Fig. 4.11, these changes do not affect in any way the evolution of the inner part of the void (i.e. its underdense part) because of its spherical symmetry. However, they evidently change the total size of the void, hence extending the range of its associated iSW effect accordingly (Fig. 4.11).

What are then the consequences of these remarks on our previous results and observations? They show that the arbitrary assumption about the size of compensating shell does have some influence on the shape and amplitude of the predicted iSW signal. A larger (thinner) shell leads to a wider (narrower) signal, adding a longer "tail" to the profile (or shortening it), but I found that this only translated into small changes (less than 0.5°) in the scale highlighted by aperture photometry. The size of the shell however has the effect of noticeably modifying the amplitude of iSW signal, with the largest compensating shells yielding the strongest signal. This phenomenon can be intuitively understood by considering the limit case where the compensated shell has been "stretched" infinitely far from the underdense part of the voids. From the point of view of a crossing photon, the structure would become quasi-equivalent to a non-compensated voids, which are know to yield a more pronounced iSW effect than their compensated

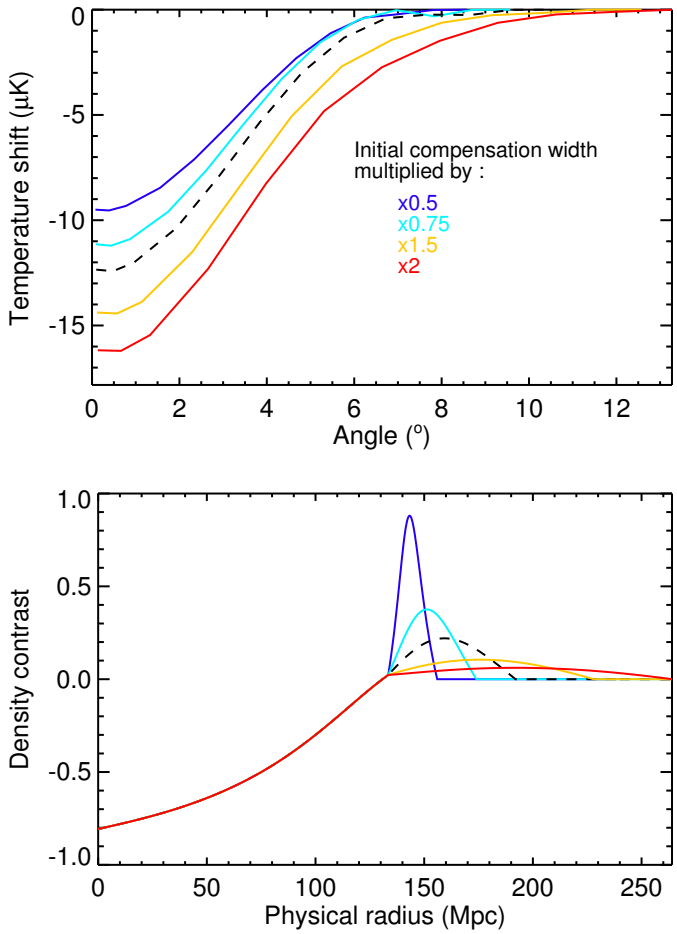

FIGURE 4.11: *Top panel:* Effect of a change in the width of the void compensation shell on the predicted iSW profile, for a void with a radius of ~ 130 Mpc at $z = 0.44$. The original profile (black dashed curve) is plotted against the profiles resulting from a multiplication of the initial width of the compensation as indicated on the graph (coloured solid curves). *Bottom panel:* Density contrast profiles of the corresponding voids as a function of the physical radius, computed using my LTB framework and plotted at $z = 0.44$.

counterparts (Pápai and Szapudi, 2010, Zhan, 2011). It is then reasonable to believe that in the intermediate cases, a void with a larger and more diluted compensating shell would produce an iSW effect with higher amplitude.

This test therefore shows that my results on the simulated Gr08 voids may indeed depend of the initial assumptions about the void density profiles. However, on the one hand the scale of the signal (as highlighted by aperture photometry) remains largely unchanged (as it can be intuited from the profiles Fig. 4.11), therefore not affecting my conclusions on the matter. On the other hand, if we were to try to boost the predicted signal so that the photometry would reach the level associated with the actual Gr08 voids, it would require an unrealistically large compensation (several times the size of the underdense part of the void). This stresses once again the peculiarities of the Granett et al. (2008) results, notably the presence and rôle of the measured "hot ring" in the

measured signal: so far in my study, I found no way of reproducing this very intriguing feature of the temperature profile.

At this point in the study, it would be interesting to relax some of the constraints I put on my LTB models (i.e. the reproduction of the Gr08 voids features) and to conduct a broader exploration of its parameters, which might give us a better insight on the variety of obtainable iSW signal.

4.3.2 Dependences on initial parameters

Beside their sizes, two of the main features of the Gr08 voids that I managed to reproduce accurately were the measured mean and central density contrasts of these objects (as I defined them in Sec. 4.2.1). Whether simply to explore the freedom of my LTB framework, or to consider the possibility that my assumptions on the density were somewhat biased, I decided to study the effect of these particular parameters on the predicted iSW profile. Some of the results of this exploration are shown in Fig. 4.12: one constant here is that any decrease in the density (central and/or mean) of the underdense part of the void results in an amplified iSW signal, and also a natural increase in the density of the compensation. However, one of the most interesting feature of these results is the presence of a small "hot" signal at the edges of the iSW profile for the voids with a very deep density contrast ($\delta \sim 0.9$). This is a unique case so far in the present chapter, most probably because the density contrasts of the Gr08 voids were not very deep (as already mentioned in Sec. 4.2.1). Indeed, this quantity seems to be fundamental in determining whether the iSW signature of a void will possess such positive signal, as pointed out by other works in the literature. In Vadas (1995) for example, the author also remarked that the theoretical signature of a compensated void in the CMB was linked to its current evolutionary phase: a linear ($\delta \ll 1$) or quasi-linear ($\delta \simeq [-0.9, -0.1]$) void yields an entirely cold spot, while a non-linear void ($\delta \simeq -1$) shows a cold spot surrounded by a hot ring. In my case, it is likely that the deepest voids in Fig. 4.12 is nearing the non-linear regime, hence the apparition of the small hot signal at its edges.

One important note, considering the signal that I am trying to reproduce: the hot feature of the predicted iSW signal is confined to the edge of the void and appears quite narrow. Reconsidering our initial choices for the Gr08 density contrasts, it might be possible to raise the amplitude of this positive signal at the edges by exploring the LTB parameter space for deeper voids, but even then the resulting positive signal would never be as large in spatial extent as the "hot ring" measured in the stacking of the actual Gr08 voids, which is nearly as large as the mean radius of the voids themselves. This would indeed imply a compensating shell with roughly the same dimensions, but with a drastically

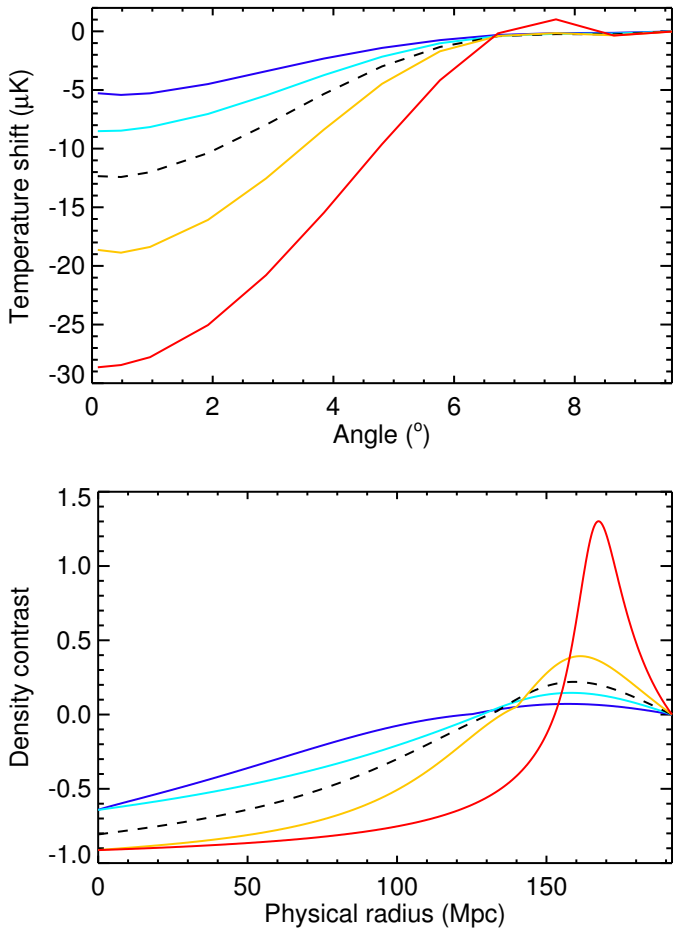

FIGURE 4.12: *Top panel:* Effect of a change of the void density parameters on the predicted iSW profile, for a void with a radius of ~ 130 Mpc at $z = 0.44$. The original profile (black dashed curve) is plotted against two pairs of profiles (blue-cyan and orange-red): each pair corresponds to voids with the same central density contrast, but different mean density. *Bottom panel:* Density contrast profiles of the corresponding voids as a function of the physical radius, computed using my LTB framework and plotted at $z = 0.44$.

lower density which would not reproduce a positive iSW signal. As a last argument, if we suppose that the density contrasts of the Gr08 voids are indeed actually deeper that what I considered and are (at least partially) the reason for such a high signal, this would actually be problematic with respect to the standard cosmological picture. Indeed, as Nadathur et al. (2012) showed in their work, the probability of obtaining within the SDSS volume 50 supervoids with the required features, i.e. the same size as the Gr08 ones ($\sim 100 - 150$ Mpc) and such low density contrast, is negligibly small.

Adding these few remarks with the findings of the previous subsection, this exploration of the LTB model demonstrates that the features of the signal measured by Gr08 (attributed to the iSW effect) are hard to reproduce theoretically without making some important concessions to the ΛCDM paradigm, or even unreasonable assumptions on the voids features.

4.3.3 A statistical oddity?

At this point in the study, I already explored quite thoroughly the LTB framework that I devised, and may have reached its limits in terms of how closely it can reproduce the Gr08 signal while staying within realistic assumptions.

To close this chapter, instead of looking further into the theoretical side of the problem, it might be a good opportunity to change our approach and look back at the data itself. Indeed, an important point that was stressed multiple times in the last chapter was the influence of the CMB on the stacking results and the necessity to account for its variance. We know that in the measured temperature and photometry profiles, a portion of the signal is purely due to the random contamination by the primordial CMB itself – a contribution that can be estimated using stacked images at random position in the sky. A question comes then naturally to the mind: if we account for this contamination, is it possible to reconcile the LTB predictions with the measured signal?

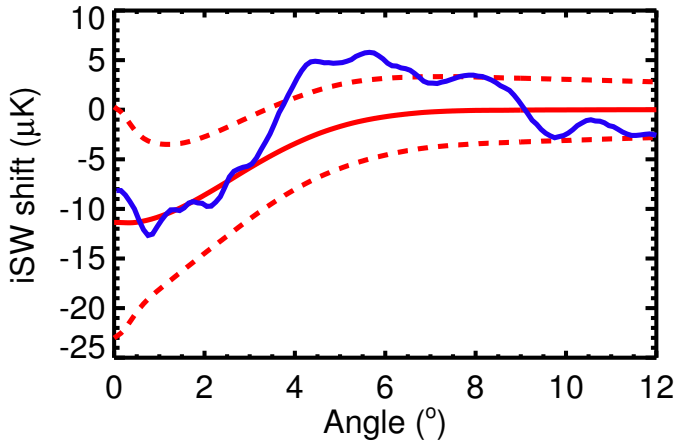

FIGURE 4.13: Mean temperature profile (solid red line) and $1\,\sigma$ contours (red dashed lines) obtained from the stacking of the Gr08 voids on the map of Fig. 4.9 with a randomly generated primordial CMB added to it, with (right panel) or without (left panel) rescaling the patches prior to stacking. The actual temperature profile from the real CMB data is plotted in blue.

The results shown in Fig. 4.13 aim at answering this question. Similarly to the results of Fig. 4.10, I redid the stacking at the location of the voids in my simulated LTB map (cf. Fig. 4.9), but this time adding on top of it a simulated primordial CMB (using the latest ΛCDM parameters from *Planck*). I repeated this procedure many times and computed the temperature profile of the stacked image each time. Then I plotted in Fig. 4.13 the mean and $1\,\sigma$ limits of this distribution of profiles (in a fashion similar to what I did back in Chap. 3), as well as the actual measured temperature profile of the stacked Gr08 voids. We notice that the mean profile of the distribution is naturally identical to the mean iSW signal from the 50 Gr08 voids (red dashed curve of Fig. 4.8). If we compare now the measured profile to the contours, we find a reasonable agreement

between them. The signal lies within the $1\,\sigma$ limit for most of it, except for a small portion of the positive part of the signal which is still below the $2\,\sigma$ threshold. We note for the sake of completeness that an additional error should be accounted for: the numerical uncertainty mentioned in Sec. 4.1.4, that we safely ignored here due to its relatively low value ($\sim 1\,\mu$K) compared to the primordial CMB contamination.

This result seems like a step in the right direction, tightening the agreement between theory and measurements, although it does not solve the issue of the ~ 10 Gr08 voids out of the 50 that I showed to be the most contributing ones in theory (cf. end of Sec. 4.2.2). But it also points out another caveat concerning the whole study: the number of voids in the Gr08 sample remains particularly low to allow us to draw any definitive conclusions! As shown in Fig. 4.13, the variance of the CMB gives so much latitude that a large variety of theoretical predictions would also fit reasonably the data.

In the near future, I intend to assemble all the work and results discussed in this chapter into an article, as well as extend the study to much larger samples of voids such as those I used in the previous chapter, from Pan et al. (2012) and Sutter et al. (2012). Exploiting the latter might prove fruitful as its catalogue contains a significantly larger amount of data on the detected voids, including information on their density profiles.

Chapter 5

Studying Dark Matter through the lens of the reionisation

Stars are not eternal: they are known to go through a series of phases, from their births in gaseous nebulae to their often cataclysmic ends and final transformation into stellar remnants. It follows through that, if we go back in time far enough, there was an era where the Universe was too young to have any stars yet, but was old and cool enough to be transparent to photons. Without any light to illuminate the Universe, this particular era was naturally nicknamed "the Dark Ages" by cosmologists. The physical processes that occurred through this period are a hot topic of research, as they laid the foundations for the birth of the first stars and thus the beginning of another era that will be the focus of this chapter: the reionisation of our Universe. In parallel to all the primary work that I described in the previous chapters, I also took a particular interest during my thesis to the rôle that played in this era one less obvious actor present in the Universe, namely: the Dark Matter, whose possible influence I will describe in the next few sections.

5.1 From the first to the second light of the Universe

5.1.1 The reionisation of the Universe

As mentioned in Chapter 1, about 400,000 years after the Big Bang, the Universe's density decreased enough so that its temperature fell below 3000 K, allowing ions and electrons to (re)combine into neutral hydrogen and helium with only a negligible fraction of heavier elements. Immediately afterwards, photons decoupled from baryons and the Universe became transparent, leaving a relic signature known as the cosmic microwave background radiation, making it effectively the "first light" to roam the Universe. As

mentioned in the introduction of this chapter, this event ushered the Universe into a period of darkness, the so-called Dark Ages. They ended about 400 million years later when the first galaxies formed and started emitting ionising radiation, lighting up the Universe for the first time since recombination and thus starting the era known as the epoch of reionisation (EoR).

Initially during the EoR, the intergalactic medium (IGM) was mostly composed of neutral hydrogen (HI) and helium (HeI) except in regions surrounding the first ionising objects (the so-called Strömgren spheres), such as the first generation of stars (the so-called population III stars). As this reionisation progressed, these regions of ionised hydrogen (HII) and helium (HeII) evolved and expanded: very schematically, after a sufficient number of UV-radiation emitting objects formed the temperature and the ionised fraction of the gas in the Universe increased rapidly. Eventually, all ionised regions percolated and permeated to fill the whole Universe, thus ending the EoR and leaving only traces of neutral matter in the IGM.

The current observational constraints (discussed in Sec. 5.1.3) allow us to roughly situate the whole EoR in a redshift range between $z \sim 6$ (according to Lyman-α observations) and $z \sim 15$ (see e.g. Choudhury and Ferrara, 2006). However, the details of the reionisation history are still poorly constrained yet to be clarified: it requires a knowledge of fundamental issues in cosmology, galaxy formation, quasars, the physics of very metal poor stars and radiative transfer in a clumpy medium. I will describe in the next section the basics of the mechanisms of the reionisation, and mention some key equations and parameters used in the study of the EoR. However, as it does not constitute my primary topic of research, I will not delve much into the details of the era although substantial theoretical and observational efforts are currently dedicated to understanding the physical processes that trigger the EoR and govern its evolution.

5.1.2 Physics of the reionisation and key parameters

The starting point is given by a series of equations called the Saha equations, which describe the degree of ionisation of a plasma as a function of the temperature, density, and ionisation energies of its atoms, assuming a local thermal equilibrium. In our case, they allow us to determine the populations of the ionisation states for the atoms that populate the Universe during the Dark Ages and the EoR. We then consider the balance that takes places in any situation between two competing processes: the recombination of the ions with the free electrons in the medium, against the ionisation of atoms by photons (photoionisation). This all results in an equality between probabilities: the one of an atom to be ionised (which in turn involve the photon density and photoionisation

cross-section), and the one of an atom to capture an electron on a certain level (which depends on the speed and density of free electrons, and the capture cross-section). For a population of particles (e.g. atoms) at a given level k (i.e. a given degree of ionisation), the whole equilibrium can be put in the form of an equation:

$$n_k n_e \sum_j a_j = \sum_j n_j b_j, \tag{5.1}$$

where n_e is the free electrons density, and n_X is is the density of particles at the X level. The a_j and b_j coefficients are respectively the recombination and photoionisation coefficients and are determined from the aforementioned probabilities. The sums ere are made over all the possible levels of the particle. As the lifetime of excited levels are often very short compared to the interval between two photoionisations, we can safely consider that ionisations happen only from the fundamental level, i.e. $\sum_j n_j b_j = n_f b_f$ where the subscript f indicates the fundamental. If we also set $a = \sum_j a_j$, Eq. (5.1) reduces to:

$$n_k n_e a = n_f b_f. \tag{5.2}$$

As a convention, most of the reionisation-related works in the literature choose to divide all the densities by the total density of hydrogen in all its forms, $n_{\rm H}$, and work instead with "ionised fractions":

$$n_{\rm H} x_k x_e a = x_f b_f \quad \text{with} \quad x_i = \frac{n_i}{n_{\rm H}} \tag{5.3}$$

If this equilibrium between recombination and ionisation is disrupted, we get the equation for the evolution of the ionised fraction x_k:

$$\frac{dx_k}{dt} = n_{\rm H} x_k x_e a - x_f b_f \tag{5.4}$$

These equations govern the evolution of the population of neutral (HI) and ionised hydrogen (HII), as well as neutral (HeI), singly (HeII) and doubly ionised helium (HeIII). After the recombination at $z \sim 1100$, they lead initially to an almost-neutral Universe around $z \sim 100$, with some residuals of ionised matter due the very low free electron density and associated probability of capture. The key parameter whose evolution we want to study here is the "total ionised fraction" x_e, i.e. the (spatial averaged) ratio of the density of free electrons over $n_{\rm H}$, which is equal to the sum of the ionised fraction of hydrogen and helium – or more precisely:

$$x_e = x_{\rm HII} + x_{\rm HeII} + 2 \times x_{\rm HeIII}. \tag{5.5}$$

where the factor 2 in front of x_{HeIII} represents the two electrons that an atom of helium releases when fully ionised. When the reionisation process starts later in the era, this ionised fraction is thought to have sharply increased over a short period of time. In current cosmological codes and models not precisely dedicated to the study of the EoR, it is simply modelled as a step function for x_e. At the beginning of the reionisation, it starts from its residual value from recombination determined by the equations mentioned earlier (more details about the precise calculation of these residuals can be found in Seager et al., 1999). After this, x_e is made to increase sharply until it reaches a final value slightly higher that one: indeed, it corresponds to a Universe with all the hydrogen ionised and the helium singly ionised, hence in Eq. (5.5) we have $x_{\mathrm{HeIII}} = 0$, $x_{\mathrm{HII}} = 1$ and x_{HeII} is equal to the He/H number ratio[1] and its end around $z \sim 6$ (from Lyman-α data, cf. Sec. 5.1.3.1). Lastly, at some point later in the history of the Universe, thought to be around $z \sim 3 - 3.5$, it is thought that the deposition of energy in the IGM has reached a sufficient level for the second ionisation of helium (from HeII to HeIII) to occur, which further raises the total ionised fraction to $x_e = 1 + 2f_{\mathrm{He}}$. This particular phase will be discussed again later in this chapter (see Sec. 5.3.2).

The other important variable in the history of the reionisation is the temperature of the intergalactic gas as a function of time, as it impacts the interaction between particles and the distribution of matter in general. Before recombination, its evolution is straightforward: the matter temperature is identical to the temperature of the photons it is coupled with, i.e. the one of a black body undergoing an adiabatic cooling due to the expansion of the universe:

$$T_{\mathrm{mat}}(z) = T_\gamma(z) = T_0(1+z), \tag{5.6}$$

with T_0 the temperature of photons (i.e. the CMB) today. This is equivalent to the following equation for the evolution of the temperature:

$$\frac{dT_{\mathrm{mat}}}{dz} = \frac{T_{\mathrm{mat}}}{1+z} \tag{5.7}$$

After decoupling of the baryonic matter and photons, without any source of energy, only two processes are competing: the adiabatic cooling of matter (alone), and its interaction with the background photons – either cooling or heating, depending on their relative temperature. Without delving too much into details, the equation for the evolution of

[1] This ratio is equal to $Y_P/(K(1-Y_P))$, with $K \simeq 3.9715$ the ratio of the helium-4 atomic mass to the hydrogen one, and Y_P the primordial helium abundance (the latest value of this parameter was determined by Planck Collaboration, 2013e, to be 0.24771 ± 0.00014) $f_{\mathrm{He}} \sim 0.08$. This particular choice of a simple scenario is motivated by the lack of constraints on the detailed reionisation history; however, the current consensus over the available observations places the "middle" of reionisation (i.e. x_e equal to half its maximum value) around $z \sim 11.4$ (Planck Collaboration, 2013e)

matter temperature can be then expressed as follows:

$$\frac{dT_{\rm mat}}{dz} = \frac{8}{3}\frac{a\sigma_T}{m_e c}\frac{x_e T_\gamma^4}{1+x_e+f_{\rm He}}\frac{T_{\rm mat}-T_\gamma}{H(z)(1+z)} + \frac{2T_{\rm mat}(z)}{1+z}. \tag{5.8}$$

where σ_T is the Thomson cross-section, a is the so-called radiation constant (derived from the Stefan-Boltzmann constant), m_e is the mass of the electron and c is the speed of light. The first term of Eq. 5.8 represents the photon-baryon interaction, while the second term corresponds to the adiabatic dilation of matter: the factor 2 that appears compared to Eq. (5.7) is due the transition of matter from a relativistic to a non-relativistic regime after decoupling. Just as Eq. (5.4) for the evolution of x_e, the previous equation covers the basic evolution of the matter temperature, to which heating or cooling from others processes can be then added, which will be especially the case during reionisation. The probing and the use of the IGM temperature in the context of the EoR will be the central point of Sec. 5.3.

5.1.3 Observational constraints

To date, the majority of observations related to the EoR provide weak and model dependent constraints on the reionisation history. However, there are currently a number of observations which impose strong constraints on the broad picture of the reionisation.

5.1.3.1 Lyman-α observations

One of the existing probes uses an absorption phenomenon seen in the spectra of background quasi-stellar objects (QSOs, or quasars). Releasing extraordinary amounts of energy, QSOs are even detectable as far back as the epoch of reionisation and even a little beyond. As their light travels through the Universe, it interacts with and excites atoms along the line of sight, and in particular atoms of neutral hydrogen. This interaction produces an absorption line in the spectra of the QSO at the wavelength of Lyman-α transition of hydrogen (i.e. 1215.67 Å). However, due to the expansion of the Universe, this absorption line becomes redshifted as it reaches us, by an amount proportional to the redshift of the considered cloud of neutral hydrogen. As the light of QSOs goes though multiple HI clouds at various redshifts, it produces a series of absorption lines known as the Lyman-α forest, with each individual cloud leaving its fingerprint at a different position in the observed spectrum (see Fig. 5.1). The large cross-section for the Lyman-α absorption makes this effect a very powerful technique for studying gas in the intergalactic medium over a large range of redshift: indeed, even for low levels of

neutral hydrogen, absorption is highly likely as the associated cross-section scales as the neutral fraction $x_{\rm HI}$ times 10^5!

As we observe more and more distant quasars, the density of absorbing lines in their spectra increases with redshift (see Fig. 5.1). In fact, at redshifts above 4, the density of the absorption features becomes so high that it is hard to define them as separate absorption features. Instead, one sees only the flux in-between the absorption minima which looks as if they were emission rather than absorption lines. As a consequence, the best approach to exploit these spectra is to extract from them a quantity known as the "optical depth" for absorption of Lyman-α photons. We know the theoretical expression of this optical depth, which involves the proper number density of neutral hydrogen $n_{\rm HI}$ along the line of sight of the quasar (for details, see e.g. Zaroubi, 2013). This allows us to extract information on the density of hydrogen in the IGM, or as it is more frequently used, on the neutral fraction of hydrogen $x_{\rm HI}$ defined as $x_{\rm HI} = n_{\rm HI}/n_{\rm H}$, where $n_{\rm H}$ is the total number density of hydrogen (both neutral and ionised).

So far, observations of Lyman-α forests up to redshifts of ~ 6 have shown the neutral fraction to be of the order of 10^{-4} meaning that the Universe is highly ionised at least below $z \sim 6$. However, an important discovery was made using high resolution spectroscopy of high redshift Sloan Digital Sky Survey (SDSS) quasars (reported in Fan et al., 2003, 2006). The SDSS discovered about 19 QSOs with redshifts around 6: the spectra of some of these QSO exhibit an absence of the expected sharp Lyman-α spectral lines – or rather, the density of the lines is so high that we observe instead a trough in these spectra. This feature indicates that the quasar's light has travelled through a large, spread out region of neutral hydrogen, and is commonly called a Gunn-Peterson trough (Gunn and Peterson, 1965) which increases the aforementioned Lyman-α optical depth. From the SDSS data, it was shown for the first time that this optical depth significantly increases around $z \sim 6.3$: although the precise interpretation of this rise is subject to debate, all authors agree that this is a sign of an increase in the Universes neutral fraction at high redshifts, marking the tail end of the reionisation process. This explains why quasars below a certain redshift do not show the Gunn-Peterson trough (though they do show the Lyman-alpha forest), while quasars emitting light prior to the end of reionisation will feature a Gunn-Peterson trough. To summarize, the main conclusion from the Lyman-α optical depth measurements is that it provides us with a lower limit for the end of the EoR, with a highly ionised Universe at redshifts below 6, and an increase of its neutral fraction at about $z = 6.3$.

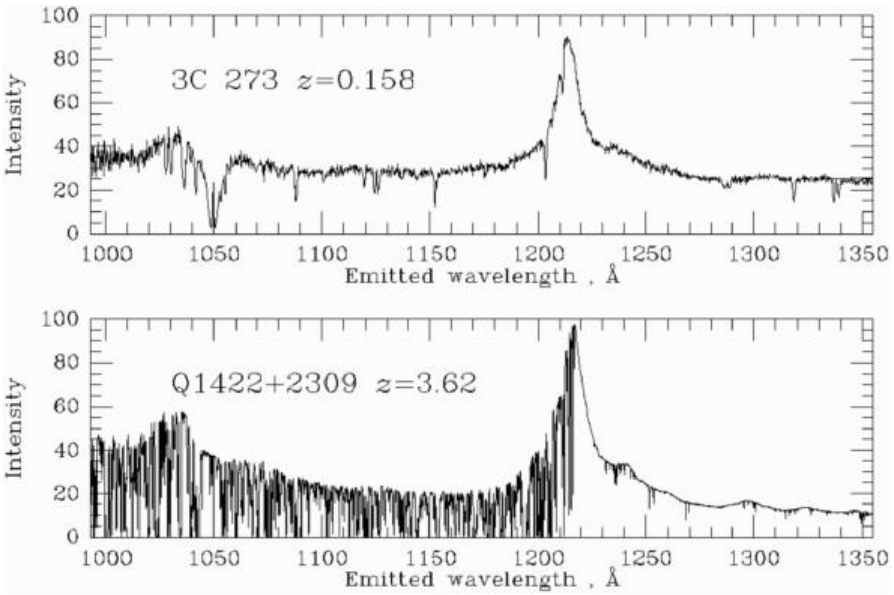

FIGURE 5.1: Comparison of the spectra of two quasars at very different redshifts, 3C 273 at $z = 0.158$ and 1422+2309 at $z = 3.62$, both rescaled to the restframe wavelength of their Lyman-α emission line – the strong and broad emission peak in the shown spectra. It is almost chopped in half by the onset of the Lyman-α forest in the high-redshift quasar. At low redshift, 3C 273 shows only a handful (but distinctly more than zero) Lyman alpha absorbers. On the other hand, hundreds of lines can be identified in the spectrum of 1422+2309. Figure borrowed from Bill Keel website.

5.1.3.2 Thomson scattering and the CMB

Another way to constrain the reionisation era comes from the study of CMB anisotropies. It is known that the Universe has indeed recombined and became largely neutral at $z \simeq 1100$. If recombination had been absent or substantially incomplete, the resulting high density of free electrons would imply that photons could not escape Thomson scattering until the density of the Universe dropped much further. This scattering would inevitably destroy the correlations at subhorizon angular scales seen in the CMB data (see e.g. Sugiyama, 1995). However, a similar scattering must have occurred due to the reionisation of the Universe and the reintroduction of free electrons into the IGM.

In order to calculate the effect of reionisation on CMB photons, a function often defined is the visibility function:

$$g(\eta) = -\dot{\tau} e^{-\tau(\eta)}, \tag{5.9}$$

where $\eta \equiv \int dt/a$ is the conformal time, a is the scale factor of the Universe and $\dot{\tau}$ is the derivative of the optical depth with respect to η. The optical depth for Thomson scattering is given by $\tau(\eta) = -\int_{\eta}^{\eta_0} d\eta\, \dot{\tau} = \int_{\eta}^{\eta_0} d\eta\, a(\eta)\, n_e\, \sigma_T$, where η_0 is the present time and n_e is the electron density. The visibility function gives the probability density that a photon had scattered out of the line of sight between η and $\eta + \mathrm{d}\eta$. The influence

of reionisation on the CMB temperature fluctuations is obtained by integrating Equation 5.9 along each line of sight to estimate the temperature fluctuation suppression due to the scattering. The suppression probability turns out to be roughly proportional to $1 - e^{-\tau}$ (Zaldarriaga, 1997). Since the amount of suppression in the measured power spectrum is small, the optical depth for Thomson scattering must be small too. The left hand panel in Figure 5.2 shows the impact on the CMB temperature fluctuations power spectrum of increasing the value of τ. The right hand panel shows the reionisation history of the Universe assumed in the left panel.

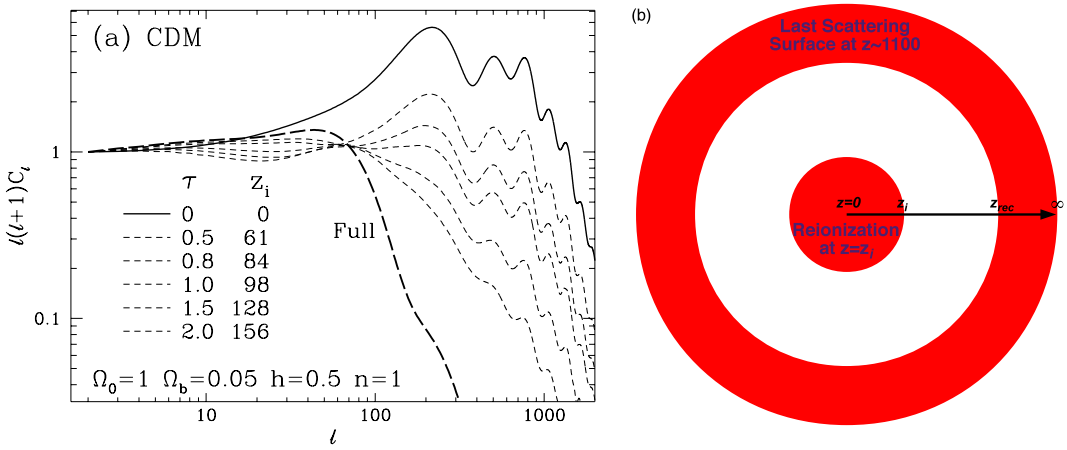

FIGURE 5.2: *Left hand panel* (a): Influence of reionisation on the CMB temperature angular power spectrum. Reionisation damps anisotropy power under the horizon (diffusion length) at last scattering. The models here are fully ionised out to a reionisation redshift z_i. Notice that with high optical depth, fluctuations at intermediate scales are regenerated as the fully ionised (long-dashed) model shows. This figure is taken from Wayne Hu's Ph.D. thesis (Hu, 1995). *Right panel* (b) shows the assumed reionisation history used, with a uniform and sudden reionisation model at the reionisation redshift z_i.

While temperature anisotropies on small scales are erased, polarisation anisotropies of the CMB are actually introduced because of reionisation, most precisely in the E modes (see Kaplinghat et al., 2003, and references therein). By looking at the CMB anisotropies observed, and comparing with what they would look like had reionisation not taken place, the electron column density at the time of reionisation can be determined. With this, the age of the universe when reionisation occurred can then be calculated, provided a model is assumed for the history of $x_e(z)$. Furthermore, the process of reionisation is the only one that can produce a large scale E mode polarisation signal, a "bump" in the power spectrum at low multipoles. Such large scale correlation in the E-mode has been measured by the WMAP team (see Bennett et al., 2012, for the final results of the mission), and its existence, as well as its characteristics give a strong indication that the Universe became ionised around redshift $z \sim 10$. The argument in essence is mostly geometric, namely it has to do with the scale of the E-mode power spectrum as well as

the line of sight distance to the onset of the reionisation front along a given direction (see Zaldarriaga, 1997, more details). Unfortunately however, the large cosmic variance at large scales limits the amount of possible information one can extract from the large scale bump shape, and more detailed constraints on reionisation are hard to obtain (see e.g. Lewis et al., 2006).

In the end, the current best constraints on reionisation from CMB data come from the measurement of the optical depth τ for the Thomson scattering mentioned earlier, found to be around $0.089 + 0.012/-0.014$ (found in Planck Collaboration, 2013e, from the combination of WMAP and *Planck* constraints). This value can in turn be used to constraint the global reionisation history through the integral:

$$\tau = \int_0^{z_{dec}} \sigma_T n_e \frac{cH_0^{-1} dz}{(1+z)\sqrt{\Omega_m (1+z)^3 + \Omega_\Lambda}}, \tag{5.10}$$

where z_{dec} is the decoupling redshift. This formula can be applied for the optical depth along each line of sight but allows also an estimation for the mean electron density, i.e. the mean reionisation history of the Universe. An important point to notice here is that, in order to turn τ into a measurement of the reionisation redshift, one needs a model for x_e as a function of redshift. Hence, one has to be careful when using the reionisation redshift given by CMB papers as in most cases a gradual (step-like) reionisation is assumed (see previous Sec. 5.1.2). Sudden reionisation gives a one to one correspondence between the measured optical depth and the reionisation redshift: here, the WMAP measurement for the optical depth τ implies $z_i = 11.0 \pm 1.4$. However, sudden reionisation is very unlikely and most models predict a more gradual evolution of the electron density as a function of redshift (see the related perspective discussed in Chap. 6).

5.1.3.3 The 21 cm line as a probe of the EoR

Even with the quasar data roughly in agreement with the CMB anisotropy data, there are still a number of questions, especially concerning the energy sources of reionisation and the effects on, and rôle of, structure formation during reionisation. The last probe that I will mention in this section, the 21-cm line in hydrogen, is potentially a mean of studying this period, as well as the Dark Ages that preceded reionisation. The 21-cm line occurs in neutral hydrogen, due to differences in the ground energy between the parallel and anti-parallel spin states of the electron and proton. This transition is forbidden, meaning it occurs extremely rarely. The transition is also highly temperature dependent, meaning that as objects form in the Dark Ages and emit Lyman-alpha photons that are absorbed and re-emitted by surrounding neutral hydrogen, it will produce a

21-cm line signal in that hydrogen (for reference, see Zaroubi, 2013). By studying 21-cm line emission, it will be possible to learn more about the early structures that formed. While there are currently no results, there are a a number of telescopes dedicated to measure this faint radiation. In the short term, these consist of: The Low Frequency Array (LOFAR), the Murchison Widefield Array (MWA), Precision Array to Probe Epoch of Reionization (PAPER) and Giant Metrewave Radio Telescope (GMRT), while, on a somewhat longer time scales the Square Kilometer Array (SKA). One of the most challenging tasks in studying the EoR is to extract and identify the cosmological signal from the data and interpret it correctly. This is because the detectable signal in the frequency range relevant to the EoR is composed of a number of components: the cosmological EoR signal, extragalactic and galactic foregrounds, ionospheric distortions, instrumental response and noise, each with its own physical origin and statistical properties.

5.2 Contribution of the decay and annihilation of Dark Matter to the EoR

The EoR is a watershed epoch in the history of the Universe. Prior to it, the formation and evolution of structure was dominated by Dark Matter alone, while baryonic matter played a marginal rôle. The EoR marks the transition to an era in which the rôle of cosmic gas in the formation and evolution of structure became prominent and, on small scales, even dominant. However, to this day we still do not know precisely what are the sources of energies responsible for the reionisation of the Universe. Quasars, population III stars and dwarf early galaxies are very often cited as candidates, but other sources may have played a rôle in the process. Despite its "secondary rôle" in the history of the EoR, the Dark Matter may potentially have played a rôle, during the Dark Ages and the earliest stages of the reionisation epoch, as well as after the EoR ended. This idea will be the topic of the two sections, present and 5.3, of this chapter, with a particular focus on what we could learn on DM thanks to the study of the EoR.

5.2.1 The Dark Matter mystery

The nature of Dark Matter (DM) is one of the crucial open questions in cosmology. Originally hypothesized to account for discrepancies between calculations of the mass of galaxies from velocity measurements, Dark Matter's existence has been since inferred from a myriad of other gravitational effects on visible matter and by the gravitational lensing of background radiation. Indeed, although Dark Matter is estimated to constitute 84.5% of the total matter in the universe and 26.8% of the total energy content of the

Universe (according to the latest results of Planck Collaboration, 2013d, in the standard model of cosmology) any direct detection has yet to be confirmed (cf. the DAMA/LIBRA experiment, COGENT, XENON, etc.) mainly due to its absence of light emission or absorption at any significant level, and its supposed weak interaction with ordinary matter.

In the standard model of cosmology, DM particles are defined as "cold" particles, because of their negligible free-streaming length (i.e. the length below which Dark Matter fluctuations are suppressed). The most famous alternative model to CDM is called warm Dark Matter (WDM), where particles have longer free-streaming length. Recently, there has been a lot of interest regained in these WDM theories, as they could alleviate some of the caveats of the CDM theories (see e.g. Biermann et al., 2013, for a review), such as the so-called substructure crisis.

At present, there is no definitive evidence which allows us to exclude one of the two scenarios and even the properties (mass, lifetime, etc.) of CDM and/or WDM particles are substantially unknown. From an observational point of view, one of the most direct ways to detect DM particles, and maybe distinguish between the existing CDM and WDM models, is represented by particle decays and annihilation. Indeed, depending on the considered DM model, a fraction of DM particles is expected to decay or annihilate, the rate of these processes generally depending on their density, mass, and cross-section. These involve the emission of photons (although not directly, but through a cascade of products) at wavelengths depending in the particle mass, so that it would be theoretically possible to distinguish DM models using observations of these photons. However, at the moment, constraints on the radiation emitted by such particle decays and annihilation are loose and no definite detection has been made yet, although a large number of experiments are now involved in the present and future of this search, such as the Fermi Gamma-ray Space Telescope, the High Energy Stereoscopic System (HESS), the Cherenkov Telescope Array, the Alpha Magnetic Spectrometer (AMS), the General Antiparticle Spectrometer (GAPS) and PAMELA experiment. For a review of recent results on the topic, see e.g. Muñoz (2012), Porter et al. (2011), Strigari (2012).

5.2.2 Dark Matter and reionisation

Of particular interest to me here is that it has also been pointed out in the literature (see Mapelli et al., 2006, and references therein) that photons eventually due to particle decays or annihilations can be sources of partial early reionisation and heating of the intergalactic medium: these ideas will be at the centre of the work that I will present in the rest of this chapter, revolving around the possible influence of DM on the reionisation

history and parameters, as well as the potential constraining power of the EoR on various DM models and properties. In this work, I did not pretend to present a complete overview of DM candidates. Instead, I wanted to give a global description of the effects of standard DM candidates, aiming to point out the differences among the considered DM particles and their relations to the cosmic reionisation. Therefore I considered only two types of Dark Matter among the most popular models, each time making the assumption that the DM is composed of one single species of particles:

- First, a light kind of Dark Matter (abbreviated LDM, Bœhm et al., 2001, Hooper and Wang, 2004) whose mass does not exceed 100 MeV, or else its disintegration products would contain easily detectable muons that are incompatible with observations. The axino is a representative of such light Dark Matter particles.
- Another type of Dark Matter, with a mass greater that 30 GeV, that I will call "heavy Dark Matter" (hDM) and that includes particles such as the often quoted neutralinos.

As mentioned earlier, these DM particles can potentially contribute to the reionisation of the Universe through two processes: spontaneous decay and self-annihilation. Both produce new elements whose energy will contribute to three main processes: the ionisation, the excitation and the heating of the IGM. In my work, I considered two different scenarii of energy injection due to Dark Matter:

- The decay of the LDM particles, based on the assumption that if these are light enough, their lifetime will be short enough for a non-vanishing part of its population to decay over the history of the Universe – but long enough for Dark Matter to be still present today. According to existing models, the DM could decay into a variety of products (photons, electron-positron pairs, etc) which can then in turn inject energy into the IGM (e.g. by photoionisation) and therefore contribute to the reionisation of the Universe. If we simplify the problem by assuming that the only products are photons, then the photon emission rate is simply given by an exponential law:
$$\frac{dn}{dt} = \frac{n_0}{\tau} e^{(t_0 - t(z))/\tau}, \tag{5.11}$$
with n_0 the current density of the considered DM particles, τ their half-life, t_0 and $t(z)$ the times passed from the Big Bang to now and to the redshift z respectively. Following Mapelli et al. (2006), I defined τ as a function of the particle mass m_{LDM} as $\tau = 4 \times 10^{26} \mathrm{s}\,(m_{LDM}/\mathrm{MeV})^{-1}$, meaning that larger DM particles naturally have a lower lifetime.

- The annihilation of hDM particles with their anti-particles (possibly themselves) ; we rule out a possible decay of these particles, because if they could, their lifetime would then be very short due to their massive nature and therefore they could not be a viable DM candidate. Assuming the same hypothesis as for the LDM decay products, the photon emission rate is given by:

$$\frac{dn}{dt} = n_0^2 \, (1+z)^3 \, <\sigma v> C, \tag{5.12}$$

  where $<\sigma v>$ is the annihilation cross-section – typically of the order of $10^{-24}\mathrm{cm}^3.\mathrm{s}^{-1}$ in optimistic cases, 10^{-26} for more conservative models – averaged over the temperature. The variable C stands for the "clumping factor", defined as $C = \langle n^2 \rangle / \langle n \rangle^2$ with n being the local matter density. It characterises the tendency of matter to aggregate, which boosts the number of interactions, hence the potential annihilations and the number of produced photons. In the literature, this factor is often chosen to be equal to unity, due to a lack of detailed understanding of the dynamics of DM and the processes involved in its clumping. Moreover, on global scales in the young Universe, this assumption should not be too far from reality.

In both of these scenarii, the injection rate of energy per baryon is written simply as:

$$\epsilon_{DM} = \frac{dn}{dt} \frac{E_\gamma}{n_b} \tag{5.13}$$

where E_γ is the energy of the emitted photons (in theory, half the mass of the DM particle in case of decay, or the whole mass for annihilations) and n_b the current number density of baryons today. Part of this released energy will ionise the hydrogen and helium atoms, while another part will heat the IGM. In order to estimate these different fractions, we use the approximation of Chen and Kamionkowski 2004 (itself based on the work of Shull and van Steenberg, 1985). Qualitatively this approximation states that initially, when the IGM is still neutral ($x_e = 0$), the energy is distributed equally into the heating and the two ionisation processes (of HI and HeI). Conversely, when the universe is fully ionised ($x_e = 1$), all of the energy goes into the heating of the IGM; and in between, the different fractions evolve linearly with x_e. Once I set up the framework, the next step for me was to compute the evolution of the key parameters of the EoR in the context of these scenarii in order to have a first assessment of the effect of DM on the history of the IGM.

5.2.3 Recombination code and customisation

In order to test and exploit the different models of DM and associated reionisation histories, my main tool was the numerical RECFAST created by Seager et al. (1999) whose main purpose is to compute the history of the IGM through the ionised fractions of hydrogen and helium, as well as the temperature of the IGM. Initially, the code does not account for any reionisation model and computes the aforementioned quantities starting from a time before the recombination (around $z \sim 8000$) and goes to $z = 0$. I therefore modified the code to suit my needs by including additional terms to the evolution equations, corresponding to sources of reionisation. More precisely, I modified the three equations that govern the evolution of $x_{\rm HII}$, $x_{\rm HeII}$ and $T_{\rm mat}$ (see Sec. 5.1.2 for definitions of these parameters), adding the following terms:

$$-\delta\left(\frac{dx_{\rm HII}}{dz}\right) = \frac{\epsilon_{DM}}{E_{th,\,H}}\frac{1-x_{\rm HII}}{3\,(1+f_{\rm He})}\,\mathcal{E} \tag{5.14}$$

$$-\delta\left(\frac{dx_{\rm HeII}}{dz}\right) = \frac{\epsilon_{DM}}{E_{th,\,He}}\frac{1-x_{\rm HeII}}{3\,(1+f_{\rm He})}\,\mathcal{E} \tag{5.15}$$

$$-\delta\left(\frac{dT_{\rm mat}}{dz}\right) = \frac{2\,\epsilon_{DM}}{3\,k_B}\frac{1+2\,x_{\rm HII}+f_{\rm He}\,(1+2\,x_{\rm HeII})}{3\,(1+f_{\rm He})}\,\mathcal{E}, \tag{5.16}$$

where $E_{th,\,H} = 13.6$ eV ($E_{th,\,He} = 24.6$ eV) is the ionisation energy of hydrogen (helium) atoms, k_B the Boltzmann constant and $\mathcal{E} \equiv [H(z)(1+z)]^{-1}$. Aside from these three equations, I also added the computation of another important variable of the EoR, the optical depth τ which is one of the most accessible observable in the data, that I already mentioned and defined in Sec. 5.1.3.2.

After applying this modification to the RECFAST code, I first tried and succeeded in recovering the results of a previous and similar study by Mapelli et al. (2006) for a few cases of DM models. My results are presented in Fig. 5.3.

Three masses of LDM are considered for decay: according to the results, these particles may be considered as a potential source of significant reionisation, especially for the highest considered mass (10 MeV). Indeed, the ionised fraction x_e (see Eq. 5.5) reaches a value of 0.8 even without any other source of reionisation: we remember that the maximum value for x_e is around 1.2 and corresponds to $x_{\rm H} = x_{\rm He} = 1$) which really makes the contribution of LDM non-negligible. We note however that the value of x_e is ten times lower at a redshift of $z = 6$, a time when reionisation is supposed to be already finished according to current observations: this acts as a reminder for the need of other, astrophysical sources of reionisation. Naturally, the effect of the LDM decay fades rapidly when considering lower masses: its impact on the IGM temperature is nonetheless important even for these cases, with a temperature significantly higher as

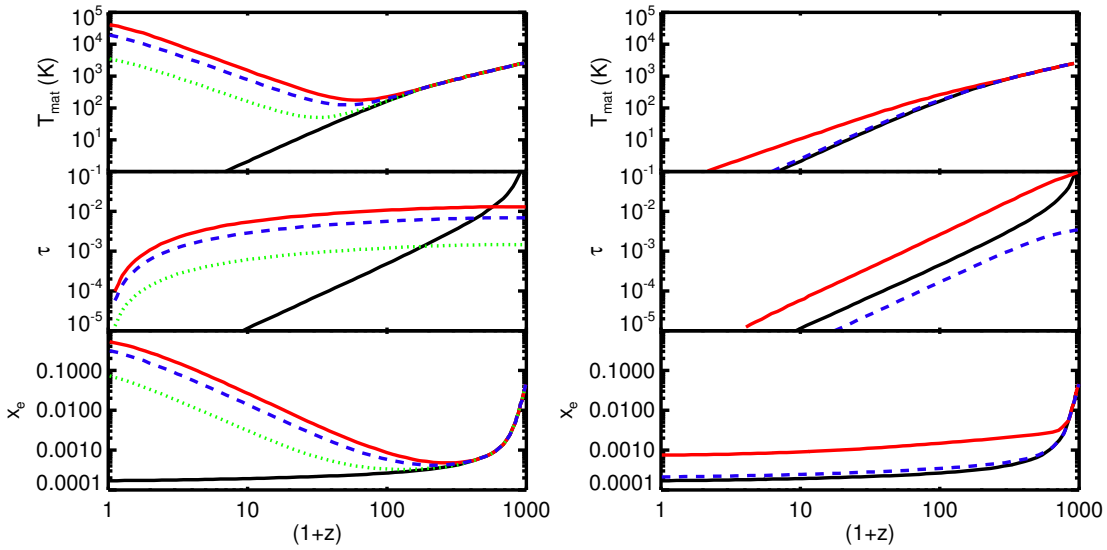

FIGURE 5.3: Ionised fraction (bottom panels), Thomson optical depth (central panels) and matter temperature (upper panels) as a function of redshift as computed by my modified RECFAST code. *Left panels:* Results for the decaying LDM of masses 1 (thick dotted line), 5 (dashed) and 10 MeV (solid). The thin solid line represents the case without any reionisation source. *Right panels:* Results for the annihilation of hDM $\langle \sigma\, v \rangle = 2 \times 10^{-26}$ (thick dashed line) and 10^{-24} cm^3 s^{-1} (solid). In both the cases the particle mass is 100 GeV. The thin solid line is the same as in the left panels.

soon as $z = 20 - 30$. On the other end, the annihilation of hDM is clearly insufficient to provide a significant reionisation of the Universe or heating of the IGM at $z = 0$, no matter the annihilation cross-section considered. However, the effect of hDM on the ionised fraction, although weak, occurs much earlier in the history of the Universe than for the LDM – as soon as $z = 600 - 700$ – due to the simple fact that the annihilation rate depends on the square of the matter density (which is much higher at earlier redshifts) whereas decay rates are only linear in density. This difference has repercussions on the Thomson optical depth, as it is (roughly) related to the integral of the ionised fraction: indeed, we observe in Fig. 5.3 that the most influencing model of LDM reaches only a optical depth of 0.01 at $z = 1000$ while the optimistic model of hDM gets close 0.05 (this has to be put into perspective of the measured value of 0.08).

In any case, these first results allow us to see that DM particles, even in the most optimistic cases, cannot have reionised the Universe by themselves. However, can we determine if they contributed to this process significantly and especially, if they had a measurable impact ? Tentative answers to these questions lie in the next section, where I performed a more detailed analysis of the rôle of DM within the known paradigm of the EoR.

5.2.4 Additional in-depth analysis

As discussed in Sec. 5.1.3, we know from observation that the reionisation of the Universe occurred around a redshift of $z = 10$ and was mostly finished before $z = 6.5$. In order to account for this knowledge in my study, I added in my version of RECFAST a classic (cf. end of Sec. 5.1.3.2) arbitrary, step-like reionisation, starting around $z = 20$ from whichever value x_e reached at that time, and ending around $z = 6$. Thus, by adding simultaneously the effect of DM particles, one can observe its relative impact on the reionisation history. At the same time, an original part of my work is that I also decided to include a similarly shaped increase of the temperature of the IGM up to a few 10^4K – a value motivated by the knowledge of the temperature within Strömgren spheres and the thermal history of the IGM (cf. Valageas and Silk, 1999). However, unlike the ionised fraction that stays at its maximum value, the temperature of the IGM keeps on evolving after the end of reionisation (if only because of the adiabatic cooling). An interesting fact: although it remains quite arbitrary, my simple step-like model for the temperature proved to be quite pertinent, as it happened to match quite accurately more sophisticated models that I found in the literature and aimed at a more physical modelling of the sources of heating in the EoR (see again Valageas and Silk, 1999).

To further improve the relevance and accuracy of my code, I also included an additional sophistication to it: I considered a departure from the simplistic assumption about the clumping factor C involved in the DM annihilation process. Simply fixing it to unity is reasonable only for high redshifts, when the Universe is still homogeneous ($z \gg 10$), but it becomes invalid for low redshifts with the onset of the virialisation of structures and the apparition of the "cosmic web". Therefore, I devised instead a more coherent formulation of this factor based on two observations: the fact that the apparition of the first structures can be dated below $z = 60$, and the mean matter density of the Universe which is known to evolve proportionally to $(1 + z)^3$. The resulting expression that I chose is the following:

$$C = 1 \quad \text{for z} > 60, \qquad C = \left(\frac{61}{1+z}\right)^3 \quad \text{for } 0 < \text{z} < 60, \tag{5.17}$$

a form similar to tho one used in e.g. Chuzhoy (2008). Although not very complex, this new expression is still physically consistent: in the linear regime at high redshifts, the clumping factor stays equal or very close to 1, and increases accordingly with the apparition of structures over the course of the Universe. For the sake of completeness, I wish to mention that I also explored two other sophistications, in the form of two additional sources of reionisation: namely the annihilation of LDM annihilation and the excitation of hydrogen by Lyman-α photons. However, I found that both processes have

in the end a negligible impact on each key observable (the ionised fraction, optical depth and IGMtemperature).

Let us now carry on to the results of this extended analysis: I will focus here each time on the most optimistic models of DM in terms of impact on the reionisation (witnessed in the previous section). We start with the decay of 10 MeV LDM particles, shown in Fig. 5.4. Here again, LDM alone is not enough to fully reionise the Universe; what is worse is that the impact of the DM is completely overshadowed by the sudden, "astrophysical" reionisation, except for a redshift range between 10 and 100. Although small, this difference (of the order of 0.01) may imply a surplus of free electrons in the IGM which may have had consequences on the evolution of the intergalactic gas, as the ionised fraction is still multiplied by a factor of 100 around $z = 20$. Concerning the optical depth results, we note first that the observable value of τ (obtained through CMB studies) corresponds roughly to the plateau observed in the middle panel of Fig. 5.4. We see that the impact of DM here is quite negligible, with only tenuous differences at high redshift when the step-like reionisation is added. In contrast to this mildly exciting results, the evolution of the IGM temperature is much more affected by DM particles: I will not go into much detail into the implication of this impact as it will be the focus of the last section of this chapter. Still, we note that DM particles alone can yield enough heating to bring the IGM temperature to a level similar to (or even higher than) the step-like heating. We can also see very distinct phases in the temperature evolution for the full (step + LDM) scenario, with a cooling of the IGM until $z = 100$ where it is overcome by the DM heating, then the step corresponding to the ignition of astrophysical sources, and finally after $z = 6$, the competition between the adiabatic cooling and the DM heating again.

The situation is somewhat different for the results with the annihilation of hDM particles: its impact on the history of the ionised fraction remains weak, but its integrated effect on the optical depth and its plateau is more significant than in the LDM case (see Fig. 5.5). It could even reach detectable levels, although we have to remember that I considered here an optimistic annihilation cross-section. Even more interesting is the impact on the IGM temparature, which is boosted compared to the previous section thanks to the change in the clumping factor. This has the effect of bringing it to similar levels as the lone step-like reionisation and the heating of LDM decays, making it a suitable candidate for further exploration, as we will se in Sec. 5.3.

The various effects on the optical depth that we have observed, although not very important, should have nonetheless an effect on the visibility function (mentioned in Sec. 5.1.3.2) and therefore on the CMB and its fluctuations, as we will see briefly on the next and last subsection.

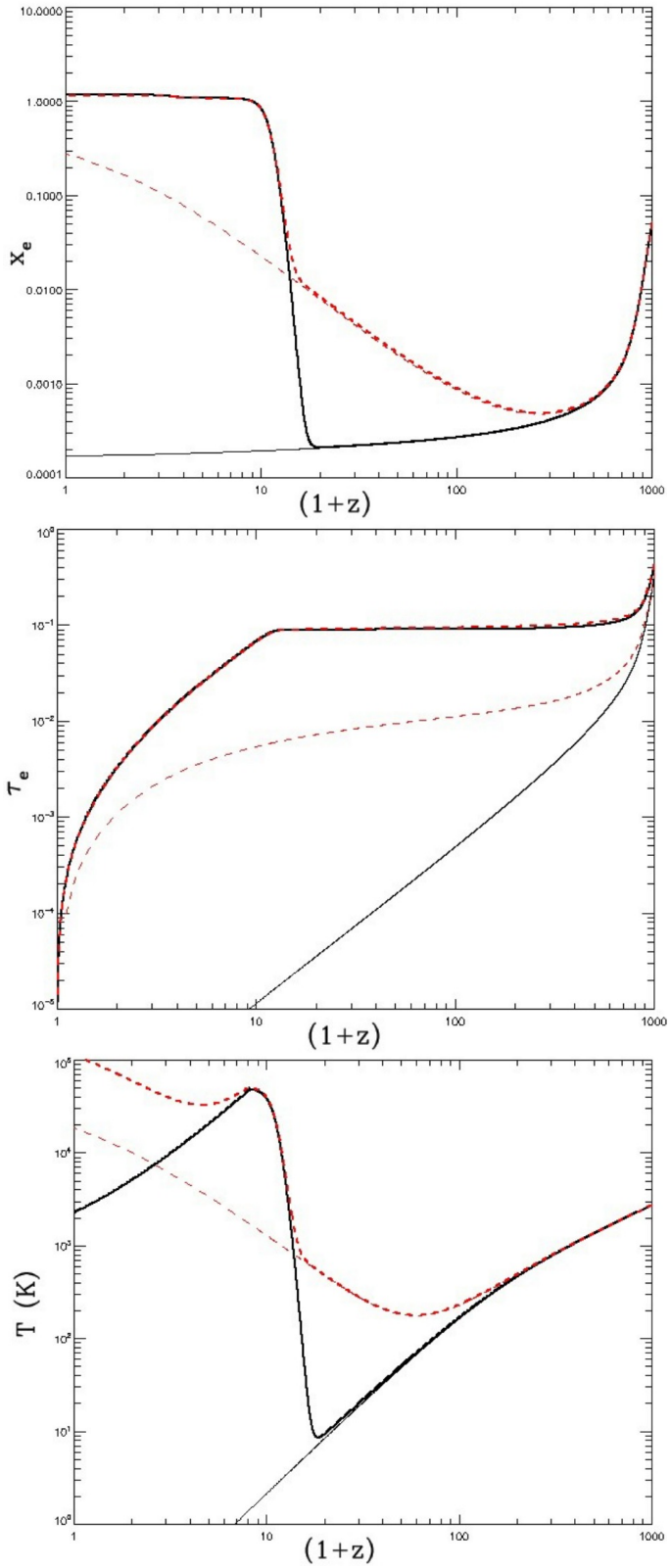

FIGURE 5.4: Ionised fraction (top), optical depth (middle) and IGM temperature as a function of redshift, in a scenario without any reionisation (thin black line), with a step-like reionisation only (thick black), and the same two scenarii with the addition of the decay of LDM particles (thin and thick red).

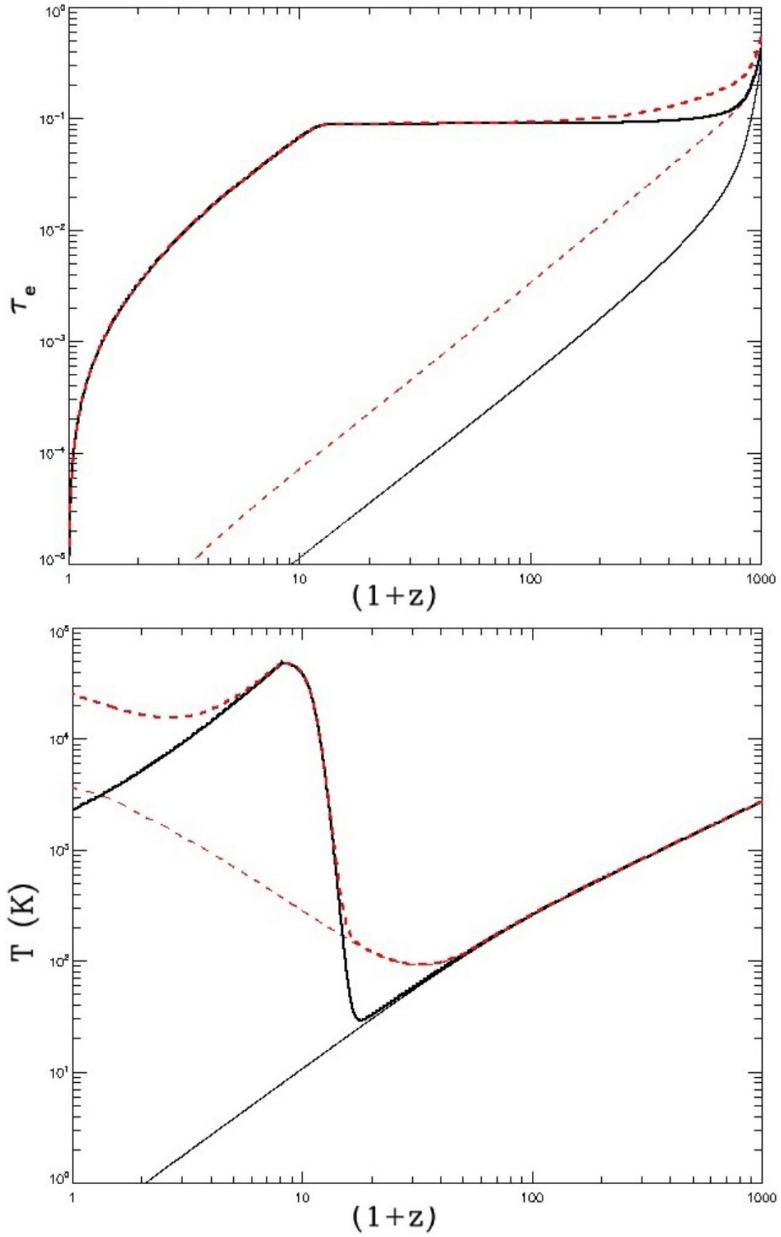

FIGURE 5.5: Same legend as Fig. 5.4 for the optical depth and IGM temperature in the context of the addition of annihilation of hDM particles.

5.2.5 Effects on the CMB spectrum

The first effect that is dependent on the reionisation history is a deviation of the spectral energy distribution of the CMB from a perfect black body spectrum. This deviation is caused by the sum of interactions between free electrons and CMB photons along their paths; it can be quantified by the Compton parameter y, defined as:

$$y = \frac{\sigma_T k_B}{m_e c^2} \int_{z=0}^{z=1100} \frac{x_e(z) n_b(z)}{(1+z)H(z)} (T_{\rm mat} - T_\gamma) dz \tag{5.18}$$

using the same notations as previous equations. The current constraints on this parameter are only in the form of an upper bound found to be around 2.5×10^{-5} by the FIRAS instrument of the COBE satellite (Mather et al., 1994). This is a useful parameter for eliminating models that may predict a too large modification of the CMB spectrum. In my case, among all the reionisation models that I tested, the maximum value of y that I found was equal to 10^{-7}. Although it does not validate these models, it is still a viability criterium for these theories.

As mentioned earlier, the reionisation history has a direct effect on the power spectrum of the CMB anisotropies. Some of our models did have a somewhat significant impact on the ionisation fraction, with respect to the value due to relic electrons, already at high redshift. This fact should therefore leave some imprint on the CMB spectrum. To check whether these effects are measurable, I simulated the expected CMB spectrum in the case we take into account DM decays. This has been done by implementing our modified version of RECFAST in the cosmological code CAMB that I already mentioned in the previous chapters.

Fig. 5.6 shows the temperature-temperature (TT), temperature-polarisation (TE) and polarisation-polarisation (EE) spectra, in the case of 10 MeV decaying LDM (i.e. the particle for which we obtained the maximum contribution to the reionisation among the considered cases), compared with the results of the WMAP 3 mission. In all cases, the contribution due to DM decays alone is negligible: their effect is tiny and concentrated at low multipoles. Knowing that there existed other sources of reionisation besides DM decays, their influence on the CMB is indistinguishable from a scenario without any DM.

Because 10 MeV LDM particles produce the highest ionisation fraction among the considered models, the effects on the CMB spectra due to other species of DM particles will be far more negligible. One the other end, we remember from the previous section the promises shown by the impact of DM particles on the IGM temperature: the clear influence of DM there made me reconsider my approach. In the light of this results, it would be wise to tackle the problem from a different angle, maybe using the temperature of the IGM as a way to detect and constrain the presence of DM through it heating of the medium: the purpose of the last section of this chapter.

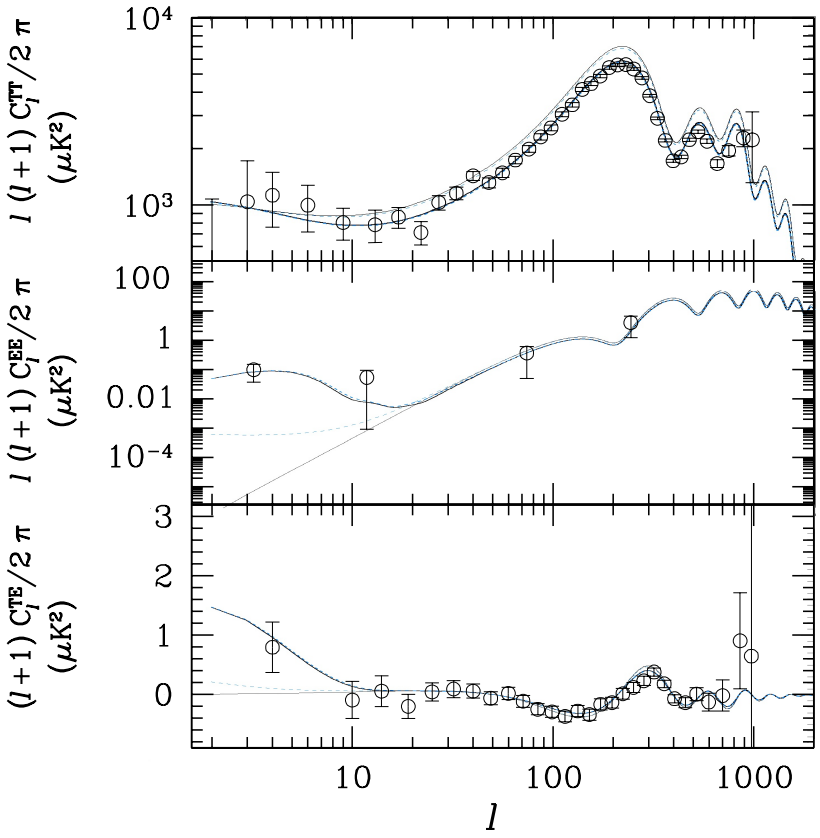

FIGURE 5.6: Temperature-temperature (top panel), polarisation-polarisation (central panel) and temperature-polarisation (bottom panel) spectra. Thick lines indicate the CMB spectrum derived assuming the WMAP 3 value of the Thomson optical depth $\tau_e \sim 0.09$ and a step-like reionisation model (consistent with the 3-year WMAP data); thin lines indicate the CMB spectrum derived assuming no reionisation. Dashed (solid) lines indicate the CMB spectrum obtained (without) taking into account the decays of 10 MeV LDM particles. The two thick lines, solid and dashed, appear superimposed, because the contribution of decaying particles (the dashed line) is completely hidden by the stronger effect of a sudden reionisation. Open circles in all the panels indicate the WMAP 3 data.

5.3 Constraints on Dark Matter from the temperature of the IGM

The potential of the IGM temperature for constraining DM models is very promising, as shown in the results that I mentioned previously. However, no matter how encouraging it looks, this particular method – just as any other one – will require robust and precise measurements of the IGM temparature to compare our predictions to.

5.3.1 Probing the IGM temperature evolution

Due to its low density, the intergalactic medium cooling time is long and retains some memory of when and how it was last heated. Hence, measuring the IGM temperature at a certain redshift (typically up to $z \sim 6$) allows us to reconstruct, under certain assumptions, its thermal history up to the reionisation phase where the IGM has been substantially heated.

Such measurements have been carried out by a number of authors: they are obtained using high resolution data of the forest of intergalactic Lyman α absorption lines observed in the spectra of bright quasars. Indeed, the widths of these Lyman α absorption lines are sensitive to the temperature of the IGM through a combination of thermal (Doppler) broadening and pressure (Jeans) smoothing of the underlying gas distribution (e.g. Haehnelt and Steinmetz, 1998, Peeples et al., 2010), in addition to broadening from peculiar motions and the Hubble flow (e.g. Hernquist et al., 1996, Theuns et al., 2000). Consequently, using a statistics sensitive to the thermal broadening kernel combined with an accurate model for measurement calibration (typically high-resolution hydrodynamical simulations of the IGM), various authors have placed constraints on the thermal evolution of the IGM. In my work, I used the recent measurements of the IGM temperature by Becker et al. (2011), Bolton et al. (2012) and Garzilli et al. (2012) alongside earlier, less constraining IGM temperature data (Ricotti et al., 2000, Schaye et al., 2000, Zaldarriaga et al., 2001).

5.3.2 Refining the reionisation model

In the previous section of this chapter, I illustrated how the impact of Dark Matter can be clearly seen in the history of the IGM temperature. Since measurements of this temperature are available, a simple comparison of this data with the evolution predicted by my previous calculations should be enough to validate or exclude the various DM models considered. However, I was faced with an additional difficulty: indeed, the aforementioned measurements only constrain the IGM temperature in a range of redshifts comprised between $z \sim 0$ and $z \sim 6$, with most of the data in $z \sim [2, 4.5]$. The reason why this is problematic is that this period overlaps a particular phase that is poorly constrained, namely the second ionisation of helium (briefly mentioned in Sec. 5.1.2).

Indeed, in the current picture for the evolution of the baryons, there are thought to be two reionisation events which turned the neutral gas in the IGM into an completely ionised medium. The first reionisation event that I already discussed happened where

neutral hydrogen and neutral helium were ionised by early galaxies. The second reionisation event is expected instead to have been driven by quasars at lower redshifts, which produce a hard ionising spectrum that can reionise singly ionised helium into HeIII by $z \sim 3$ (Furlanetto and Oh, 2008, Madau et al., 1999, McQuinn et al., 2009).

As a consequence, we expect naturally that photo-heating during both of these reionisation events leaves a "footprint" on the thermal state of the IGM, while I only considered and implemented the first one in the numerical code that I described in the previous section. To rectify this caveat, I added another "step-like" increase in temperature and ionised fraction, similar to the the previous reionisation event. However, as this second event is much less constrained, I did not fix the characteristics of this step, and ended up with three new free parameters: the redshift and width of the HeII ionisation, and the amplitude of the IGM temperature boost. In order to limit the number of free parameters in my model, I fixed the amplitude (at $\sim 2.5 \times 10^4$ K) of the first temperature boost associated to the reionisation of hydrogen, justified by related works in the literature (cf. Valageas and Silk, 1999,Hui and Haiman, 2003). It should be noted that adding the HeII temperature step does result in a more rigorous modelling of the reionisation history, but this additional freedom may introduce some degeneracies with the DM parameters.

As a last sophistication, I also included an additional heating term in the evolution of the IGM temperature after the first reionisation event: in addition to the processes already considered – the adiabatic cooling of matter, its interaction with CMB photons, and the impact of DM – I added the contribution of the photo-heating due to the ionising background of sources (see Bolton et al., 2009, for details), as the population of objects that appeared during the Dark Ages and the EoR (the first stars, galaxies and quasars) are logically expected to have had an influence during the entire duration of the reionisation.

5.3.3 Setting up the framework

With this completed model, I focused back on the use of data for constraining DM models. Exploring the possible DM models "by hand" and comparing each time their prediction with the available data would have been very fastidious, time-consuming and not representative. After compiling all the measurements of the IGM temperature, I therefore devised a protocol based on an MCMC analysis of the parameter space of my model, which I limited to five parameters:

- Two parameters for the Dark Matter, considering the same models as in the previous section: the mass m_{LDM} and the life-time τ_{LDM} for Light DM decay models,

and the mass m_{hDM} and annihilation cross-section σ_{hDM} for annihilating Heavy DM models. I ran several MC chains and derived constraints for both models separately;

- Three parameters for the less-constrained second reionisation of helium, already mentioned in the previous section: its redshift $z^{\rm He}_{\rm reion}$ and width $\Delta z^{\rm He}_{\rm reion}$, and the amplitude of the IGM temperature boost $\Delta T^{\rm He}_{\rm reion}$.

The rest of the parameters of the reionisation parameters are fixed, namely here the redshift of the HI/HeI ionisation (taken to be $z = 10.4$, the WMAP7 best-fit value) and the amplitude of its temperature boost chosen to be $\Delta T = 2.5 \times 10^4$K. Finally, since the heating induced by DM prior to the HI/HeI reionisation is washed out by astrophysical sources (and inaccessible by our datasets), I thus switched on that DM contribution only for redshift lower than the end of the first reionisation ($z \sim 10$).

5.3.4 Results and discussion

I present here the results of this analysis, although it should be kept in mind that these are still work in progress. Using the combined data of several MCMC runs, I show here first in Fig. 5.7 the evolution of the IGM temperature as predicted by the LDM and hDM models of Sec. 5.2.2 with the best-fit parameters of each model, i.e. the sets of parameters that give the best agreement between the model and the data measurements – also included in the graph.

Once again, the contrast between the impact of both DM models can be seen here: the hDM annihilations tend to have a more pronounced influence at earlier times when the matter density – and consequently the annihilation rate – was higher. On the other hand, their impact at low redshifts is much less visible than in the case of LDM decays, whose rate does not depend on density and is not affected by the expansion of the Universe. For intermediate redshifts, around the second reionisation of helium, the two models are not significantly different: as a consequence, the most extreme points of data (in terms of redshift) will have a particular importance in our analysis.

When comparing the χ^2 of both best-fit models with respect to the data points, we find a slight advantage for the LDM model (both models have a χ^2 around 60): the relative matching of the two with respect to the data is indeed balanced as the hDM model fits more tightly the points at the lowest redshifts, while the LDM model performs better at higher z. However, it should be noted that both DM models are actually quite bad fits to the data (having reduced χ^2 approaching 2), although the models themselves are not entirely to blame. Indeed, a quick look at the data points used here shows some

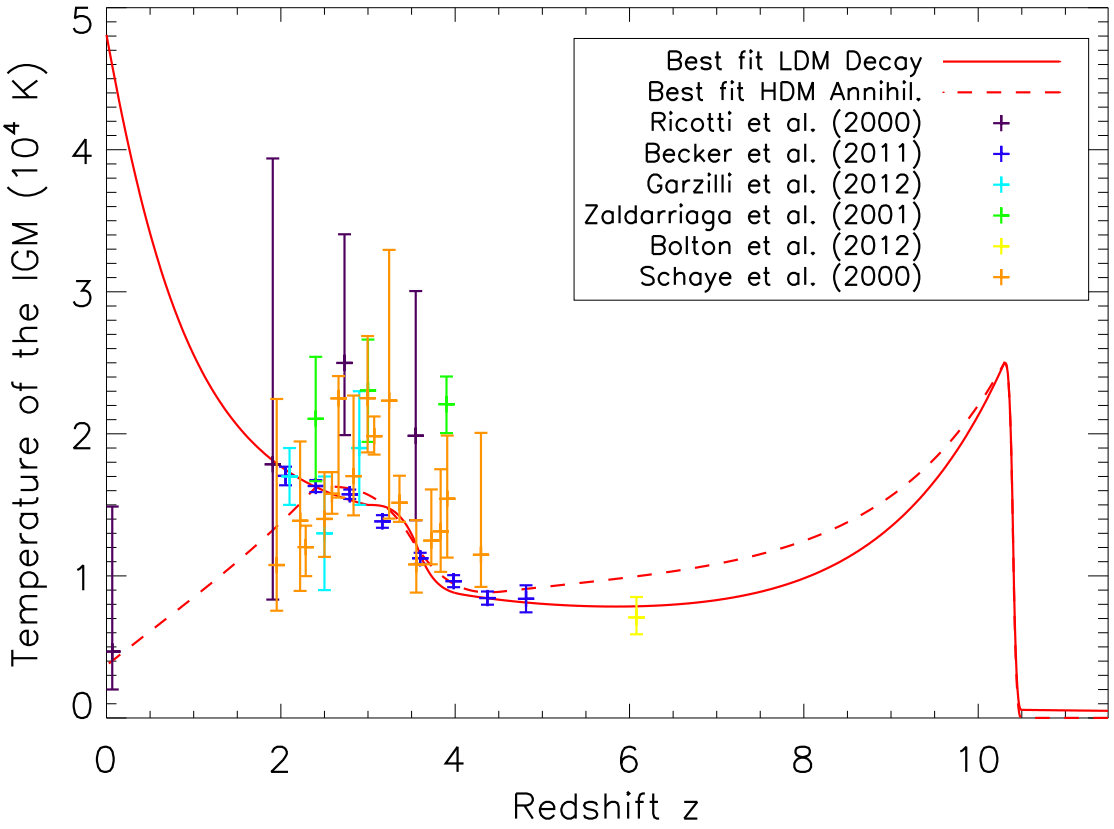

FIGURE 5.7: Evolution of the IGM temperature as predicted by the best fit models for the LDM decay (solid line) and for hDM annihilation (dashed) when compared to the data points of various work of the literature (crosses of various colours).

contradictions between the values of the IGM temperature obtained by the various studies, over the same range of redshifts (e.g. the difference between the Zaldarriaga et al. 2001 and Becker et al. 2011 points). These discrepancies may be due to a difference in the quality of the source data used to derive these temperatures, as the most recent works (Becker et al., 2011, Bolton et al., 2012, Garzilli et al., 2012) seem to have more coherent and tighter constraints. We can actually already witness in Fig. 5.7 that the best fits are strongly driven by these points, especially those of Becker et al. (2011). A possibility for a future revision of this work would be to discard some of the oldest datasets to keep only the (seemingly) most robust ones. Another important test would be to compare the previous χ^2 (from the DM models) to the value of the χ^2 yielded by a simple model without any influence of DM,[2] to see how it fares against the data and to show if the inclusion of DM is really necessary. Moving on to the rest of the analysis, the results of the MCMC exploration for the LDM and hDM models are illustrated respectively in Fig. 5.8 and Fig. 5.9 (again, these are preliminary results of a work in progress). In both models of DM, we see that the mass of the considered DM particles remains largely unconstrained; however in the Light DM decaying case, the temperature

[2]Of course, this simple model would have two less parameters (the DM ones), i.e. two less degrees of freedom that will have to be accounted for when comparing it to the χ^2 of the DM models.

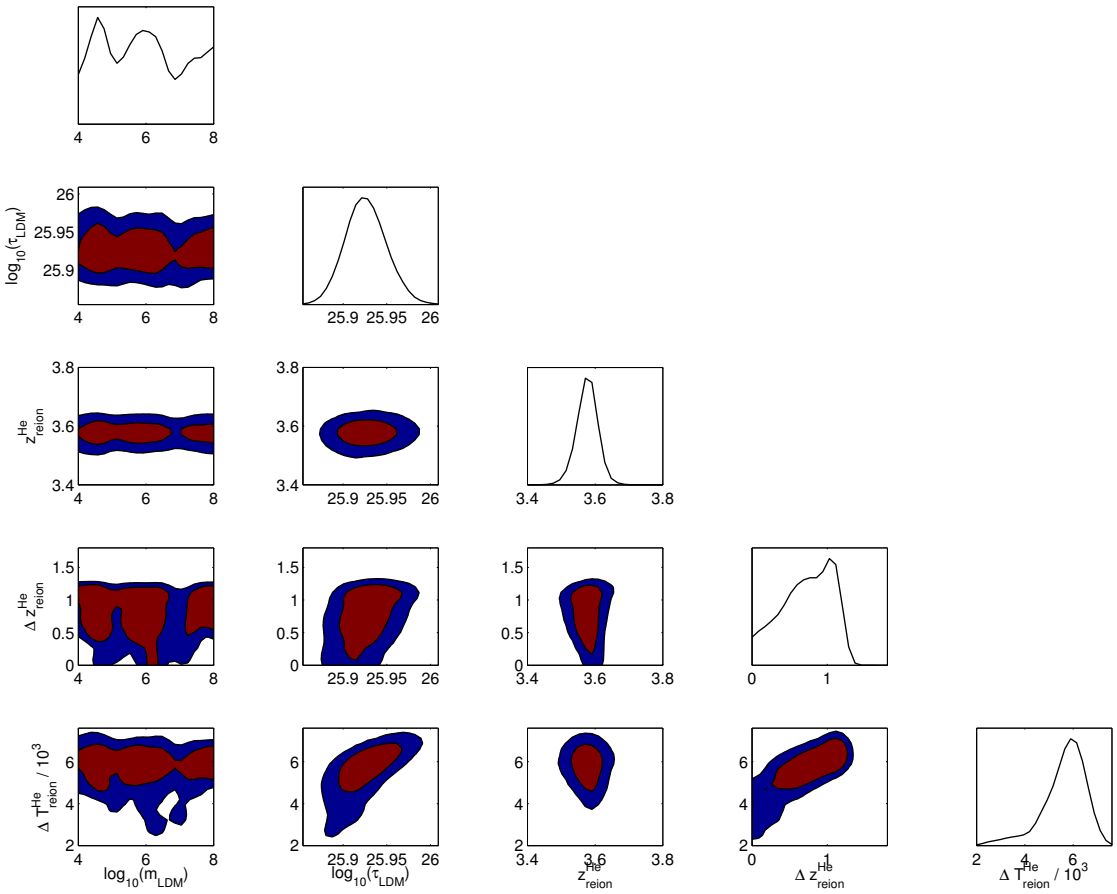

FIGURE 5.8: For LDM decay models, marginalized posterior distributions and 2-D contour plots showing the ranges of and correlations between the parameters and the 68% and 95% confidence limits. The units of m_{LDM}, τ_{LDM} and $\Delta T^{\rm He}_{\rm reion}$ are respectively eV, s, and K.

data seem to favour a tightly defined life-time around $10^{25.93}$ s, corresponding to $\sim 2.7 \times 10^9$ Gyrs. According to the same model, the reionisation of HeII is found to have preferably occurred at $z^{\rm He}_{\rm reion} \simeq 3.58$ and rapidly ($\Delta z^{\rm He}_{\rm reion} \simeq 1$). Annihilating DM models seem more compatible with an extended HeII reionisation $\Delta z^{\rm He}_{\rm reion} \simeq 2.2$ occurring slightly later ($z^{\rm He}_{\rm reion} \simeq 3.48$). However, the annihilation cross-section of hDM particles is loosely constrained. Interestingly, in both cases, the energy deposited by DM is sufficient to allow a temperature increase associated to HeII reionisation photoheating, $\Delta T^{\rm He}_{\rm reion} \simeq 6 - 7 \times 10^3$ K, slightly lower than that of theoretical estimates ($\simeq 1 - 4 \times 10^4$ K, e.g. Bolton et al., 2009) but consistent with current estimates (Becker et al., 2011). As mentioned earlier, additional work is currently underway to assess the need of a non-zero DM contribution, as only a comparison of likelihoods with and without DM will determine whether present data prefer or not the addition of this non-astrophysical source of energy. Furthermore, I am also considering and running tests with a more sophisticated (and redshift dependent) modelling of the fraction of the DM energy that goes into heating (inspired by Evoli et al., 2012, whose author I am in contact with).

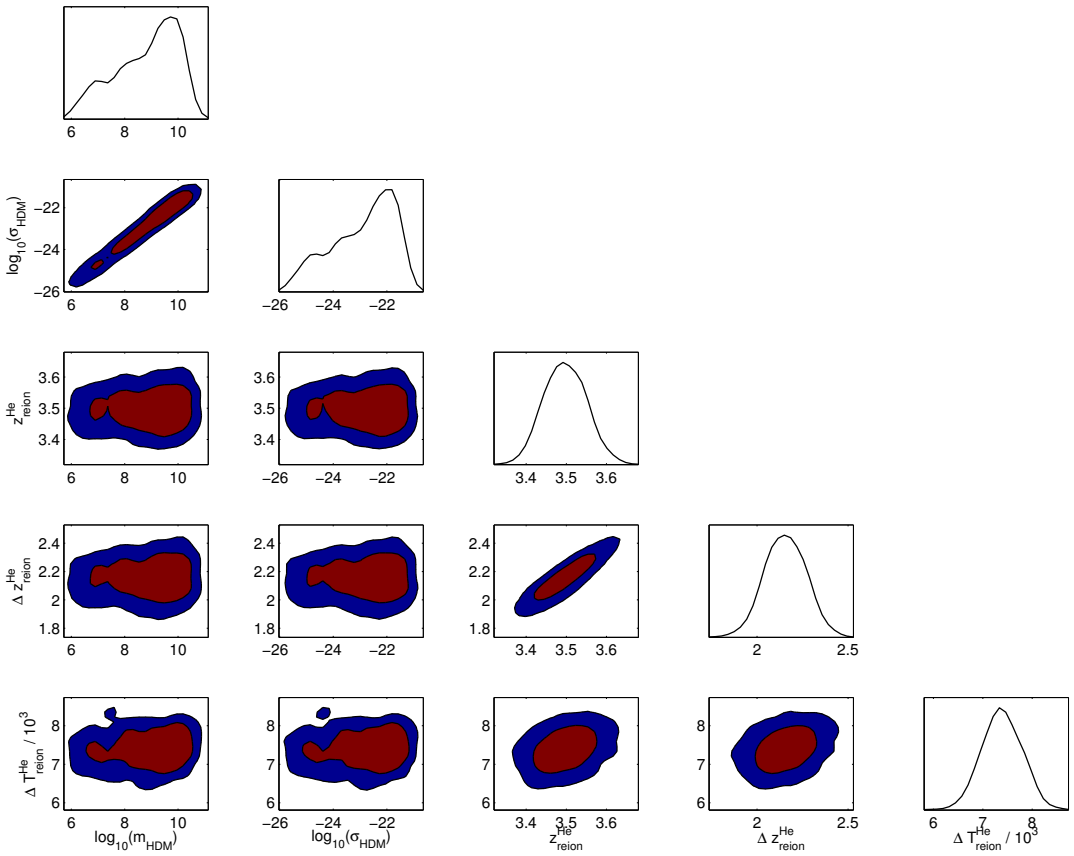

FIGURE 5.9: Similar content and legend as Fig. 5.8 in the case of hDM annihilation models. The units of m_{hDM} and σ_{hDM} are respectively eV and $cm^3.s^1$.

As an example, the energy deposition in a fully ionised medium is far from trivial and instantaneous, as the mean free path of photon becomes noticeably longer.

5.4 Related personal publications

• Ilic S., April 2012, "Updated constraints on Dark Matter from the temperature of the Intergalactic Medium", poster presented at the "Epoch of Reionization" conference in Strasbourg, France

Constraints on Dark Matter from the Temperature of the Intergalactic Medium

Stéphane Ilić, Mathieu Langer, Marian Douspis
Institut d'Astrophysique Spatiale – Université Paris Sud
stephane.ilic@ias.u-psud.fr, mathieu.langer@ias.u-psud.fr, marian.douspis@ias.u-psud.fr

Context : The elusive nature of Dark Matter

The nature of the Dark Matter is one of the crucial open questions in cosmology. At present, there are no direct nor indirect detections of DM particles yet. While many theoretical models have been proposed, we do not have any definitive knowledge of their properties. From the phenomenological point of view, one of the most interesting ways to detect them, and possibly distinguish between different models, is provided by the decay and/or the annihilation of DM particles throughout the history of the Universe. These two processes lead to the production of photons and light standard model particles at energies and rate that depend on the parent DM particle mass and on the DM density. Therefore, in principle, it is possible to distinguish among various classes of models. However, the detection of such decay or annihilation products has remained inconclusive so far, and the constraints on DM are still relatively loose.

Thermal History of the IGM

DM decays and annihilations are a source of additional energy input into the Inter-Galactic Medium. Alongside astrophysical sources, they might contribute to the ionisation, the heating and the excitation of the baryonic gas. While several works have studied those effects on the Epoch of Reionisation itself (e.g. box below), the impact on the thermal history of the IGM has been investigated to a lesser extent, focusing mostly on the thermal state before or during the reionisation of Hydrogen.
Here we revisit (Ilić et al. 2012) the impact of DM particles on the thermal history of the IGM down to low redshifts, especially those covering the second reionisation of Helium. For that purpose, we use the recent measurements of the IGM temperature by Becker et al. (2011) and Bolton et al. (2012) alongside earlier, less constraining, IGM temperature data.

Method

We performed an MCMC analysis of a five dimensional parameter space subtended by $\{z^{\rm He}_{\rm reion}, \Delta z^{\rm He}_{\rm reion}, \Delta T^{\rm He}_{\rm reion}\}$ and either $\{m_{\rm LDM}, \tau_{\rm LDM}\}$ or $\{m_{\rm HDM}, \sigma_{\rm HDM}\}$. The first three are the redshift and duration of the HeII reionisation and the IGM temperature boost it generates. The last two are either the Light DM mass and life-time (decays) or the Heavy DM mass and annihilation cross-section.
We modified the public code RECFAST (Seager et al. 1999) so as to include the ionisation and heating rates due to the DM. We modelled the simultaneous H and HeI reionisation as a step function with fixed WMAP-7 parameters, but we allowed the parameters of the HeII reionisation to vary. We also took into account the photo-heating due to the ionising background of sources (Bolton et al. 2009).

Impact of DM on the CMB

The figure below (Mapelli et al. 2006) shows simulated CMB power-spectra. Thick versus thin lines indicate that the spectra were simulated respectively with and without the inclusion of a standard step-like reionisation (consistent with the WMAP-3 data, open circles) in the model. Dashed lines indicate the CMB spectra obtained taking into account the decays of 10-MeV LDM particles. It appears that the impact of LDM decays on those spectra is completely washed out by those induced by standard reionisation of astrophysical origin. The effects of neutralino annihilations is even less noticeable.

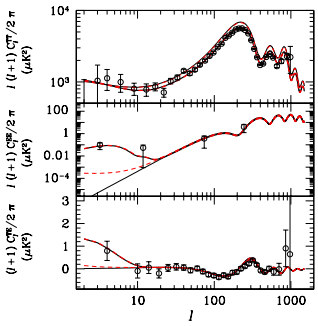

Results : Impact on IGM temperature

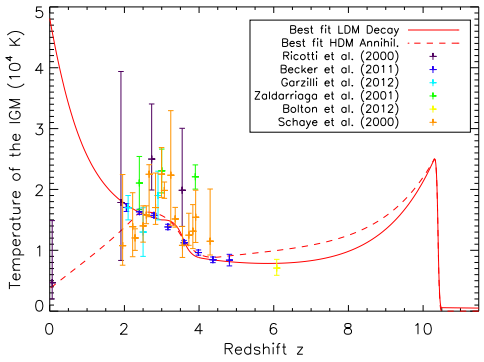

Top left : Our best fit models for the LDM decay (solid line) and for HDM annihilation (dashed). Heating induced by DM prior to H reionisation is washed out by astrophysical sources, and we thus switched off that contribution for $z > 11$.
Bottom : Marginalized posterior distributions and 2-D contour plots showing the ranges of and correlations between the parameters and the 68% and 95% confidence limits. Left: case of LDM decays; Right : case of HDM annihilations. In both cases, the DM mass is essentially unconstrained.

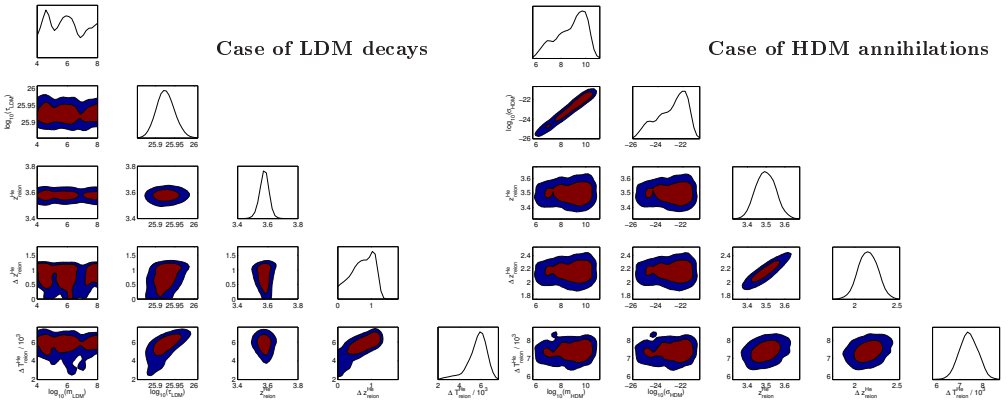

References

Becker, G. D +, 2011, MNRAS, 410, 1096
Bolton, J. S. +, 2009, MNRAS, 395, 736
Bolton, J. S. +, 2012, MNRAS, 419, 2880
Evoli, C. +, 2012, MNRAS, 422, 420
Ilić S. +, 2012, in prep.
Mapelli, M. +, 2006, MNRAS, 369, 1719
Seager S. +, 1999, ApJL, 523, 1

Discussion & Prospects

While the mass remains unconstrained in both models of DM, in the Light decaying case, the temperature data seem to favour a tightly defined life-time of 2.7×10^9 Gyrs. The reionisation of HeII occurs at $z^{\rm He}_{\rm reion} \simeq 3.58$ and rapidly ($\Delta z^{\rm He}_{\rm reion} \simeq 1$). Annihilating DM seems more compatible with an extended HeII reionisation $\Delta z^{\rm He}_{\rm reion} \simeq 2.2$ occurring slightly later ($z^{\rm He}_{\rm reion} \simeq 3.48$). Interestingly, in both cases, the energy deposited by DM is sufficient to allow a temperature increase associated to HeII reionisation photoheating, $\Delta T^{\rm He}_{\rm reion} \simeq 6 - 7 \times 10^3$ K, slightly lower than that of theoretical estimates ($\simeq 1 - 4 \times 10^4$ K, e.g. Bolton et al 2009) but consistent with current estimates (Becker et al. 2011). Additional work is being done to assess the need of a non-zero DM contribution. In the end, comparison of likelihoods with and without DM will determine whether present data prefer or not the addition of this non-astrophysical source of energy. Furthermore, we are running tests with a redshift dependent fraction of the DM energy that goes into heating (Evoli et al. 2012). All these, and more, are discussed in Ilić et al. (2012).

Chapter 6

Conclusions & perspectives

In this thesis, I explored the potential of new and innovative probes of the nature of Dark Energy, by combining large scale structure data and a late time CMB anisotropies known as the integrated Sachs-Wolfe effect. This peculiar feature can arise only in special circumstances, and in particular in the presence of Dark Energy.

In Chapter 2, I have described the cross-correlation technique between the CMB and tracers of matter commonly used to evidence the iSW effect, and shown how the measurement of this effect is a method to constrain cosmology in general and Dark Energy in particular. I insisted on the crucial rôle of the features of the galaxy surveys usually considered as such tracers. Starting from there I presented a series of tools aimed at fully exploiting the constraining power of the future large scale surveys. I extensively tested my framework on simulated data whose analysis yielded promising results. In the same chapter, I investigated the cross-correlation between the CMB and the Cosmic Infrared Background, an alternative and original tracer of the matter distribution. I studied the detectability of this correlation under various observational situations, after calculating the theoretical angular power spectrum of the CMB-CIB cross-correlation at several frequencies and for different instruments. Developing an advanced S/N analysis which included the main sources of noise, both instrumental and astrophysical, and all their possible correlations, I pointed out the most promising frequencies, and obtained very encouraging results (with significance as high as $7\,\sigma$ in the most ideal case, $sim5\,\sigma$ for more realistic scenarii) especially when compared to the current constraints from classical galaxy-CMB correlations. The results of this work will be valuable in the forthcoming years of analysis and exploitation of the *Planck* data. I actually recently started applying my formalism to CIB maps extracted from the *Planck* data at several frequencies and cleaned using data from the Parkes Galactic All-Sky Survey (GASS Kalberla et al., 2010). These resulting CIB maps currently cover approximatively 10% of the sky

and will be improved in the upcoming months by the dedicated group of the Planck Collaboration. I already managed to perform some very simple, model-independent correlation tests (in real & harmonic space) with the CMB from *Planck*. I found a positive correlation each time but with only a $\sim 1\,\sigma$ significance, assessed by confronting the results to correlations between these CIB maps and 1000 random Gaussian realisations of the CMB. Although it may seem disappointing at first, many further tests have yet to be performed on this CIB data, as it will be progressively improved in the near future. Techniques need to be developed to reduce the contamination from dust, in particular to account for the spatial variations of its properties (e.g. its spectral index). When the data will be clean enough, an interesting prospect would be to use the multiple observed frequencies of the CIB to reconstruct the contributions from different redshift bands, in order to obtain several decorrelated CIB maps corresponding to these redshift slices. The resulting independent CIB maps could then be individually correlated with the CMB, with the promise of a signal with even higher significance.

I took quite a different approach to the iSW effect and its detection in Chapter 3, namely through the impact that individual structures in the Universe should have on the CMB temperature. I first revisited the stacking of structures in CMB maps of a previous work by Granett et al. (2008) which claimed a very significant signal, at odds with ΛCDM predictions. I thereby devised a new complete protocol for the stacking procedure, from a careful choice of maps to a rigorous estimation of the significance. Although I did not find any strong difference, my tools allowed me to discover some peculiar features in these results. I then extended the analysis to two more recent and consequent void catalogues, one of whom (Sutter et al., 2012) hinted at significant signals (although not as strong as the previous Gr08 results) with a preferred scale in the signal ($\sim$ half the mean size of the voids used in the stacking). The amplitude and scale of this signal were more coherent with our expectations about the iSW effect compared to the Gr08 results and their peculiarities. As an important note, I also discussed extensively the robustness of the detection and the validity of the catalogues of structures used. One of the main conclusions of my work is that, in regard to all the results that I obtained and the objects and catalogues studied, it would be premature to either claim a detection of an iSW-like signal and/or claim an oddity with respect to ΛCDM. The oddity in question may very well be found in the data itself, especially in the case of the Gr08 catalogue and its odd inconsistencies. In parallel, as a member of the Core Team of the HFI Planck Collaboration, I undertook the task of reiterating the stacking analysis on the Gr08 and other catalogues with the new Planck data, and I led the corresponding section of the paper released in March 2013 along with the other cosmological papers. In the upcoming years, I intend to extend the exploration of the stacking methods using the upcoming catalogues that will be derived from the next generation of galaxy

surveys; not only for the iSW detection, but also for further cosmological studies, such as Alcock-Paczynski test, another promising probe of DE, based on the measurement of void shapes in surveys. As another objective, I plan to personally undertake all the steps of a stacking study, and in particular the identification of structures inside a survey using cluster and void finding algorithms, which would give me a unique insight on some of the interrogations that arose during my previous analyses, as well as on possible improvements.

Directly along the lines of some of the results and questions that arose from the stacking analysis, I decided that it is necessary to reconsider and revise the intuitions one can have about the iSW effect and its relation to the properties of the structures that generate it. Requiring an accurate prediction of the impact of such objects on the CMB temperature, I worked extensively on a theoretical framework (presented in Chapter 4) to predict the thermal impact in the CMB of individual structures, based on the modelling of each structure as a spherical object with the use of the LTB metric. I was able to reproduce all the physical characteristics of the Gr08 structures and derive the temperature profile of their full (not only linear) theoretical iSW effect. Although I found that the predicted mean shift in temperature was comparable to the level measured with the Gr08 void sample, I also discovered several discrepancies, most notably concerning the relative contribution of each void in the sample and the impossibility to reproduce a peculiar hot ring observed in the stacking of the actual Gr08 voids. I also derived many interesting results from a more general exploration of my LTB framework, from which I gained a valuable insight on the relations between the void characteristics and its resulting iSW signature. My framework can be now applied to any possible case and be used from now on as a benchmark for computing the expected iSW signal produced by a structure. As a work in progress, I intend to refine and extend this analysis very soon to the other catalogues of voids mentioned in Chapter 3. In the longer term, I plan to go further by relaxing the assumptions of spherical symmetry and consider axisymmetric dust solutions, possibly including pressure effects. This would be a necessary step towards accurate predictions for existing structures in the Universe, and their use for constraining cosmological models, as it allows for a much better account of the geometries (often ellipsoidal) of these objects.

In parallel to all these works dedicated to the study of the iSW effect, I also turned to an other type of cosmological information encoded in the large scale structure of the Universe. In the fifth and final chapter of my thesis, I discussed a part of my Ph.D. work that I dedicated to the study of the epoch of reionisation – or rather, to the study of Dark Matter trough its potential influence on the EoR. Indeed, I investigated the possible contribution from the annihilation and decay of DM particles to the reionisation history, studying several models of DM particles of various masses and cross-sections. I

focused mainly on their impacts on the temperature of the IGM before, during and after reionisation, taking great care in studying and modelling the energy deposition of these particles, considering all the possible mechanisms and associated efficiencies. I then compiled all the recent measurements of the IGM temperature and confronted them to my theoretical predictions. Using MCMC simulations, I computed constraints on the properties of several chosen flagship DM models allowed by the data. The preliminary results of this work in progress are promising, both in themselves and also when combined with other DM constraints where they might break degeneracies. This is however not the only work that I am currently conducting on the EoR. In the context of CMB experiments, only a few cosmological parameters are extracted from the data with the use of current numerical codes. These assume a fairly simple step-like modelling of the reionisation history (mentioned in Chapter 5) that I found to be too crude, especially with the advent of more precise CMB experiments. I therefore set out to develop a new, more complete parametrisation of the reionisation history, which can account for a broader range of scenarii: as a notable example, a two-stage, asymmetrical reionisation which are relevant in terms of the physics of the processes involved at that epoch. I developed and I started apply my new parametrisation in the context of the *Planck* Reionisation Working Group; the results of this ongoing work will contribute to the next release of *Planck* papers scheduled in the next few months.

To conclude, the work presented in my thesis can be summarised as a series of very encouraging successes to better probe and understand some of the most fundamental properties of the Universe through the observations of its large scale structure and the secondary anisotropies created in the cosmic microwave background.

Bibliography

J. K. Adelman-McCarthy, et al. The Sixth Data Release of the Sloan Digital Sky Survey. ApJS, 175:297–313, April 2008. doi: 10.1086/524984.

N. Afshordi. Integrated Sachs-Wolfe effect in cross-correlation: The observer's manual. Phys. Rev. D, 70(8):083536, October 2004. doi: 10.1103/PhysRevD.70.083536.

N. Aghanim, S. Majumdar, and J. Silk. Secondary anisotropies of the CMB. *Reports on Progress in Physics*, 71(6):066902, June 2008. doi: 10.1088/0034-4885/71/6/066902.

M. A. Agüeros, et al. Candidate Isolated Neutron Stars and Other Optically Blank X-Ray Fields Identified from the ROSAT All-Sky and Sloan Digital Sky Surveys. *AJ*, 131:1740–1749, March 2006. doi: 10.1086/500049.

H. Aihara, et al. The Eighth Data Release of the Sloan Digital Sky Survey: First Data from SDSS-III. ApJS, 193:29, April 2011. doi: 10.1088/0067-0049/193/2/29.

R. A. Alpher, H. Bethe, and G. Gamow. The Origin of Chemical Elements. *Physical Review*, 73:803–804, April 1948. doi: 10.1103/PhysRev.73.803.

L. Amendola and S. Tsujikawa. *Dark Energy: Theory and Observations*. Cambridge University Press, 2010.

C. Baccigalupi, L. Amendola, and F. Occhionero. Imprints of primordial voids on the cosmic microwave background. MNRAS, 288:387–396, June 1997.

G. D. Becker, J. S. Bolton, M. G. Haehnelt, and W. L. W. Sargent. Detection of extended He II reionization in the temperature evolution of the intergalactic medium. MNRAS, 410:1096–1112, January 2011. doi: 10.1111/j.1365-2966.2010.17507.x.

C. L. Bennett, G. F. Smoot, and A. Kogut. COBE DMR Maps of the Microwave Sky. In *Bulletin of the American Astronomical Society*, volume 22 of *Bulletin of the American Astronomical Society*, page 1336, September 1990.

C. L. Bennett, et al. Seven-year Wilkinson Microwave Anisotropy Probe (WMAP) Observations: Are There Cosmic Microwave Background Anomalies? ApJS, 192:17, February 2011. doi: 10.1088/0067-0049/192/2/17.

C. L. Bennett, et al. Nine-Year Wilkinson Microwave Anisotropy Probe (WMAP) Observations: Final Maps and Results. *ArXiv e-prints*, December 2012.

E. Bertschinger. Cosmological dynamics. *NASA STI/Recon Technical Report N*, 96: 22249, January 1995.

M. Béthermin, H. Dole, G. Lagache, D. Le Borgne, and A. Penin. Modeling the evolution of infrared galaxies: a parametric backward evolution model. *A&A*, 529:A4, May 2011. doi: 10.1051/0004-6361/201015841.

M. Béthermin, et al. A Unified Empirical Model for Infrared Galaxy Counts Based on the Observed Physical Evolution of Distant Galaxies. *ApJ*, 757:L23, October 2012. doi: 10.1088/2041-8205/757/2/L23.

P. L. Biermann, H. J. de Vega, and N. G. Sanchez. Towards the Chalonge Meudon Workshop 2013. Highlights and Conclusions of the Chalonge Meudon workshop 2012: warm dark matter galaxy formation in agreement with observations. *ArXiv e-prints*, May 2013.

T. Biswas, R. Mansouri, and A. Notari. Non-linear structure formation and 'apparent' acceleration: an investigation. JCAP, 12:017, December 2007. doi: 10.1088/1475-7516/2007/12/017.

T. Biswas, A. Notari, and W. Valkenburg. Testing the void against cosmological data: fitting CMB, BAO, SN and H_0. JCAP, 11:030, November 2010. doi: 10.1088/1475-7516/2010/11/030.

M. Blanton, R. Cen, J. P. Ostriker, and M. A. Strauss. The Physical Origin of Scale-dependent Bias in Cosmological Simulations. ApJ, 522:590–603, September 1999. doi: 10.1086/307660.

C. Bœhm, P. Fayet, and R. Schaeffer. Constraining dark matter candidates from structure formation. *Physics Letters B*, 518:8–14, October 2001. doi: 10.1016/S0370-2693(01)01060-7.

E. Boldt. The cosmic X-ray background. *Phys. Rep.*, 146:215–257, 1987. doi: 10.1016/0370-1573(87)90108-6.

J. S. Bolton, S. P. Oh, and S. R. Furlanetto. Photoheating and the fate of hard photons during the reionization of HeII by quasars. MNRAS, 395:736–752, May 2009. doi: 10.1111/j.1365-2966.2009.14597.x.

J. S. Bolton, et al. Improved measurements of the intergalactic medium temperature around quasars: possible evidence for the initial stages of He II reionization at z $\sim$ 6. MNRAS, 419:2880–2892, February 2012. doi: 10.1111/j.1365-2966.2011.19929.x.

H. Bondi. Spherically symmetrical models in general relativity. MNRAS, 107:410, 1947.

P. Bull, T. Clifton, and P. G. Ferreira. Kinematic Sunyaev-Zel'dovich effect as a test of general radial inhomogeneity in Lemaître-Tolman-Bondi cosmology. Phys. Rev. D, 85(2):024002, January 2012. doi: 10.1103/PhysRevD.85.024002.

Y.-C. Cai, M. C. Neyrinck, I. Szapudi, S. Cole, and C. S. Frenk. A Detection of the Cold Imprint of Voids on the Microwave Background Radiation. *ArXiv:1301.6136*, January 2013.

M.-N. Célérier. Do we really see a cosmological constant in the supernovae data? *A&A*, 353:63–71, January 2000.

X. Chen and M. Kamionkowski. Particle decays during the cosmic dark ages. Phys. Rev. D, 70(4):043502, August 2004. doi: 10.1103/PhysRevD.70.043502.

T. R. Choudhury and A. Ferrara. Updating reionization scenarios after recent data. MNRAS, 371:L55–L59, September 2006. doi: 10.1111/j.1745-3933.2006.00207.x.

L. Chuzhoy. Impact of Dark Matter Annihilation on the High-Redshift Intergalactic Medium. *ApJ*, 679:L65–L68, June 2008. doi: 10.1086/589504.

C. Clarkson and M. Regis. The cosmic microwave background in an inhomogeneous universe. JCAP, 2:013, February 2011. doi: 10.1088/1475-7516/2011/02/013.

J. J. Condon, et al. The NRAO VLA Sky Survey. *AJ*, 115:1693–1716, May 1998. doi: 10.1086/300337.

A. Cooray and R. Sheth. Halo models of large scale structure. *Phys. Rep.*, 372:1–129, December 2002. doi: 10.1016/S0370-1573(02)00276-4.

P.-S. Corasaniti, T. Giannantonio, and A. Melchiorri. Constraining dark energy with cross-correlated CMB and large scale structure data. Phys. Rev. D, 71(12):123521, June 2005. doi: 10.1103/PhysRevD.71.123521.

R. G. Crittenden and N. Turok. Looking for a Cosmological Constant with the Rees-Sciama Effect. *Physical Review Letters*, 76:575–578, January 1996. doi: 10.1103/PhysRevLett.76.575.

Georges Darmois. *Les équations de la gravitation einsteinienne*. Gauthier-Villars, 1927. URL http://eudml.org/doc/192556.

R. H. Dicke, P. J. E. Peebles, P. G. Roll, and D. T. Wilkinson. Cosmic Black-Body Radiation. ApJ, 142:414–419, July 1965. doi: 10.1086/148306.

S. Dodelson. *Modern cosmology*. Academic Press, 2003.

M. Douspis, P. G. Castro, C. Caprini, and N. Aghanim. Optimising large galaxy surveys for ISW detection. *A&A*, 485:395–401, July 2008. doi: 10.1051/0004-6361:200809499.

F.-X. Dupé, A. Rassat, J.-L. Starck, and M. J. Fadili. Measuring the integrated Sachs-Wolfe effect. *A&A*, 534:A51, October 2011. doi: 10.1051/0004-6361/201015893.

R. Durrer. Cosmological Perturbation Theory. In E. Papantonopoulos, editor, *Lecture Notes in Physics, Berlin Springer Verlag*, volume 653 of *Lecture Notes in Physics, Berlin Springer Verlag*, page 31, 2004. doi: 10.1007/b99562.

G. Dvali, G. Gabadadze, and M. Porrati. 4D gravity on a brane in 5D Minkowski space. *Physics Letters B*, 485:208–214, July 2000. doi: 10.1016/S0370-2693(00)00669-9.

D. J. Eisenstein, et al. Spectroscopic Target Selection for the Sloan Digital Sky Survey: The Luminous Red Galaxy Sample. *AJ*, 122:2267–2280, November 2001. doi: 10.1086/323717.

D. J. Eisenstein, et al. Detection of the Baryon Acoustic Peak in the Large-Scale Correlation Function of SDSS Luminous Red Galaxies. ApJ, 633:560–574, November 2005. doi: 10.1086/466512.

K. Enqvist. Lemaitre Tolman Bondi model and accelerating expansion. *General Relativity and Gravitation*, 40:451–466, February 2008. doi: 10.1007/s10714-007-0553-9.

C. Evoli, M. Valdés, A. Ferrara, and N. Yoshida. Energy deposition by weakly interacting massive particles: a comprehensive study. MNRAS, 422:420–433, May 2012. doi: 10.1111/j.1365-2966.2012.20624.x.

X. Fan, et al. A Survey of z¿5.7 Quasars in the Sloan Digital Sky Survey. II. Discovery of Three Additional Quasars at z¿6. *AJ*, 125:1649–1659, April 2003. doi: 10.1086/368246.

X. Fan, et al. A Survey of z¿5.7 Quasars in the Sloan Digital Sky Survey. IV. Discovery of Seven Additional Quasars. *AJ*, 131:1203–1209, March 2006. doi: 10.1086/500296.

S. February, J. Larena, M. Smith, and C. Clarkson. Rendering dark energy void. MNRAS, 405:2231–2242, July 2010. doi: 10.1111/j.1365-2966.2010.16627.x.

D. J. Fixsen. The Temperature of the Cosmic Microwave Background. ApJ, 707:916–920, December 2009. doi: 10.1088/0004-637X/707/2/916.

S. Flender, S. Hotchkiss, and S. Nadathur. The stacked ISW signal of rare superstructures in ΛCDM. JCAP, 2:013, February 2013. doi: 10.1088/1475-7516/2013/02/013.

S. R. Furlanetto and S. P. Oh. The History and Morphology of Helium Reionization. ApJ, 681:1–17, July 2008. doi: 10.1086/588546.

J. Garriga, L. Pogosian, and T. Vachaspati. Forecasting cosmic doomsday from CMB-LSS cross-correlations. Phys. Rev. D, 69(6):063511, March 2004. doi: 10.1103/PhysRevD.69.063511.

A. Garzilli, J. S. Bolton, T.-S. Kim, S. Leach, and M. Viel. The intergalactic medium thermal history at redshift z = 1.7-3.2 from the Lyα forest: a comparison of measurements using wavelets and the flux distribution. MNRAS, 424:1723–1736, August 2012. doi: 10.1111/j.1365-2966.2012.21223.x.

T. Giannantonio, et al. Combined analysis of the integrated Sachs-Wolfe effect and cosmological implications. Phys. Rev. D, 77(12):123520, June 2008. doi: 10.1103/PhysRevD.77.123520.

T. Giannantonio, R. Crittenden, R. Nichol, and A. J. Ross. The significance of the integrated Sachs-Wolfe effect revisited. MNRAS, 426:2581–2599, November 2012. doi: 10.1111/j.1365-2966.2012.21896.x.

K. M. Górski, et al. HEALPix: A Framework for High-Resolution Discretization and Fast Analysis of Data Distributed on the Sphere. ApJ, 622:759–771, April 2005. doi: 10.1086/427976.

B. R. Granett, M. C. Neyrinck, and I. Szapudi. An Imprint of Superstructures on the Microwave Background due to the Integrated Sachs-Wolfe Effect. *ApJ*, 683:L99–L102, August 2008. doi: 10.1086/591670.

J. E. Gunn and B. A. Peterson. On the Density of Neutral Hydrogen in Intergalactic Space. ApJ, 142:1633–1641, November 1965. doi: 10.1086/148444.

M. G. Haehnelt and M. Steinmetz. Probing the thermal history of the intergalactic medium with Lyalpha absorption lines. MNRAS, 298:L21–L24, July 1998. doi: 10.1046/j.1365-8711.1998.01879.x.

C. Hernández-Monteagudo and R. E. Smith. On the signature of nearby superclusters and voids in the Integrated Sachs-Wolfe effect. *ArXiv:1212.1174*, December 2012.

C. Hernández-Monteagudo, et al. The SDSS-III Baryonic Oscillation Spectroscopic Survey: Constraints on the Integrated Sachs Wolfe effect. *ArXiv e-prints*, March 2013a.

C. Hernández-Monteagudo, et al. The SDSS-III Baryonic Oscillation Spectroscopic Survey: Constraints on the Integrated Sachs Wolfe effect. *ArXiv:1303.4302*, March 2013b.

L. Hernquist, N. Katz, D. H. Weinberg, and J. Miralda-Escudé. The Lyman-Alpha Forest in the Cold Dark Matter Model. *ApJ*, 457:L51, February 1996. doi: 10.1086/309899.

S. Ho, C. Hirata, N. Padmanabhan, U. Seljak, and N. Bahcall. Correlation of CMB with large-scale structure. I. Integrated Sachs-Wolfe tomography and cosmological implications. Phys. Rev. D, 78(4):043519, August 2008. doi: 10.1103/PhysRevD.78.043519.

D. Hooper and L.-T. Wang. Possible evidence for axino dark matter in the galactic bulge. Phys. Rev. D, 70(6):063506, September 2004. doi: 10.1103/PhysRevD.70.063506.

F. Hoyle and M. S. Vogeley. Voids in the Point Source Catalogue Survey and the Updated Zwicky Catalog. ApJ, 566:641–651, February 2002. doi: 10.1086/338340.

W. Hu. Wandering in the Background: A CMB Explorer. *ArXiv Astrophysics e-prints*, August 1995.

W. Hu and R. Scranton. Measuring dark energy clustering with CMB-galaxy correlations. Phys. Rev. D, 70(12):123002, December 2004. doi: 10.1103/PhysRevD.70.123002.

W. Hu, N. Sugiyama, and J. Silk. The physics of microwave background anisotropies. *Nature*, 386:37–43, March 1997. doi: 10.1038/386037a0.

J. Huchra, M. Davis, D. Latham, and J. Tonry. A survey of galaxy redshifts. IV - The data. ApJS, 52:89–119, June 1983. doi: 10.1086/190860.

L. Hui and Z. Haiman. The Thermal Memory of Reionization History. ApJ, 596:9–18, October 2003. doi: 10.1086/377229.

V. Icke. Voids and filaments. MNRAS, 206:1P–3P, January 1984.

S. Ilic. Cosmic Microwave and Infrared Backgrounds cross-correlation for ISW detection. *ArXiv e-prints*, May 2012.

S. Ilić, M. Douspis, M. Langer, A. Pénin, and G. Lagache. Cross-correlation between the cosmic microwave and infrared backgrounds for integrated Sachs-Wolfe detection. MNRAS, 416:2688–2696, October 2011. doi: 10.1111/j.1365-2966.2011.19221.x.

S. Ilić, M. Langer, and M. Douspis. Detecting the integrated Sachs-Wolfe effect with stacked voids. *A&A*, 556:A51, August 2013. doi: 10.1051/0004-6361/201321150.

K. T. Inoue and J. Silk. Local Voids as the Origin of Large-Angle Cosmic Microwave Background Anomalies. I. ApJ, 648:23–30, September 2006. doi: 10.1086/505636.

K. T. Inoue and J. Silk. Local Voids as the Origin of Large-Angle Cosmic Microwave Background Anomalies: The Effect of a Cosmological Constant. ApJ, 664:650–659, August 2007. doi: 10.1086/517603.

W. Israel. Singular hypersurfaces and thin shells in general relativity. *Nuovo Cimento B Serie*, 44:1–14, July 1966. doi: 10.1007/BF02710419.

W. Israel. Singular hypersurfaces and thin shells in general relativity. *Nuovo Cimento B Serie*, 48:463–463, April 1967. doi: 10.1007/BF02712210.

N. Jarosik, et al. SEVEN-YEAR WILKINSON MICROWAVE ANISOTROPY PROBE (WMAP) OBSERVATIONS: SKY MAPS, SYSTEMATIC ERRORS, AND BASIC RESULTS. ApJS, 192(2):14, February 2011. ISSN 0067-0049. doi: 10.1088/0067-0049/192/2/14. URL http://stacks.iop.org/0067-0049/192/i=2/a=14?key=crossref.cac40d39f12a2a6ca4cbe19eea9f75a3.

T. H. Jarrett, et al. 2MASS Extended Source Catalog: Overview and Algorithms. *AJ*, 119:2498–2531, May 2000. doi: 10.1086/301330.

G. Jürgens and B. M. Schäfer. Integrated Sachs-Wolfe tomography with orthogonal polynomials. MNRAS, 425:2589–2598, October 2012. doi: 10.1111/j.1365-2966.2012.21125.x.

P. M. W. Kalberla, et al. GASS: the Parkes Galactic all-sky survey. II. Stray-radiation correction and second data release. *A&A*, 521:A17, October 2010. doi: 10.1051/0004-6361/200913979.

M. Kaplinghat, et al. Probing the Reionization History of the Universe using the Cosmic Microwave Background Polarization. ApJ, 583:24–32, January 2003. doi: 10.1086/344927.

L. Knox, A. Cooray, D. Eisenstein, and Z. Haiman. Probing Early Structure Formation with Far-Infrared Background Correlations. ApJ, 550:7–20, March 2001. doi: 10.1086/319732.

L. A. Kofman and A. A. Starobinskii. Effect of the Cosmological Constant on Largescale Anisotropies in the Microwave Background. *Soviet Astronomy Letters*, 11:271–274, September 1985.

E. W. Kolb, S. Matarrese, and A. Riotto. On cosmic acceleration without dark energy. *New Journal of Physics*, 8:322, December 2006. doi: 10.1088/1367-2630/8/12/322.

G. Lagache and J. L. Puget. Detection of the extra-Galactic background fluctuations at 170 mu m. *A&A*, 355:17–22, March 2000.

D. Larson, et al. Seven-year Wilkinson Microwave Anisotropy Probe (WMAP) Observations: Power Spectra and WMAP-derived Parameters. ApJS, 192:16, February 2011. doi: 10.1088/0067-0049/192/2/16.

G. Lemaître. L'Univers en expansion. *Annales de la Societe Scietifique de Bruxelles*, 53: 51, 1933.

A. Lewis, J. Weller, and R. Battye. The cosmic microwave background and the ionization history of the Universe. MNRAS, 373:561–570, December 2006. doi: 10.1111/j.1365-2966.2006.10983.x.

E. Lifshitz. On the Gravitational stability of the expanding universe. *J.Phys.(USSR)*, 10:116, 1946.

D. N. Limber. The Analysis of Counts of the Extragalactic Nebulae in Terms of a Fluctuating Density Field. II. ApJ, 119:655, May 1954. doi: 10.1086/145870.

E. V. Linder. The dynamics of quintessence, the quintessence of dynamics. *General Relativity and Gravitation*, 40:329–356, February 2008. doi: 10.1007/s10714-007-0550-z.

A. Lue, R. Scoccimarro, and G. Starkman. Differentiating between modified gravity and dark energy. Phys. Rev. D, 69(4):044005, February 2004. doi: 10.1103/PhysRevD.69.044005.

P. Madau, F. Haardt, and M. J. Rees. Radiative Transfer in a Clumpy Universe. III. The Nature of Cosmological Ionizing Sources. ApJ, 514:648–659, April 1999. doi: 10.1086/306975.

M. Mapelli, A. Ferrara, and E. Pierpaoli. Impact of dark matter decays and annihilations on reionization. MNRAS, 369:1719–1724, July 2006. doi: 10.1111/j.1365-2966.2006.10408.x.

J. C. Mather, et al. Measurement of the cosmic microwave background spectrum by the COBE FIRAS instrument. ApJ, 420:439–444, January 1994. doi: 10.1086/173574.

H. Matsuhara, et al. ISO deep far-infrared survey in the "Lockman Hole". II. Power spectrum analysis: evidence of a strong evolution in number counts. *A&A*, 361:407–414, September 2000.

M. McQuinn, et al. He II Reionization and its Effect on the Intergalactic Medium. ApJ, 694:842–866, April 2009. doi: 10.1088/0004-637X/694/2/842.

A. Meszaros. Voids in the Tolman-Bondi universe. *Ap&SS*, 207:5–15, September 1993. doi: 10.1007/BF00659125.

M.-A. Miville-Deschênes, G. Lagache, and J.-L. Puget. Power spectrum of the cosmic infrared background at 60 and 100 \umwith IRAS. *A&A*, 393:749–756, October 2002. doi: 10.1051/0004-6361:20020929.

C. Muñoz. Indirect dark matter searches and models. *Nuclear Instruments and Methods in Physics Research A*, 692:13–19, November 2012. doi: 10.1016/j.nima.2012.01.053.

S. Nadathur, S. Hotchkiss, and S. Sarkar. The integrated Sachs-Wolfe imprint of cosmic superstructures: a problem for ΛCDM. JCAP, 6:042, June 2012. doi: 10.1088/1475-7516/2012/06/042.

M. C. Neyrinck. ZOBOV: a parameter-free void-finding algorithm. MNRAS, 386:2101–2109, June 2008. doi: 10.1111/j.1365-2966.2008.13180.x.

M. C. Neyrinck, N. Y. Gnedin, and A. J. S. Hamilton. VOBOZ: an almost-parameter-free halo-finding algorithm. MNRAS, 356:1222–1232, February 2005. doi: 10.1111/j.1365-2966.2004.08505.x.

D. W. Olson and J. Silk. Primordial inhomogeneities in the expanding universe. II - General features of spherical models at late times. ApJ, 233:395–401, October 1979. doi: 10.1086/157400.

D. C. Pan, M. S. Vogeley, F. Hoyle, Y.-Y. Choi, and C. Park. Cosmic voids in Sloan Digital Sky Survey Data Release 7. MNRAS, 421:926–934, April 2012. doi: 10.1111/j.1365-2966.2011.20197.x.

M. Panek. Cosmic background radiation anisotropies from cosmic structures - Models based on the Tolman solution. ApJ, 388:225–233, April 1992. doi: 10.1086/171146.

P. Pápai and I. Szapudi. Cosmological Density Fluctuations on 100 Mpc Scales and their ISW Effect. ApJ, 725:2078–2086, December 2010. doi: 10.1088/0004-637X/725/2/2078.

S. G. Patiri, J. Betancort-Rijo, and F. Prada. On an analytical framework for voids: their abundances, density profiles and local mass functions. MNRAS, 368:1132–1144, May 2006. doi: 10.1111/j.1365-2966.2006.10202.x.

J. A. Peacock and R. E. Smith. Halo occupation numbers and galaxy bias. MNRAS, 318:1144–1156, November 2000. doi: 10.1046/j.1365-8711.2000.03779.x.

M. S. Peeples, D. H. Weinberg, R. Davé, M. A. Fardal, and N. Katz. Pressure support versus thermal broadening in the Lyman α forest - I. Effects of the equation of state on longitudinal structure. MNRAS, 404:1281–1294, May 2010. doi: 10.1111/j.1365-2966.2010.16383.x.

A. Pénin, O. Doré, G. Lagache, and M. Béthermin. Modeling the evolution of infrared galaxies: clustering of galaxies in the cosmic infrared background. *A&A*, 537:A137, January 2012. doi: 10.1051/0004-6361/201117489.

A. A. Penzias and R. W. Wilson. A Measurement of Excess Antenna Temperature at 4080 Mc/s. ApJ, 142:419–421, July 1965. doi: 10.1086/148307.

W. J. Percival, et al. Measuring the Baryon Acoustic Oscillation scale using the Sloan Digital Sky Survey and 2dF Galaxy Redshift Survey. MNRAS, 381:1053–1066, November 2007a. doi: 10.1111/j.1365-2966.2007.12268.x.

W. J. Percival, et al. The Shape of the Sloan Digital Sky Survey Data Release 5 Galaxy Power Spectrum. ApJ, 657:645–663, March 2007b. doi: 10.1086/510615.

S. Perlmutter, et al. Measurements of Omega and Lambda from 42 High-Redshift Supernovae. ApJ, 517:565–586, June 1999. doi: 10.1086/307221.

A. Pisani, G. Lavaux, P. M. Sutter, and B. D. Wandelt. Real-space density profile reconstruction of stacked voids. *ArXiv e-prints*, June 2013.

Planck Collaboration. Planck early results. XVIII. The power spectrum of cosmic infrared background anisotropies. *A&A*, 536:A18, December 2011a. doi: 10.1051/0004-6361/201116461.

Planck Collaboration. Planck early results. VI. The High Frequency Instrument data processing. *A&A*, 536:A6, December 2011b. doi: 10.1051/0004-6361/201116462.

Planck Collaboration. Planck 2013 results. XII. Component separation. *ArXiv:1303.5072*, March 2013a.

Planck Collaboration. Planck 2013 Results. XXIV. Constraints on primordial non-Gaussianity. *ArXiv:1303.5084*, March 2013b.

Planck Collaboration. Planck 2013 results. XIX. The integrated Sachs-Wolfe effect. *ArXiv:1303.5079*, March 2013c.

Planck Collaboration. Planck 2013 results. I. Overview of products and scientific results. *ArXiv:1303.5062*, March 2013d.

Planck Collaboration. Planck 2013 results. XVI. Cosmological parameters. *ArXiv:1303.5076*, March 2013e.

Planck Collaboration, et al. Planck 2013 results. XXIII. Isotropy and Statistics of the CMB. *ArXiv e-prints*, March 2013.

T. A. Porter, R. P. Johnson, and P. W. Graham. Dark Matter Searches with Astroparticle Data. *ARA&A*, 49:155–194, September 2011. doi: 10.1146/annurev-astro-081710-102528.

J.-L. Puget, et al. Tentative detection of a cosmic far-infrared background with COBE. *A&A*, 308:L5, April 1996.

A. Rakić, S. Räsänen, and D. J. Schwarz. The microwave sky and the local Rees-Sciama effect. MNRAS, 369:L27–L31, June 2006. doi: 10.1111/j.1745-3933.2006.00167.x.

B. Ratra and P. J. E. Peebles. Cosmological consequences of a rolling homogeneous scalar field. Phys. Rev. D, 37:3406–3427, June 1988. doi: 10.1103/PhysRevD.37.3406.

M. J. Rees and D. W. Sciama. Large-scale Density Inhomogeneities in the Universe. *Nature*, 217:511–516, February 1968. doi: 10.1038/217511a0.

M. Ricotti, N. Y. Gnedin, and J. M. Shull. The Evolution of the Effective Equation of State of the Intergalactic Medium. ApJ, 534:41–56, May 2000. doi: 10.1086/308733.

A. G. Riess, et al. Observational Evidence from Supernovae for an Accelerating Universe and a Cosmological Constant. *AJ*, 116:1009–1038, September 1998. doi: 10.1086/300499.

R. K. Sachs and A. M. Wolfe. Perturbations of a Cosmological Model and Angular Variations of the Microwave Background. ApJ, 147:73, January 1967. doi: 10.1086/148982.

N. Sakai and K. T. Inoue. Cosmic microwave background anisotropy from nonlinear structures in accelerating universes. Phys. Rev. D, 78(6):063510, September 2008. doi: 10.1103/PhysRevD.78.063510.

N. Sakai, N. Sugiyama, and J. Yokoyama. Effect of Void Network on Cosmic Microwave Background Anisotropy. ApJ, 510:1–10, January 1999. doi: 10.1086/306550.

H. Sato and K. Maeda. The Expansion Law of the Void in the Expanding Universe. *Progress of Theoretical Physics*, 70:119–127, July 1983. doi: 10.1143/PTP.70.119.

U. Sawangwit, et al. Cross-correlating WMAP5 with 1.5 million LRGs: a new test for the ISW effect. MNRAS, 402:2228–2244, March 2010. doi: 10.1111/j.1365-2966.2009.16054.x.

B. M. Schäfer. Mixed three-point correlation functions of the non-linear integrated Sachs-Wolfe effect and their detectability. MNRAS, 388:1394–1402, August 2008. doi: 10.1111/j.1365-2966.2008.13526.x.

B. M. Schäfer, A. F. Kalovidouris, and L. Heisenberg. Parameter estimation biases due to contributions from the Rees-Sciama effect to the integrated Sachs-Wolfe spectrum. MNRAS, 416:1302–1310, September 2011. doi: 10.1111/j.1365-2966.2011.19125.x.

J. Schaye, T. Theuns, M. Rauch, G. Efstathiou, and W. L. W. Sargent. The thermal history of the intergalactic medium*. MNRAS, 318:817–826, November 2000. doi: 10.1046/j.1365-8711.2000.03815.x.

P. Schneider. Weak Gravitational Lensing. *ArXiv Astrophysics e-prints*, September 2005.

S. Seager, D. D. Sasselov, and D. Scott. A New Calculation of the Recombination Epoch. *ApJ*, 523:L1–L5, September 1999. doi: 10.1086/312250.

U. Seljak and M. Zaldarriaga. A Line-of-Sight Integration Approach to Cosmic Microwave Background Anisotropies. ApJ, 469:437, October 1996. doi: 10.1086/177793.

J. M. Shull and M. E. van Steenberg. X-ray secondary heating and ionization in quasar emission-line clouds. ApJ, 298:268–274, November 1985. doi: 10.1086/163605.

L. Sodré, Jr. Cosmology with large galaxy redshift surveys. In J. Alcaniz, et al., editors, *American Institute of Physics Conference Series*, volume 1471 of *American Institute of Physics Conference Series*, pages 22–26, October 2012. doi: 10.1063/1.4756806.

D. N. Spergel, et al. First-Year Wilkinson Microwave Anisotropy Probe (WMAP) Observations: Determination of Cosmological Parameters. ApJS, 148:175–194, September 2003. doi: 10.1086/377226.

V. Springel, et al. Simulations of the formation, evolution and clustering of galaxies and quasars. *Nature*, 435:629–636, June 2005. doi: 10.1038/nature03597.

L. E. Strigari. Galactic Searches for Dark Matter. *ArXiv e-prints*, November 2012.

N. Sugiyama. Cosmic Background Anisotropies in Cold Dark Matter Cosmology. ApJS, 100:281, October 1995. doi: 10.1086/192220.

P. M. Sutter, G. Lavaux, B. D. Wandelt, and D. H. Weinberg. A First Application of the Alcock-Paczynski Test to Stacked Cosmic Voids. ApJ, 761:187, December 2012. doi: 10.1088/0004-637X/761/2/187.

P. M. Sutter, Guilhem Lavaux, Benjamin D. Wandelt, and David H. Weinberg. A PUBLIC VOID CATALOG FROM THE SDSS DR7 GALAXY REDSHIFT SURVEYS BASED ON THE WATERSHED TRANSFORM. ApJ, 761 (1):44, December 2012. ISSN 0004-637X. doi: 10.1088/0004-637X/761/1/44. URL http://arxiv.org/abs/1207.2524http://stacks.iop.org/0004-637X/761/i=1/a=44?key=crossref.1ec5ccdd2908f446556ebd656771ba47.

N. Suzuki, et al. The Hubble Space Telescope Cluster Supernova Survey. V. Improving the Dark-energy Constraints above z ¿ 1 and Building an Early-type-hosted Supernova Sample. ApJ, 746:85, February 2012. doi: 10.1088/0004-637X/746/1/85.

N. Taburet, C. Hernández-Monteagudo, N. Aghanim, M. Douspis, and R. A. Sunyaev. The ISW-tSZ cross correlation: ISW extraction out of pure CMB data. *ArXiv e-prints*, December 2010.

M. Tegmark, et al. Cosmological constraints from the SDSS luminous red galaxies. Phys. Rev. D, 74(12):123507, December 2006. doi: 10.1103/PhysRevD.74.123507.

T. Theuns, J. Schaye, and M. G. Haehnelt. Broadening of QSO Lyα forest absorbers. MNRAS, 315:600–610, July 2000. doi: 10.1046/j.1365-8711.2000.03423.x.

R. C. Tolman. Effect of Inhomogeneity on Cosmological Models. *Proceedings of the National Academy of Science*, 20:169–176, March 1934. doi: 10.1073/pnas.20.3.169.

S. L. Vadas. The Signatures of Voids and the CMBR. In H. Böhringer, G. E. Morfill, and J. E. Trümper, editors, *Seventeeth Texas Symposium on Relativistic Astrophysics and Cosmology*, volume 759 of *Annals of the New York Academy of Sciences*, page 710, 1995. doi: 10.1111/j.1749-6632.1995.tb17641.x.

P. Valageas and J. Silk. The reheating and reionization history of the universe. *A&A*, 347:1–20, July 1999.

R. A. Vanderveld, É. É. Flanagan, and I. Wasserman. Luminosity distance in "Swiss cheese" cosmology with randomized voids. I. Single void size. Phys. Rev. D, 78(8): 083511, October 2008. doi: 10.1103/PhysRevD.78.083511.

D. A. Wake, et al. The 2dF-SDSS LRG and QSO Survey: evolution of the clustering of luminous red galaxies since z = 0.6. MNRAS, 387:1045–1062, July 2008. doi: 10.1111/j.1365-2966.2008.13333.x.

S. Weinberg. The cosmological constant problem. *Reviews of Modern Physics*, 61:1–23, January 1989. doi: 10.1103/RevModPhys.61.1.

S. Weinberg. *Cosmology*. Oxford University Press, 2008.

C. Wetterich. Cosmology and the fate of dilatation symmetry. *Nuclear Physics B*, 302: 668–696, June 1988. doi: 10.1016/0550-3213(88)90193-9.

E. L. Wright. Angular Power Spectra of the COBE DIRBE Maps. ApJ, 496:1, March 1998. doi: 10.1086/305345.

M. Zaldarriaga. Polarization of the microwave background in reionized models. Phys. Rev. D, 55:1822–1829, February 1997. doi: 10.1103/PhysRevD.55.1822.

M. Zaldarriaga, L. Hui, and M. Tegmark. Constraints from the Lyα Forest Power Spectrum. ApJ, 557:519–526, August 2001. doi: 10.1086/321652.

S. Zaroubi. The Epoch of Reionization. In T. Wiklind, B. Mobasher, and V. Bromm, editors, *Astrophysics and Space Science Library*, volume 396 of *Astrophysics and Space Science Library*, page 45, 2013. doi: 10.1007/978-3-642-32362-1_2.

H. Zhan. Rees-Sciama Effect and Impact of Foreground Structures on Galaxy Redshifts. ApJ, 740:26, October 2011. doi: 10.1088/0004-637X/740/1/26.